# Rheology dependent on the distance to a Propagating Fault Tip

## The Microstructural Record of Fault Rocks at Hypocentral Depth

Lisa Marie Brückner

*Dissertation zur Erlangung des Doktorgrades*
*an der Fakultät für Geowissenschaften*
*der Ludwig-Maximilians-Universität München*

München, 21.08.2023

*…. the principle espoused is that the property of the whole is a function of the property of the parts (Scholz, 1990).*

Erstgutachterin: Prof. Dr. Claudia A. Trepmann

Zweitgutachter: Prof. Dr. Jörn H. Kruhl

Tag der Disputation: 11.12.2023

# Summary

The microfabric of fault rocks from the base of the seismogenic zone, i.e., for the continental crust at depths of greenschist facies conditions, is crucial for the understanding of the seismic cycle. It provides information about the rheology during episodic deformation, controlling the strength of crustal rocks, and is thus relevant for large-scale geological processes in tectonic active regions.

In this thesis, fault rocks of the Silvretta basal thrust in the central Alps and the Defereggen-Antholz-Vals (DAV) strike-slip shear zone in the Eastern Alps were analyzed to unravel the deformation, as well as stress and strain-rate histories within fundamentally different geological settings. Various fault rocks, containing pseudotachylytes and (ultra-)mylonites, were selected for the model case of the Silvretta basal thrust and compared to mylonitic pegmatites and cataclasites of a strike-slip tectonic setting (DAV), to evaluate the question of whether there is more than one transient high-stress deformation event recorded in one rock and the relation to the long-term shear zone activity. Fault rocks from both localities were deformed at greenschist facies conditions, i.e., they originate from the base of the seismogenic zone. The focus is on the microstructural record displaying a specific sequence of deformation mechanisms, to infer different stress and strain-rate conditions at hypocentral depth, not directly accessible for in situ measurements. The findings are compared to gneisses of the Vredefort impact structure in South Africa, which were shocked to relatively low shock conditions at depths comparable to those at the base of the seismogenic zone. These deformation conditions are compared and contrasted to those at hypocentral depth.

At the base of the Silvretta nappe, pseudotachylyte-bearing amphibole-rich gneisses and quartz-rich layers concordant to the foliation occur, which record the decoupling of the nappe from its original substratum. Hornblende within the amphibole-rich lithology frequently shows $(\bar{1}01)[101]$ mechanical twins, (010) kink bands, and microfractures associated with pseudotachylytes, indicating high-stress dislocation glide-controlled deformation together with microfracturing. Mechanical amphibole twins reveal transient high peak stresses of >400 MPa during coseismic deformation and formation of pseudotachylytes. Quartz in contact with twinned amphiboles shows deformation lamellae, short-wavelength undulatory extinction, as well as microfracturing, with new grains (<15 μm) along cracks displaying a crystallographic preferred orientation (CPO) controlled by the host. These microstructures indicate dislocation glide-controlled deformation, coeval with high-stress amphibole deformation, and associated with coseismically pseudotachylyte formation during thrusting. In contrast, concordant quartz-rich lithologies are deformed by dislocation creep, as evident from homogeneous recrystallized aggregates with a CPO related to <a> dislocation glide. Systematic differences in the distribution and grain sizes of the recrystallized grains indicate deformation at differential stresses from a few tens to hundred MPa. No evidence of increasing strain towards the contact with the amphibole-rich lithology can be observed. Instead, a decreasing number of recrystallized grains towards the contact is locally recorded. Furthermore, quartz is affected by

shear fractures related to pseudotachylytes, offsetting the recrystallized microfabric. This and the decreasing or rather missing dislocation creep-related strain gradient indicate that quartz dislocation creep is preceding and not directly related to high-stress/high strain-rate deformation. At greenschist facies conditions amphibole represents the strong phase during creep, but the weak phase during transient coseismic high-stress events, due to lower fracture toughness and melting temperature, as well as higher shear modulus, relative to quartz. A major influence of thermal runaway can be ruled out for pseudotachylyte formation, as it cannot be explained by instabilities during dislocation creep of the quartz-rich lithologies. The observed heterogeneous deformation behaviors are interpreted to be controlled by the distances to the tip of the seismic fault during nappe decoupling.

Ancient earthquakes are associated with the decoupling of the Silvretta nappe, recorded by the overprinting relationship of different generations of pseudotachylytes. Pseudotachylytes formed associated with high-stress crystal plasticity ($\sigma_d$ >400 MPa), whereas mylonitic quartz clasts enclosed within deformed pseudotachylytes and mylonitic vein-quartz, hosting folded pseudotachylyte injection veins, reflect creep at lower stresses (~100 MPa) after seismic rupturing. These deformed pseudotachylytes can be crosscut by pristine pseudotachylytes at lithological heterogeneities, indicating a second, independent stage of coseismic rupturing. Given the evidence of dynamic dislocation creep of quartz after the first pseudotachylyte formation event and the presence of stilpnomelane and epidote associated with all fault rocks, similar ambient greenschist facies conditions during all stages of deformation are indicated. Whereas the deformed first generation of pseudotachylytes represents an independent precursor tectonic stage before nappe decoupling in Upper Cretaceous to Paleocene times, the intermediate stage of creep is interpreted as deformation at a large distance to the propagating thrust tip. Pristine pseudotachylytes stand for the last imprint of the affected rocks finally leading to the decoupling of the Silvretta nappe. The deformed pseudotachylytes reveal that pseudotachylytes are representing the lower viscosity lithology during creep in relation to the host rocks. This assumes that deformation during thrust fault propagation primarily affects rocks that have not yet been ruptured during the same event and pseudotachylytes are the high strength phase during coseismic high-stress plasticity. Fast relaxation rates from peak stresses of the second coseismic high-stress event were recorded by the growth of strain-free new grains, at quasi-isostatic stress conditions, aligned along the damage zone of the high-stress imprint, i.e., deformed pseudotachylytes or former microcracks within the mylonitic quartz.

Valuable microstructural indicators, which display episodic deformation that only transiently prevails at hypocentral depth, are commonly obscured. To identify the conditions, which are responsible for the formation of such unique microfabrics, fine-grained quartz aggregates localized along cleavage planes in coarse quartz crystals within pseudotachylyte-bearing breccias are compared and contrasted to those in gneisses, shocked to relatively low dynamic pressure conditions from the Vredefort impact structure. The recrystallized strings occur in sets parallel to *r*- and *z*-rhombohedral planes for both localities and additionally along basal planes in Vredefort gneisses. In the Silvretta fault rocks, they exclusively occur in coarse vein-quartz clasts within tensional domains associated with the asymmetry of the propagating

pseudotachylyte-related fault tip, indicating cleavage fracturing occurred simultaneously with pseudotachylyte generation. Almost coeval with cleavage fracturing localized comminution and cataclasis occurred during shearing, resulting in microcrystalline quartz-rich zones along planes of high shear strain (i.e., pseudotachylytes). Within Vredefort gneisses cleavage of quartz is related to shock during impact cratering. Cleavage fracturing along planes of minimum free surface energy is suggested to be the result of fast unloading from high transient stresses in both geological settings: unloading from >400 MPa within seconds or minutes during faulting and from <20 GPa within milliseconds during impacting. An additional influence also of thermal shock caused by frictional heating is likely. Within both geological settings, strain-free grains grew in situ restricted to the damage zone surrounding the cleavage fractures at quasi-isostatic stress conditions by recrystallization, which requires sufficiently high temperature conditions (about >300 °C). Comparing the rock record of fundamentally different geological settings allows the evaluation of microstructural criteria diagnostic for the rheological behavior during the deformation history.

As the signature of the stress/strain history at the base of the seismogenic zone might be different for various tectonic regimes, although formed at the same metamorphic conditions, the deformation record of the Defereggen-Antholz-Vals (DAV) strike-slip shear zone is investigated. Mylonitic pegmatites situated north of the DAV shear zone record episodic deformation at constant greenschist facies conditions after the Eo-Alpine tectonometamorphic event and before uplift in the Oligocene. Fluorapatite-allanite-epidote coronae around monazite formed at about 60 Ma and postdate a main mylonitic foliation and predate a second shear band foliation. Quartz shows distinct differences in deformation microstructures, controlled by the crystallographic orientation. Rhombohedral and prism <a> dislocation glide in favorable orientations, i.e., low-Schmid factor orientations, forms elongated high aspect ratio grains. Localized recrystallization (i.e., dislocation creep) takes place at sites of increased dislocation densities in less favorable oriented quartz and microcracking in unsuitable orientations for dislocation glide. Distributed quartz microcracking occurred quasi-instantaneously coeval with cataclastic deformation of garnet and tourmaline, indicating transient high stresses during coseismic deformation. During subsequently decreasing stresses, within the shear band boundaries, precipitation of small isometric quartz grains took place from the pore fluid, probably derived from the recrystallization of fluid-rich quartz porphyroclasts. Coeval or subsequent transient deformation is recorded by cataclasites with mylonitic components, which were interpreted to reflect the main activity of the DAV during the uplift below greenschist facies conditions. The mylonitic pegmatites record systematically changing deformation mechanisms during episodic deformation at greenschist facies conditions dominantly governed by changing stresses and strain-rates, as opposed to changing temperatures. Discrete stages of transient deformation during the long-term activity of the shear zone are recorded after and before a stage of creep at decreasing stresses.

The rock record of the different geological settings gives new insights into the deformation processes of rupturing events at hypocentral depth. The microstructures preserved within pseudotachylyte-related (fault) rocks indicate high stresses (>400 MPa), that prevail only transiently at the base of the seismogenic zone, and are diagnostic for coseismic deformation. These coseismically high stresses are associated with stress redistribution, controlled by the distance to the tip of the propagating fault instead of depending on local heterogeneities, as evident by systematic variations of deformation mechanisms at the same greenschist facies conditions. The specific stress and strain-rate conditions are decisive regarding the rheological rock behavior during seismic faulting, as opposed to a change in pressure and temperature. Deformation conditions during major earthquakes, revealed by these commonly modified microstructures, are comparable to those realized during impact cratering at relatively deep parts of the impact structures characterized by relatively low shock conditions and allow evaluation of the material behavior at non-steady state conditions. Pseudotachylytes, representing the last imprint after the passage of the rupture, are therefore not the only microstructural marker of coseismic deformation and ancient earthquakes. The findings from this thesis highlight the importance of the different strengths of crustal rocks and the time-dependent rheology at specific stress/strain-rate conditions during the seismic cycle at the base of the seismogenic zone.

# Contents

# 1 Introduction

## 1.1 State of the Art - The Geological Record of the Seismic Cycle

### *1.1.1 Rock Deformation during the Seismic Cycle*

Large earthquakes nucleate and ruptures propagate within the seismogenic zone of the lithosphere (Brace and Byerlee, 1970; Scholz, 2002, 1998), i.e., the temperature-depth region, where hypocenters are located. During earthquakes, continental rocks behave by localized pressure-dependent brittle failure within the *schizosphere*, whereas the *plastosphere* is characterized by distributed temperature- and strain-rate-dependent creep, resulting in faults and shear zones, which are deep continuations of seismic active faults (Fig. 1.1; e.g., Scholz, 2002; Sibson, 1977). The base of the seismogenic zone (Marone and Scholz, 1988) coincides with the temperature-depth area, characterized by upper greenschist facies conditions and the onset of crystal-plastic deformation of wet quartz, i.e., temperatures and depth of approximately 300 ± 50 °C and ~10-15 km depth, respectively (Fig. 1.1; e.g., Hirth et al., 2001; Hirth and Tullis, 1994; Marone and Scholz, 1988; Scholz, 1988; Stipp et al., 2002; Stöckhert et al., 1999; van Daalen et al., 1999), depending on the assumed geotherm (Burov and Watts, 2006). The transition from pressure-dependent deformation (*schizosphere*) to thermally controlled creep-related deformation (*plastosphere*), is defined as the maximum rupture depth of large earthquakes (Scholz, 2002). The base of the seismogenic zone is therefore at a shallower depth as the maximum depth of a rupture during seismic events and corresponds to the upper limit of the transitional area (Fig. 1.1). Seismic rupture can propagate upwards towards the surface, as well as some distance downwards (e.g., Lin et al., 2003; Scholz, 1988; Sibson, 1983). The depth of the "*schizosphere-plastosphere* transition" is changing through the seismic cycle, which is usually divided into: *preseismic*, *coseismic*, *postseismic,* and *interseismic* phases, based on geodetic observations (e.g., Scholz, 2002, and references therein).

The deformation within shear zones during the seismic cycle, is episodic and controlled by stress loading and stress relaxation (e.g., Ellis and Stöckhert, 2004a; Nüchter and Ellis, 2010, Ellis et al., 2006). Trough interseismic periods, the shear zone reloads the *schizosphere* which is envisaged in the "deep slip model" by Scholz (2002). Seismic slip along a fault occurs within timescales of a few seconds and correlates with the duration of coseismic stress redistribution (e.g., Wald and Heaton, 1994). In contrast, stress relaxation during postseismic stages is expected to have a duration lower than typical recurrence intervals of $10^2$-$10^3$ years (Yeats, 1997, and references therein). The highest differential stresses within the continental crust are realized in the transitional area, whose strength is controlled by processes at low temperature and high stress conditions (e.g., Sibson, 1983; Stünitz et al., 2017; Trepmann et al., 2017). Therefore, the region, marked by upper greenschist metamorphic conditions, below the seismogenic zones to the maximum rupture depth (Fig. 1.1), is considered to be the most important area regarding rock rheology during the seismic cycle and long-lived shear zone activity.

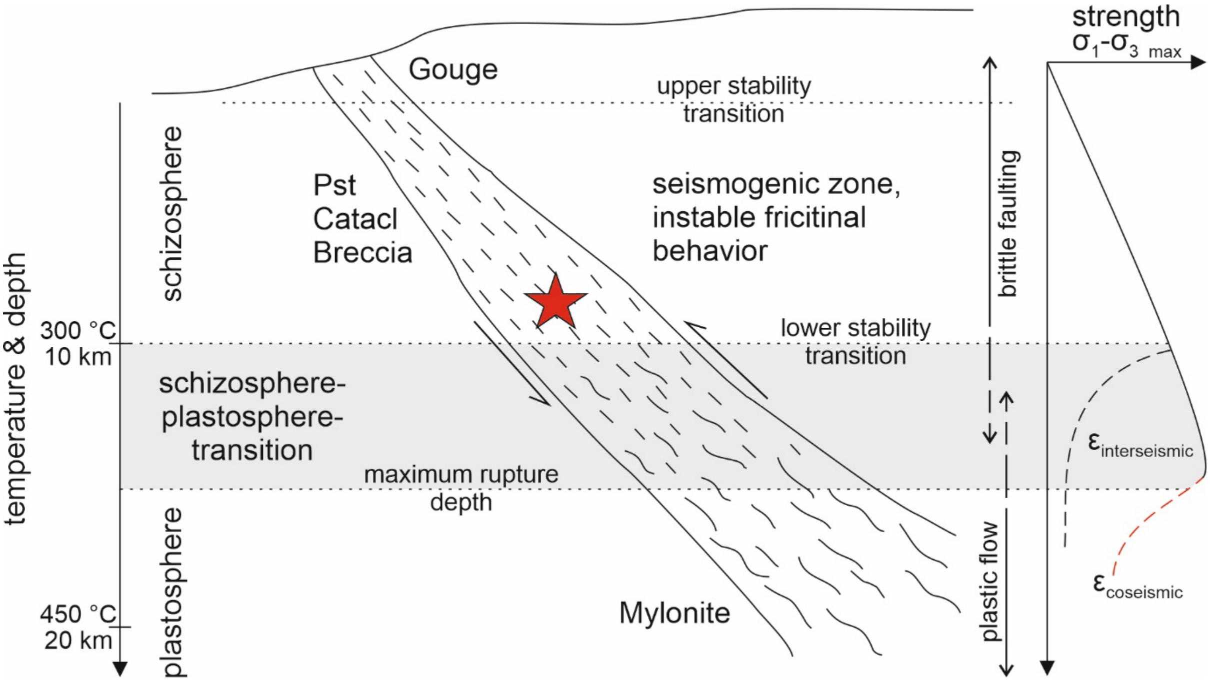

**Figure 1.1:** Conceptual shear zone model with major geological and seismological features, including the respective fault rocks: gouges, pseudotachylytes (Pst), cataclasites (Catacl), breccias and mylonites. Temperatures of ~300 °C and ~450 °C, as well as depths of ~10 km and ~20 km coincide with the onset of quartz and feldspar crystal plasticity, respectively, depending on the geotherm. Red star marks the typical hypocenter of large earthquakes. Modified after Scholz (1988) and Sibson (1983, 1977).

Numerical models simulated transient high stresses in the uppermost *plastosphere*, that can be induced within a few seconds by coseismic slip, i.e., during large earthquakes, within the *schizosphere* (Ellis and Stöckhert, 2004a; Nüchter and Ellis, 2010; Nur and Mavko, 1974; Savage and Prescott, 1978), causing postseismic creep at initially high and then relaxing stresses (Ellis et al., 2006; Ellis and Stöckhert, 2004a, 2004b; Nüchter and Ellis, 2011, 2010). This view is consistent with the natural record of exhumed shear zone rocks (e.g., Küster and Stöckhert, 1999; Trepmann et al., 2017; Trepmann and Stöckhert, 2003, 2002, 2001). Twin paleopiezometry indicates short-term temporary peak stresses of several hundred MPa (Trepmann and Stöckhert, 2001). Especially, quartz microfabrics are known to be largely modified during deformation associated with the seismic cycle and systematically changing stresses well-below hypocentral depths (Famin et al., 2004; Küster and Stöckhert, 1999; Nüchter and Stöckhert, 2008, 2007; Trepmann and Stöckhert, 2003a). Quartz is therefore highly suitable for identifying transient stresses during periods of co- and postseismic deformation by overprinting microstructures. Also, the upper border of the *schizosphere-plastosphere* transition correlates with the onset of crystal-plastic behavior of quartz (Fig. 1.1). Furthermore, quartz deformation processes are very well reported from experimental and natural microstructural observations (e.g., Hirth and Tullis, 1994, 1992; Hobbs, 1968; Trepmann et al., 2017, 2007; Trepmann and Stöckhert, 2013, 2003).

Grain-scale processes, displayed by the microstructural record, control the deformation of rocks at depth, which in turn is responsible for large-scale tectonic processes, i.e., during long-term shear zone activity, and have therefore an influence on the earth surface, i.e., offsetting crustal blocks during orogeny. However, the deformation conditions, controlling the rock behavior at hypocentral depth, and their role during the seismic cycle are still critically discussed, as they are not directly accessible for in situ measurements. They are difficult to unravel, because no seismological data of the transitional area is available, as well as distinct information from the inversion of postseismic surface deformation (e.g., Bürgmann and Dresen, 2008). Furthermore, deformation experiments do not expose the relevant range of scales in time and space, which, in contrast can be deciphered by the natural (micro-)structural record of exhumed fault-related rocks.

### *1.1.2 Evidence of more than one High-Stress event within large Shear Zones*

Large shear zone systems might comprise interacting fault systems with complex networks. Within these settings, recurring earthquakes are predicted which refers to the period of loading cycles or the time between subsequent rupturing, respectively (Scholz, 2002, and references therein). The recurrence of large earthquakes is complicated to study, due to large time intervals. Previous studies focused on the formation of pseudotachylytes, representing coseismic deformation. They commonly show evidence of single slip events (Barker, 2005; Di Toro and Pennacchioni, 2005; Wenk et al., 2000) and stay intact due to strain-hardening processes, but can re-rupture during subsequent slip events (Rowe et al., 2018; Swanson, 1992). Within large shear zones several generations of pseudotachylytes are reported being themselves partially deformed and/or displaying a multiple crosscutting relationship, also with the associated mylonites (e.g., Altenberger et al., 2013, 2011; Braathen et al., 2004; Koch and Masch, 1992; Lin, 2008b; Moecher and Steltenpohl, 2009; Pittarello et al., 2012; Sibson and Toy, 2006; Takagi et al., 2000; White, 2012, 2004), which is often interpreted to represent repeated rupturing during successive seismic cycles (Koch and Masch, 1992; Passchier, 1982a; Pennacchioni and Cesare, 1997; Rowe et al., 2018; Sibson, 1980; Swanson, 1992). However, unambiguous microstructural evidence of more than one transient high-stress event recorded within the same rock, is currently missing. This might be unexpected, as displacement of large crustal blocks over several tens of kilometers (i.e., during orogeny) along seismic active fault zones requires incremental fault growth, which is predicted with multiple earthquake cycles for large shear zone systems and by correlations between accumulated displacement and diameter of a fault plane (e.g., Cowie and Scholz, 1992a, 1992b, 1992c; Dawers et al., 1993; Schlische et al., 1996; Stein et al., 1988; Walsh and Watterson, 1988).

Earthquakes in the upper crust and below the seismogenic zone can be triggered by transiently localized high stresses/strain-rates, due to the mechanical contrast of heterogeneities, leading to plastic instabilities by internal feedback mechanisms (e.g., Hobbs et al., 1986; Hobbs and Ord, 1988; John et al., 2009; Koch and Masch, 1992; Regenauer-Lieb and Yuen, 2004; Thielmann et al., 2015; White, 2012, 1996). However, stresses at depths corresponding to the base of the seismogenic zone can also change “externally” during seismic activity in the upper crust (Ellis and Stöckhert, 2004a, 2004b; Nüchter and Ellis, 2010). At greenschist facies conditions, where rocks undergo long-term creep, high stress-loading rates are characteristic for stress redistribution related to seismic rupturing, as opposed to relatively continuous stress build-up due to local heterogeneities, i.e., rigid inclusions within a soft matrix or different lithologies (Küster and Stöckhert, 1999; Trepmann et al., 2017; Trepmann and Seybold, 2019; Trepmann and Stöckhert, 2009, 2003, 2002, 2001). However, these factors with the main difference in the “source of the stress pulses” (“internal” and “external” stress-build up and strain variations), are not mutually exclusive. The model proposed by Nüchter et al. (2013) demonstrates the unique imprint of a single high-stress event, with deformation at peak stresses after a preceding stage of creep at lower stresses, at one specific location depending on the distance to the fault tip at constant crustal depth (i.e., at greenschist facies conditions). During coseismic thrust fault propagation a characteristic sequence of ductile to brittle deformation structures and finally pseudotachylytes develop.

The generation of pseudotachylytes is suggested to reduce the strength of crustal rocks (e.g., Handy et al., 2001). In contrast, Mitchell et al. (2016) discuss that pseudotachylyte formation, inhibit further shear on the same slip surface and subsequent failure is accommodated at a new site. This view is consistent with deformation experiments (“*kick-cook-kick*” experiments), simulating a cycle of coseismic loading (“*kick*”) and postseismic creep (“*cook*”), followed by another high-stress stage (“*kick*”) (Trepmann et al., 2013). In addition, exhumed metamorphic rocks, indicating fast loading to high stresses followed by creep during stress relaxation (Birtel and Stöckhert, 2008; Küster and Stöckhert, 1999; Matysiak and Trepmann, 2012; Nüchter and Stöckhert, 2008, 2007; Trepmann et al., 2017; Trepmann and Stöckhert, 2003, 2002, 2001), can be related to the rupture of nearby seismically active faults leading in the formation of pseudotachylytes (Nüchter et al., 2013). In dependence of varying stresses and strain-rate, i.e., as realized during seismic and interseismic periods, different microstructures and lithologies within affected rocks have at given ambient temperature-pressure conditions a different strength (Evans and Kohlstedt, 1995; Kohlstedt et al., 1995). Furthermore, many other factors, as e.g., mineralogy, fluids, texture, grain size, etc. lead to softening and hardening processes within the fault rocks and can have an influence on the rock rheology and thus on the signature of the seismic cycle, as well as the development of the fault zone (e.g., Handy, 1989; Scholz, 2002).

Evidence of the complex episodic seismic history, including different deformation mechanisms and varying stress/strain-rate conditions, is often overprinted due to the long-term activity of large shear zones (e.g., Handy et al., 2007). However, not only the preservation but also the identification of microstructures indicating mutually seismic events is complex (Handy et al., 2007; Lin et al., 2005; Price et al., 2012; Sibson, 1980; Sibson and Toy, 2006; White, 1996). The distinction between pseudotachylytes related to the same high-stress event but derived from different host rocks, due to interaction of smaller-scaled faults during simultaneous rupture, and pseudotachylytes associated with different seismic events and separated by an inactive hiatus is difficult. Due to this complexity, it is still not sufficiently resolved how the presence of various fault-related rocks influence the strength of the continental crust, and thus the long-term activity of large shear zones with recurring earthquake cycles.

### *1.1.3 Rock Deformation related to different Tectonic Regimes*

Large-scale deformation during orogeny is governed by grain-scaled deformation processes located within shear zones. Also, other specific factors, as e.g., lithology, bulk displacement, external stress pulses, as well as large-scaled factors like variations in the mode of faulting, play a critical role during seismic rupturing. The geological record from the base of the seismogenic zone, is expected to exhibit differences in the deformation and stress history, depending on the tectonic regime, due to the different characteristic geometries and thus different orientations of principal normal stresses (e.g., Scholz, 2002). Numerical models simulated, that also the fault geometry can control coseismic stress perturbation (Nüchter and Ellis, 2011, 2010). The brittle strength, providing the framework for the maximum differential stresses in the transitional area, is the lowest for normal fault and the highest for thrust fault tectonic setting, respectively (Scholz, 2002). Simplified models based on laboratory investigations predict that thrust faulting requires higher stresses compared to normal faulting. Strike-slip fault settings show intermediate stresses and lie in between (Brace and Kohlstedt, 1980; Kirby, 1980; Sibson, 1986). Greater damage zones are expected for thrust fault settings due to the higher shear resistance compared to normal faults, assuming similar depth and fluid-pressure conditions (e.g., Sibson, 1986, 1974; Sibson and Toy, 2006).

After seismic events with high peak stresses ambient pressure-temperature conditions and far-field tectonic stresses can have an effect on subsequent relaxation and deformation processes, which in turn will affect stress relaxation rates. Microstructural investigations of natural fault rocks within pseudotachylyte-related strike-slip and thrust fault settings indicate similar coseismic loading rates, but characteristically differences in transiently peak stresses and stress relaxation rates, although they formed at the same ambient greenschist facies conditions and exhibit similar lithologies, as well as deformation mechanisms (Trepmann et al., 2017). Far-field extension and stress transfer due to post-seismic creep within the lower crust result in a gradual reloading of the fault within the upper crust (e.g., Freed, 2005; Huc et al., 1998; Kenner, 2004; Nüchter and Ellis, 2010; Thatcher, 1983).

After decoupling of a nappe during thrusting over underlying foreign tectonic units, as is the case with, e.g., the Silvretta nappe, lower stress conditions are relevant in comparison to relatively higher long-term stresses, that can be expected for rocks associated with a steeply dipping strike-slip geometry with a horizontal and vertical component, such as the DAV. This probably causes inferred systematic differences in the deformation histories (Trepmann et al., 2017). Additionally, thrust faults are characterized by low pressure-temperature gradients resulting from the fault plane's shallow dip angle. This is also observed in strike-slip fault systems, where there is minimal vertical displacement. Normal faults exhibit a significant vertical offset, that leads to a distinct pressure-temperature gradient during prolonged shear zone activity (e.g., Scholz, 2002). Consequently, the different tectonic regimes could exhibit systematic variations in the signature of multiple seismic events below the seismogenic zone.

## 1.2 Background information - Fault Rocks

Two different main types of fault rocks occur at the Silvretta basal thrust: pseudotachylytes and (ultra-)mylonites. Whereas it is generally accepted that pseudotachylytes are a typical expression of seismic slip along active brittle shear fractures and are produced at shallow crustal levels <10 km (Maddock, 1986; Passchier, 1982a, 1982b; Scholz, 1988), mylonites are generated by ductile deformation at greater depth (e.g., Sibson, 1977). In the mid- to lower crust, within the transitional regime (Fig. 1.1; Sibson, 1980, 1977), the formation of mylonite and pseudotachylytes can overlap (e.g., Hobbs et al., 1986; Sibson, 1980; White, 1996).

### *1.2.1 Pseudotachylytes*

Tectonic pseudotachylytes are quenched friction-induced melts, involving cataclasis and reflect coseismic deformation due to high strain-rates of about $10^{-2}$-10 m/s along the fault plane (e.g., Cowan, 1999; Grocott, 1981; Maddock, 1986; Magloughlin, 1992; Passchier, 1982a, 1982b; Passchier and Trouw, 2005; Philpotts, 1964; Rowe and Griffith, 2015; Sibson, 1975; Spray, 1995, 1992, 1987; Swanson, 1992). They appear commonly within dry intact crystalline host rocks, as a result of high-stress rupturing in association with the seismic cycle (e.g., Handy et al., 2007; Sibson and Toy, 2006; Spray, 1995). Pseudotachylytes are unique indicators of "fossil earthquakes", i.e., markers of paleo-seismic activity decorating the fault slip surfaces and overprinting the existing rock fabric (e.g., Cowan, 1999; Grocott, 1981; Maddock, 1983; McKenzie and Brune, 1972; Rowe and Griffith, 2015; Sibson, 1975; Spray, 1987; Swanson, 1992). Typically, they are representatives of fault rocks in the upper brittle crust (McKenzie and Brune, 1972; Philpotts, 1964; Wenk, 1978), but downward slip propagation can lead to deep-crustal pseudotachylytes (Lin, 2008b; Moecher and Steltenpohl, 2009; Sibson, 1980; Sibson and Toy, 2006) up to granulite facies conditions (Clarke and Norman, 1993). Pseudotachylytes are also known to form related to non-tectonically contexts along large landslide basis (e.g., Heuberger et al., 1984; Legros et al., 2000) or by impact cratering (e.g., Daly, 1947; Spray, 1998). Furthermore, formation of pseudotachylyte has been documented in continental collision and subduction zone regimes at greater depth (>60 km) (Andersen and Austrheim, 2006; Sherlock and Hetzel, 2001), even at eclogite facies high pressure conditions (e.g., Austrheim and Boundy, 1994).

Commonly pseudotachylytes, found within large fault zones exhumed from <20 km depth (Sibson and Toy, 2006), are often mentioned to be a result of different mechanisms that include previously mentioned (1) friction-induced melting during seismic rupture (McKenzie and Brune, 1972), (2) ultracataclasis (Hayward et al., 2016; Wenk, 1978) and (3) thermal runaway (e.g., Braeck and Podladchikov, 2007; John et al., 2009; Thielmann et al., 2015) and/or ductile instabilities (Hobbs et al., 1986) (ductile shear heating without frictional failure). At very low displacement rates Pec et al. (2012) demonstrated an amorphization without the production of a melt phase. The initial stage of pseudotachylyte formation is cataclasis by comminution due to mechanical grain size reduction and thus surface increase (e.g., Spray, 2010, 1995; Swanson, 1992), wherefore pseudotachylytes have been commonly reported associated with cataclasites (e.g., Magloughlin, 1992; Magloughlin and Spray, 1992; O'Hara, 1992). When the melting temperature of rock-forming minerals during coseismic slip on the fault plane is exceeded by frictional heating, pseudotachylytes are formed (Magloughlin and Spray, 1992; Spray, 1992; Swanson, 1992). In contrast to tectonic pseudotachylytes, cataclasites were generated by brittle comminution, i.e., fault gouge formation, and subsequent healing due to precipitation and/or grain boundary migration (e.g., Spray, 2010). The transition from cataclasite, without melt involvement, and pseudotachylyte is gradual (Spray, 1995). Disequilibrium melting results in inhomogeneous melts with similar compositions of the source rock (O'Hara, 1992; Spray, 2010, 1992; Swanson, 1992). Furthermore, pseudotachylyte formation within the seismogenic zone can appear together with the development of mylonites, causing the pseudotachylytic veins being reworked in the foliation of the host rock (Koch and Masch, 1992; Sibson, 1980; White, 1996). Thereby, crosscutting relationships are commonly destroyed and thus only difficult to detect within deformed and sheared pseudotachylytes.

The term "pseudotachylyte" was established by Shand (1916) due to its similarity with tachylytes, (volcanic glasses often occurring as dark veins). In the field, pseudotachylytes can show a huge range of appearances regarding color and geometry. Often, they were described as an amorphous material (e.g., Pec et al., 2012) and/or an aphanitic, dark rock (e.g., Lin, 2008b; Sibson, 1977; Sibson and Toy, 2006; Wenk, 1978) that shows evidence of a melt phase (e.g., Magloughlin and Spray, 1992; Sibson, 1977; Sibson and Toy, 2006). The commonly vein-shaped layers exhibit a very fine-grained matrix and display injection veins, intruding with a sharp contact into the host rock at a high angle, due to propagating fractures. Pseudotachylytic injection veins have been interpreted as filled tensile cracks, which were opened and displaced driven by the injection of a pressurized melt (e.g., Di Toro et al., 2005; Di Toro and Pennacchioni, 2005; Grocott, 1981; Sibson, 1975; Swanson, 1992), even if it is unclear whether cracks filled with injected material propagated in advance of the penetrating melt, or whether the cracks were succeeded, or a combination of both (Grocott, 1981). Injection veins quenched within ~1-$10^2$ s (Dixon and Dixon, 1989) and preserve, therefore, the strain in the host rock around the crack, as well as the conditions during coseismic to instantly subsequent post-seismic stage (Rowe et al., 2012). Glassy to very fine-grained microcrystalline matrix, together with observed chilled margins suggest rapid cooling due to extreme temperature gradients between the melt and the surrounding host material. The characteristic fabric of the pseudotachylyte matrix relates mainly to the solidification time of the melt, which depends on the temperature contrast to the host rock and therefore also on the depth (Scholz, 1988; Spray, 2010). Melting temperatures of 650-1730 °C (average ~1200 °C) are considered on the fault vein during seismic rupturing (Andersen and Austrheim, 2006; Austrheim and

Boundy, 1994; Caggianelli et al., 2005; Camacho et al., 1995; Di Toro and Pennacchioni, 2004; Lin and Shimamoto, 1998; O'Hara, 2001). Information about the melting temperature is difficult to reconstruct due to the non-equilibrium melting of pseudotachylytes. Acicular and skeletal-shaped microliths, spherulites, and devitrification structures can be found in crystalline pseudotachylytes (Passchier, 1982a), suggesting sufficient time during a slow crystallization at deeper crustal levels and not a formation due to ultracataclasis (Maddock, 1983; Sibson, 1975). The pseudotachylyte composition strongly depends on the degree of melting of host rock minerals and therefore on the lithology (Koch and Masch, 1992; Spray, 1992). Minerals like water-bearing phyllosilicates and amphiboles preferentially melt first and form the pseudotachylyte matrix, whereas other minerals, i.e., quartz and feldspar, stay intact and occur as remaining clasts within the matrix (e.g., Koch and Masch, 1992; Lin, 2008a; Maddock, 1992; O'Hara, 1992; Philpotts, 1964; Sibson, 1975; Spray, 2010, 1992; Swanson, 1992), depending on the fracture toughness and yield shear strength (e.g., Spray, 2010, 1992). Within the matrix frequently mineral and (host-)rock fragments, generally with a rounded shape due to mutual collision, occur. The presence of different minerals and/or the composition of microlites can help to determine the melting temperatures and pressure-temperature conditions during the formation of pseudotachylytes (Magloughlin, 1992). Radiogenic dating techniques are used to calculate the age of pseudotachylytes, which, however, are hampered by the presence of abundant host rock clasts (Bachmann et al., 2009; Thöni, 1988).

### *1.2.2 Mylonites*

Mylonites are ductile deformed cohesive rocks, which show a lineated and strong foliation, occurring in high-strain zones. Therefore, exhumed mylonites are often mentioned as an expression of fossil ductile shear zones, dominated by crystal-plastic deformation (e.g., Passchier and Trouw, 2005; Sibson, 1977). Viscous deformation is generally associated with deeper crustal levels, where the temperature rises and the rocks become weaker. In a depth of 10-15 km, depending on the geothermal gradient, the crust is deformed by flow rather than fracture. At that depth of the continental crust (i.e., lower greenschist facies) mylonites occur, which are commonly characterized by plastic deformation quartz, including, e.g., dynamic recrystallization, and brittle fracturing of feldspar. Strain localization, associated with strain-softening processes including, e.g., grain size reduction, is required for shear zone formation and the related mylonitic rocks (Tullis, 1990; White et al., 1980). Syntectonically recrystallization during plastic deformation is leading to grain size reduction rather than cataclasis (Carter et al., 1964; Sibson, 1977; Tullis et al., 1973; White, 1973). With increasing metamorphic conditions recrystallization and recovery mechanisms becoming more frequent.

Mylonitic zones are known from micrometer to kilometer-wide scale and can occur within any type of rock (Bak et al., 1975; Hanmer, 1988; Watterson, 1979). Dependent on the lithology and parent rock structure, different conditions are needed for mylonitization, resulting in wider high-grade shear zones and narrower low- to very low-grade shear zones, due to less efficient localized softening mechanisms (Hanmer et al., 1995; Whitmeyer and Simpson, 2003). In the field, mylonites show one or more tightly spaced and bent foliations with sheard offsets. The contact zone with the undeformed wall rock usually displays a gradual transition regarding the fabric and grain sizes (Passchier and Trouw, 2005). Commonly, porphyroclasts can be found within the matrix, together with lenses and/or layers of fine-grained material. Contained minerals show a shape-preferred and crystallographic-preferred orientation (SPO and CPO, respectively) due to the crystal plastic deformation. Mylonites can be classified as protomylonites (50-90 % porphyroclasts; 10-50 % matrix), (meso-)mylonites (10-50 % porphyroclasts; 50-90 % matrix), and ultramylonites (<10 % porphyroclasts; >90 % matrix) (Passchier and Trouw, 2005 and references mentioned within).

### *1.2.3 Silvretta Pseudotachylytes and Mylonites*

Based on isotopic investigations of pristine pseudotachylytes of the Silvretta nappe, their formation took place in Upper Cretaceous to Paleocene times (Rb/Sr about 75 Ma: Thöni, 1988; Ar/Ar 62-78 Ma: Bachmann et al., 2009). The Alpine mineral paragenesis, including stilpnomelane, indicates their development at lower greenschist facies conditions reaching 300 to 400 °C (Koch, 1990; Koch and Masch, 1992; Masch, 1970; Schmutz, 1995) and is consistent with related microfabrics in the host rocks of the pseudotachylytes (Bachmann et al., 2009; Trepmann et al., 2017). The occurrence of the fault rocks is associated to the basal thrust fault (Fig. 1.2) with a restriction of the pseudotachylyte-bearing zone of 300 m above the thrust plane (Koch and Masch, 1992; Masch, 1974, 1970; Schmutz, 1995). At the northwestern border to the Engadine Window, they can cover up to 40 % of the outcrops (Bachmann et al., 2009). Given the field occurrence in relation to the thrust contact and the observation that no components of the Penninic units occur in the pseudotachylytes, as well as the absence of pseudotachylytes in the footwall of the basal thrust shows that they have formed during the initial nappe decoupling before transport over the Penninic units (Koch, 1990; Koch and Masch, 1992; Laubscher, 1983; Schmutz, 1995).

Pseudotachylytes can be found in all gneisses (Koch and Masch, 1992), but are most common in amphibole-rich gneisses and less common with mica-rich gneisses (Schmutz, 1995). Pseudotachylytes occur as concordant (strike: N to NW; dip: shallow W to SW), discordant (strike: NE; dip: NW), and branching veins and/or either in breccias (Masch, 1970; Schmutz, 1995). Different generations of pristine and deformed pseudotachylytes can be found, displaying partially crosscutting relationships (Koch, 1990; Koch and Masch, 1992; Masch, 1974, 1970; Pittarello et al., 2022; Schmutz, 1995). Recently, Pittarello et al. (2022) suggested that only the relatively less common deformed pseudotachylytes represent deformation at greenschist facies conditions based on the presence of intergrown epidote-feldspar aggregates and that pristine pseudotachylytes formed at temperatures <250 °C during subduction of the Penninic Unit in the Paleogene. Pseudotachylytes can also occur within mylonites, where they crosscut the mylonitic foliation (predominantly subparallel to the Variscan foliation) and thus are interpreted to be younger than the mylonites (Koch, 1990; Koch and Masch, 1992; Masch, 1970). Mylonites are only found in quartz-rich gneisses, not in amphibole-rich gneisses.

Koch (1990) and Koch and Masch (1992) presented a model of a cyclic sequence of mylonitic deformation followed by pseudotachylyte formation in a closely related event, resulting in an overprinting and crosscutting relationship due to internal feedback mechanisms generated by lithological contrasts. The higher flow strength of Silvretta amphibolites, which were less affected by mylonitic deformation compared to quartz-rich gneisses, is supposed to trigger stress concentrations. As a consequence, pseudotachylytes were formed and developed more pronounced within the amphibole-rich lithology. After nappe decoupling and during its transport at Eo-Alpine metamorphic conditions, ultramylonites are generated, representing deformed pseudotachylytes with sharp boundaries crosscutting the host rock foliation. Furthermore, ultramylonites are described to occur in gradual transition to mylonites (Koch, 1990; Koch and Masch, 1992). However, pseudotachylytes are often observed without the occurrence of mylonites and vice versa (Koch and Masch, 1992; Schmutz, 1995).

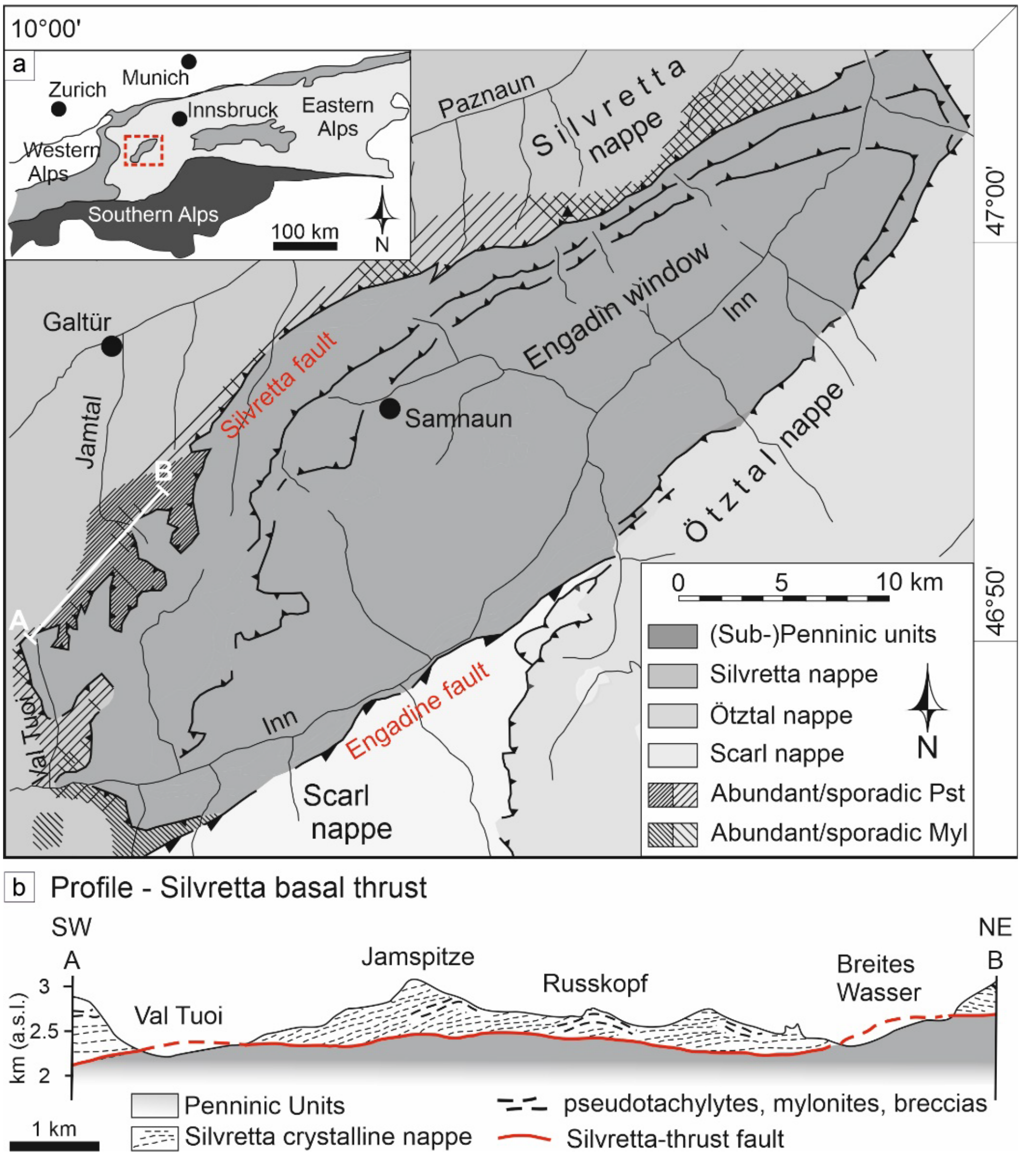

**Figure 1.2:** Geological overview of the Silvretta crystalline. **(a)** Schematic geological map of the study area at the western contact of the Silvretta nappe to the Penninic units of the Engadine Window with the distribution of pseudotachylytes (Pst) and mylonites (Myl) (modified after Koch and Masch, 1992). **(b)** Schematic geological profile of the basal thrust fault along the AB profile line in (a) (modified after Schmutz, 1995).

## 1.3 Aims of the Study

In this thesis, the temporal and spatial scale-dependent rock rheology related to seismic faulting at hypocentral depth is investigated by analyzing the Silvretta basal thrust fault rocks. The findings are compared to the DAV strike-slip fault rocks and shocked gneisses from the Vredefort impact structure. The rheology of rocks and the interaction between seismic and aseismic deformation at the base of the seismogenic zone during the seismic cycle, i.e., at the associated changing stress/strain(-rate) conditions, is crucial for the activity of shear zones along which crustal blocks are offset during orogeny. For this, rheological information over a wide range of scales, including time and space, has to be integrated: coseismic deformation related to seismic rupturing along the fault (seconds to minutes), postseismic creep below hypocentral depths ($10^1$ to $10^3$ yrs.) and long-term shear zone activity ($10^6$ yrs.). The findings of this thesis are expected to contribute to a better understanding of this interaction, and thus the record of past deformation.

Detailed multi-scale field-based studies of (fault) rocks, exhumed from hypocentral depth, are necessary to identify the controlling conditions for the formation of specific macro- and microscopic structures, which are valuable indicators of the commonly obscured deformation history controlling seismic faulting and creep. The Silvretta basal thrust, as well as the DAV strike-slip shear zone represent model cases for evaluating the role of transient deformation on the long-lived shear zone activity, since they can yield information of the deformation processes at depth, i.e., at greenschist facies conditions, which are otherwise not accessible or only indirectly measurable by geophysical techniques.

In this sense, the mutual overprinting of the various fault rocks (pseudotachylytes and (ultra-)mylonites), as well as the related distribution pattern of deformation structures within different host rock lithologies, will be analyzed in close relation to microstructural analyses. A special focus is on systematically changing deformation conditions regarding the temporal and spatial scale-dependent rheology of crustal rocks related to the distance of a propagating seismic fault tip. Thereby the stress/strain history during the different stages of the seismic cycle can be constrained, which in turn can be used to unravel the differentiation of various transient high stress-related deformation events in a particular rock. The identification of specific deformation sequences (e.g., several overprinting coseismic high-stress events) in connection with a systematic absence of such observations, will be used to evaluate how the presences of fault rocks control the strength of the continental crust and furthermore to understand the long-term activity of large shear zones including the recurrence of high-stress events, fault growth, as well as the processes during nappe decoupling.

# 2 Author Publications and Contributions

Parts of the research presented in Chapters 5 to 8 in this thesis are based on manuscripts already published for publication in peer-reviewed journals. The respective method and geological overview sections of the manuscripts have been compiled in Chapters 3 and 4, respectively, to better explain the relationships and avoid repetition. In the following an overview of the manuscripts and the author's contributions are given:

1) Chapter 5: Manuscript by Brückner, L. M. and Trepmann, C. A. (2021): Stresses during pseudotachylyte formation - Evidence from deformed amphibole and quartz in fault rocks from the Silvretta basal thrust (Austria). *Tectonophysics*, 817, 229046. https://doi.org/10.1016/j.tecto.2021.229046

   LB and CT designed the study. Fieldwork, sampling (including sample preparation), and microstructural analyses, including EBSD measurements, were carried out by LB under the supervision of CT. Figures were prepared by LB with contributions from CT. LB assembled the data and drafted the manuscript, in which all authors contributed to data analysis and discussions.

2) Chapter 6: Manuscript by Brückner, L. M., Trepmann, C. A., and Kaliwoda, M. (2023): Rheology dependent on the distance to the Propagating Thrust Tip – (Ultra-)Mylonites and Pseudotachylytes of the Silvretta basal Thrust. *Tectonics*, 42, 10. https://doi.org/10.1029/2023TC008010

   LB and CT developed the conceptual idea of the study. LB carried out fieldwork, sampling (including sample preparation) and thin section analyses, including SEM analysis, under the supervision of CT. Raman spectroscopy was carried out by LB and analyzed by the support of MK. LB prepared the figures, combined the data, and wrote the manuscript. All authors contributed to the interpretation and discussions of the data.

3) Chapter 7: Manuscript by Brückner, L. M., Dellefant, F., and Trepmann, C. A. (2024): Quartz Cleavage Fracturing and subsequent Recrystallization along the Damage Zone recording fast Stress Unloading. *Journal of Structural Geology*, 178, 105008. https://doi.org/10.1016/j.jsg.2023.105008

   LB was responsible for fieldwork, sampling, and thin section analyses for the Silvretta area, including SEM analysis. FD was responsible for data analyses regarding Vredefort samples. LB combined the data and wrote the original draft, whereas FD and CT were responsible for reviewing and editing. All authors contributed to the conceptualization, visualization and investigation. In addition, the manuscript was prepared under the supervision of CT.

4) Chapter 8: Manuscript by Hentschel, F., Janots, E., Magnin, V., Brückner, L. M., and Trepmann, C. A. (2022): Transient deformation and long-term tectonic activity in the Eastern Alps recorded by mylonitic pegmatites. *Journal of Structural Geology*, 155, 104507. https://doi.org/10.1016/j.jsg.2021.104507

   FH, LB, and CT developed the underlying conceptual idea of this study. FH and CT performed fieldwork data acquisition. EJ, EM, and FH were responsible for the EMS analysis. FH and CT prepared the figures and drafted the manuscript with major contributions from LB. All authors contributed to data interpretation and discussions.

# 3 Geological setting

All (pseudotachylyte-bearing) gneisses, discussed in this thesis were sampled from the Silvretta basal thrust, directly at the border of the Engadine Window, and are part of the Austroalpine basement in the Eastern Alps (Figs. 1.2; 3.1 and Appendix A1, 2). The mylonitic pegmatites, discussed in Chapter 8, stem from the southern part of the western Tauern Window and are also part of the Austroalpine basement (Fig. 3.1 and Appendix A1).

In Paleozoic times the collision of Laurussia and Gondwana resulted in the supercontinent Pangea and the Variscan orogen. The resulting amphibolite facies rocks comprise mainly gneisses and amphibolites, forming the crystalline basement, which was then incorporated within the later Alpine orogeny (e.g., Pfiffner, 2009; Wenk, 1934). In Jurassic times the Penninic oceans were opened between the continental African and European plates. During Cretaceous to Oligocene, progressively the Penninic oceans were closed and several microplates underwent multiphase collisions, which resulted in the formation of the Alps with a complex structure of crystalline basement nappes, as well as sedimentary cover material (Pfiffner, 2009). The convergence between the Adriatic continent and Europe resulted in the East-West oriented 500 km long belt (Froitzheim et al., 1994; Pfiffner, 2009; Schmid et al., 2004).

## 3.1 The Geology of the Eastern Alps

The basement of the Eastern Alps (Fig. 3.1) can be divided into several units, that underwent different geological evolution during (pre-)Variscan and Alpine times (Frisch and Neubauer, 1989). Two main tectonic phases are responsible for their development. The closing of the Neotethys resulted in the formation of the Austroalpine units by the superposition of several nappes. This called Eo-Alpine or early-Alpine orogeny started in Cretaceous times (Pfiffner, 2009) and reached greenschist to amphibolite facies conditions with locally up to eclogitic metamorphic conditions (Schweinehage, 1993; Thöni, 2006). From North to South the metamorphic grade is increasing constantly until it suddenly drops at the “Southern border of alpine Metamorphism” (SAM), which is closely located north of the Periadriatic lineament and represented by several Cenozoic fault systems (Hoinkes et al., 1999). To the north of the SAM, the Eo-Alpine units are developed and to the South pre-Alpine rocks can be found.

The Austroalpine units arise exclusively in the Eastern Alps (Fig. 3.1) and have been more or less completely eroded in the western part of the Alps (Schmid et al., 2004). During the Eo-Alpine orogeny at shallower structural levels, several nappes of the Austroalpine were piled up by thrusting and folding of covering sedimentary rocks (Mandl, 2000; Neubauer et al., 2000). The Austroalpine basement is detached from its original substratum and exposed between the Periadriatic line and the Salzach-Ennstal-Mariazell-Puchberg system (Schmid et al., 2013). It surrounds two main tectonic Windows: The Tauern Window directly at the Defereggen-Antholz-Vals shear zone (DAV) and the Engadine widow directly in contact with the Silvretta nappe. The Austroalpine unites can be roughly divided into Upper and Lower Austroalpine, with both, the Silvretta units, as well as the unites south to the western Tauern Window, belonging to the Upper Austroalpine (Fig. 3.1).

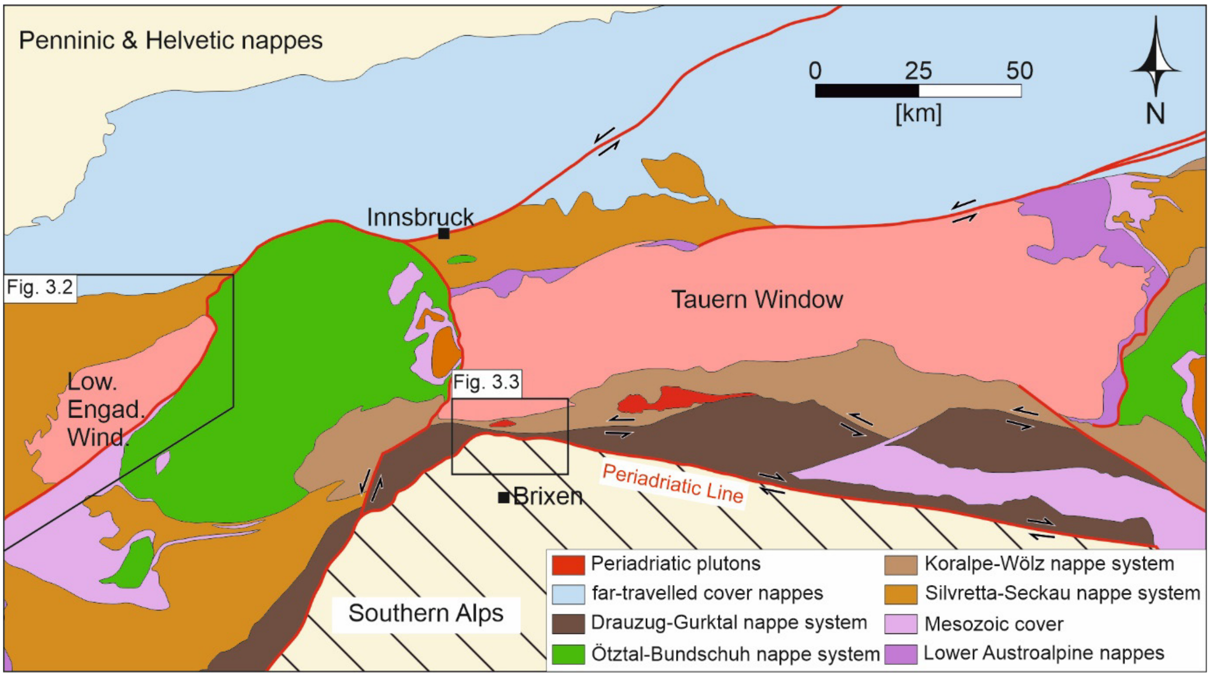

**Figure 3.1:** Geological map of the Eastern Alps (modified after Schmid et al., 2013, 2004). Black rectangles mark the location of the study areas (Silvretta nappe: Fig. 3.2; DAV shear zone: Fig. 3.3).

Upper and Lower Austroalpine, consist of polymetamorphic basement rocks and cover sediments of the Mesozoic age (Schmid et al., 2004). Basement rocks mainly comprise metamorphic high-grade Variscan and intrusive rocks (Spiess et al., 2010) of early carboniferous ages (~355-330 Ma: e.g., Thöni, 2006). Older structures and mineral assemblages were mostly destroyed during the cretaceous orogeny based on petrological and geochronological data (Hoinkes et al., 1991; Morauf, 1982, 1980). Greenschist to eclogite metamorphic peak conditions at 115 to 82 Ma (Hurford et al., 1989; Maggetti and Flisch, 1993; Thöni, 2006, 1981), during nappe stacking in the Cretaceous, influenced the Upper Austroalpine. Structurally the Upper Austroalpine can be divided into four different systems (Fig. 3.1): (1) *Silvretta-Seckau* nappe, (2) *Koralpe-Wölz* nappe, (3) *Ötztal-Bundschuh* nappe, and (4) *Drauzug-Gurktal* nappe.

During the Tertiary, the upper Apulian plate, which is now represented by the Austroalpine basement, was thrusted over the Penninic units, now developed as the Lower Engadine Window. This second major tectonic phase (young-Alpine orogeny) followed due to the subduction of the Tethys Ocean during Paleogene times and resulted in a continental collision (Froitzheim et al., 1996; Schmid et al., 2004), which persists in a continuous moderate form to this day.

## 3.2 The Silvretta nappe in the Eastern Alps

The Silvretta basal thrust based in the central Alps and adjacent to the Engadine Window (Figs. 3.1 and 3.2) represents one of the Upper Austroalpine basement nappes (Froitzheim et al., 1994; Schmid et al., 2004) and resulted from a complex sequence of magmatic, sedimentary and metamorphic tectonic events (Maggetti and Flisch, 1993). It covers about 1600 km$^2$ and is mainly composed of Variscan polymetamorphic para- and orthogneisses and amphibole-rich gneisses with a mylonitic overprint (Maggetti and Flisch, 1993; Masch, 1970; Schweinehage, 1993; Thöni, 1988, 1981; Wenk, 1934). Rare pre-Variscan gabbroic rocks also occur locally (Müller et al., 1995; Schaltegger et al., 1997). During Proterozoic times mainly greywackes and clays and probably basaltic rocks were generated and deposited followed by intrusions. These rocks were deformed under amphibolite to eclogitic metamorphic conditions during orogeny and subduction processes and are now represented by older para- and orthogneisses and amphibolites, as well as mica-schists (Maggetti and Flisch, 1993).

During Ordovician rifting intermediate melts intruded in the older rocks, now represented as younger orthogneisses due to the overprinting Variscan deformation (Maggetti and Flisch, 1993; Pfiffner, 2009). The Variscan orogeny reaches amphibolite to locally eclogite facies conditions with peak conditions of 600 to 650 °C and 550 to 750 MPa at about 370 ± 17 Ma (Rb-Sr: Maggetti and Flisch, 1993). Pangea tholeiites intruded during the late Carboniferous due to the rise of the Silvretta crystalline and extensional tectonics (Maggetti and Flisch, 1993). After the extensive Variscan metamorphism and deformation, during Permian, continuous extensional tectonics dominated (Maggetti and Flisch, 1993), which resulted in basaltic dyke formation and volcanic deposits (Mercolli and Oberhänsli, 1988).

The Silvretta nappe is assumed to have a similar composition as its original crystalline substratum, the Insubric crystalline (Schmutz, 1995). The foliation of the gneisses and mylonites is mainly subparallel to the Variscan foliation, striking WE to NE with shallow dip angles of 10 to 30° (Hammer, 1914; Koch and Masch, 1992; Masch, 1970; Schmutz, 1995). Based on petrographic and geochronological investigations, the Eo-Alpine metamorphic peak conditions in Lower to Upper Cretaceous times (110-85 Ma) increase systematically from the West to the East with temperatures of 350-540 °C and 300 to 400 MPa directly at the contact to the Engadine Window (Hurford et al., 1989; Maggetti and Flisch, 1993; Thöni, 1981). The Eo-Alpine metamorphism was followed by uplift and the decoupling of the nappe from its original crystalline substratum (Insubric crystalline) during the Alpine orogeny and thrust over the Penninic units with a N to NW transport at 60 to 55 Ma ago (Laubscher, 1983; Maggetti and Flisch, 1993). The Penninic units of the Engadine Window comprise calcareous flysch with embedded ophiolites. During the initial decoupling of the Silvretta nappe, the formation of fault rocks happened, which comprise pseudotachylytes, mylonites, and ultramylonites (Bachmann et al., 2009; Koch, 1990; Koch and Masch, 1992; Maggetti and Flisch, 1993; Masch, 1974, 1970; Pittarello et al., 2022; Schmutz, 1995; Thöni, 1981; Wenk, 1934). In Cenozoic times, subduction of the Penninic wedge and later uplift followed. In Tertiary, the units of the Silvretta crystalline were affected by the vaulting of the Lower Engadine Window.

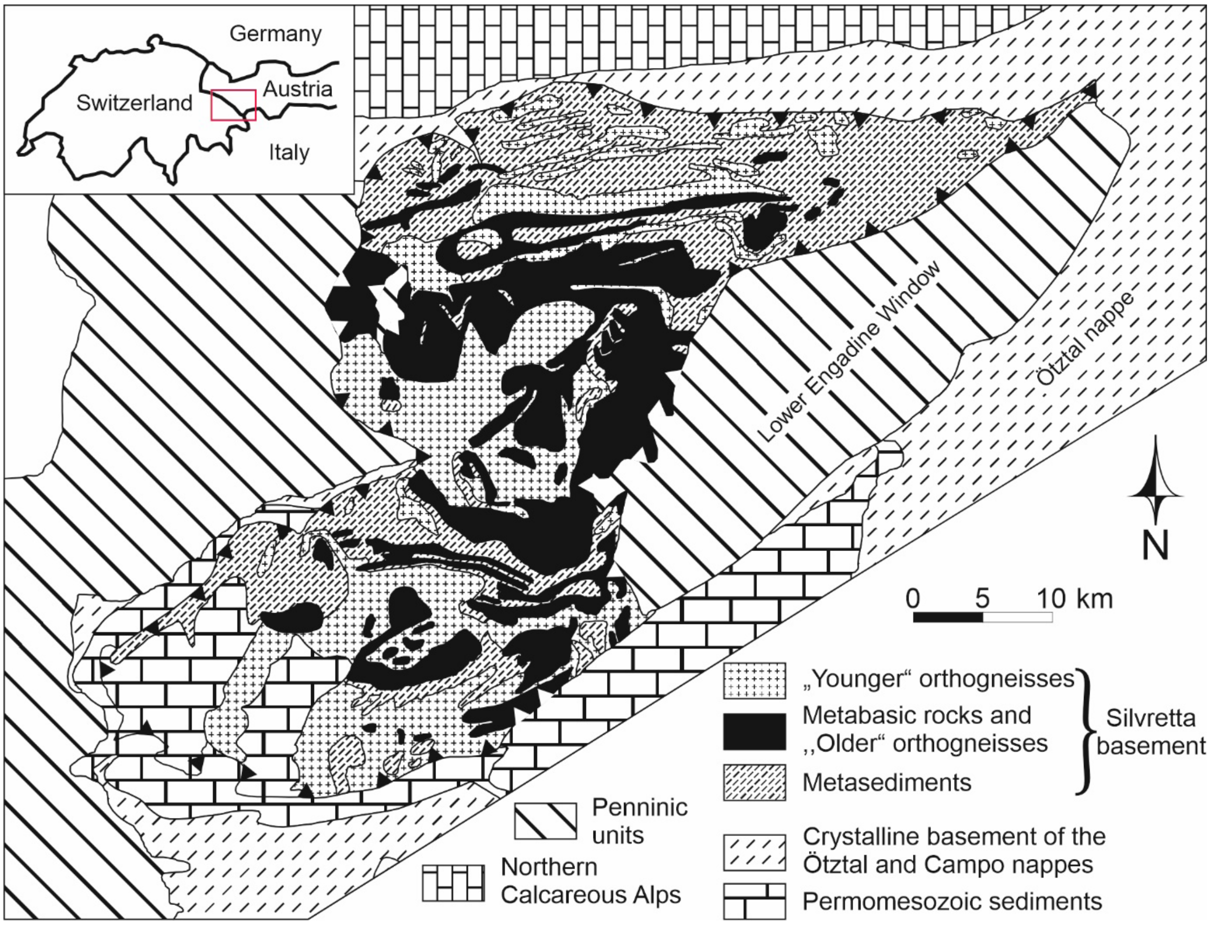

**Figure 3.2:** Geological map of the Silvretta nappe in the Eastern Alps (modified after Müller et al., 1995 and Schweinehage, 2000). Close-up marks the location of the Silvretta nappe (red rectangle) in Europe.

## 3.3 The Austroalpine Basement south of the western Tauern Window

The Austroalpine basement south of the western Tauern Window is divided into a northern and southern part, structurally separated by the Defereggen-Antholz-Vals (DAV) shear zone (Figs. 3.1 and 3.3). The northern block belongs to the *Koralpe-Wölz* nappe system (Schmid et al., 2013, 2004) and consist primarily of Permian pegmatites and polymetamorphic rocks, including e.g., metapsammitic rocks, marbles, amphibolites, quartzites, augen- and paragneisses, as well as shists (Hentschel et al., 2020, 2019; Hofmann et al., 1983; Kleinschrodt, 1987; Mancktelow et al., 2001; Stöckhert, 1987). The Tertiary and the Eo-Alpine tectonometamorphic event affected the rocks at conditions of 350 ± 50 °C and ~0.5 GPa, as well as 450 ± 50 °C and ~0.7 GPa, respectively (Stöckhert, 1987, 1984, 1982). Muscovite indicates ages of 102 ± 2 Ma (Stöckhert, 1984), in contrast to biotite, which shows Oligocene ages ~30 Ma (e.g., Steenken et al., 2002 and references within). Oligocene to middle Miocene cooling is revealed by Zircon fission-track data (Klotz et al., 2019; Steenken et al., 2002). Permian pegmatites do not occur in the southern block, which is part of the *Drauzug-Gurktal* nappe system and comprised of Variscan psammopelitic gneisses (288-299 Ma), that have been only affected by a minor metamorphism associated with a weak brittle deformation at temperatures of <300 °C and no alpine metamorphic overprint (Borsi et al., 1978; Hofmann et al., 1983; Kleinschrodt, 1987; Schulz, 1994; Stöckhert, 1982).

The DAV shear zone is mainly composed of mylonites and cataclasites and defines the southern border of Alpine greenschist facies metamorphism and deformation. Along the DAV a displacement of tens of kilometers of a horizontal component, but also a vertical uplift of several kilometers is recorded (Hoinkes et al., 1999; Kleinschrodt, 1987; Mancktelow et al., 2001; Schulz, 1989; Stöckhert et al., 1999). The vertical uplift of the northern block relative to the southern block is confirmed by recent thermochronological data, including U-Th/He dating (apatite) and fission-track analysis (apatite and zircon) (Klotz et al., 2019). Ages of 30-33 Ma of newly formed white mica north to the DAV are figured out by Rb-Sr dating (Müller et al., 2001, 2000) and are associated to the long-term activity with a sinistral movement and deformation along the DAV (Kleinschrodt, 1987; Mancktelow et al., 2001). Since the Eo-Alpine, distributed deformation occurred in the entire northern block (Hentschel et al., 2020; Mancktelow et al., 2001). Rock deformation and mineral reactions occur at lower greenschist facies conditions from the middle Cretaceous to the Oligocene, which is evident from geochronological and microstructural data (Hentschel et al., 2020; Stöckhert, 1987, 1984, 1982). DAV related pseudotachylytes with an age of ~20 Ma (Ar-Ar isotopic analyses) have been reported by Mancktelow et al. (2001). However, these are much less represented compared to the pseudotachylytes of the Silvretta nappe.

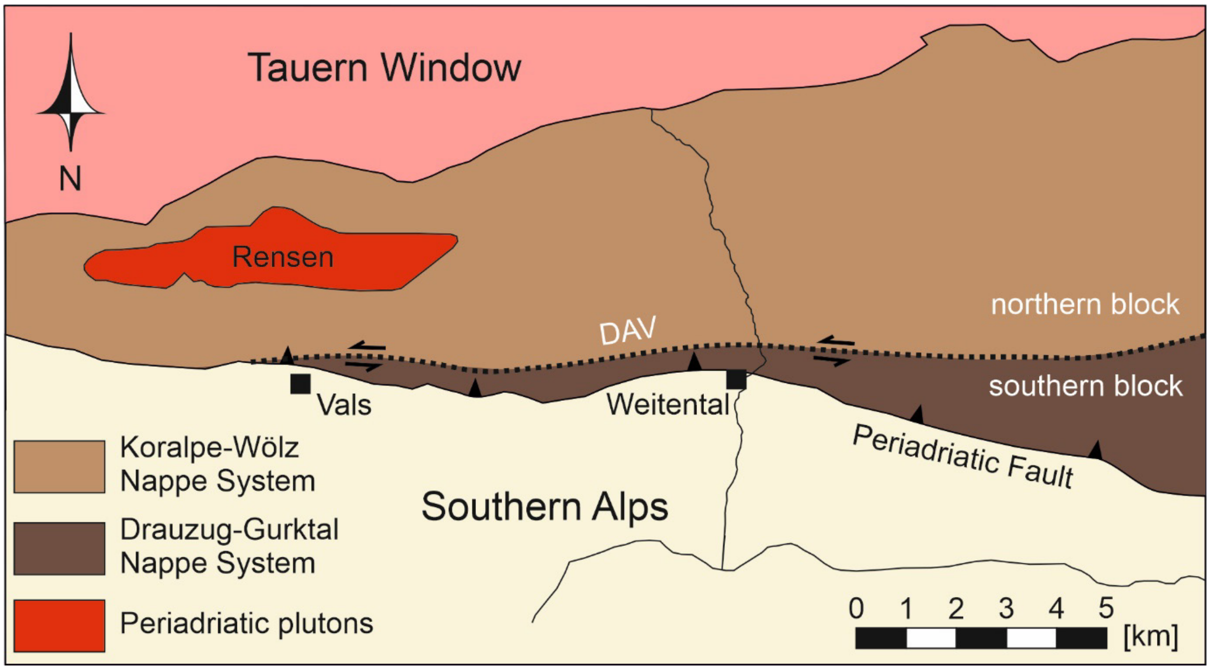

**Figure 3.3:** Simplified geological map of the DAV shear zone in the Alps (modified after Mancktelow et al., 2001).

# 4 Methods

A multi-scale field-based approach is selected, including macroscopic structural and lithologic field observations and detailed microstructural analyses. For this purpose, 92 samples were collected in total during fieldwork in the Silvretta crystalline, and 227 thin sections (Appendix A1 and A2) were examined by polarized light microscopy, electron microscopy including microtextural analysis by EBSD, as well as Raman spectroscopy. Already available first sets of Silvretta samples, mylonitic pegmatite samples of the DAV (Chapter 8), as well as samples of the Vredefort impact structure (Chapter 7), were considered and studied (Appendix A1).

## 4.1 Fieldwork

Fault rocks and gneisses were collected at the border of the Silvretta crystalline to the units of the Engadine Window in Austria and Switzerland (Appendix A1 and A2) during four different field campaigns between 2019 and 2021. Pseudotachylyte-bearing and mylonitic samples were selected, which show a lithological contact between amphibole-rich gneisses and quartz-rich layers concordant with the foliation of the gneisses. In addition to the appearance and distribution pattern of typical deformation structures and rock types, the mutual overprinting of the various related fault rocks was analyzed in the field.

## 4.2 Microstructural and Texture Analysis

For micro-scaled investigations of selected fault rock samples, the direction perpendicular to the foliation is considered as $z$-axis and the stretching lineation, if present, is taken as $x$-axis of the strain ellipsoid. All samples were cut vertical to the main foliation (i.e., parallel $z$) and parallel to the stretching lineation ($x$-axis). To judge the 3D shape of specific microstructures, e.g., shear bands, also $yz$ cuts, perpendicular to both, the foliation and lineation, were prepared. Thin sections with a thickness of ca. 30 µm were mechanically polished and, if necessary, coated with a 5-10 nm thin layer of carbon. The samples were investigated by polarized light microscopy and scanning electron microscopy (SEM, Department of Earth and Environmental Sciences, LMU Munich) with electron backscattered diffraction (EBSD). SEM investigations were performed using a SU5000 Hitachi field emission gun equipped with an HKL Nordlys-Nano electron backscatter diffraction detector. Energy dispersive spectroscopy (EDS) was compiled using an acceleration voltage of 20 kV, spot intensity of 38, and a 10 mm working distance. For EBSD investigations, thin sections were chemo-mechanically polished for about 1.5 h with an alkaloid colloidal suspension (Syton) and partly carbon coating. A pre-tilted sample holder with an angle of 70° relative to the beam was used to measure the samples automatically. EBSD patterns were automatically indexed with a step size of 0.5 to 2 µm, depending on the required resolution, grain size, porosity, and measured area size. Working distances of 15-25 mm and an acceleration voltage of 20 kV with a spot intensity of 50 were deployed. For acquiring and processing the data, the Aztec 4.2, CHANNEL 5, as well as the Aztec 6 and Aztec Crystal software of Oxford Instruments was used. Additionally, the MTEX toolbox for MATLAB (https://mtex-toolbox.github.io/, v5.7.0, last access: June 2021; e.g., Bachmann et al., 2010) was operated for EBSD data evaluation of the DAV pegmatites in Chapter 8. A misorientation angle of 10° was applied as a threshold limit for grain reconstruction. To prevent artifacts, grains with diameters smaller than twice the step size were neglected. For data acquisition 57 and 92 reflectors for quartz and amphibole, respectively, 1×1 or 2×2 binning and detected 6 bands (band centers) were utilized. The grain diameter is given as the mean (geometric) diameter of a circle of equivalent area with standard deviation. The aspect ratio is given as the ratio of the long and short axes of an ellipse of the equivalent area with standard deviation. All crystallographic orientations were presented as pole figures, which are displayed as equal-angle stereographic projections (Chapter 5, 6, and 8) or as equal-area projections (Chapter 7) of the lower hemisphere. The stretching lineation (X) and the pole to the foliation (Z) are oriented East-West and North-South, respectively. The pole figures show all points from the measured area, unless otherwise stated in the figure caption. Rotation axes were projected in crystal coordinates. Misorientation angle distributions were analyzed using randomly selected grains. To index the crystallographic orientation of twin and kink band boundaries, as well as cleavage fractures, the 3D orientations were measured by a universal tilting stage (U-stage) mounted on a polarized light microscope and compared to the EBSD measurements. The spacing between the cleavage fractures (Chapter 7) was determined with a polarization microscope by measuring the distance between two adjacent strings and repeated for the perpendicular strings. To display and evaluate the 2D orientation data of the long grain axes (rose diagrams) the Stereo32 software (Röller and Trepmann, 2003) was used.

## 4.3 Raman Spectroscopy

Raman spectroscopy was carried out by using a HORIBA JOBIN YVON XploRa ONE micro Raman machine located at the Mineralogical State Collection Munich (SNSB). Measurements were conducted with a 2ω-Nd:YAG laser with a wavelength of 532 nm in an attenuated mode of 25 % laser power, corresponding to i.e., 2.5 mW on the sample surface. A 100 long working distance objective and 1800T grating for better spectral resolution were operated. Hole and slit were 100 µm and 50 µm. Furthermore, an acquisition time (s) and accumulation of 8 and 2 was used, respectively. Wavelength calibration was performed with a pure Si wafer chip on the predominant 520 ± 1 $cm^{-1}$ peak and the precision is estimated at ± 1.5 $cm^{-1}$. Raman data were acquired and processed with LabSpec 6.6.1 software of Horiba Scientific (Horiba Scientific, 2022). For stilpnomelane identification within the Silvretta pseudotachylytes and (ultra-)mylonites a standard from Wurlitz/Oberkotzau, Germany (#23472), was consulted belonging to the Mineralogical State Collection Munich (SNSB).

## 4.4 Microprobe

The chemical composition of monazite was analyzed on carbon coated (55-60 nm) thin sections using electron microprobe (EMP) measurements on a JOEL JXA-8230 EMP at the ISTerre in Grenoble, with operating conditions of 15 kV and 200 nA following the protocol of (Hentschel et al., 2020). Concentrations of Pb, Th and U were measured with a counting time of 480 s, 160 s and 300 s, respectively. Under these conditions, EMP measurement detection limits are in the range of 135 ppm, 130 ppm, and 105 ppm for U, Th and Pb, respectively. To monitor instrumental drift, Madagascar monazite standard (e.g., Grand'Homme et al., 2018) was run as unknown (3 points) before, in-between and after analyses of the mylonitic pegmatite monazite. Ages were individually calculated by the following formula (Montel et al., 1996):

$$(1) \qquad \mathrm{Pb} = \frac{\mathrm{Th}}{232}\left[\exp\left(\lambda^{232}\tau\right)-1\right]208 + \frac{\mathrm{U}}{238.04}0.9928\times\left[\exp\left(\lambda^{238}\tau\right)-1\right]206 + \frac{\mathrm{U}}{238.04}0.0072 \times \left[\exp\left(\lambda^{235}\tau\right)-1\right]207$$

# 5 Stresses during pseudotachylyte formation – Evidence from deformed amphibole and quartz in fault rocks from the Silvretta basal thrust (Austria)

This chapter is based on the manuscript: Brückner, L. M., and Trepmann, C. A. (2021). Stresses during pseudotachylyte formation – Evidence from deformed amphibole and quartz in fault rocks from the Silvretta basal thrust (Austria). *Tectonophysics*, 817, 229046. https://doi.org/10.1016/j.tecto.2021.229046

## 5.1 Introduction

Stress is the first order control-factor for seismic faulting and deformation of rocks in general. The microfabric analysis of fault rocks deformed at depths inaccessible for in situ stress measurements is powerful to constrain the stress and strain-rate history during deformation. Amphiboles in polyphase metamorphic rocks are known as high-strength rock-forming minerals acting as rather rigid inclusions at temperature conditions below 650-700 °C, without significant strain accumulation by dislocation creep (e.g., Berger and Stünitz, 1996; Brodie and Rutter, 1985; Cao et al., 2010; Imon et al., 2004; Nyman et al., 1992; Shelley, 1994). At high stresses and strain-rates, amphibole deforms by kinking and twinning associated with cataclasis (e.g., Borg, 1972; Buck, 1970; Hacker and Christie, 1990; Nyman et al., 1992; Park et al., 2020; Rooney et al., 1975, 1970; Shelley, 1994; Sobott, 1979). Given its relatively low fracture toughness and low melting temperature, amphibole is prone to comminution and melting at high strain-rates during seismic faulting, in contrast to quartz (e.g., Koch and Masch, 1992; Spray, 2010). In this respect, amphibole-rich lithologies represent "weak" layers during pseudotachylyte formation as opposed to quartz-rich lithologies.

Mechanical twins are important microstructures to indicate differential stresses during faulting because they form at a critical resolved shear stress on the twin system, which is in a first approximation independent of temperature and strain-rate (e.g., Tullis, 1980). Therefore, extrapolations from laboratory measurements to natural conditions are not as critical as for other deformation mechanisms, i.e., dislocation glide. Furthermore, mechanical twins can easily be detected by their specific crystallographic relationship to the host orientation, even after modification by twin boundary migration (e.g., Cao et al., 2010). Given the high critical resolved shear stress of 200-400 MPa for amphibole $(\bar{1}01)[101]$ twins, constrained by experiments of Rooney et al. (1970), they ideally can detect deformation at transient high differential stress conditions.

Local and transient stress-strain concentrations resulting from high-viscosity inclusions in a low-viscosity creeping matrix has been suggested to lead to "plastic instabilities" and "thermal runaway", finally causing the formation of pseudotachylytes at depth, whereas in the long term the rocks behave by creep (Hobbs et al., 1986; Hobbs and Ord, 1988; John et al., 2009; Kaus and Podladchikov, 2006; Koch and Masch, 1992; Regenauer-Lieb and Yuen, 2004; Schmid and Casey, 1986; Sibson, 1980; Thielmann et al., 2015; White, 2012, 1996). However, unequivocal microstructural evidence for thermal runaway, for example systematic variations in grain sizes that document increasing strain towards pseudotachylytes, is still missing (Papa et al., 2020).

Transient high-stress deformation at greenschist facies conditions, where the rocks undergo creep on long-term, however, has also been reported to be caused by stress redistribution related to the rupture of nearby seismically active faults (e.g., Küster and Stöckhert, 1999; Trepmann and Stöckhert, 2003, 2002, 2001), leading to the formation of pseudotachylytes at small distances to the tip of the seismically active fault (Nüchter et al., 2013). High stress-loading rates are characteristic of such a scenario as opposed to the relatively continuous stress built up within high-viscosity inclusions surrounded by a creeping low-viscosity matrix (Trepmann and Seybold, 2019; Trepmann and Stöckhert, 2009; Trepmann et al., 2017).

The Silvretta basal thrust fault in the central European Alps (Figs. 1.2; 3.1 and 3.2) is known for the well-developed pseudotachylyte-bearing amphibole-rich gneisses that occur in association with mylonites and ultramylonites formed at the same depths (Bachmann et al., 2009; Koch, 1990; Koch and Masch, 1992; Masch, 1970; Schmutz, 1995). Koch and Masch (1992) interpreted the amphibole-rich gneisses as high-viscosity inclusions in a low-viscosity matrix of quartz-rich gneisses that are undergoing creep. However, unambiguous microstructural evidence that this viscosity contrast can explain the occurrence of pseudotachylytes is still missing. Furthermore, the deformation record of amphibole in the host gneisses has so far not been used to unravel the deformation history. Here, the microfabrics of amphibole and quartz in pseudotachylyte-bearing gneisses, as well as the microfabrics in neighboring quartz-rich layers concordant with the foliation of the gneisses from the Silvretta basal thrust are analyzed. The aim is (1) to constrain the deformation history by analyzing the microfabrics of amphibole associated with pseudotachylytes in the gneisses in relation to the quartz microfabric, and (2) to test whether a gradient of increasing strain within quartz-rich layers towards pseudotachylyte-bearing, amphibole-rich layers can be observed that would indicate thermal runaway.

## 5.2 Results

### *5.2.1 Samples*

Pseudotachylyte-bearing gneisses were collected from the border of the Silvretta crystalline to the units of the Engadine Window from the Ochsental, Jamtal and Val Tasna as well as the Hexenkopf (Fig. 1.2). Samples that show a lithological contact between amphibole-rich gneisses and quartz-rich layers concordant to the foliation of the gneisses were selected for this study: LB20-22 (47°01‘00“N/10°28‘00“E), CT623, CT628 (46°53'15.37"N/10°10'55.55"E), and CT772 (46°50'54.97"N/10°12'18.24"E) (Appendix A1 and A2). The investigated amphibole-rich gneisses (Fig. 5.1) contain about 60-80 % amphibole, 20-40 % plagioclase (oligoclase), 10-20 % quartz and 0-5 % biotite. Accessory constituents include sphene, ilmenite, and zircon. The green hornblendes are calcic amphiboles $(Na, K)_{0.3-0.6}(Ca, Mn)_2(Mg_{2.2}Fe_{1.8}Al)(Si_7Al)O_{22}(OH)_2$ with a Mg# between 0.5-0.6, space group C 2/m. There is no systematic intracrystalline variation in chemical composition within deformed amphibole grains. The amphibole grain size varies with long axes around 100-800 µm. Quartz-rich (>90 % quartz) layers concordant to the foliation of the gneisses are typically a few cm to dm wide (Fig. 5.1). The amphibole-rich gneisses also show boudinaged layers when in contact to quartz-rich lithologies (Fig. 5.1b). Pseudotachylytes in the investigated samples commonly show vein geometries of a few µm to several mm (Figs. 5.1b, c and 5.2a-e). In amphibole-rich layers, they show a fine-grained matrix containing rounded clasts of mainly amphibole (<1 µm to several µm in diameter) and in decreasing abundance feldspar, sphene, ilmenite and quartz (Fig. 5.2c-f). Yet, the composition of the pseudotachylytes varies strongly dependent on the local host lithology. For a detailed description of the different types of pseudotachylytes and host gneisses, the reader is referred to Koch and Masch (1992) and Schmutz (1995).

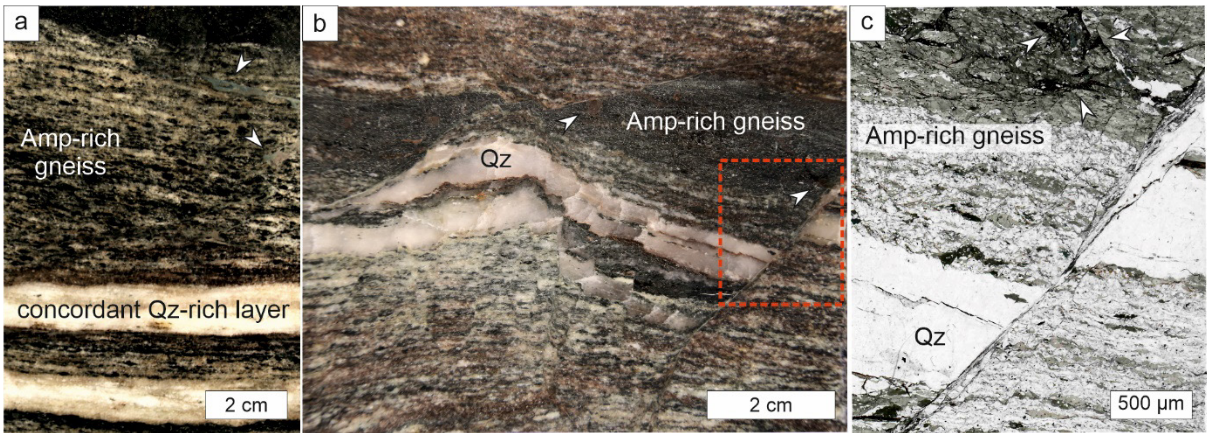

**Figure 5.1:** Silvretta pseudotachylyte-bearing gneisses. **(a)** Amphibole-rich gneiss (Amp) and concordant quartz-rich layers (Qz), sample LB22. **(b, c)** LB21 sample micrograph and thin section micrograph (position shown by red rectangle in (b)), resepectively, of amphibole-rich gneisses and concordant quartz layers. Pseudotachylytes are indicated by white arrows.

### *5.2.2 Amphibole microfabrics*

Amphibole shows undulatory extinction, lamellar mechanical twins, kink bands and microcracks (Fig. 5.2a, b) commonly associated with pseudotachylytes (Fig. 5.2c-f). Two different lamellar twins are observed (Fig. 5.3). Most common are $(\bar{1}01)[101]$ twins, characterized with EBSD analysis in combination with U-stage measurements by the $(\bar{1}01)$ twin plane, rotation axes parallel to [101] and a misorientation angle of 180°. The $(\bar{1}01)[101]$ twins show typically a width of 5-10 µm and a spacing of 20-50 µm (Figs. 5.3; 5.4a-b; 5.5a and 5.6). The highest observed twin density is about 0.15/µm. The $(\bar{1}01)[101]$ twins characteristically deflect the {110} cleavage planes (Fig. 5.2g). Less common are (100)[001] twins, characterized by the (100) twin plane, rotation axes parallel to [001] and a misorientation angle of 180° (Figs. 5.3 and 5.6a-c). The (100)[001] twins show typically width of about 20 μm and a larger spacing, compared to the $(\bar{1}01)[101]$ twins. The (100)[001] twins appear to cross cut the $(\bar{1}01)[101]$ twins (Fig. 5.3c). In association with twinned amphiboles, pseudotachylyte veins occur that contain fine-clastic (3 ± 0.5 μm in diameter) amphibole (compare Figs. 5.2e, f and 5.4a green-rimmed area) with almost random crystallographic orientations, as indicated by the polefigures (Fig. 5.4f), density plots (multiple of uniform distribution <2) (Fig. 5.4g), and misorientation angle distribution (Fig. 5.4e).

Kink bands are observed with boundaries parallel to (010), where the poles of the kink band boundaries are parallel to the ***b***-axis of the amphibole measured by U-stage (Figs. 5.2b and 5.5). Generally, kink bands are characterized by the curvature of the crystal, which is concentrated into well-defined sharp regions, i.e., kink band boundaries, separating regions of the crystal with different orientation (usually ≥10° misorientation angle) that are not curved (Nicolas and Poirier, 1976). The kink bands observed here, show misorientation angles between 15-30° relative to the host amphibole and a rotation axis scattering around [001] (Fig. 5.5). They occur as single kink bands (Fig. 5.4b) or lamellar with a width of about 10 μm and spacing of 40-70 μm (Fig. 5.5). The kink bands appear to crosscut the $(\bar{1}01)[101]$ twins (Fig. 5.5a, d). There is no systematic chemical variation associated with the kink band or the twin boundaries.

Both twins mostly show straight boundaries (Figs. 5.3b, c and 5.4a, b) if not affected by kink bands (Fig. 5.5a, d). Rarely, the twin boundaries are sutured (Fig. 5.6). The sutures are characterized by wavelengths and amplitudes of few μm and they are not associated with a second phase or any chemical gradients (Fig. 5.6e). Microfaults occur parallel to (001) (Fig. 5.7a), in addition to {110} cleavage fractures (Figs. 5.4b, c; 5.5d, e and 5.7a, c). The undulatory extinction observed in the polarized light microscope (Figs. 5.2a, b and 5.3a) is characterized via EBSD by domains with relative misorientation angles up to 30-40° (Figs. 5.4b, d; 5.5a and 5.7). However, both, the relative misorientation (Fig. 5.7a), as well as the local misorientation for angles <5° and a kernel size of 3x3 (Fig. 5.7b), indicate that the misorientations are mostly related to fractures. The orientations of the fine-grained (3 ± 0.5 μm in diameter) new grains along the microfaults scatter largely around the crystallographic orientation of the host crystal (Fig. 5.7d). Rotation axes are almost randomly oriented, especially for the dominating misorientation angles <90° (Fig. 5.7e). The rotation axes for the less frequent misorientation angles >90° show a weak clustering around the plane normal of (001), which coincides with the orientation of one dominating crack plane of the host (Fig. 5.7c).

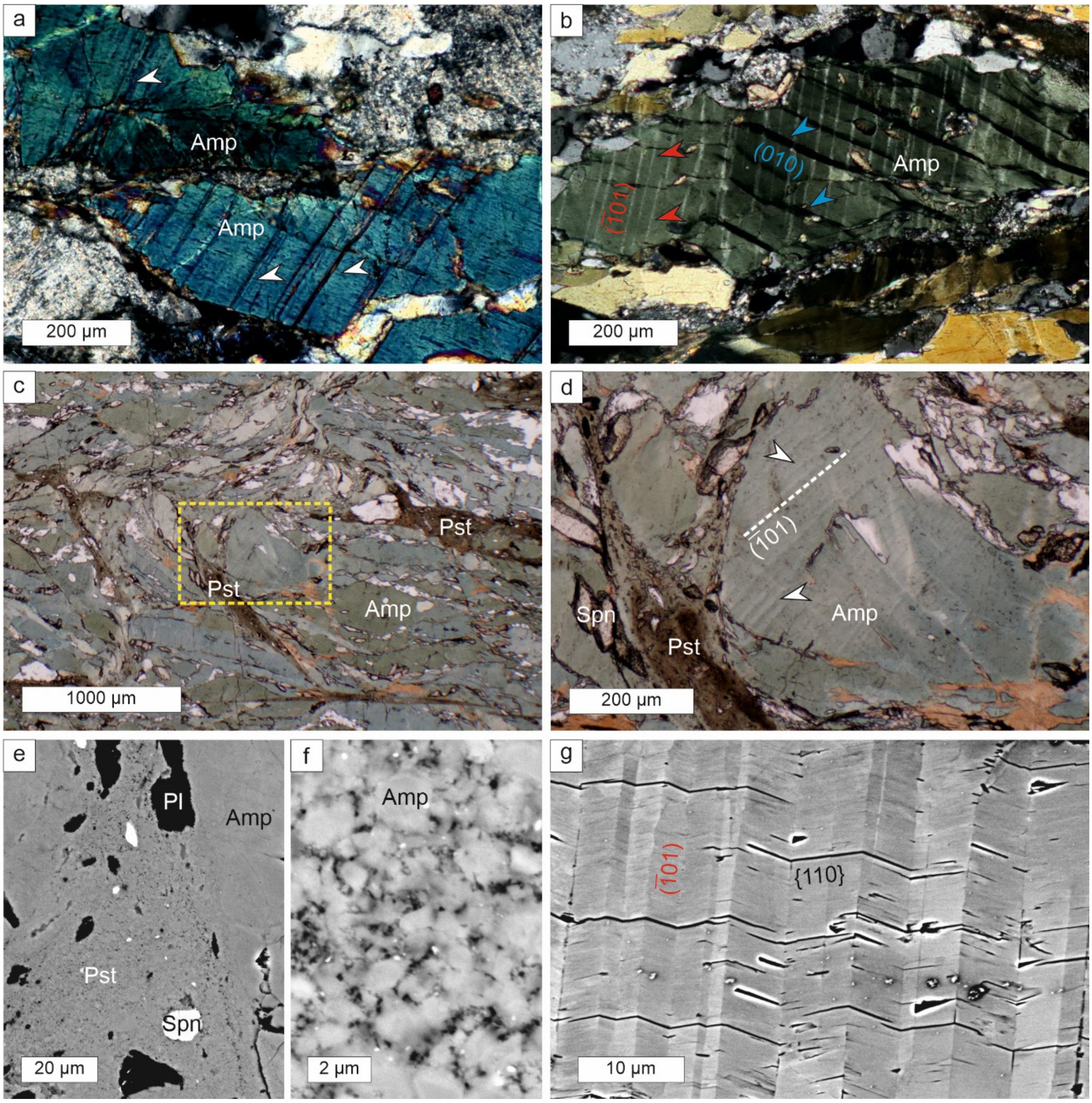

**Figure 5.2:** Amphibole microfabrics of Silvretta fault rocks. **(a)** Polarized light micrograph (crossed polarizers) showing $(\bar{1}01)[101]$ twins in amphibole (Amp) (white arrows), sample CT628. **(b)** $(\bar{1}01)[101]$ twins (red arrows) and (010) kink bands (blue arrows) in deformed amphibole (polarized light micrograph), sample LB22 (compare Fig. 5.5). **(c, d)** Polarized light micrographs of amphibole-rich layer with pseudotachylytes (Pst), sample LB21. In (d), $(\bar{1}01)$ twins are visible by slight difference in colour (pleochroism, white arrows; position is indicated by yellow rectangle in (c)). **(e, f)** BSE images of pseudotachylytic vein with amphibole, plagioclase (Pl) and sphene (Spn), sample LB21. **(g)** BSE image showing the characteristic deflection of the {110} cleavage planes by the $(\bar{1}01)[101]$ twins, sample LB22.

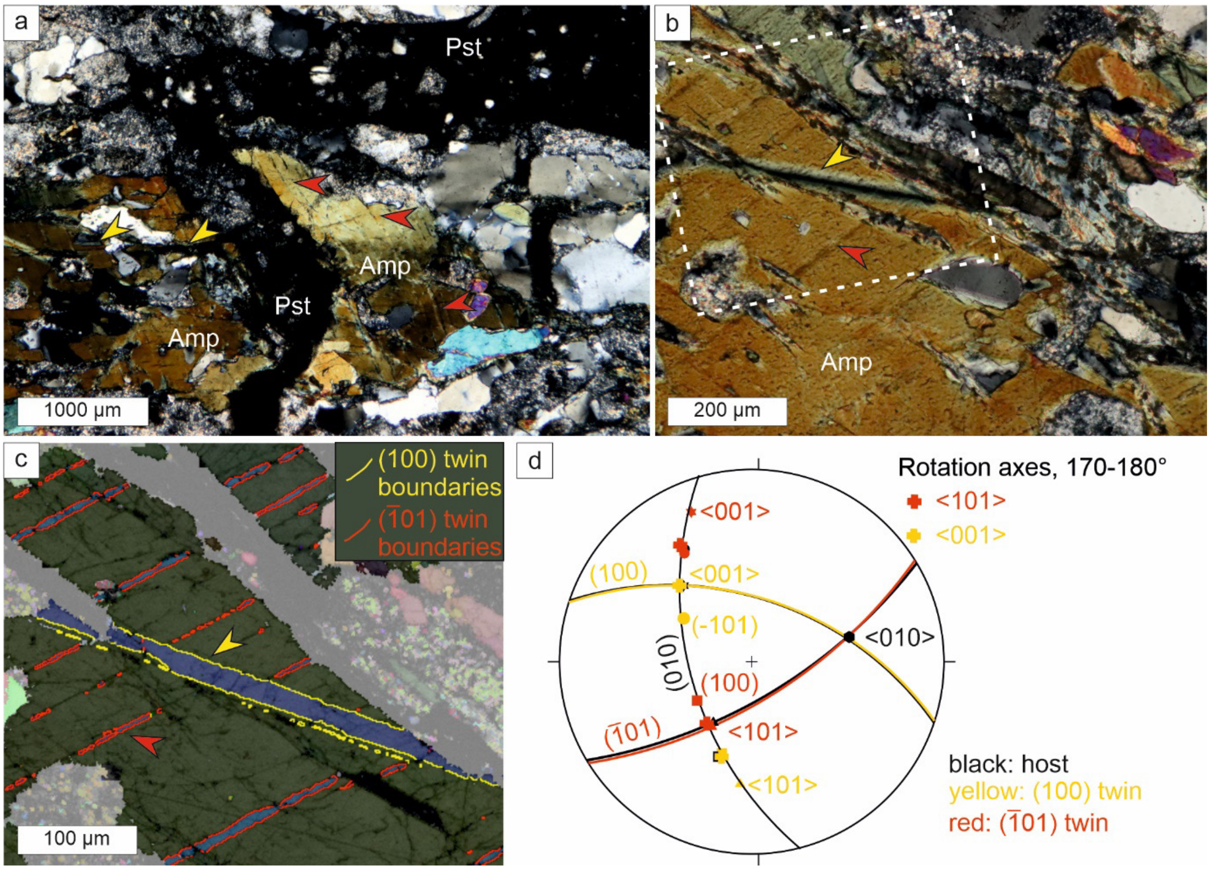

**Figure 5.3:** Mechanical amphibole twins in the direct vicinity with pseudotachylyte. **(a, b)** Polarized light micrograph (crossed polarizers) of amphibole (Amp) in contact with a pseudotachylyte (Pst) with $(\bar{1}01)[101]$ twins marked by red arrows and (100)[001] twins marked by yellow arrows, sample CT623d. **(c)** EBSD map of white-rimmed area in (b) displaying the crystallographic orientation (all Euler angles) and twin boundaries (yellow: (100) twins, red $(\bar{1}01)$ twins). Note that the (100)[001] twins appear to crosscut the $(\bar{1}01)[101]$ twins. **(d)** Stereographic projection of both twin domains and the host orientation, as well as the respective rotation axes with misorientation angles of 170-180°.

## *5.2.3 Quartz microfabrics*

### *5.2.3.1 Quartz in spatial relation to twinned amphibole and pseudotachylytes*

Quartz in spatial relation to twinned amphibole and pseudotachylytes in the gneisses typically shows a grain size of several hundred µm to mm, short wavelength undulatory extinction (SWUE) and subbasal deformation lamellae (Fig. 5.8a-c). SWUE is characterized by lamellar domains subparallel to $\{10\bar{1}1\}$ rhombohedral planes with misorientation angles of 0-25° degrees (Fig. 5.8c, d). Along rhombohedral planes, fine recrystallized grains with a diameter of <15 µm occur (Fig. 5.8a, d-g). The crystallographic orientation of these new grains is similar to that of the host (Fig. 5.8e, f). However, also grain orientations that largely deviate from that of the host grain occur, as shown also by the misorientation angle distribution histogram (Fig. 5.8g).

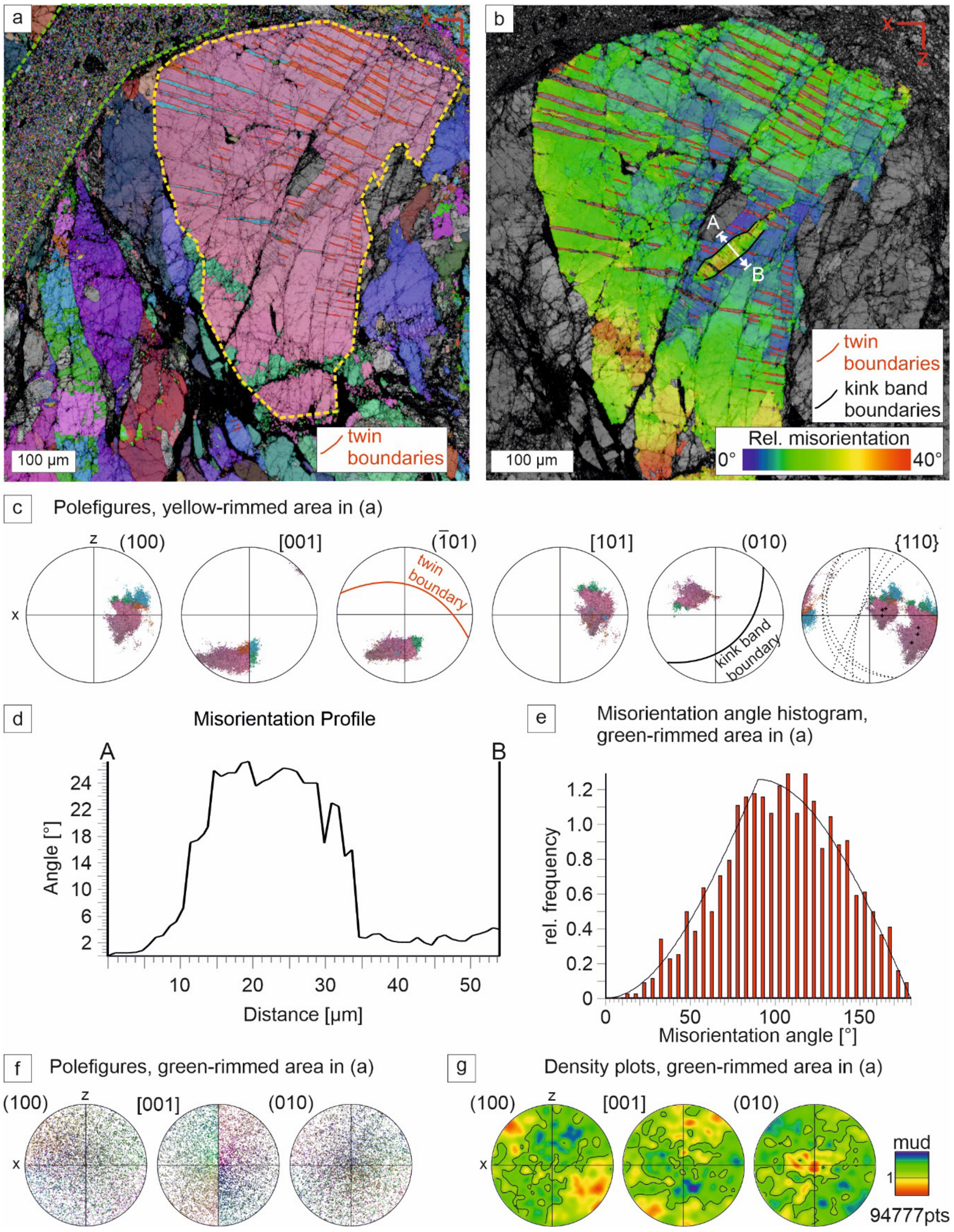

**Figure 5.4:** EBSD data of deformed amphibole (yellow-rimmed area) in association with a pseudotachylytic vein (green-rimmed area), sample LB21. **(a)** All Euler angles map showing different crystallographic orientations. **(b)** Relative misorientation (0-40°) of yellow-rimmed area in (a). **(c)** Pole figures of twinned amphibole (yellow-rimmed area) with great circle of $(\bar{1}01)[101]$ twin boundaries (red), great circle of kink band boundary (black) and of {110} cleavage planes (dashed). **(d)** Misorientation angles along profile line across a kink band shown in (b). **(e)** Misorientation angle histogram in pseudotachylytic vein (green-rimmed area) shown in (a). **(f)** Stereographic projections show random texture of amphibole orientations in pseudotachylytic vein (green-rimmed area). **(g)** Density plots (stereographic projections) of amphibole orientations in pseudotachylytic vein (green-rimmed area).

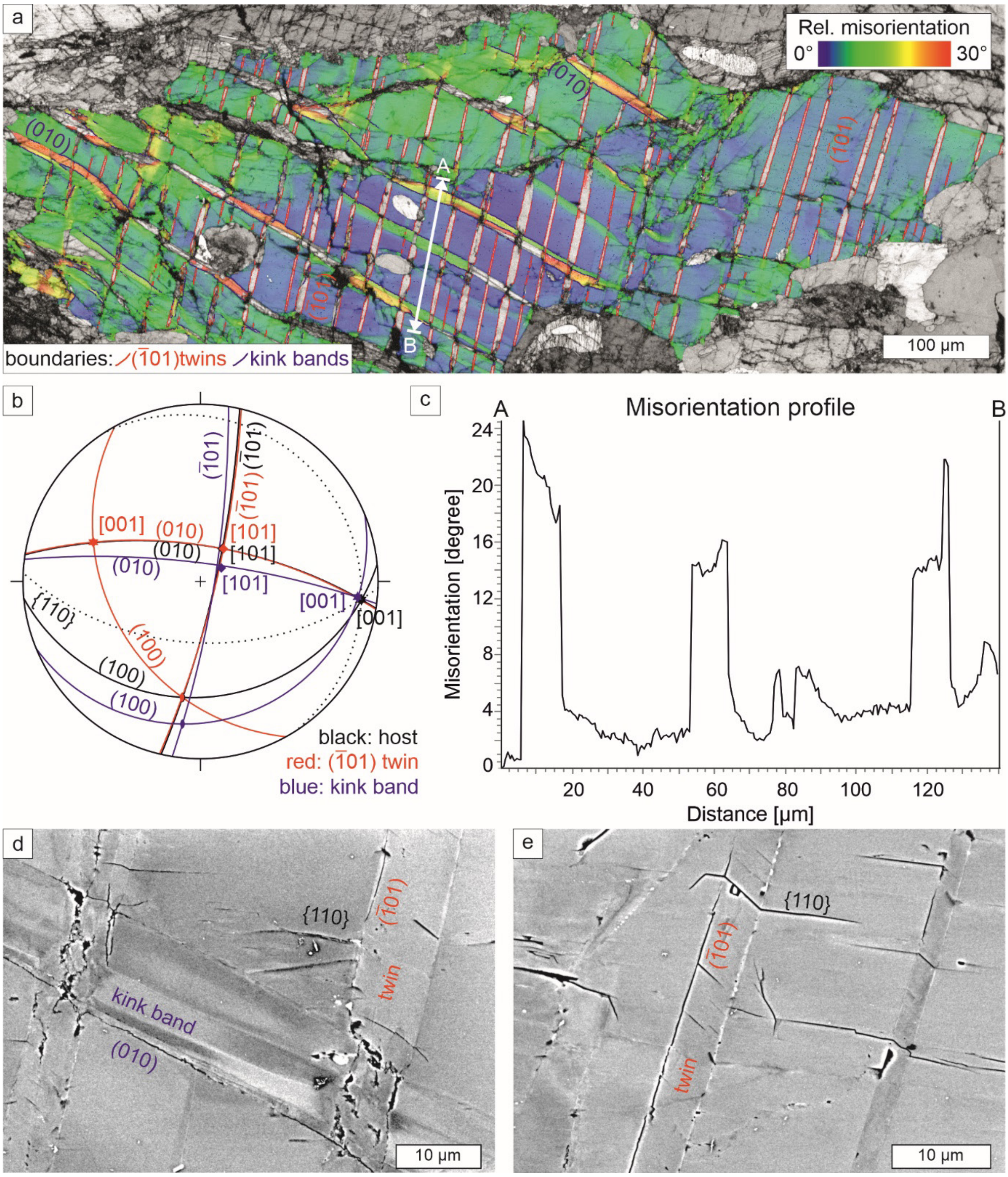

**Figure 5.5:** SEM data of deformed amphibole (compare Fig. 5.2b), sample LB22. **(a)** EBSD map showing the relative misorientation (0-30°) of amphibole with undulatory extinction, $(\bar{1}01)[101]$ twin boundaries (red) and (010) kink band boundaries (blue). **(b)** Stereographic projection of amphibole host orientation in black, $(\bar{1}01)[101]$ twin orientation in red, kink band orientation in blue. **(c)** AB misorientation profile as shown in (a). **(d, e)** BSE images of twins and kink bands. Note the characteristic deflection of the {110} cleavage planes by the $(\bar{1}01)[101]$ twins.

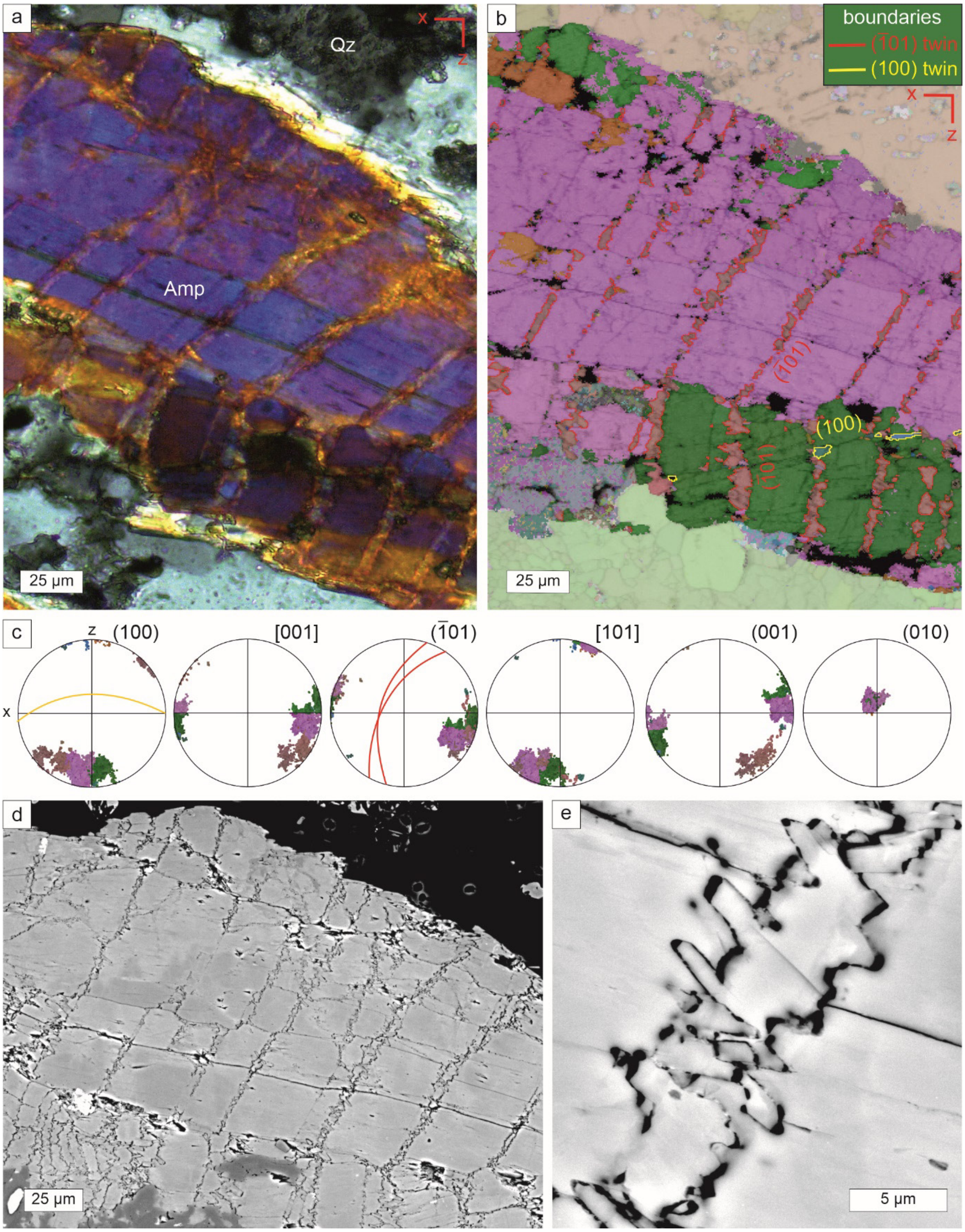

**Figure 5.6:** Amphibole displaying sutured mechanical twin boundaries, sample CT772. **(a)** Polarized light micrograph (crossed polarizers) and **(b)** EBSD map (all Euler angles) of twinned amphibole (Amp) in contact to quartz (Qz). Note sutured $(\bar{1}01)[101]$ and (100)[001] twin boundaries. **(c)** Stereographic projections with great circles for twin boundaries. **(d, e)** BSE images of sutured twin boundaries.

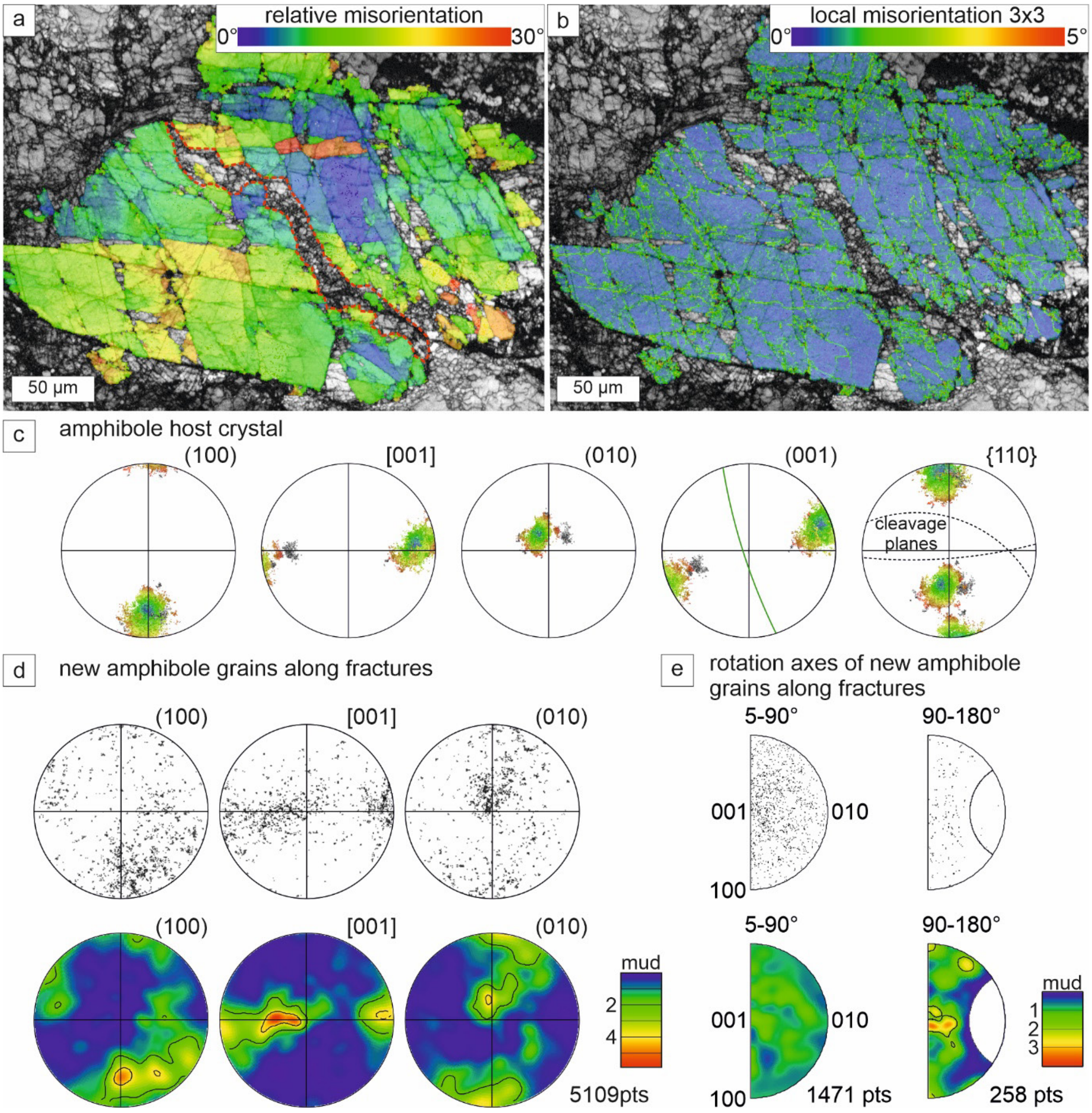

**Figure 5.7:** Amphibole with microcracks, sample CT628b. **(a, b)** EBSD maps showing relative misorientation map (0-30°) and local misorientation map (0-5°), respectively, of fractured amphibole with undulatory extinction. **(c)** Stereographic projections of crystallographic directions and planes of the host crystal. Microcracks appear to be subparallel to (001) shown by green line and {110} cleavage planes (black dashed lines). **(d)** Stereographic projections and density plots of crystallographic directions and planes of the new amphibole grains within the red-rimmed area (grains in analyzed subset were selected manually) in (a). **(e)** Rotation axes in crystal coordinate projections for the new amphibole grains along fractures (red-rimmed area in (a)).

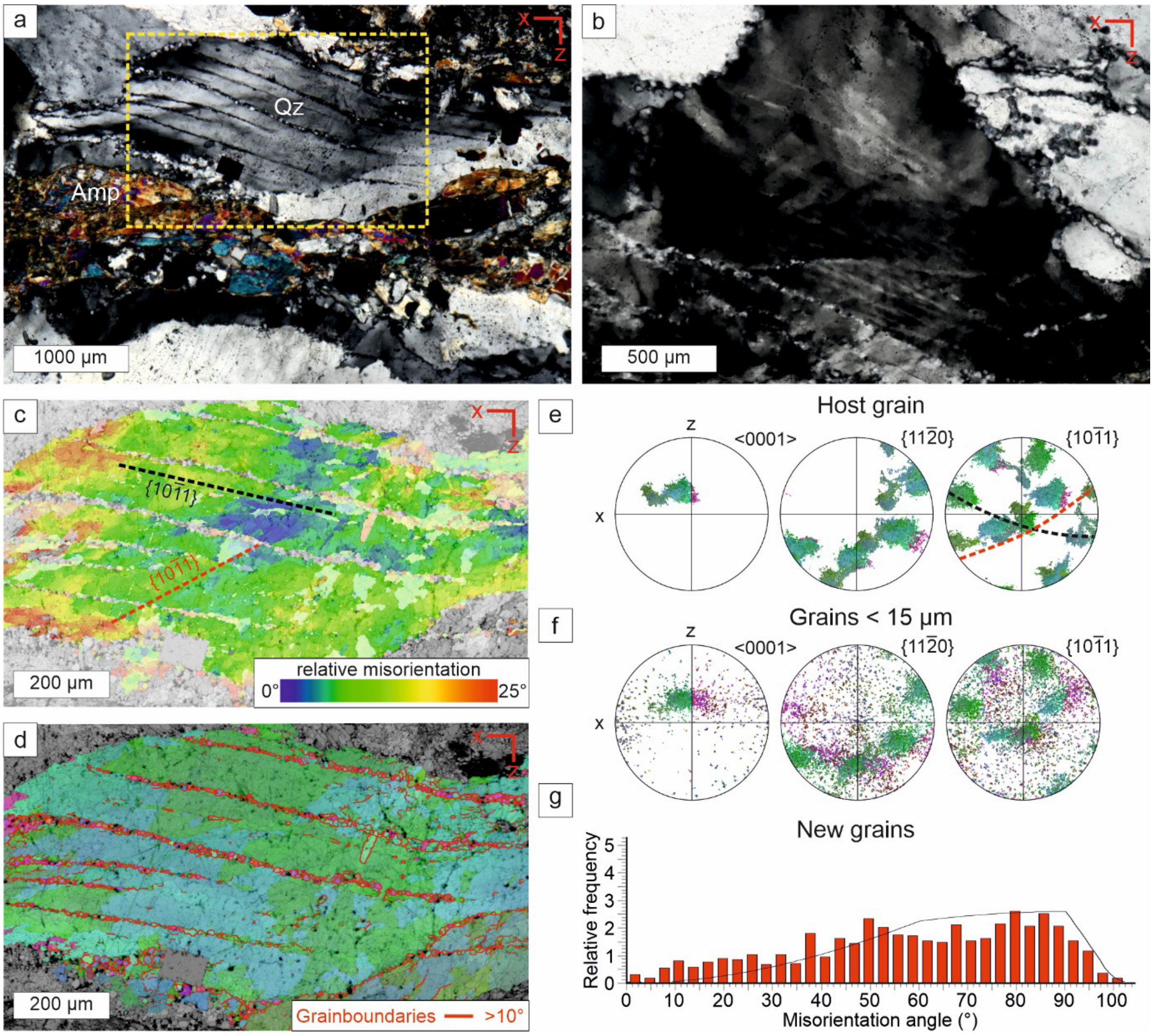

**Figure 5.8:** Quartz microfabrics in amphibole-rich gneisses, sample CT772. **(a)** Polarized light micrograph (crossed polarizers) of quartz (Qz) showing undulatory extinction and recrystallized grains along cracks in direct contact with deformed amphibole (Amp). **(b)** Polarized light micrograph (crossed polarizers) of quartz showing short wavelength undulatory extinction (SWUE). **(c, d)** EBSD maps showing relative misorientation (misorientation angles 0-25°) and crystallographic orientation (all Euler angles), respectively (position is marked by yellow rectangle in (a)). Grain boundaries are shown by red lines. Traces of rhombohedral planes are indicated by dashed lines. **(e, f)** Stereographic projections of both host grain and new grains with grain sizes <15 µm, respectively. The subset for the new grains was selected manually. Great circles of rhombohedral planes are indicated by dashed lines in (c). **(g)** Misorientation angle distribution of new grains (randomly selected measurements). Theoretic random distribution is shown by black solid line.

### *5.2.3.2 Quartz-rich layers*

Quartz rich layers with >90 % quartz that contain some plagioclase (5-15 %) with grain diameters of about (50-300 µm) and hornblende (ca. 5 %) occur concordant to the foliation of the amphibole gneisses (Fig. 5.1). Quartz in these layers is showing quite different microstructures (Figs. 5.9 and 5.10). Mostly the quartz is recrystallized with homogeneous aggregates that show a marked crystallographic preferred orientation (CPO) (Figs. 5.9 and 5.10). The distribution and recrystallized grain size within the different samples, however, varies strongly. Two different “endmembers” are distinguished. A type-A microstructure shows a relatively coarse recrystallized grain size of ~30 ± 14 µm and a homogenous distribution with no systematic change towards the lithological contact to the amphibole rich layer (Fig. 5.9). There, the CPO is characterized by [c]-axes preferentially oriented in two maxima along the ***yz***-plane of the gneisses and <a>-axes at about 30° to the stretching lineation (***x***-axis) (Fig. 5.9g). Transgranular fractures and cataclastic zones can cut through the recrystallized quartz grains (Fig. 5.9a-c). The type-B microstructure is characterized by a finer grain size of ~10 ± 4 µm and a decreasing number of recrystallized grains towards the contact to amphibole-gneisses (Fig. 5.10). There, the CPO of the large porphyroclasts is showing [c]-axes close to the hemisphere, whereas the [c]-axis of recrystallized grains are rather close to the ***y***-axis of the gneisses (Fig. 5.10g, h). The <a>-axes preferentially oriented in a plane about 45° to the foliation and about 90° to the girdle maximum of the [c]-axes (Fig. 5.10g, h). The rotation axes show the same characteristics for both types of microstructures with a preferred orientation parallel <a> for misorientation angles below 70° and parallel poles to {r} and {z} rhombohedra for misorientation angles >70° (Figs. 5.9h and 5.10i). The strong maximum parallel <c> at 50-70° (multiple of uniform distribution >40) is related to Dauphiné twin domains. The preferred rotation axes parallel <a> and poles to {r} and {z} rhombohedra for the other misorientation angles indicates <a> dislocation glide (e.g., Kilian and Heilbronner, 2017). In both types of microstructures, porphyroclasts show subgrains with similar shape and size compared to the recrystallized grains (Figs. 5.9d, e and 5.10e, f).

## 5.3 Discussion

### *5.3.1 High-stress deformation of amphibole*

The $(\bar{1}01)[101]$ twin system of amphiboles is known from high-stress experiments (Buck, 1970; Morrison-Smith, 1976; Rooney et al., 1975, 1970; Wilks and Carter, 1990) and has rarely been reported from naturally deformed rocks, either related to pseudotachylytes (Rooney et al., 1970; Sobott, 1979), or from meteorite impact craters / related to nuclear explosions (Borg, 1972; Chao, 1967). (100) twins are observed more commonly from various fault rocks, including mylonites (Baratoux et al., 2005; Biermann, 1981; Cao et al., 2010; Cumbest et al., 1989; Kenkmann, 2000). Both types of twins are related to glide of partial dislocations $1/2\,[00\bar{1}]$ in (100) octahedral layers (Hacker and Christie, 1990; Kirby and Christie, 1977; Rooney et al., 1975). A critical resolved shear stress on the order of 200-400 MPa has been inferred for nucleation and propagation of $(\bar{1}01)[101]$ twins in deformation experiments in a solid medium Griggs-type deformation apparatus on single amphibole crystals by Rooney et al. (1970). According to the Schmid formula (1), a differential stress ($\sigma_d$) of twice the critical resolved shear stress ($\tau_{CRSS}$) is required to twin a crystal in the most suitable orientation for twinning (i.e., at a Schmid factor of 0.5). Considering the uncertainty of the experimental calibration of the critical resolved shear stress on the one hand and the fact that twinned amphiboles are widespread and occur also in grains at different crystallographic orientations (i.e., also at somewhat lower Schmid factors), 400 MPa is a conservative lower bound for the differential stress.

$$\sigma_d = \tau_{CRSS} / (\cos\gamma \cdot \cos\theta) \qquad (1)$$

where $\gamma$ and $\theta$ are the angles between $\sigma_1$ and the twin plane normal $(\bar{1}01)$ and the glide direction [101], respectively.

(100)[001] is generally assumed to be the most effective glide system, because it does not require to break the relatively strong covalent Si-O bonds (e.g., Nicolas and Poirier, 1976). Dislocation glide of amphibole with [001] burgers vectors has been indicated by TEM measurements (Biermann, 1981; Cumbest, 1988; Morrison-Smith, 1976; Rooney et al., 1975). Biermann and van Roermund (1983) observed planar defect structures parallel to (010) bound by partial [001] screw dislocations in clinoamphiboles naturally deformed at 450-600 °C. Also, kink bands with boundaries normal to [001] and rotation axes of [010] have been taken as evidence for (100)[001] dislocation glide (Dollinger and Blacic, 1975; Wilks and Carter, 1990). The kink bands observed here, however, show boundaries perpendicular to [010] and the rotation axis is scattering around [001] (Figs. 5.4b, c and 5.5a, b). Kinking is commonly found in crystals with only one glide plane, when no effective glide on this system is geometrically possible and when the shortening direction is at low angles to the glide plane (Nicolas and Poirier, 1976). Kink band boundaries are therefore significantly different to subgrain boundaries that are generated by the arrangement of geometrically necessary dislocations, requiring both, effective dislocation glide and climb, i.e., recovery, and subgrain boundaries have lower misorientation angles of <10°. The formation of kink bands involves glide of dislocations with directions roughly perpendicular to the kink band boundary, where the glide plane is defined by the glide direction and the external axis of rotation (e.g., Christie et al., 1964; Nicolas and Poirier, 1976; Raleigh, 1968). Therefore, the observed kink bands indicate (100)[010] glide. (100)[010] glide is only possible with partial dislocations of Burgers vectors 1/x [010] and at high resolved shear stresses, as the dislocation energy is proportional to the square of the magnitude of the Burgers vector, which is with ~18 Å for [010] in clinoamphiboles very high (e.g., Hacker and Christie, 1990).

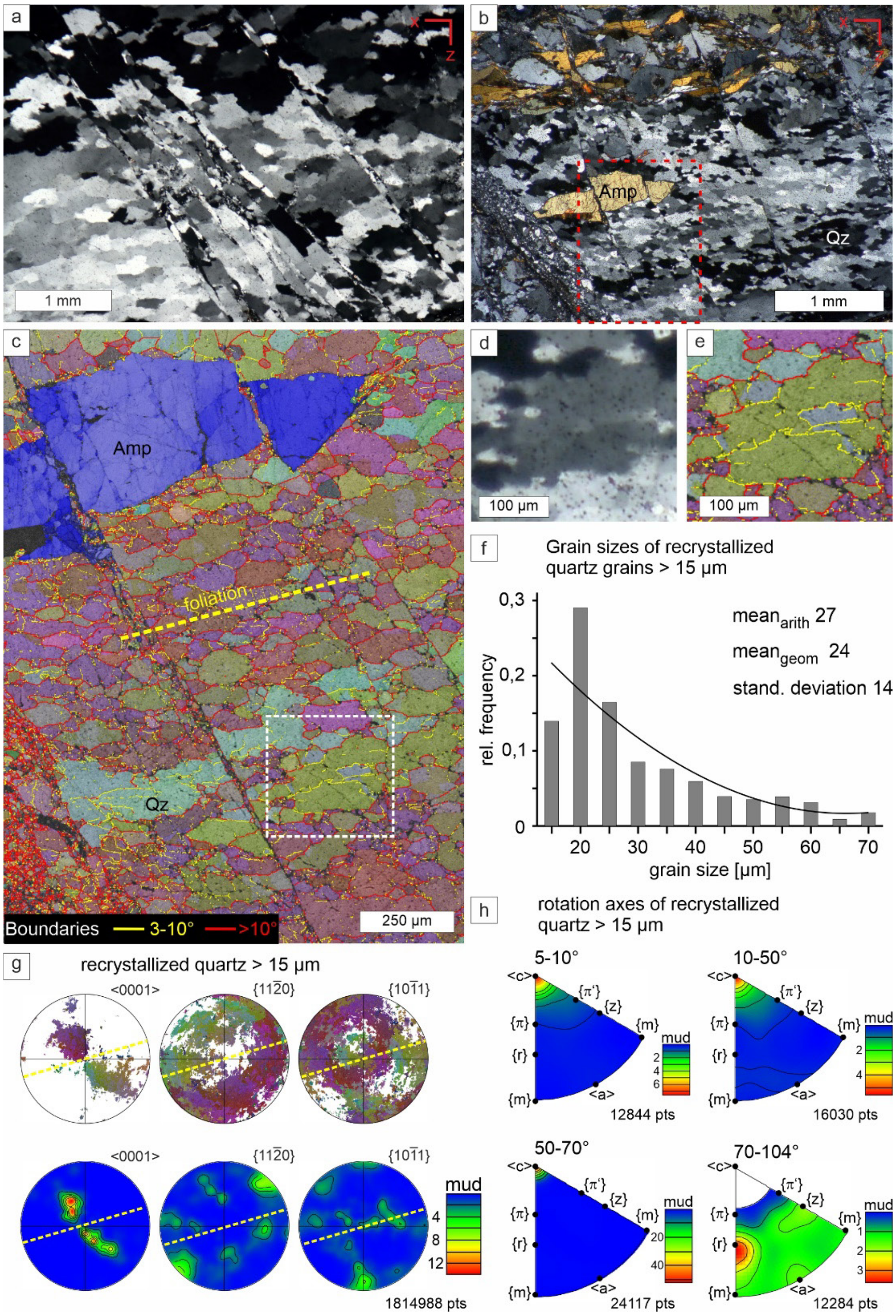

**Figure 5.9:** Microfabric of quartz-rich layer, sample LB21. **(a)** Polarized light micrograph (crossed polarizers) showing dynamically recrystallized quartz aggregates cut by transgranular fractures. **(b)** Polarized light micrograph (crossed polarizers) showing transgranular fractures in recrystallied quartz (Qz) and fractured amphibole (Amp). **(c)** EBSD map (all Euler angles) of red rimmed area shown in (b) of recrystallized quartz with low angle grain boundaries (yellow) and high angle grain boundaries (red). Fractured amphibole is colour coded in blue. Note cataclastic deformation of amphibole and quartz related to the transgranular fractures. The foliation is indicated by the yellow dashed line. **(d, e)** Polarized light micrograph (crossed polarizers) and EBSD map (all Euler angles) with low angle (yellow) and high angle (red) grain boundaries of the white-rimmed area shown in (c). Subgrains show similar shape and size compared to the recrystallized grains. **(f)** Grain size distribution of recrystallized quartz grains (>15 µm). Area-weighted grain size distribution is splotted as frequency against square root of grain size – equivalent grain diameters. Trend curve, arithmetic and geometric mean values and standard deviation are given. **(g)** Stereographic projections and density plots of recrystallized quartz grains (>15 µm). The foliation is indicated by the yellow dashed line. **(h)** Rotation axes projected in crystal coordinates for recrystallized quartz grains.

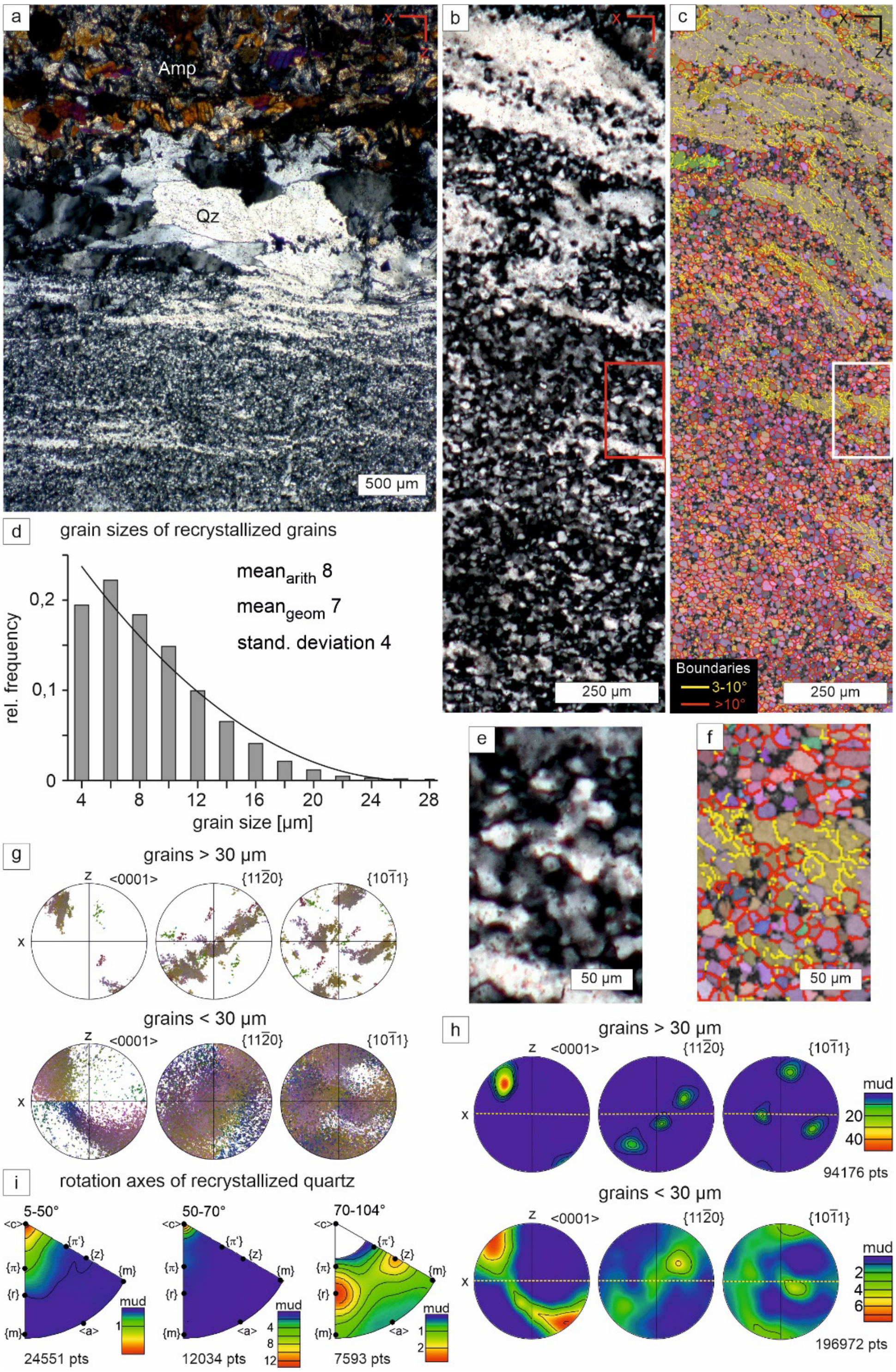

**Figure 5.10:** Microfabric in quartz-rich layer, sample CT772. **(a, b)** Polarized light micrograph (crossed polarizers) of quartz-rich layer (Qz), in contact with amphibole-rich gneiss (Amp). **(c)** EBSD map showing crystallographic orientation (all Euler angles) of quartz with low angle grain boundaries (yellow) and high angle grain boundaries (red). **(d)** Grain size distribution of recrystallized grains (<30 µm). Area-weighted grain size distribution is splotted as frequency against square root of grain size – equivalent grain diameters. Trend curve, arithmetic and geometric mean values and standard deviation are given. **(e, f)** Polarized light micrograph (crossed polarizers) and EBSD map (all Euler angles) with low angle (yellow) and high angle (red) grain boundaries of the red- and white-rimmed area shown in (b, c). Larger porphyroclasts show subgrains with similar shape and size compared to the recrystallized grains. **(g)** Stereographic projections of coarse quartz porphyroclasts (>30 µm) and recrystallized quartz grains (<30 µm). **(h)** Density plots (stereographic projections) of coarse quartz porphyroclasts (>30 µm) and recrystallized quartz grains (<30 µm). The foliation is indicated by the yellow dashed line. **(i)** Rotation axes projected in crystal coordinates of recrystallized quartz grains.

Twinning and kinking as dislocation glide-controlled deformation mechanisms occur together with microfracturing, cataclasis and the formation of pseudotachylytes (Figs. 5.2c-g; 5.3a and 5.4). The fine-grained amphibole, present within pseudotachylyte veins (Figs. 5.2e, f and 5.4a) is interpreted to be predominantly due to cataclasis given their distribution and almost random crystallographic orientation (Fig. 5.4f, g). Also, the new grains along microfractures with a CPO controlled by the host (Fig. 5.7a, b) with almost randomly oriented rotation axes (Fig. 5.7d, e) are interpreted to be predominantly due to cataclasis, as a major contribution of dislocation glide to their formation is not evident. The observed relative misorientation between larger fragments (Fig. 5.7a, b) is indicating rigid body rotation related to microfracturing, as opposed to a relative misorientation related to subgrains generated by recovery. Low angle grain boundaries are not observed. Therefore, no major contribution of dislocation climb and recovery is apparent from the amphibole microstructures.

The locally observed sutured twin boundaries (Fig. 5.6) indicate that the boundaries migrated after twinning. As no secondary phase or any systematic chemical difference is apparent along the twin boundaries, the driving force for the migration is likely a strain gradient. This implies a stage of deformation by dislocation glide at which different amounts of geometrically necessary dislocations were produced in the twins compared to the host crystal given their different crystallographic orientation. Strain-induced migration of twin boundaries is commonly observed in calcite (Burkhard, 1993). For amphiboles, Cao et al. (2010) interpreted new grains to develop from strain-induced twin-boundary migration and suggested the term “twinning nucleation recrystallization”.

Apart from this local indication strain-induced grain boundary migration after twinning, no evidence of amphibole deformation by dislocation creep (dislocation glide associated with recovery and recrystallization) is apparent. This is consistent with the general observation that amphibole is deforming by dislocation creep only at pressure-temperature conditions markedly above greenschist facies conditions (e.g., Biermann and Van Roermund, 1983; Brodie and Rutter, 1985; Cumbest et al., 1989; Díaz Aspiroz et al., 2007; Hacker and Christie, 1990; Kruse and Stünitz, 1999; Skrotzki, 1992). The deformation related to the pseudotachylyte formation in the Silvretta is constrained to be at greenschist facies conditions given the mineral assemblage in the pseudotachylytes with stilpnomelane and amphibole (Bachmann et al., 2009; Koch, 1990; Koch and Masch, 1992; Masch, 1970; Schmutz, 1995).

Taken together, the ubiquitous $(\bar{1}01)[101]$ twins and (010) kink bands of amphibole indicate high-stress dislocation glide-controlled deformation together with microcracking. The pseudotachylytes indicate associated cataclasis with comminution and fusion. A subsequent stage of dislocation glide and strain-induced twin-boundary migration is recorded by sutured twin boundaries.

### *5.3.2 High-stress dislocation glide-controlled deformation of quartz*

The quartz microcracks, sub-basal deformation lamellae and SWUE, as well as the strings of tiny quartz grains along $\{10\bar{1}1\}$ cleavage planes occur exclusively in spatial relation to twinned amphibole and pseudotachylytes (Figs. 5.8 and 5.9) and are not spatially related to the quartz-amphibole-gneiss contact (Fig. 5.10a). Therefore, these quartz microstructures are interpreted to have formed coeval with the high-stress deformation of amphibole and pseudotachylytes. The formation of fine-grained quartz aggregates in direct vicinity to pseudotachylytes has been interpreted to result from dynamic recrystallization at frictionally generated thermal pulses (Bestmann et al., 2012, 2011). Sub-basal deformation lamellae, SWUE, together with strings of new grains along highly-damaged zones in a host grain are reported to be characteristic of transient high-stress dislocation glide-controlled deformation of quartz at greenschist facies conditions during coseismic deformation and subsequent modification at decreasing stresses during postseismic creep - also without involvement of frictional melts (Trepmann and Stöckhert, 2013, 2003; Trepmann et al., 2013, 2007). Consistently, the new grains here are interpreted to be due to growth from highly damaged zones along intragranular fractures that were initially generated at high-stress dislocation glide-controlled deformation.

### *5.3.3 Dislocation creep of quartz*

Despite the varying distribution and size of recrystallized quartz, represented by the type-A and type-B quartz microstructures, both show evidence of dislocation creep, i.e., dislocation glide associated with dynamic recovery and recrystallization, by relatively homogenous aggregates of recrystallized quartz with marked CPO indicating <a>-glide (Figs. 5.9 and 5.10; e.g., Hirth and Tullis, 1992; Kilian and Heilbronner, 2017; Stipp and Tullis, 2003). In few larger remnants, the similar size and shape of subgrains compared to the recrystallized grains suggest subgrain rotation recrystallization (e.g., Hobbs, 1968; Stipp and Kunze, 2008; Urai et al., 1986), which allows to apply the recrystallization paleopiezometer by Stipp and Tullis (2003). The grain size of about ~30 µm for the type-A microstructure (Fig. 5.9) and the ~10 µm for the type-B microstructure (Fig. 5.10) indicate differential stresses of ~45 MPa and ~100 MPa, respectively. Markedly, the coarser type-A microstructure recording the lower flow stress is also showing a more homogeneous distribution of recrystallized grains with no gradient towards the amphibole-rich gneisses (Fig. 5.9). In contrast, the finer-grained recrystallized microstructure is showing a decreasing number of recrystallized grains towards the contact to the amphibole-rich gneiss, where large porphyroclasts are preserved (Fig. 5.10). Transgranular fractures cut through the recrystallized quartz microfabric with related cataclasis of quartz (Fig. 5.9a-c). Thus, the different dislocation creep microstructures are interpreted to represent a separate stage, predating both, pseudotachylyte formation and the related high-stress dislocation glide-controlled deformation of quartz and amphibole in the amphibole-rich gneisses.

The temperature-pressure conditions during dislocation creep of quartz are assumed to be about the same conditions as for pseudotachylyte formation, i.e., greenschist facies conditions, given the mineral assemblage in the pseudotachylytes with stilpnomelane and amphibole on one hand and the general Alpine greenschist facies metamorphic conditions of the Silvretta crystalline on the other (Bachmann et al., 2009; Koch, 1990; Koch and Masch, 1992; Masch, 1970; Schmutz, 1995). Therefore, the different quartz deformation behavior in the amphibole-rich layers associated to the pseudotachylytes, as well as the differences in the type-A and type-B microstructures in the quartz-rich layers cannot be mainly controlled by different temperature-pressure conditions.

A stage of creep preceding a stage of high-stress deformation at constant PT-conditions is commonly taken to indicate stress concentrations due to the viscosity contrast of rigid blocks in a weak matrix causing the formation of pseudotachylytes at depth below the seismogenic zone (e.g., Campbell et al., 2020; Hawemann et al., 2019; Papa et al., 2020). During the stage of dislocation creep in the quartz-rich layers, amphibole-rich layers are interpreted to have acted as rigid inclusion in a weak matrix, which might have induced some stress-strain concentrations, for example resulting in the formation of the observed boudinage of the amphibole-rich gneisses (Fig. 5.1b). Depending on the relative volumes, the amphibole-rich gneisses, locally even resulted in a *”strain shadow”* within quartz-rich layers with lower amount of recrystallized grains at the direct contact (Figs. 5.10 and 5.11). If this documented mechanical contrast would have resulted in the formation of pseudotachylytes (1) an increasing number of recrystallized grains and decreasing grain size towards the lithological contact and (2) the direct spatially related occurrence of pseudotachylytes would be expected. Yet, neither a strain gradient with increasing numbers of dynamically recrystallized quartz grains towards the amphibole-rich gneisses (rather the opposite, Figs. 5.10 and 5.11) is observed, nor a spatial relationship between the recrystallized quartz microstructure and pseudotachylytic and cataclastic zones associated with twinned amphibole. Therefore, the preceding stage of dislocation creep in the quartz-rich lithologies observed here cannot explain the high differential stresses recorded by the amphibole and quartz microstructures within the amphibole-rich gneisses and the associated pseudotachylyte formation.

### *5.3.4 Deformation controlled by the distance to the thrust fault*

The different microstructures in the pseudotachylyte-bearing amphibole-rich layers, as well as that in the type-A and type-B microstructures in the quartz-rich layers at the same pressure-temperature conditions can also not be explained by the different lithology alone, as discussed above. The difference in the deformation behavior are suggested to be controlled by the different distance to the tip of the seismogenic zone, following the model by Nüchter et al. (2013) (Fig. 5.11). During the decoupling of a large crystalline nappe, as the Silvretta nappe, incremental fault growth with related stress concentrations at the fault tip need to be considered (e.g., Cowie and Scholz, 1992c; Pollard and Segall, 1987; Stein et al., 1988; Walsh and Watterson, 1988). Therefore, the model of Nüchter et al. (2013) proposed for a given observation site, i.e., the investigated rock sample, a characteristic sequence of deformation at systematically decreasing distance to the propagating thrust fault. Following this model, the different microstructures are suggested to represent deformation at more or less constant depths, yet at different distances to the propagating tip of the basal thrust fault during decoupling of the Silvretta nappe (Fig. 5.11). For decreasing distance, this would include:

1) Quartz dislocation creep-dominated stages at stresses from a few tens of MPa (type-A microstructure with relatively coarse grain diameters and homogeneous distribution of recrystallized grains) to a hundred of MPa (type-B microstructure with fine-grained recrystallized aggregates and *"strain-shadow"* at the contact to the amphibole-rich layer). The higher the distance to the seismic active fault, the more distributed the deformation. During this long-term creep, quartz-rich layers accumulate the higher amount of strain in relation to the amphibole-rich gneisses, consistent with a lower flow strength of quartz related to dislocation creep (e.g., Gleason and Tullis, 1995; Hirth et al., 2001; Luan and Paterson, 1992) as opposed to amphibole (e.g., Berger and Stünitz, 1996; Brodie and Rutter, 1985; Cao et al., 2010; Díaz Aspiroz et al., 2007; Imon et al., 2004; Shelley, 1994).

2) Dislocation glide-controlled deformation of quartz is preferentially occurring in coarse quartz grains as opposed to the fine-grained recrystallized aggregates consistent with the inverse relationship between strength and grain size during dislocation glide, where grain boundaries act as obstacles (e.g., Fredrich et al., 1990; Hall, 1951; Hirth, 1972; Petch, 1953). This dislocation-glide controlled deformation of quartz is directly related to twinned amphibole, as well as cataclastic and pseudotachylytic zones. Given the lower fracture toughness, the higher shear modulus and lower melting temperature in relation to quartz, amphibole is preferentially responding by comminution and fusion (e.g., Spray, 2010). Therefore, the observation that pseudotachylytes are more common in the amphibole-rich gneisses containing coarse quartz indicates that they represent the "weak" lithology and the finer-grained recrystallized quartz layers represent relatively the "stronger" lithology during the high-stress, high strain-rate deformation that caused the formation of pseudotachylytes.

The heterogeneous microstructures of preserved coarse quartz aggregates on one hand and twinned amphibole indicating high-stress conditions ≥400 MPa at the same PT-conditions on the other, require transient high-stress conditions characterized by fast stress-loading rates and rapidly decreasing stresses (Trepmann and Seybold, 2019; Trepmann et al., 2017). Such high stresses during the pseudotachylyte-forming stage are well consistent to the stresses inferred by jadeite twins from metagranites in the Sesia zone, which were related to coseismic deformation (Trepmann and Stöckhert, 2001). The deformation records of twinned clinoamphiboles and clinopyroxenes are ideal to detect transient peak stresses during coseismic deformation, as the characteristic microstructures are neither masked by preceding nor by subsequent stages of deformation at lower stresses, as the case for quartz, for example. They offer the unique possibility to constrain the close to peak stress conditions controlling seismic faulting at depth of the base of seismogenic zone, not directly accessible for in situ stress measurements.

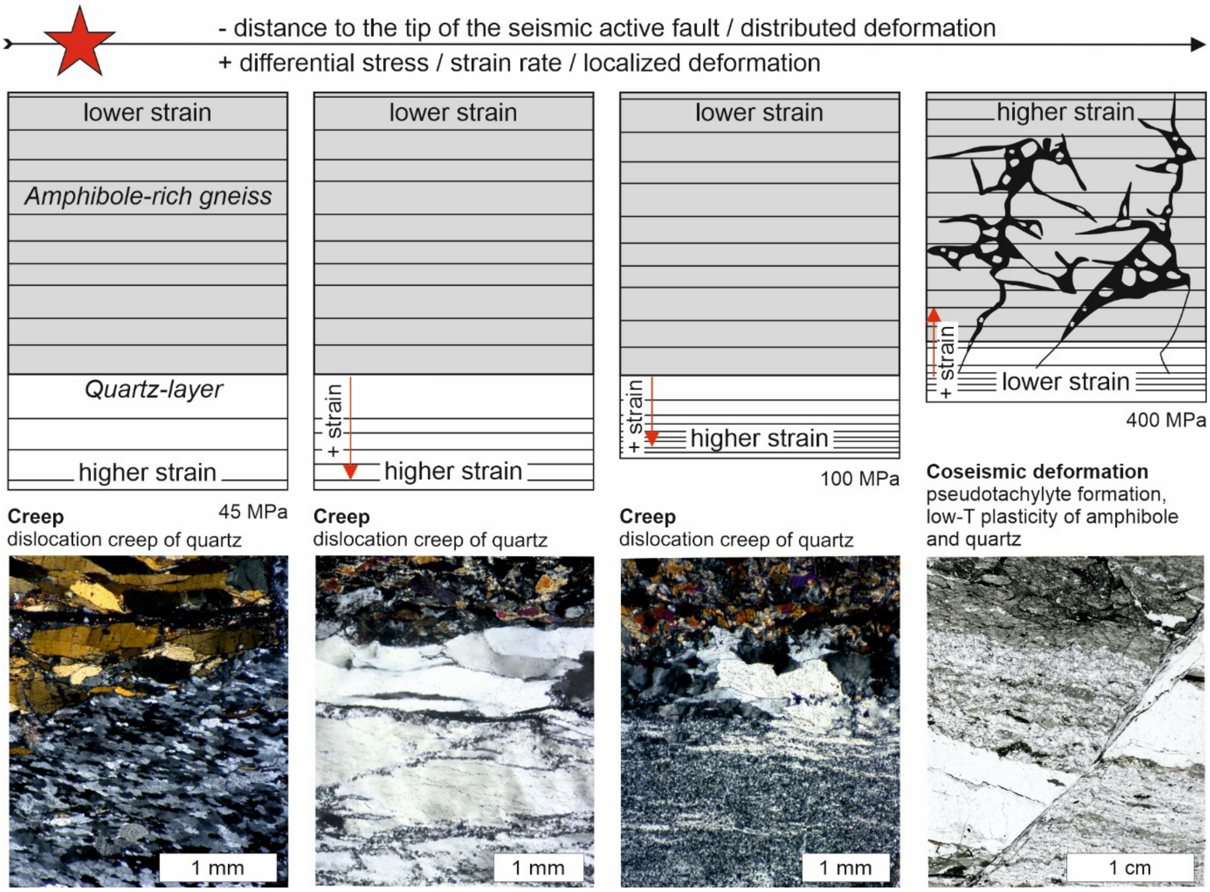

**Figure 5.11:** Conceptual sketch with polarized light micrographs showing the change of deformation behavior of different lithologies with distance to the propagating tip of the seismic active fault zone. See text for discussion.

## 5.4 Conclusions

The different microstructures are controlled by the distance to the tip of the propagating basal thrust fault during decoupling of the Silvretta nappe.

At low distances to the fault:

- Stresses of ≥400 MPa are indicated by $(\bar{1}01)[101]$ mechanical twins in amphibole.
- Amphibole twinning and kinking occur together with cataclasis and pseudotachylyte formation, as well as dislocation-glide controlled deformation of quartz. No spatial relationship of these high-stress/high strain-rate microstructures to the lithological contact to quartz-rich layers has been observed.
- During the high-stress/high strain-rate deformation, amphibole-rich gneisses were accumulating a higher amount of strain relative to quartz-rich lithologies, given the lower fracture toughness, the higher shear modulus, and lower melting temperature of amphibole compared to quartz.

At larger distances to the fault:

- Quartz-rich lithologies are accumulating a higher amount of strain given the lower flow strength of quartz related to dislocation creep in comparison to amphibole.
- Deformation at few tens of MPa to a hundred of MPa (depending on the distance to the fault), quartz-rich layers were deformed by dislocation creep, as indicated by homogenously recrystallized grains with CPO.

This pseudotachylyte formation at the base of the Silvretta crystalline cannot be explained by instabilities during dislocation creep of the quartz-rich lithologies, ruling out a major influence of thermal runaway. The study demonstrates the potential of microstructures to constrain the deformation history controlling seismic faulting and creep at hypocentral depth not directly accessible for in situ stress measurements.

# 6 Rheology dependent on the distance to the Propagating Thrust Tip – (Ultra-)Mylonites and Pseudotachylytes of the Silvretta basal Thrust

This chapter is based on the manuscript: Brückner et al. (2023). Rheology dependent on the distance to the Propagating Thrust Tip – (Ultra-)Mylonites and Pseudotachylytes of the Silvretta basal Thrust. *Tectonics*, 42, 10. https://doi.org/10.1029/2023TC008010

## 6.1 Introduction

Pseudotachylytes are fault rocks resulting from the solidification of frictional melts formed along faults during seismic slip (slip rates of ~$10^{-4}$-$10^{1}$ m/s, e.g., Cowan, 1999; Rowe and Griffith, 2015; Sibson, 1975). They are commonly described to crosscut each other and being themselves deformed (Bachmann et al., 2009; Campbell and Menegon, 2022, 2019; Campbell et al., 2020; Hawemann et al., 2018; Koch and Masch, 1992; Lin, 2008a, 2008b; Lin et al., 2003; Menegon et al., 2017; Moecher and Steltenpohl, 2009; Passchier, 1982b; Pittarello et al., 2022; Price et al., 2012; Rowe et al., 2018; Sibson, 1980; Takagi et al., 2000; White, 2004, 1996). For large fault systems, incremental fault growth is predicted with multiple earthquake cycles (e.g., Cowie and Scholz, 1992c; Dawers et al., 1993; Schlische et al., 1996; Stein et al., 1988; Walsh and Watterson, 1988). Therefore, crosscutting pseudotachylyte veins have been proposed to indicate repeated rupturing during successive seismic cycles (e.g., Koch and Masch, 1992; Swanson, 1992). The formation of pseudotachylytes and mylonites can take place under the same metamorphic conditions, as recorded by mutual overprinting relationships (Altenberger et al., 2013, 2011; Koch and Masch, 1992; Moecher and Steltenpohl, 2009; Pennacchioni and Cesare, 1997; Pittarello et al., 2012; White, 2012, 2004, 1996). As such, deformed pseudotachylytes, which predate and outlast mylonites, were interpreted as recurring earthquake cycles Hawemann et al., 2018; Koch and Masch, 1992; Lin, 2008a; Moecher and Steltenpohl, 2009; Takagi et al., 2000). Complex networks of crosscutting pseudotachylytes can, however, also be generated by one single large rupturing event (Allen, 2005; Grocott, 1981; Rowe et al., 2018). During a single rupture, deformation mechanisms can vary (Kirkpatrick and Shipton, 2009) and several slip surfaces can be active in parallel (Heesakkers et al., 2011; Swanson, 2006), which can be reused in large earthquakes (Allen, 2005; Kirkpatrick and Shipton, 2009). Rowe et al. (2018) presented field observational criteria for branching and coalescing ruptures that generate complex pseudotachylyte networks formed in one single seismic event. At the basal thrust of the Preveli crystalline nappe on Crete, only one prominent and unique imprint of coseismic deformation with the formation of pseudotachylytes at one specific location is described by Nüchter et al. (2013). These authors proposed a model of coseismic thrust fault propagation, in which dependent on the distance to the propagating fault tip, a characteristic sequence of deformation structures develops. With decreasing distances ductile (e.g., kink bands) to brittle structures (quartz veins) and finally pseudotachylytes, as the last microstructural imprint recording earthquake rupturing, form. In this model, strain after the passage of the fault front is localized in the next rock increment, eventually causing the decoupling of the nappe from its original basement before subsequent transport over large horizontal distances onto a foreign tectonic unit. During nappe transport, low shear stresses are required, and further strain is localized in weak lithologies and areas of high pore fluid pressure (Bachmann et al., 2009; Cook and Aitken, 1976; Davis et al., 1983; Davis and Engelder, 1985; King Hubbert and Rubey, 1959; Koch and Masch, 1992; Laubscher, 1983; Rodgers et al., 1962). Passelègue et al. (2021) showed experimentally that pseudotachylytes are prone to deformation by diffusional creep and concluded that the rheology of pseudotachylytes can reduce the strength of the continental crust. In contrast, pseudotachylyte formation, which welds the fault plane, can prevent the occurrence of shear on the same slip surface and subsequent failure arises at a new site (Mitchell et al., 2016; Proctor and Lockner, 2016).

The question, of whether fault rocks or their host rocks control the strength of the continental crust is related to the question of their relative strength (i) during coseismic high-stress plasticity and (ii) during creep. Here, the microstructural record of the different Silvretta fault rocks (deformed and non-deformed, i.e., pristine pseudotachylytes, as well as (ultra-)mylonites) is used to evaluate the deformation conditions. The implications for the strength of the various fault rocks during the different stages and the assignment of the recorded coseismic rupturing event(s) to the Alpine stages are discussed. For the purpose of this paper, the term “mylonites” is used in the sense of localized high-strain zones, where quartz-rich layers deformed dominantly by dislocation creep developing a marked crystallographic preferred orientation (CPO) of dynamically recrystallized grains. Silvretta fault rocks are called “ultramylonites” if they are characterized by fine-grained polyphase layers containing less than 10 % porphyroclasts (Passchier and Trouw, 2005), mostly comprised of quartz deformed by dislocation creep.

## 6.2 Results

### 6.2.1 Investigated samples and field observations

The investigated pseudotachylyte-bearing Silvretta host rocks (Appendix A1 and A2; LB24: 47°01‘00“ N / 10°28‘00“ E; LB28: 46°53‘23“ N / 10°11‘16“ E; LB42: 46°52‘57“ N / 10°12‘57“ E; LB64: 46°48‘03“ N / 10°09‘06“ E; LB78: 46°52‘50“ N / 10°10‘18“ E; LB84: 46°51‘39“ N / 10°12‘47“ E; CT623: 46°55‘21“ N / 10°10‘30“ E) comprise foliated amphibole-rich gneisses (Fig. 6.1a-e) and biotite-rich gneisses (Fig. 6.1f). The gneisses commonly show concordant quartz veins containing >95 % quartz (Fig. 6.1a-d, f). The amphibole-rich gneisses comprise about 40-60 % amphibole, 20-40 % plagioclase, 10-30 % quartz, 0-10 % biotite, and 0-5 % white mica. Biotite gneisses comprise about 20-30 % quartz, 20-30 % biotite, 30-40 % feldspar, and 10-15 % green hornblende. Sphene, zircon, ilmenite, rutile, epidote, and stilpnomelane occur as accessory constituents in both gneisses.

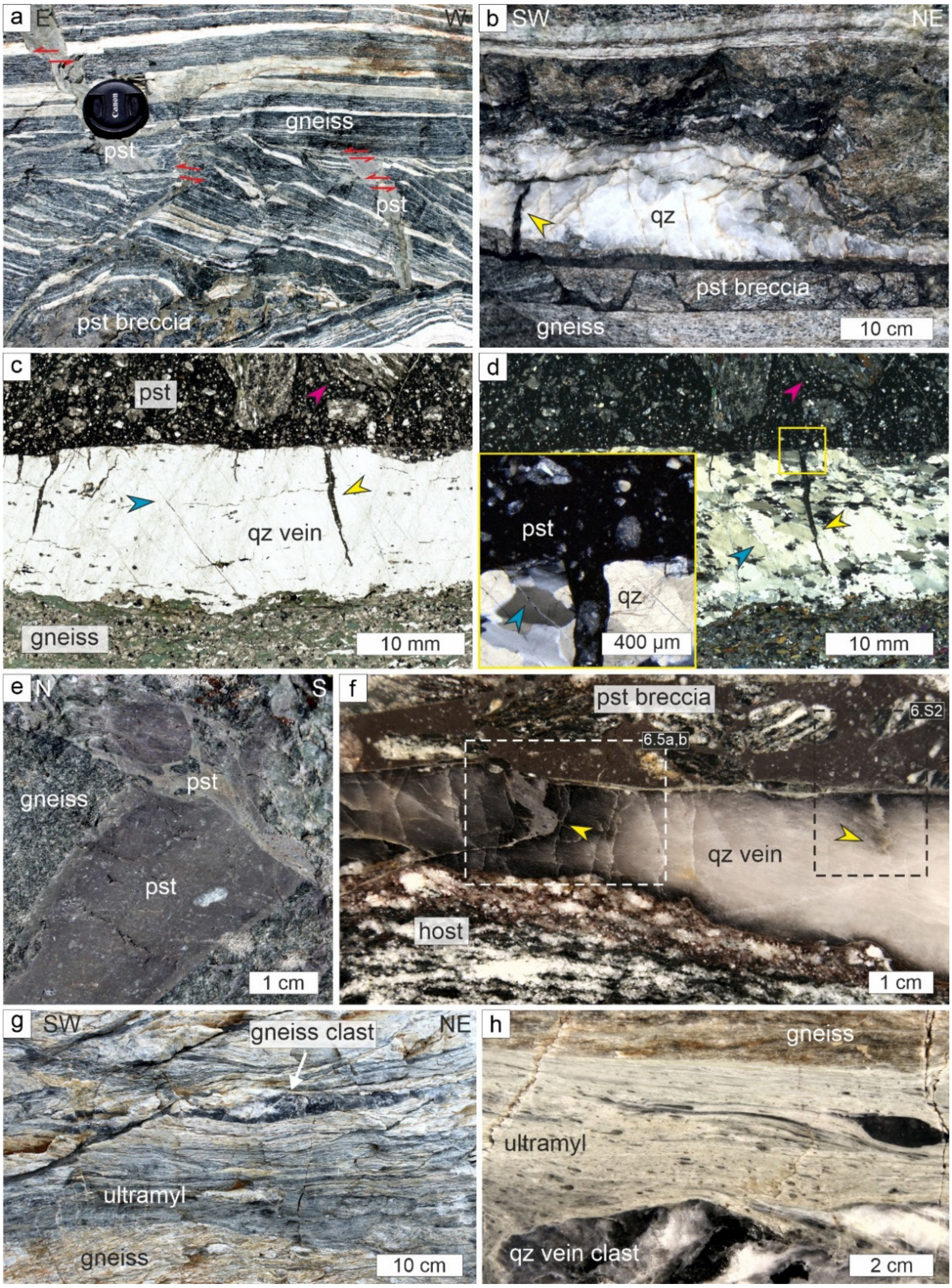

**Figure 6.1:** Fault rocks at the base of the Silvretta nappe. **(a)** Pseudotachylyte (pst) veins in brecciated amphibole-rich gneisses display offsets of several cm (red arrows). **(b)** Tabular pseudotachylyte breccia with injection vein into host quartz vein (qz, yellow arrow). **(c, d)** Polarized light micrograph, (d) is taken with crossed polarizers, showing straight injection veins (yellow arrows) from parent pseudotachylyte with a sharp boundary to coarse-grained quartz layer concordant to amphibole-rich gneiss, sample CT623c. Injection veins are affected by shear fractures (blue arrows). Clasts of amphibole-rich gneiss occur within pristine pseudotachylyte (purple arrows). Close-up in (d) is showing sharp boundaries of injection veins to the coarse recrystallized quartz vein fabric. **(e)** Pseudotachylyte vein containing brecciated clasts of a primary pseudotachylyte. **(f)** Quartz layer concordant to foliated biotite-rich gneiss (host) with pseudotachylyte breccia containing large amphibole-gneiss clasts, sample LB78. Within the quartz layer, foliated and folded pseudotachylyte injection veins occur (yellow arrows). White and black rectangles display the position of Fig. 6.5a, b and Fig. 6.S2 in supporting materials, respectively. **(g, h)** Ultramylonitic layers (ultramyl) within host gneisses that represent deformed pseudotachylytes, sample LB28. Note the low-spaced foliation, which is deflected around gneiss and vein-quartz clasts in (h).

Pseudotachylytes occur as complex vein networks within brecciated host gneisses, where the single veins are a few mm to dm in thickness (Fig. 6.1a-f). The main pseudotachylytic veins are commonly found subparallel or slightly oblique to the foliation of the host gneisses and concordant quartz veins, in which a few hundred µm to cm long and µm to mm wide injection veins at a high angle to the main pseudotachylyte can occur (Fig. 6.1a-d, f). Pseudotachylytes can crosscut other pseudotachylytes with offsets of a few hundred microns to several cm (Fig. 6.1a). Angular (Fig. 6.1a) and tabular breccias (Fig. 6.1b, f), as defined by Rowe et al. (2018) are common. Less commonly, brecciated clasts of pseudotachylytes within pristine pseudotachylytic veins occur (Fig. 6.1e). The injection veins are mostly straight (Fig. 6.1a-d) but can be affected by shear fractures within the host quartz (Fig. 6.1c, d). The hosting quartz usually shows a coarse recrystallization fabric unrelated to the crosscutting straight injection veins (Fig. 6.1d). In addition, folded injection veins can be found, which show a sharp contact with another pseudotachylyte that shows no field evidence of deformation (Fig. 6.1f). Ultramylonites, which represent deformed pseudotachylytes (e.g., dynamic recrystallization of quartz, Koch and Masch, 1992), are characterized by a low-spaced foliation deflected around cm-sized gneiss- and vein-quartz clasts (Fig. 6.1g, h).

The pseudotachylytes exhibit a fine-grained matrix with clasts of the host gneisses, several cm to dm in diameter (Fig. 6.1c-f). The strongly varying composition of the pseudotachylytes depends on the local host rock lithology (Koch and Masch, 1992; Schmutz, 1995). Within biotite-rich gneisses, pseudotachylytes often contain aggregates of intergrown epidote and feldspar, whether they are pristine (Fig. 6.2a-c) or deformed (Fig. 6.2d-f). In contrast, in the more common amphibole-rich gneisses these epidote-feldspar aggregates have not been observed. Pittarello et al. (2022) reported similar epidote aggregates in the Silvretta fault rocks and interpreted them to indicate greenschist facies conditions. Stilpnomelane is observed by polarized light microscopy and scanning electron microscopy as fine needles (width: ~1 µm; length: 30-100 µm) in both, pristine (Fig. 6.2a, c), as well as deformed pseudotachylytes (Fig. 6.2d, f), and within all types of Silvretta gneisses. The presence of stilpnomelane in the pristine and deformed pseudotachylytes has been confirmed by Raman spectroscopic investigations (Text 6.S1 and Fig. 6.S1 in supporting material). Stilpnomelane has already been described by Koch and Masch (1992) to occur in all Silvretta fault rocks and is taken to indicate greenschist facies conditions. For a detailed field description and occurrence of the pseudotachylytes, the reader is referred to Koch and Masch (1992) and Schmutz (1995).

Most of the observed crosscutting relationships of pseudotachylytes fulfill the criteria of complex networks that can be generated within a single seismic event (e.g., angular breccias in Fig. 6.1a and tabular breccias in Fig. 6.1b, as defined by Rowe et al. (2018)). The relationship between deformed and pristine pseudotachylytes, as well as (ultra-)mylonites (Figs. 6.1e-h and 6.3a), however, cannot be revealed by field observations alone. Three representative samples that contain both, deformed and pristine pseudotachylytes from more than 80 analyzed pseudotachylyte-bearing gneisses, were chosen for detailed microstructural analysis (Fig. 1b): (1) deformed pseudotachylytes (pst1) grading into ultramylonites, sample LB28 (Figs. 6.1h; 6.3 and 6.4); (2) folded and foliated injections veins (pst1) in foliated quartz vein crosscut by undeformed pristine pseudotachylytes (pst2, pst3), sample LB78 (Figs. 6.1f and 6.5-6.7) and (3) brecciated pseudotachylytes, sample LB24 (Figs. 6.1a, e and 6.8).

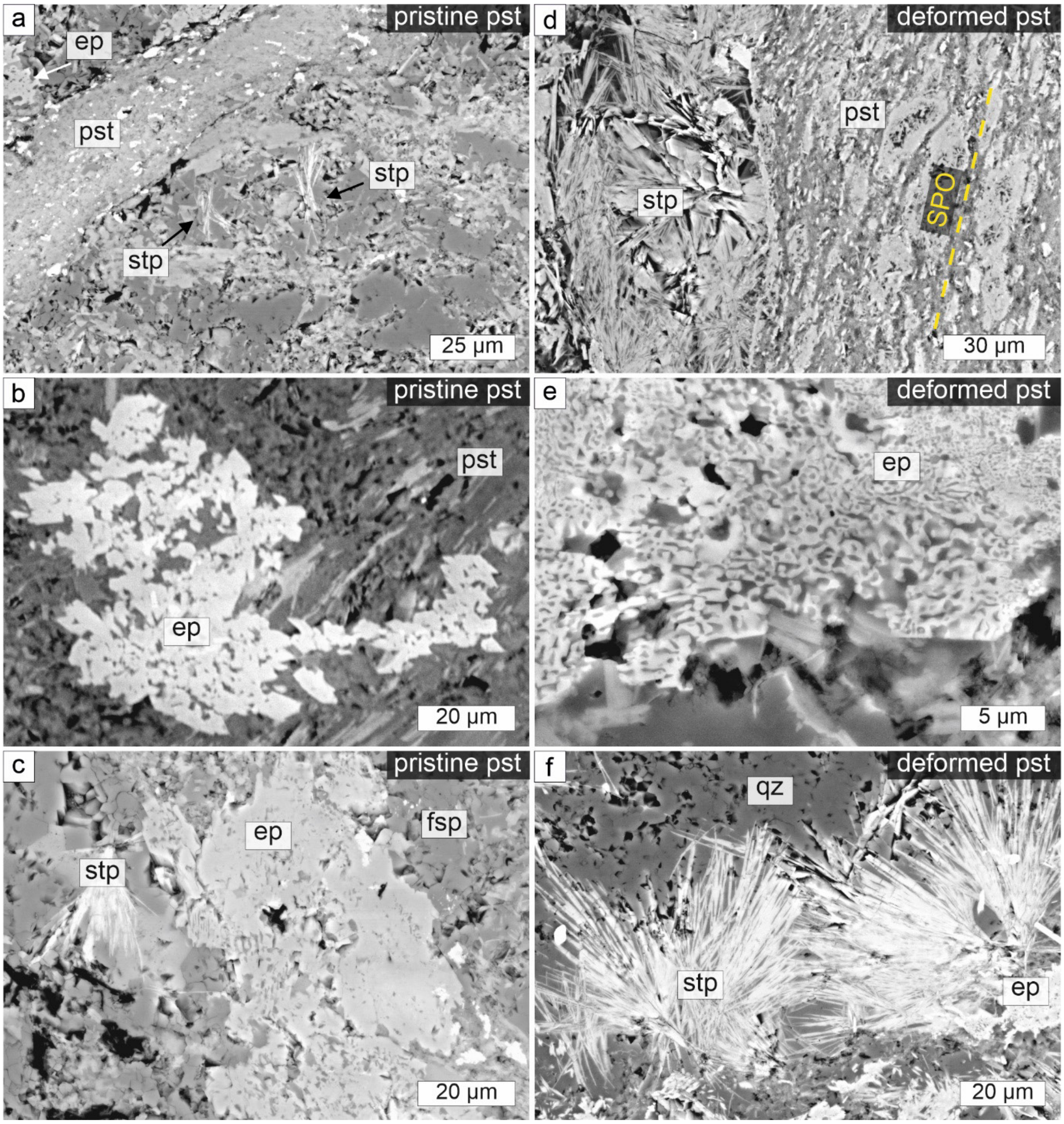

**Figure 6.2:** Backscattered electron (BSE) images of stilpnomelane and epidote within pristine (a-c) and deformed (d-f) pseudotachylytes. **(a)** Stilpnomelane (stp) and epidote (ep) associated with pristine pseudotachylyte (pst), sample LB64b. **(b)** Intergrown epidote-feldspar aggregate, sample LB84b. **(c)** Epidote and stilpnomelane aggregates embedded in a feldspar-rich (fsp) gneiss clast within pseudotachylyte, sample LB64b. **(d)** Stilpnomelane aggregates in contact with deformed pseudotachylyte showing a matrix with a shape preferred orientation (SPO, yellow dashed line), sample LB42b. **(e)** Epidote-feldspar intergrowth, sample LB78b. **(f)** Stilpnomelane together with epidote in a quartz-rich (qz) gneiss clast, sample LB42a.

### *6.2.2 Deformed pseudotachylytes grading into ultramylonites*

The deformed pseudotachylytes are characterized by a well-developed foliation deflected around larger gneiss clasts (Figs. 6.1g, h and 6.3a). The matrix grains, as well as clasts, reveal an associated shape-preferred orientation (SPO) (Fig. 4a-e). The aspect ratio of clasts gradually increases with a decreasing spacing of the foliation grading towards ultramylonite layers. In the strain shadow of the rigid gneiss clasts, the original fabric of the pseudotachylyte can be preserved with rounded and isometric clasts (Fig. 6.3b, c).

Characteristic ultramylonitic parts are defined by a fine-grained (<10 µm) mica-rich matrix with elongated larger mylonitic quartz clasts (Figs. 6.3b-e and 6.4a-c). The mylonitic quartz clasts have a high aspect ratio of 7.0 ± 1.9 (long axis: 350-2000 µm; short axis: 50-250 µm), which is considerably larger than that of the clasts within the preserved pseudotachylyte of 1.8 ± 0.5 (long axis: 150-600 µm; short axis: 50-350 µm; Fig. 6.3d-f). Larger feldspar (albite) clasts are cataclastically deformed (Fig. 6.3b, c, e). The recrystallized quartz grains show an oblique SPO with the long axes of grains at an angle of about 30-45° to the ultramylonitic foliation (Fig. 6.4c). They reveal a marked crystallographic preferred orientation (CPO) characterized by a girdle maximum at a high angle to the stretching lineation of the gneiss (X, Fig. 6.4c, d). The <a>-axes are preferentially oriented in a plane about 10-20° to the foliation (Fig. 6.4d). This quartz fabric with CPO and oblique SPO (Fig. 6.4c, d) indicates dynamic recrystallization (strain-induced grain boundary migration) during shearing. The sinistral shear sense is consistent with asymmetric strain shadows around feldspar clasts within the ultramylonite (Fig. 6.4a), indicating that the deformation of clasts is related to the formation of the ultramylonite and does not represent an inherited fabric.

### *6.2.3 Folded injection veins crosscut by pristine pseudotachylytes*

Folded and foliated injection veins (pst1) occur in deformed vein-quartz and are crosscut by pristine pseudotachylytes (pst2 and pst3; Figs. 6.1f; 6.5 and Fig. 6.S2 in supporting material). In the following, first the pseudotachylytes and then the quartz microfabrics of the hosting quartz vein are described.

#### *6.2.3.1 Pseudotachylytes*

The folded and foliated injection veins (pst1; Fig. 6.5a, b and Fig. 6.S2 in supporting material) display a fine-grained foliated matrix of quartz, feldspar, mica, and epidote, that also contains quartz-rich clasts with diameters <50 µm (Fig. 6.5a, b and Fig. 6.S2c, d in supporting material). The foliation is defined by the SPO of the matrix minerals, including the epidote-feldspar aggregates, and corresponds to the foliation of the hosting deformed quartz vein (Fig. 6.5b, c-e and Fig. 6.S2c, d in supporting material).

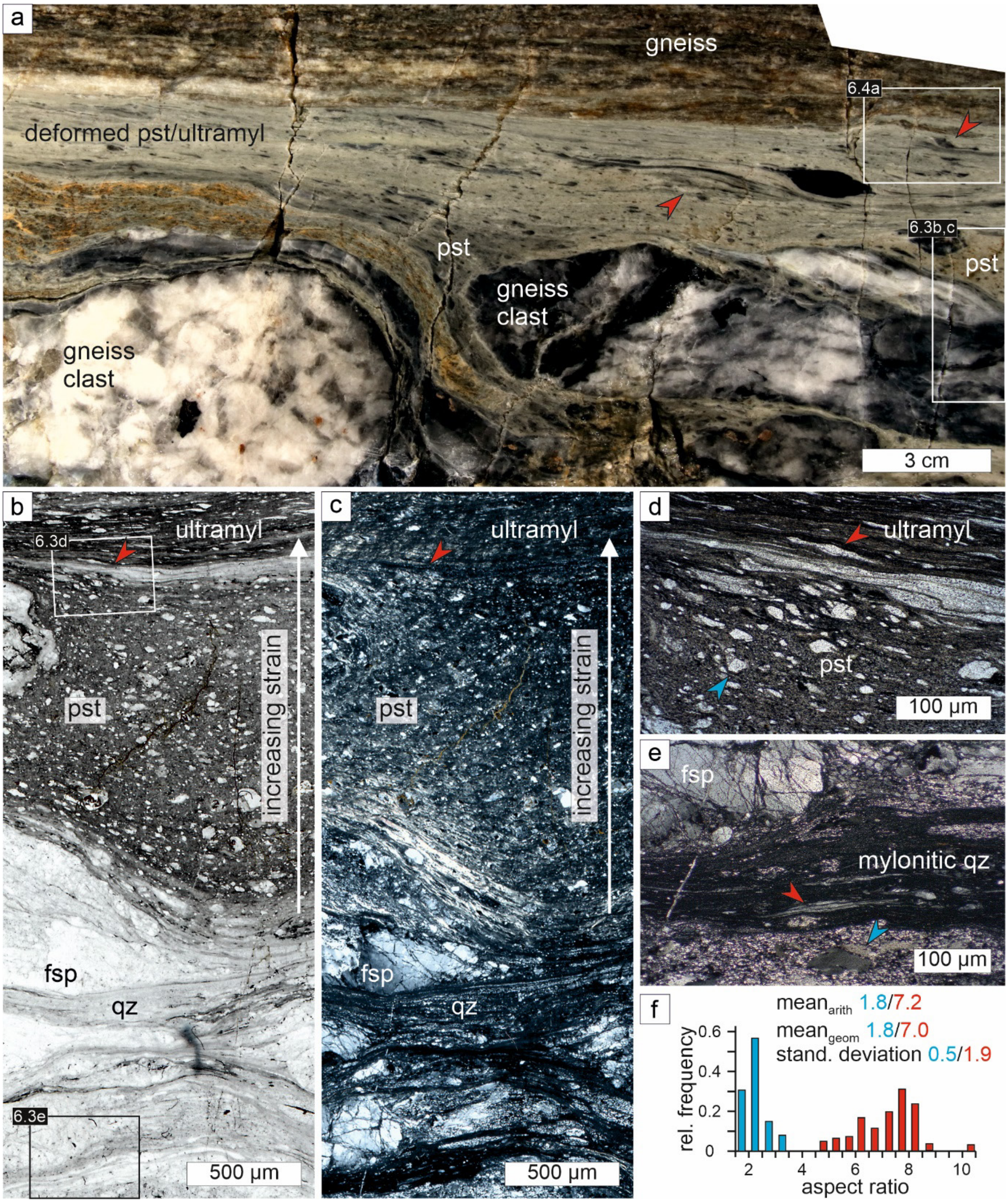

**Figure 6.3:** Deformed pseudotachylyte (pst) containing large gneiss clasts of feldspar (fsp) and quartz (qz) grading into an ultramylonitic layer (ultramyl), sample LB28. **(a)** Field and **(b, c)** thin section micrographs, respectively, (c) is taken with crossed polarizers. Aspect ratio of clasts is increasing and the spacing of the foliation is decreasing from the preserved pseudotachylyte at the bottom, finally grading to an ultramylonite at the top. Note mylonitic quartz clasts (red arrows). **(d, e)** Polarized light micrographs (crossed polarizers) of the gradual transition from pseudotachylyte to ultramylonite. Note mylonitic quartz clasts with a high aspect ratio in ultramylonite (red arrows) and isometric quartz clasts in the preserved pseudotachylyte (blue arrows). **(f)** Aspect ratio of parent quartz clasts (blue) and mylonitic quartz clasts (red) within deformed pseudotachylyte and ultramylonites, respectively.

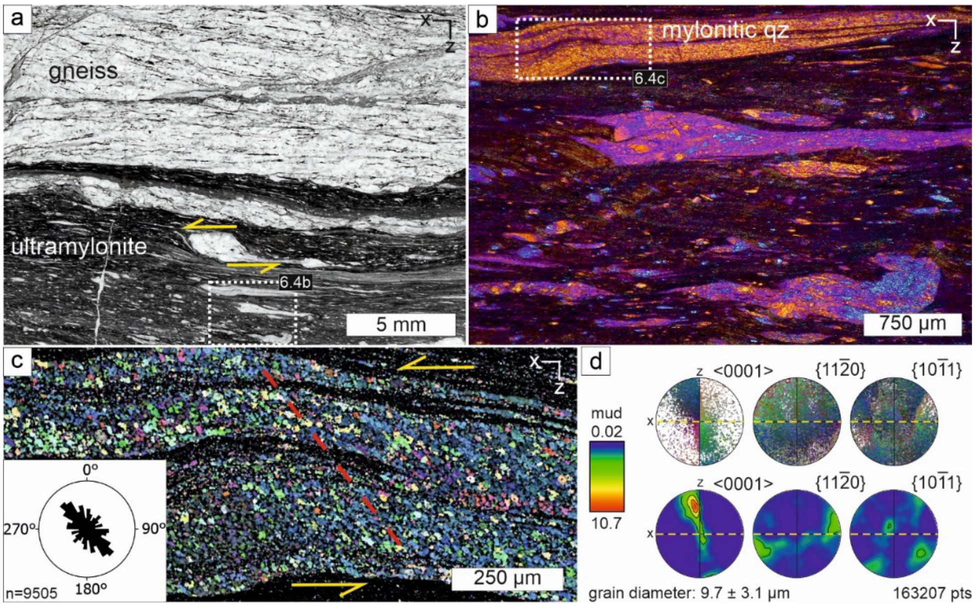

**Figure 6.4:** Mylonitic quartz microfabric in clasts of ultramylonite, sample LB28a. **(a)** Thin section micrograph of ultramylonite layer in contact with the host gneiss (position is shown in Fig. 6.3a). A sinistral shear sense (yellow arrows) is indicated by asymmetric strain shadows around feldspar clasts within the fine-grained ultramylonite. **(b)** Polarized light micrograph (crossed polarizers and compensator plate inserted) of the ultramylonite containing mylonitic quartz (qz) clasts. **(c)** Electron backscattered diffraction (EBSD) map displaying different crystallographic orientations (all Euler angles) of mylonitic quartz. Recrystallized small grains show an oblique shape-preferred orientation (SPO) with the long axis at 30-45° to the ultramylonite foliation, indicating a sinistral sense of shear (yellow arrows). The SPO is visualized by the inserted rose diagram and indicated with a red dashed line. **(d)** Stereographic projections (colors correspond to all Euler angle colors in (c)) and density plots of recrystallized quartz. The foliation of the ultramylonite is indicated by a yellow dashed line.

The pristine pseudotachylyte (pst2) contains isometric quartz clasts (<500 µm) (Fig. 6.5a, b, f) and larger clasts of amphibole-rich and biotite-rich gneisses (<3 cm) (Fig. 6.5a, b). Hornblende shows $(\bar{1}01)[101]$ mechanical twins, as generally found in pseudotachylyte-bearing amphibole-rich gneisses of the Silvretta (Brückner and Trepmann, 2021). The matrix of these pristine pseudotachylytes comprises homogenous skeleton-shaped amphibole microliths with a grain size of ~5 µm (pst2, Fig. 6.5g), in detail described by Koch and Masch (1992).

The deformed pseudotachylyte (pst1, red in Fig. 6.5a, b) and the pristine pseudotachylyte (pst2, green in Fig. 6.5a, b) are separated by another thin (<100 µm in width) pseudotachylyte layer (pst3, blue in Fig. 6.5a, b, e-g). Locally a shear offset to the deformed pseudotachylyte (pst1) of a few hundred µm can be observed (Fig. 6.5e). The third pseudotachylyte (pst3, blue) also forms an injection vein within the pristine pseudotachylyte (pst2) (Fig. 6.5a, b, f). It is mainly composed of feldspar, quartz, and amphibole (Fig. 6.5g) and shows a sharp boundary between the deformed (pst1, red) and pristine (pst2, green) pseudotachylyte (Fig. 6.5e-g). Rotated and brecciated clasts of both pseudotachylytes (pst1 and pst2) are embedded within that thin pseudotachylyte layer (pst3) (Fig. 6.5a, b, h). At the contact with the third pseudotachylyte, the amphibole microliths of the pristine pseudotachylyte matrix (pst2, green) are sheared (Fig. 6.5g).

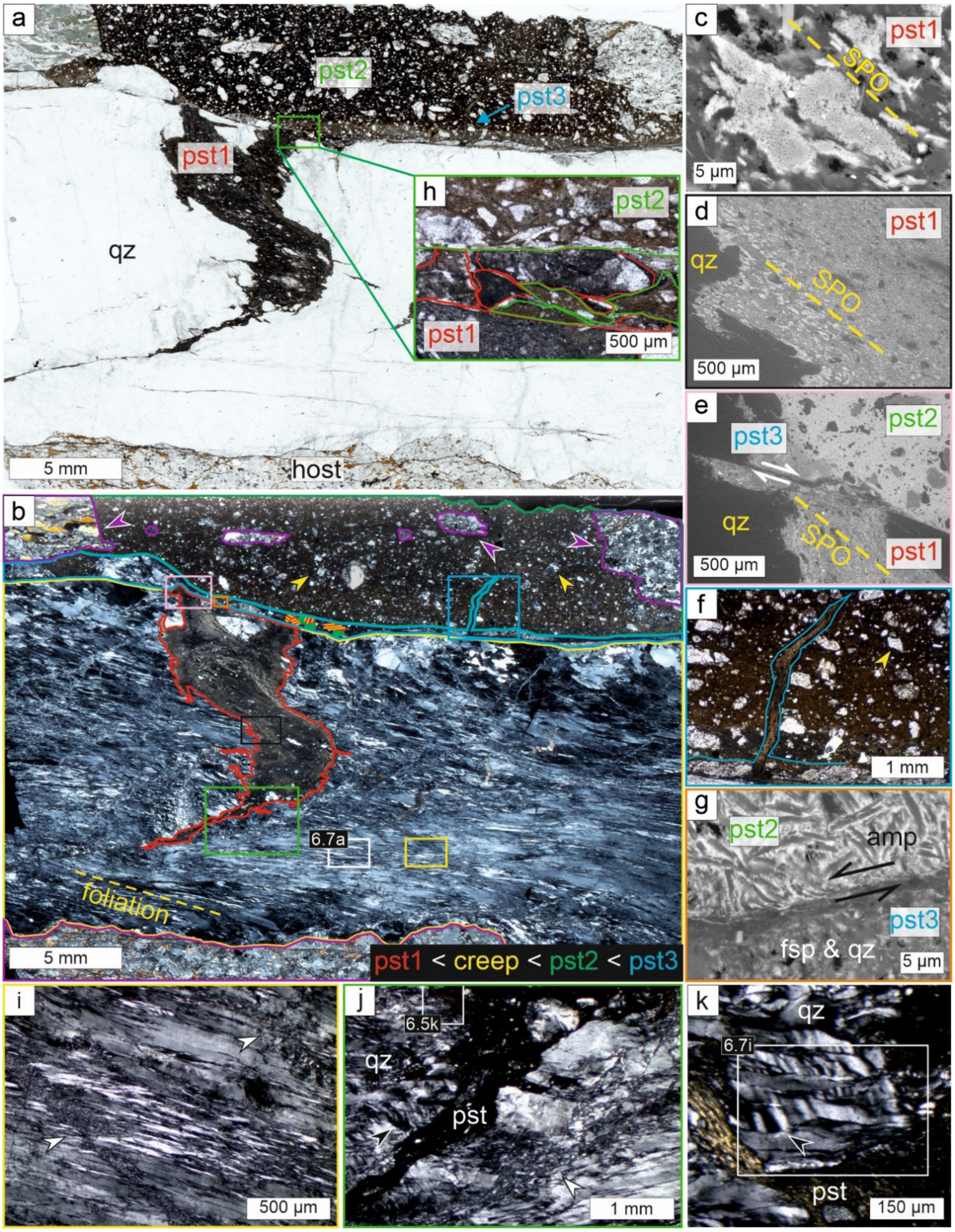

**Figure 6.5:** Microfabrics of deformed pseudotachylyte injection vein within deformed quartz vein, crosscut by pristine pseudotachylytes, sample LB78b. **(a, b)** Thin section scans (position is shown in Fig. 6.1f) showing deformed pseudotachylyte injection vein (pst1, red) in a quartz-rich (qz) layer concordant to a biotite-rich host gneiss (bottom). Younger pristine pseudotachylyte (pst2, green) with clasts of amphibole-rich gneiss (purple arrows) and undeformed quartz (yellow arrows) crosscuts the folded injection vein. At the contact between the deformed (pst1, red) and pristine (pst2, green) pseudotachylyte, a third pseudotachylytic vein (pst3, blue) is present. Colored rectangles give the position of (d-j), respectively. **(c-e)** Backscattered electron (BSE) images of the different pseudotachylyte generations. **(c)** Matrix of deformed pseudotachylyte (pst1, position shown in Fig. 6.S2d in supporting materials), which is composed of intergrown aggregates of epidote and plagioclase. The aggregates display a shape-preferred orientation (SPO) (yellow dashed line) that relates to the SPO of the hosting quartz layer. **(d)** Intergrown epidote-feldspar aggregates with SPO (yellow dashed line). **(e)** Deformed

pseudotachylyte (pst1) with an SPO (yellow dashed line) and pristine pseudotachylyte (pst2) separated by a thin pseudotachylyte layer (pst3) indicating a dextral shear offset of pst1 (white arrows). **(f)** Polarized light micrograph of an injection vein of the third pseudotachylyte (pst3, blue) penetrating the pristine pseudotachylyte (pst2), which contains undeformed rounded quartz clasts (yellow arrow). **(g)** BSE image of pristine pseudotachylyte (pst2, green) containing sheared skeleton-shaped amphibole (amp) microliths indicating a sinistral sense of shearing (black arrows) at the sharp contact with the third pseudotachylyte (pst3, blue), which is mainly composed of feldspar (fsp) and quartz. **(h)** Polarized light micrograph of the contact between the deformed (pst1, red) and pristine (pst2, green) pseudotachylyte with rotated clasts of both pseudotachylytes. **(i-k)** Polarized light micrograph (crossed polarizers) showing quartz vein microfabric. **(i, j)** Foliated quartz is crosscut by networks of small new grains (white arrows). **(k)** Quartz associated with pseudotachylyte displaying short wavelength undulatory extinction (SWUE, black arrow).

### *6.2.3.2 Microfabric of hosting quartz vein*

The hosting quartz vein shows a foliation that corresponds to that of the folded and foliated pseudotachylyte injection vein (Fig. 6.5b-e, i and Fig. 6.S2b-d in supporting material). The coarse elongate grains have long axes of several hundreds of µm to mm and aspect ratios of 5.0 ± 1.8 (Figs. 6.5i, j; 6.6 and 6.7). They contain low-angle grain boundaries that define subgrains of similar shape and aspect ratio (Fig. 6.6a, b). The CPO is characterized by a marked point maximum of <c>-axes at a high angle to both the stretching lineation (X) and the normal to the foliation (Z) of the host gneisses, close to the Y-axis (Figs. 6.6c and 6.7d). Small isometric grains (6 ± 3 µm in diameter) can be found mantling the coarse elongate grains (Fig. 6.6a, b). Their orientations show a weaker maximum around Y, almost forming a girdle-maximum in the YZ-plane (Fig. 6.6d), indicating a crystallographic control originating from the mantling coarse high aspect-ratio grains but also new orientations with <c>-axes closer to Z.

In the vicinity of pseudotachylyte veins and their tips, fine quartz grains, <5 µm in diameter, occur (Figs. 6.6a, b and 6.7a-c; yellow area). The CPO of these tiny quartz grains surrounding the pseudotachylyte is weak to almost absent with a preferred orientation of <c>-axes closer towards a horizontal orientation at a small angle to Z (Figs. 6.6e, f and 6.7e). The misorientation angle distribution of the grains reveals an almost random crystallographic orientation (Figs. 6.6h and 6.7g). In contrast, the small grains surrounding the larger grains show a higher abundance of low misorientation angles with a deficit of high misorientation angles compared to a random orientation (Fig. 6.6g).

The foliation can be crosscut by fine-grained quartz aggregates that form irregular networks (Figs. 6.5b, i, j and 6.7a-c, white area, and Fig. 6.S2b, c in supporting material), as well as fractures offsetting the elongate grains (Fig. 6.7a-c). The fine-grained aggregates contain isometric grains, of about 3.1 ± 1.5 µm in diameter showing a large orientation scatter and an almost random orientation similar to those in the vicinity of the pseudotachylytes (Fig. 6.7e-h). The grains in the networks exhibit low internal misorientations with angles below a few degrees (Fig. 6.7c, h). Locally, along these fine-grained networks, an offset of the elongated large quartz grains can be observed (Fig. 6.7a, b, white conjugated arrows). Associated with these networks of fine-grained quartz aggregates and pseudotachylyte injection veins, the coarse elongate quartz grains can show domains with a width of 10-50 µm and a spacing of 30-80 µm, characterized by alternating domains with different crystallographic orientations (Figs. 6.5k and 6.7i). The relative misorientation angles are between 15° and 30° and the domain boundaries are oriented parallel to the short axis of the elongate quartz grains and subparallel to a $\{11\bar{2}0\}$ prism plane (Figs. 6.5k and 6.7i, j). This alternating change in the crystallographic orientation, especially visible in the relative misorientation map (Fig. 6.7i), is contrasting with a systematically increasing orientation change over otherwise similar deformation bands. Thus, these microstructures may rather be compared to kink bands, where, however, the kink band boundaries typically have a more abrupt change in crystallographic orientation. Due to the alternating change in orientation over the boundaries subparallel to a $\{11\bar{2}0\}$ prism plane (Fig. 6.7i), these domains are referred to as short wavelength undulatory extinction (SWUE, Trepmann and Stöckhert, 2013).

### *6.2.4 Brecciated foliated pseudotachylytes*

Foliated pseudotachylyte clasts can occur embedded in a pristine pseudotachylyte vein (a few tens of mm to cm in width) concordant to the foliation of the host gneiss (Fig. 6.8a, b). These foliated pseudotachylyte clasts are several hundreds of µm in size (Fig. 6.8b, c) and are comprised of fine-grained layers of quartz, albite, and amphibole. Quartz and albite clasts within the main pseudotachylyte vein can be somewhat larger with diameters of several hundreds of µm. The microstructure of the brecciated pseudotachylyte is fine-grained and the mineral content is similar to other deformed pseudotachylytes. Quartz layers (few tens of µm; aspect ratio 3.7 ± 1.1) in clasts show a very weak CPO (Fig. 6.8d). The grain diameter of the quartz grains in the matrix within the clasts of 2.8 ± 1.0 µm is similar to that in the layers of 3.9 ± 2.0 µm, combined with an almost absent CPO (Fig. 6.8e).

## 6.3 Discussion

Clasts of foliated pseudotachylytes in a pseudotachylyte breccia indicate two independent stages of coseismic rupturing separated by a stage of creep (Figs. 6.1a, b, e; 6.5h and 6.8). Likewise, the deformed pseudotachylytes forming ultramylonites and the folded injection veins (pst1) cut off by pristine pseudotachylytes (pst2) unambiguously indicate two independent stages of seismic rupturing separated by a stage of aseismic creep with dynamic recrystallization of quartz (Figs. 6.1f-h and 6.3-6.5). In contrast, pseudotachylytes (pst3) offsetting and crosscutting pristine (pst2) pseudotachylytes (Fig. 6.5 and Fig. 6.S2a, b in supporting material), may reflect brittle deformation of an earlier and quenched pseudotachylyte with a somewhat later pseudotachylyte during complex rupturing, as opposed to representing another independent stage of rupturing. Hereafter, firstly the recorded deformation conditions during pseudotachylyte formation and creep, secondly the implications for the strength of the various fault rocks during the different stages, and thirdly the assignment of the recorded coseismic rupturing events to the Alpine stages are discussed.

## *6.3.1 Deformation conditions*

Pseudotachylytes are especially common at the base of the seismogenic zone of the continental crust (i.e., temperatures of 300-350 °C; 10-15 km depth), which corresponds to lower greenschist facies conditions (e.g., Allen, 2005; Hobbs et al., 1986; Lin et al., 2005; Price et al., 2012; Scholz, 2002; Shaw and Allen, 2007; Sibson, 1980, 1977, 1975; White, 1996). At these depths, modification of the microfabrics formed during high-stress crystal plasticity and fault healing during interseismic creep play an important role (e.g., Nüchter and Stöckhert, 2007; Trepmann and Stöckhert, 2003; Trepmann et al., 2017; Williams and Fagereng, 2022). The well-documented spatial relation of the fault rocks to the base of the Silvretta nappe relates their formation to the Alpine orogeny (Koch, 1990; Koch and Masch, 1992; Laubscher, 1983; Schmutz, 1995), during which the rocks experienced maximum pressure-temperature conditions of 350-540 °C and 300-400 MPa (Hurford et al., 1989; Maggetti and Flisch, 1993; Thöni, 1981).

Similar to the findings of this study, Pittarello et al. (2022) described two different generations of Silvretta pseudotachylytes (deformed and pristine pseudotachylytes). These authors, however, suggested their formation at different ambient pressure-temperature conditions. Older deformed pseudotachylytes with epidote aggregates were assumed to have formed at greenschist facies conditions and the pristine pseudotachylytes with skeletal intergrowth of plagioclase-amphibole aggregates at temperatures <250 °C, respectively. Yet, the study confirms, that the phase assembly in the described pseudotachylytes (deformed and pristine) is mostly controlled by the host lithology, which has already been reported by Koch and Masch (1992). The occurrence of the epidote-feldspar intergrowth in pseudotachylytes (Figs. 6.2 and 6.5a-c) can be associated with biotite-rich host gneisses, whereas the skeletal intergrowth of plagioclase-amphibole in pseudotachylytes (Fig. 6.5g) is associated with amphibole gneisses. Likewise, stilpnomelane is occurring in pristine (Fig. 6.2a-c) and deformed pseudotachylytes (Fig. 6.2d, f). These observations suggest that the deformed, as well as the pristine pseudotachylytes experienced greenschist facies conditions during or after their formation.

The stage of creep is characterized by dislocation creep of quartz with <a>-dislocation glide and associated recovery and recrystallization (i.e., dynamic strain-induced grain boundary migration). This is recorded by the CPO and oblique SPO of recrystallized quartz within the ultramylonites (i.e., deformed pseudotachylytes) (Fig. 6.4c, d), as well as the CPO and SPO in the host quartz layer associated with the SPO of folded injection veins (Figs. 6.6 and 6.7). This relative homogeneous recrystallization-microfabric with oblique SPO and well-developed CPO (Fig. 6.4c, d), is indicating efficient dislocation climb, which is thermally activated and requires diffusion, and thus at least lower greenschist facies conditions (e.g., Stipp et al., 2002; Stöckhert et al., 1999). Therefore, ultramylonites and mylonites (Figs. 6.1g, h; 6.3 and 6.4) record a stage of creep at temperatures of at least greenschist facies conditions before the formation of the crosscutting pristine pseudotachylytes (Fig. 6.5, pst2 and pst3). Overall, the greenschist facies conditions documented by (i) stilpnomelane and epidote present in deformed and pristine pseudotachylytes and (ii) dislocation creep of quartz in deformed pseudotachylytes precludes that the pristine pseudotachylytes formed at much lower ambient temperature conditions. Thus, all recorded deformation stages are assumed to occur at similar ambient greenschist facies conditions.

It is known that different deformation mechanisms documented by pseudotachylytes, mylonites, and ultramylonites do not necessarily reflect differences in ambient temperature-pressure conditions but can likewise reflect changing stress- and strain-rate conditions during the seismic cycle at an approximately constant crustal level (e.g., Matysiak and Trepmann, 2011; Nüchter et al. 2013; White, 2012). The Silvretta pseudotachylyte formation is related to transient coseismic high-strain/high-stress deformation at >400 MPa differential stress, recorded by $(\bar{1}01)$ mechanical amphibole twins (Brückner and Trepmann, 2021), and associated with quartz microfabrics indicating high-stress crystal plasticity (Trepmann et al., 2017). The stresses during creep estimated by the quartz recrystallization-microfabric with grain diameters on the order of 10 µm (Fig. 6.4) were on the order of hundred MPa, applying the quartz recrystallization grain size paleopiezometer of Stipp and Tullis (2003). As there is no evidence of different pressure-temperature conditions, as discussed above, the recorded changes in deformation mechanisms and different stress and strain-rate conditions are explained by the dependence on the distance to the propagating fault tip during the decoupling of the Silvretta nappe from its original basement, following the model by Nüchter et al. (2013). These authors explained the systematic sequence of ductile and subsequently brittle deformation mechanisms at constant ambient pressure-temperature conditions by a decreasing distance to the propagating seismic active thrust tip. Accordingly, the Silvretta pseudotachylytes represent deformation during seismic rupturing, i.e., high stress and/or strain-rate conditions, whereas (ultra-)mylonites indicate a stage of creep at a larger distance to the active rupture tip, i.e., lower stress and strain-rate conditions.

### *6.3.2 Relative strength of pseudotachylytes and host rocks*

The model of Nüchter et al. (2013) requires that during thrust growth coseismic strain is localized in the previously unaffected rock leading eventually to nappe decoupling from its basement. On the other hand, pseudotachylytes are commonly taken as a weak phase (Guermani and Pennacchioni, 1998; Passchier, 1982b; Passchier and Trouw, 2005; Passelègue et al., 2021; Price et al., 2012), allowing strain localization at low shear stresses during subsequent nappe transport, especially in the presence of fluid phases allowing for dissolution precipitation creep (Bachmann et al., 2009; Cook and Aitken, 1976; Davis and Engelder, 1985; Davis et al., 1983; King Hubbert and Rubey, 1959; Koch and Masch, 1992; Laubscher, 1983; Rodgers et al., 1962). Taking these two findings together suggests that pseudotachylytes have a higher strength during coseismic high-stress crystal plasticity than the host rock but a lower strength during creep. Whether the here described deformed and pristine pseudotachylytes can validate this hypothesis will be addressed in the following.

The fine-lamellar foliated ultramylonitic matrix (i.e., deformed pseudotachylyte), deflected by the ellipsoid clasts of host gneiss (Figs. 6.1g, h; 6.3 and 6.4a, b), gives evidence that the fine-grained and polyphase pseudotachylytes are accumulating a higher amount of strain during creep compared to the host gneiss. This observation confirms that during creep, the pseudotachylytes represent the lithology of lower strength compared to the host gneisses, including the coarse-grained quartz vein, consistent with what is reported from other studies (Bachmann et al., 2009; Cook and Aitken, 1976; Davis and Engelder, 1985; Davis et al., 1983; King Hubbert and Rubey, 1959; Koch and Masch, 1992; Laubscher, 1983; Rodgers et al., 1962).

The networks of small isometric new quartz grains (<5 µm) either aligned along the second pristine pseudotachylytes (Fig. 6.7a-c) or discordant to the SPO of the foliated host quartz vein, indicate nucleation and growth along former highly damaged zones, that are related to the second coseismic deformation event (e.g., Trepmann et al., 2007). These new grains in the networks are strain-free, revealing that they grew at quasi-isostatic stress conditions, i.e., they record fast stress relaxation after transient peak stresses (Trepmann et al., 2017). Furthermore, high aspect-ratio quartz grains in the host veins related to networks of new grains and pseudotachylytic veins display SWUE (Figs. 6.6k and 6.7i, j). These microfabrics overprinting the foliated quartz veins indicate high-stress dislocation glide-controlled deformation associated with microfracturing (e.g., Trepmann and Stöckhert, 2013; Trepmann et al., 2017) during the last stage of pseudotachylyte formation and after the stage of creep. In contrast, evidence of comparable high-stress crystal plasticity in the first generation of pseudotachylyte (pst1) is not apparent. Thus, during coseismic high-stress deformation, the coarse-grained quartz is accumulating a higher amount of strain than the associated pseudotachylytes and develops microstructures indicative of high-stress crystal plasticity, i.e., they have a lower strength. This is consistent with the Hall-Petch relation that smaller grain sizes impede dislocation glide (Fredrich et al., 1990; Hall, 1951; Hirth, 1972; Petch, 1953). Furthermore, "*kick-cook-kick*" experiments (Trepmann et al., 2013), simulating a cycle of coseismic loading, postseismic relaxation, and a second coseismic loading event suggest, that strain during the second transient high-stress deformation event is not localized in the same rock volume again.

Consistently, also mylonites and ultramylonites are less commonly found to contain pseudotachylytes (Koch & Masch, 1992; Schmutz et al., 1995). The indication of higher strength during high-stress plasticity of coarse gneisses in comparison to finer grained mylonites, ultramylonites, and pseudotachylytes can explain, that during the successive seismic event only those rocks, which have not been previously affected, rupture. This finding would be consistent with the concept that seismic rupturing is more likely in rock volumes with higher stored elastic strain energy (Cocco et al., 2023; Scholz, 2002), which might be the case for rocks that have not previously experienced aseismic creep, compared to those that have experienced previous creep.

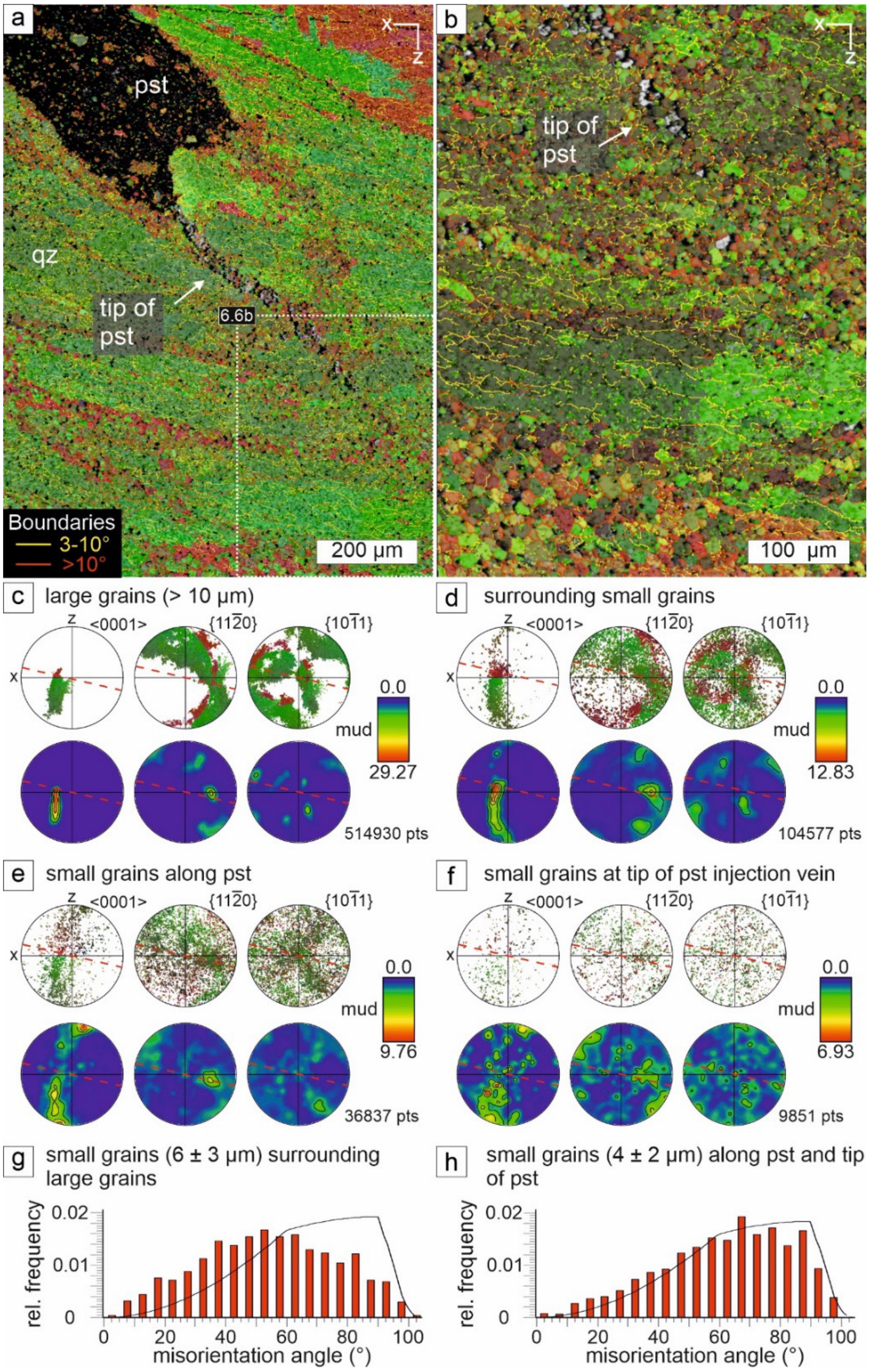

**Figure 6.6:** Electron backscattered diffraction (EBSD) data of quartz (qz) hosting deformed pseudotachylyte (pst) injection veins, sample LB78d (position is shown in Fig. 6.S2b in supporting material). **(a, b)** Map displaying different quartz crystallographic orientations (all Euler angle), as well as high- (red) and low-angle (yellow) grain boundaries. Vein quartz shows large grains with shape-preferred orientation (SPO) surrounded by smaller grains. **(c-f)** Stereographic projections (colors correspond to all Euler angle colors in (a) and (b)) and density plots of coarse high-aspect ratio grains, small grains surrounding the latter, as well as small grains surrounding and at the tip of pseudotachylytes, respectively. The foliation is indicated by the red dashed line. **(g, h)** Misorientation angle distribution of small quartz grains surrounding large grains and along the pseudotachylyte injection vein and its tip, respectively. Theoretic random distribution is shown by the black solid line.

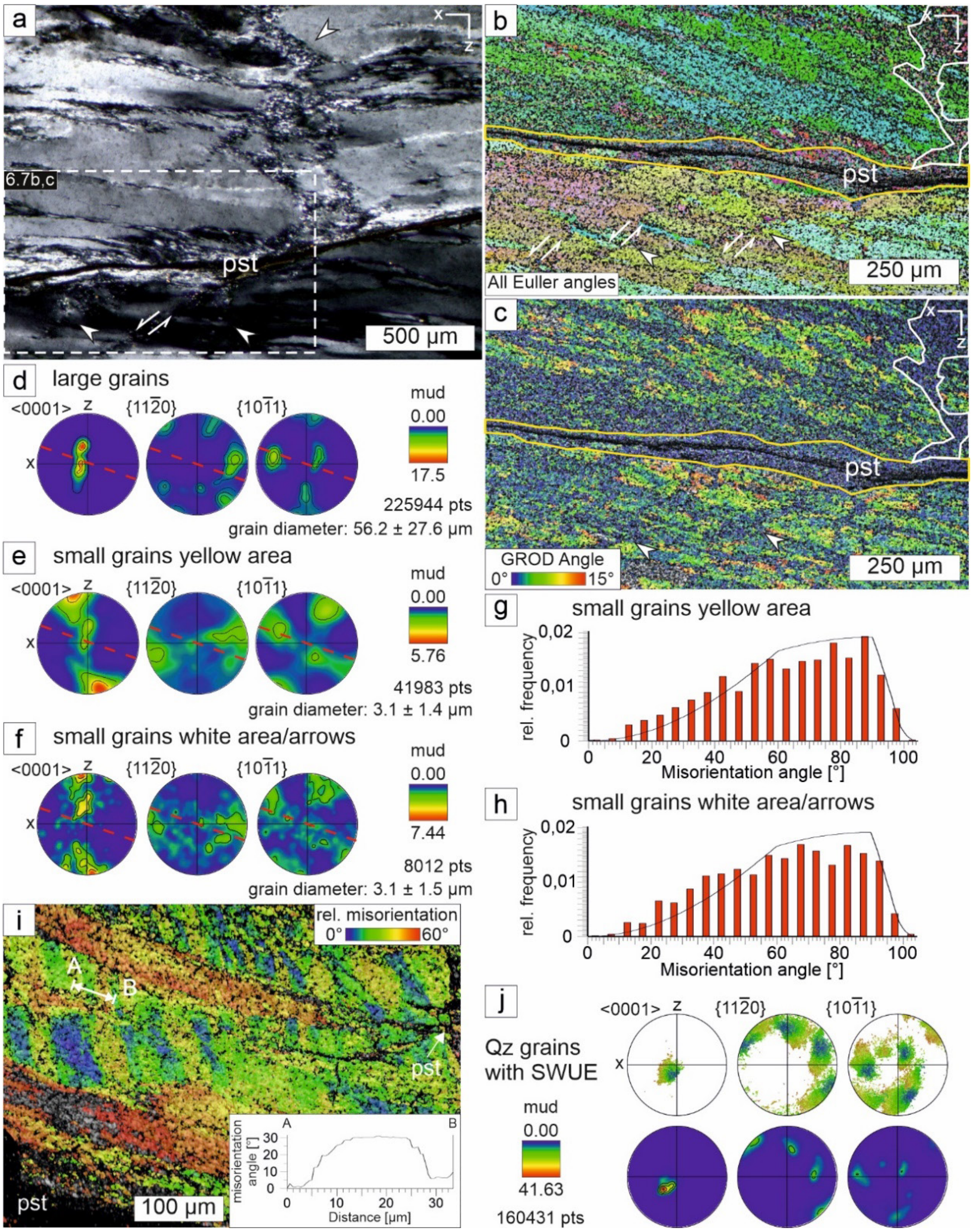

**Figure 6.7:** Quartz microfabrics in the vicinity to pseudotachylytes, sample LB78b. **(a)** Polarized light micrograph (crossed polarizers, position is shown in Fig. 6.5b) of quartz vein containing pseudotachylytes (pst), that displays large grains with shape-preferred orientation (SPO) surrounded by smaller grains. Irregular networks of fine-grained isometric quartz aggregates in special relation to pseudotachylytes are shown by white arrows. **(b, c)** Electron backscattered diffraction (EBSD) maps display different crystallographic orientations (all Euler angles) and Grain Reference Orientation Distribution (GROD; deviation angle from mean grain orientation plotted for each pixel), respectively. **(d-f)** Density plots (stereographic projections) for indicated quartz aggregates. The foliation is demonstrated with a red dashed line. **(g, h)** Misorientation angle distribution of small quartz grains along the pseudotachylyte injection vein and in discordant networks (yellow area and white area/arrows in (b) and (c), respectively). Theoretic random distribution is shown by the black solid line. **(i)** EBSD map displaying relative misorientation angle distribution and profile along AB line over domains characterized by an alternating change in crystallographic orientation (short wavelength undulatory extinction (SWUE)) with boundaries subparallel to {11$\bar{2}$0} (position is shown in Fig. 6.5k). **(j)** Stereographic projections (colors correspond to relative misorientation colors in (i)) and density plots of quartz grains with SWUE.

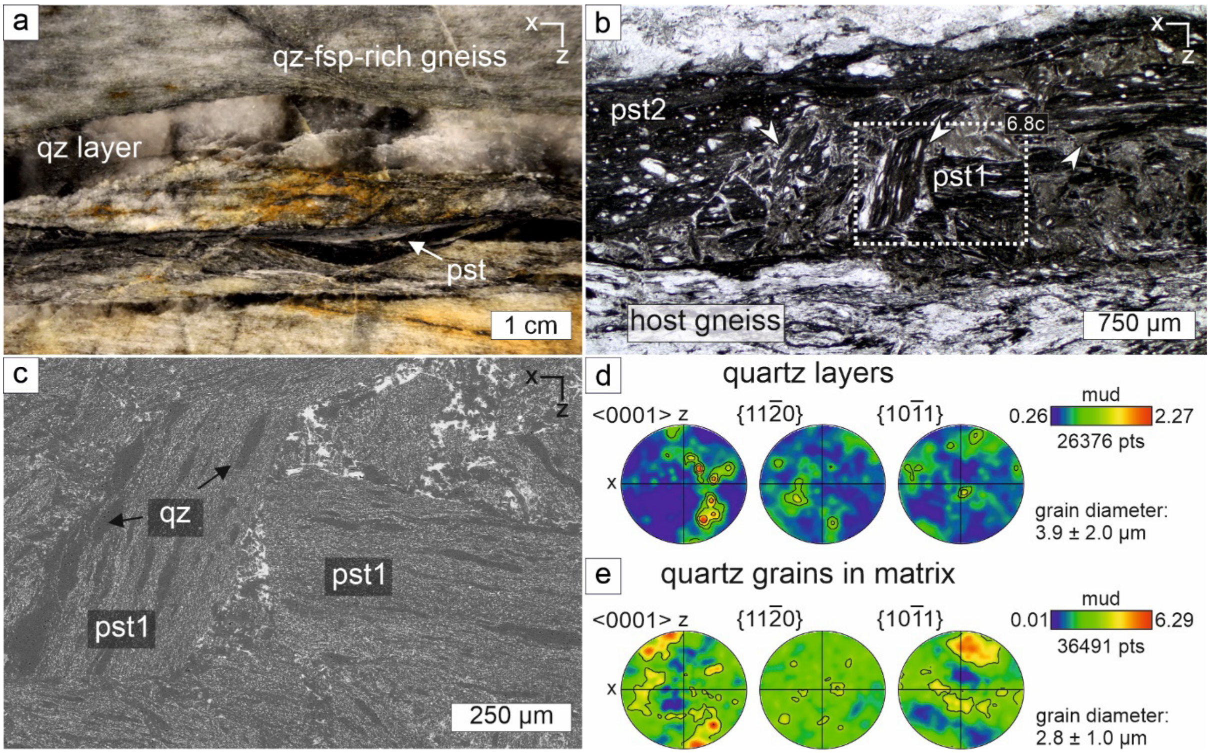

**Figure 6.8:** Foliated pseudotachylyte clasts in pseudotachylyte layer concordant to quartz veins in host gneiss, sample LB24. **(a)** Quartz-feldspar-rich host gneiss (qz; fsp) containing concordant pseudotachylyte (pst) and quartz layers. **(b)** Polarized light micrograph of a concordant and brecciated pseudotachylyte layer, containing rotated clasts of pseudotachylytes (white arrows), representing the first generation of pseudotachylyte (pst1) embedded in a second generation (pst2). **(c)** Backscattered electron (BSE) image of rotated foliated pseudotachylyte clasts comprised of fine-grained layers of quartz, albite, and amphibole. **(d, e)** Density plots (stereographic projections) of quartz in layers and quartz within the matrix of the first generation of pseudotachylyte.

Overall, the present observations indicate that pseudotachylytes accumulate a higher amount of strain during creep at a larger distance to the fault tip compared to the gneisses. In contrast, the coarse gneisses accumulate a higher amount of strain during coseismic high-stress crystal plasticity. Such “inverse” strength relationship during deformation at different distances to the tip of the seismic active fault (i.e., at different stress and strain-rate conditions and similar pressure-temperature conditions) has been similarly found in the Silvretta fault rocks for amphibole-rich gneisses and quartz veins. There, amphibole represents the lower strength phase during transient high-stress coseismic deformation, but the higher strength phase during creep, given the lower fracture toughness, the higher shear modulus, and the lower melting temperature of amphibole relative to quartz (Brückner and Trepmann, 2021).

### *6.3.3 Relation to Alpine stages*

The observations presented here are in accord with earlier interpretations that the Silvretta pseudotachylytes represent seismic rupturing during the decoupling of the crystalline nappe from its original basement, given the widespread occurrence of fault rocks restricted to 300 m of the base of the Silvretta nappe and no evidence of components of the footwall in pseudotachylytes (Insubric crystalline) (Koch and Masch, 1992; Laubscher, 1983; Schmutz, 1995; Thöni, 1988). Yet, we do not follow the interpretation of Koch and Masch (1992) that the decoupling occurred with a cyclic formation of pseudotachylytes and mylonites and that ultramylonites represent the latest stage formed at peak Eo-Alpine metamorphic conditions during transport of the nappe over the Penninic Units, as ultramylonites (deformed pseudotachylytes) and mylonites can be crosscut by pristine pseudotachylytes (Figs. 6.5 and 6.9a). In contrast, both, mylonites and ultramylonites (i.e., the deformed first generation of pseudotachylytes) are interpreted to represent deformation at a large distance to the propagating thrust tip before the final decoupling, displayed by pristine pseudotachylytes (Fig. 6.9a), following the model of Nüchter et al. (2013) (Fig. 6.9b). The pristine pseudotachylytes represent the last microstructural imprint after the passage of the seismically active fault tip of the affected rocks during the decoupling of the nappe from its original basement. The by far less common deformed pseudotachylytes are interpreted as an independent precursor tectonic event before the final decoupling (Fig. 6.9a). This view does not exclude later localized deformation at the base of the nappe during transport dominated by dissolution precipitation creep at low stresses.

The peak metamorphic conditions in the Silvretta are dated to about 110 to 85 Ma (Hurford et al., 1989; Maggetti and Flisch, 1993; Thöni, 1981). Isotopic investigations of the pseudotachylytes indicate their formation in Late Cretaceous to Paleocene epochs ($^{87}$Rb/$^{86}$Sr whole rock about 75 Ma: Thöni, 1988; $^{40}$Ar/$^{39}$Ar whole rock 62-78 Ma: Bachmann et al., 2009), which is therefore likely the age of the final decoupling of the Silvretta nappe and in accord with the findings of deformation at greenschist facies conditions for the two stages of pseudotachylyte formation separated by a stage of creep (Fig. 6.9a). However, the age determination of pseudotachylytes is hampered by the presence of abundant host rock clasts in the matrix (Bachmann et al., 2009; Thöni, 1988). Specific new radiometric dating of the various fault rocks and especially of the deformed pseudotachylytes would be required for a further assignment to the Alpine tectonic stages.

## 6.4 Conclusions

The described microstructures of the fault rocks from the base of the Silvretta nappe exemplify two stages of pseudotachylyte formation, reflecting coseismic transient high-stress (>400 MPa) deformation, which are separated by an intermediate stage of creep at lower stresses (on the order of hundred MPa) at similar greenschist facies conditions (Fig. 6.9). The stage of creep is interpreted to represent deformation at larger distances to the propagating active thrust fault before the final stage of pseudotachylyte formation resulting in the decoupling of the nappe, which allowed the superposition onto the Penninic units. The deformed pseudotachylytes are taken to represent an independent earlier precursor tectonic event.

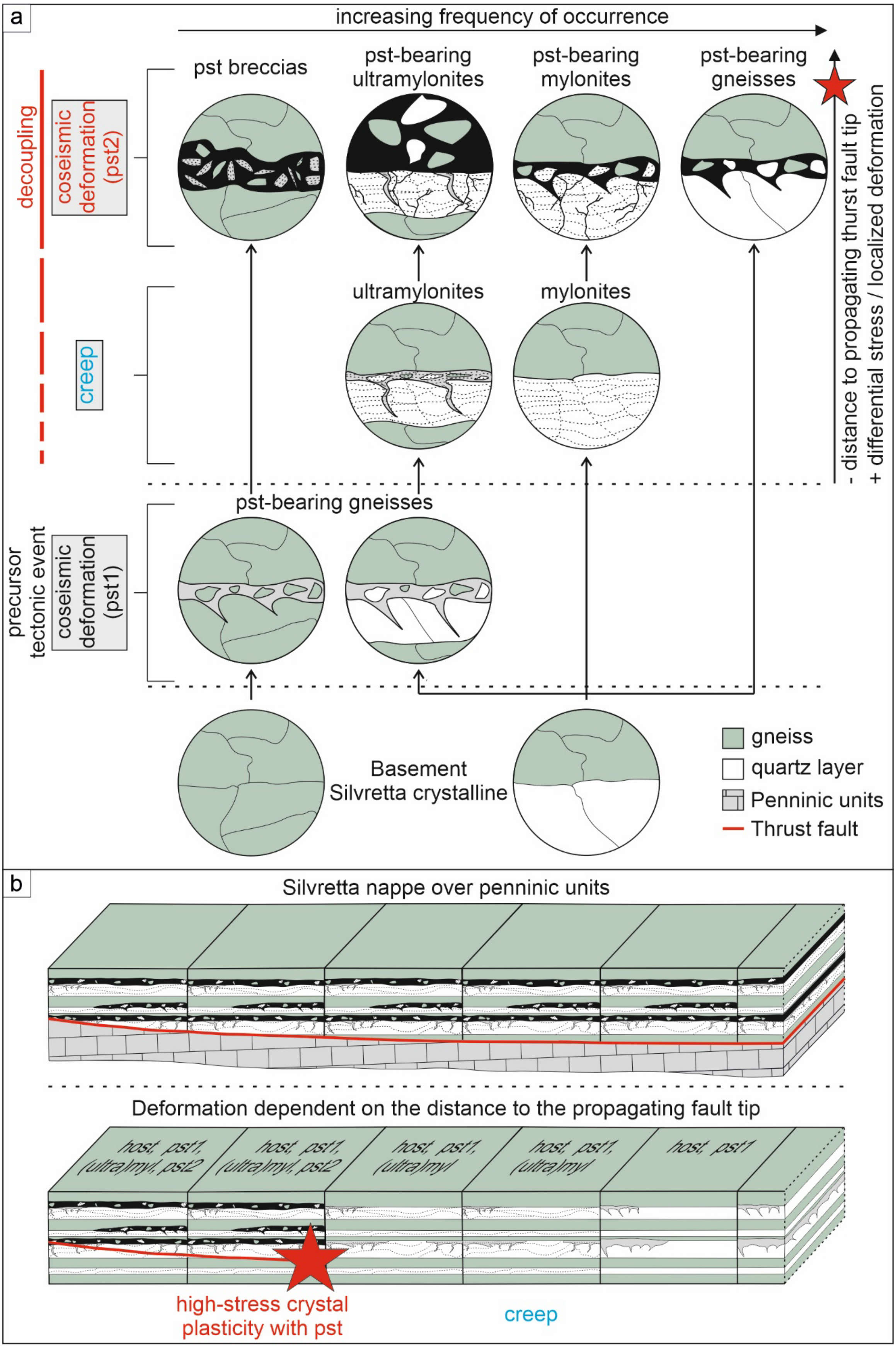

**Figure 6.9:** Conceptual sketch showing **(a)** the formation of the various Silvretta fault rocks in dependence on the distance to the propagating thrust tip during the decoupling of the nappe **(b)** following the model of Nüchter et al. (2013). See text for discussion.

During creep, the fine-grained polyphase pseudotachylytes accumulate a higher amount of strain relative to the coarse host gneisses (Figs. 6.3 and 6.4). In contrast, during coseismic high-stress crystal plasticity (associated microfracturing and dislocation glide), the coarser grained quartz-rich lithologies are accumulating a relatively higher amount of strain (Fig. 6.6). During later modification at greenschist facies conditions and rapidly relaxing stresses, SWUE and networks of new grains along the damage zone of former microcracks within the mylonitic quartz vein formed (Figs. 6.5-6.7).

The described microfabrics suggest that the specific stress and strain-rate conditions, dependent on the distance to the propagating seismic active fault tip, are decisive regarding the rheological behavior of crustal rocks at the base of the seismogenic zone during thrusting and do not reflect a change in pressure-temperature conditions. That the next rupturing event affects only rocks that have not been previously ruptured in the same event on one hand and that strain is localized in the fault rocks during creep on the other, demonstrates the importance of varying crustal rock strengths depending on specific stress and strain-rate conditions during the seismic cycle. Thus, modeling the strength of crustal blocks during orogeny requires distinguishing the rheology of rocks dependent on the distance to the seismic active fault tip.

## 6.5 Supporting Information

The supporting Information presented for the manuscript “Rheology dependent on the distance to the Propagating Thrust Tip – (Ultra-)Mylonites and Pseudotachylytes of the Silvretta basal Thrust” provides (i) important Raman spectroscopic investigations of stilpnomelane within different generations of pseudotachylytes and (ii) additional information of pseudotachylyte microfabrics.

### Text 6.S1 Raman spectroscopy of stilpnomelane

Raman spectroscopy was carried out to confirm the presence of stilpnomelane within different generations of pseudotachylytes, recording ambient metamorphic conditions. As stilpnomelane exhibits a wide range of chemical compositions, that can lead to variable Raman bands, the description of individual bands is important for the identification.

Raman spectroscopic investigations of stilpnomelane display characteristic bands, which are broad potentially due to the large size of the unit cell (Eggleton, 1972; Eggleton and Chappell, 1978; Guggenheim and Eggleton, 1994; Kuebler, 2013). The standard shows characteristic bands near 120 cm$^{-1}$, 190 cm$^{-1}$, and bands ranging between 284-308 cm$^{-1}$, and 374-381 cm$^{-1}$. Either a pronounced band at 590 cm$^{-1}$ and a weak 686 cm$^{-1}$ band or a broad shoulder with bands at 480 cm$^{-1}$ and 528 cm$^{-1}$ occur. Bands varying between 925-956 cm$^{-1}$ and 1138-1165 cm$^{-1}$ are broader and less intense. The $CH_4$ band at 2980 cm$^{-1}$ and the $H_2O$ band at 3576 cm$^{-1}$ can be weak or absent. The Raman spectra of stilpnomelane in the pristine and deformed pseudotachylyte observed here, display the characteristic bands at 191-198 cm$^{-1}$, 286-309 cm$^{-1}$, 472-480 cm$^{-1}$, ~947 cm$^{-1}$, and 1112-1115 cm$^{-1}$. The $CH_4$ bands ~2935 cm$^{-1}$ and the $H_2O$ bands ~3583 cm$^{-1}$ are well developed. Instead of a marked band around 590 cm$^{-1}$, variable bands between 531 cm$^{-1}$ and 595 cm$^{-1}$ and a marked band around 660 cm$^{-1}$ occur. The differences to the standard samples are interpreted to result from artifacts of the surrounding matrix given the small size of the stilpnomelane needles. Furthermore, small chemical differences in stilpnomelane, which exhibits a wide range of compositions, can also lead to variance in the bands.

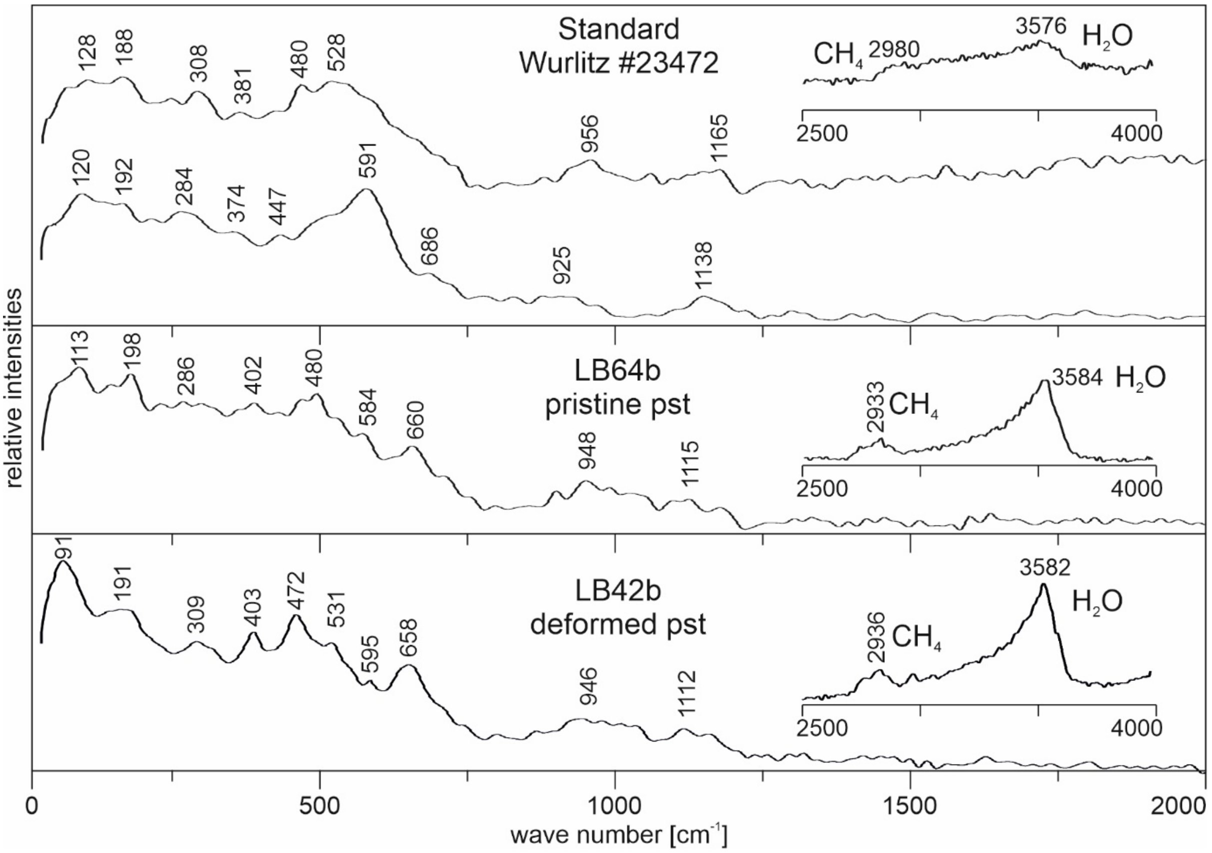

**Figure 6.S1:** Stilpnomelane Raman spectra of a pristine (LB64b) and a deformed (LB42b) pseudotachylyte in comparison with the standard stilpnomelane (Wurlitz #23472; Mineralogical State Collection Munich (SNSB)).

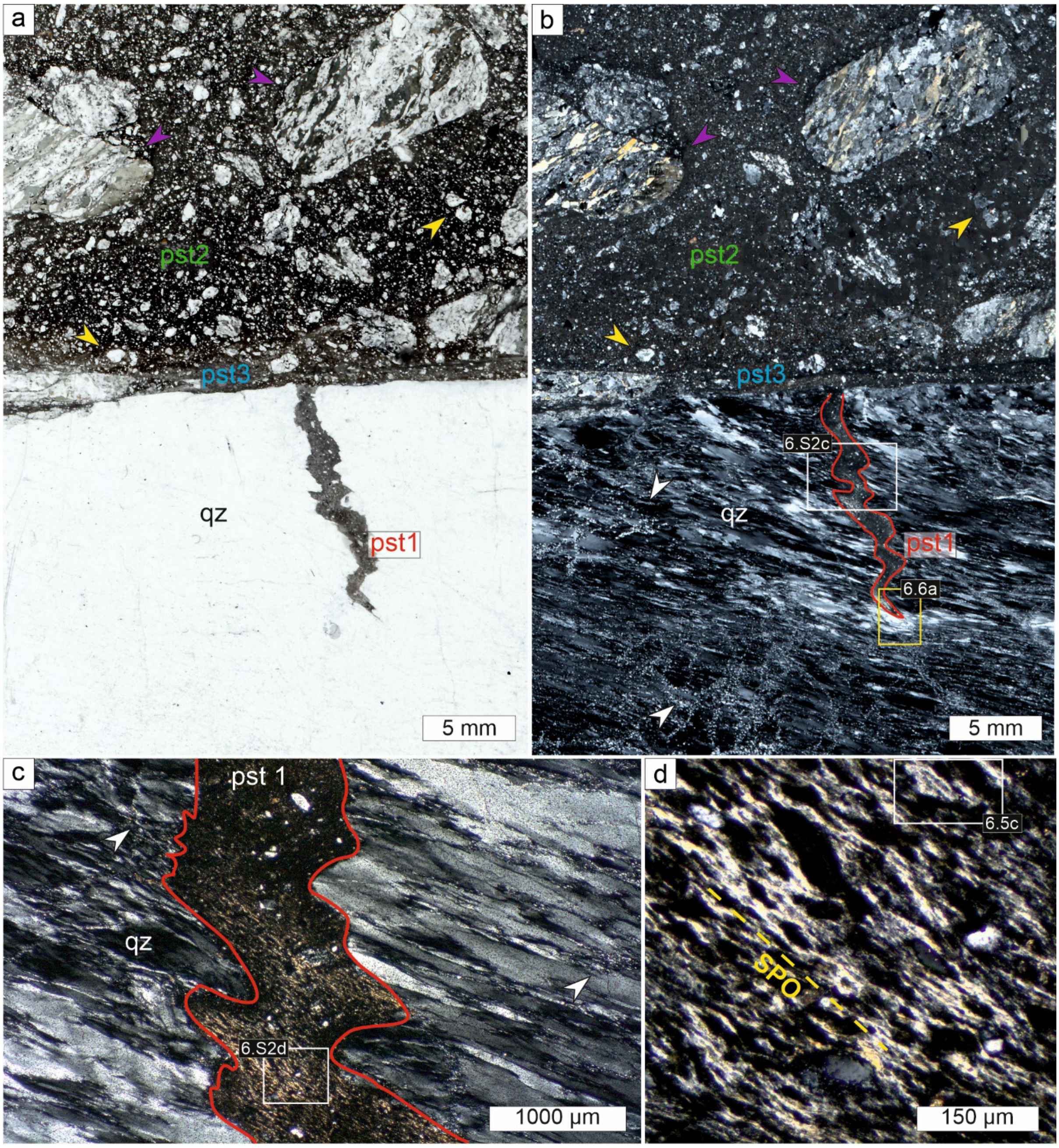

**Figure 6.S2:** Microfabrics of deformed pseudotachylitic injection vein within deformed quartz vein, crosscut by pristine pseudotachylyte, sample LB78d. **(a, b)** Thin section polarized light micrographs (position is shown in Fig. 6.1f; (b) is taken with crossed polarizers), showing knife-sharp contact between foliated quartz (qz) containing folded and foliated injection vein (pst1, red) and pristine pseudotachylytes (pst2, green and pst3, blue). Localized small isometric quartz grains in networks discordant to foliation are marked by white arrows. Pristine pseudotachylyte (pst2) contains clasts of isometric, mono- and polyphase quartz-feldspar aggregates (yellow arrows) and amphibole-rich gneiss clasts (purple arrows). **(c)** Polarized light micrograph (crossed polarizers) of folded pseudotachylyte injection vein (pst1, red) displaying a foliation that relates to the foliation of the host quartz vein. Localized small isometric quartz grains are marked by white arrows. **(d)** Close-up displays the foliated pseudotachylyte matrix with shape preferred orientation (SPO, yellow dashed line). The matrix is composed of intergrown epidote-feldspar aggregates.

## Availability statement

All data used for microstructural analyses in the study are available at Mendeley data (https://data.mendeley.com/) via https://data.mendeley.com/datasets/xhh2ktks9g/4 (DOI: 10.17632/xhh2ktks9g.4) with CC BY 4.0.

Version 4.2 of the Aztec software (Oxford Instruments, 2020), used for microstructural data acquisitions, is available at https://nano.oxinst.com/products/aztec/. Version 6.6.1 of the LabSpec software (Horiba Scientific, 2022), used for Raman processing and analysis, is available at https://www.horiba.com/aut/scientific/products/detail/action/show/Product/labspec-6-spectroscopy-suite-software-1843/. Figures were made with CorelDRAW 2021 (64 bit) version 23.1.0.389 (Corel Corporation, 2022), available under the CorelDRAW license at https://www.coreldraw.com.

# 7 Quartz Cleavage Fracturing and subsequent Recrystallization along the Damage Zone recording fast Stress Unloading

This chapter is based on the manuscript: Brückner, et al. (2024). Quartz Cleavage Fracturing and subsequent Recrystallization along the Damage Zone recording fast Stress Unloading. *Journal of Structural Geology*, 178, 105008. https://doi.org/10.1016/j.jsg.2023.105008

## 7.1 Introduction

Cleavage of single crystals is a brittle fracture process that occurs in the tensile mode, where crystalline material preferentially fractures along a planar surface determined by the crystal structure (e.g., Schultz et al., 1994). Criteria controlling the initiation of cleavage fractures include bond density, elastic modulus, surface free energy, and fracture toughness of the crystallographic planes in dependence on grain size and crystallographic orientation (e.g., Armstrong, 2015; Flörke et al., 1981; Kranz, 1983; Schultz et al., 1994; Thompson and Knott, 1993). In experiments, cleavage of quartz has been found to occur preferentially along the positive $r\{10\bar{1}1\}$ and negative $z\{01\bar{1}1\}$ rhombohedral planes, and rarely along *m* prism planes $\{10\bar{1}0\}$, basal planes $c\{0001\}$, $\xi\{11\bar{2}2\}$, $s\{11\bar{2}1\}$, and $x\{51\bar{6}1\}$ planes (Bloss and Gibbs, 1963; Kimberley et al., 2010; Martin and Durham, 1975). In nature, quartz cleavage fractures along *r*- and *z*-rhombohedral planes and basal planes are common in target rocks affected by deformation during meteorite impact cratering, where they are referred to as planar fractures (PFs) (e.g., French et al., 2004; French and Koeberl, 2010; Stöffler and Langenhorst, 1994 and references therein; Trepmann, 2008). In contrast, quartz cleavage fractures in tectonic fault rocks or shear zones are less abundant and, so far, only reported along the *r*- and *z*-rhombohedral planes (Anderson, 1945; Flörke et al., 1981; French et al., 2004; Frondel, 1962). However, in rocks from meteorite impact craters and tectonically deformed rocks, cleavage fractures occur as sets without shear offset parallel to crystallographic planes with spacing varying from a few tens to hundreds of micrometers (depending on strain). One difference, however, is the more restricted occurrence of quartz cleavage fractures parallel to *r*- and *z*-rhombohedral planes in tectonically deformed rocks. This led French et al. (2004) to suggest that quartz cleavage fractures may serve as diagnostic microstructure for relatively low shock pressure conditions (<10 GPa) during impact cratering. However, the dynamic compression experiments of Kimberley et al. (2010) showed that cleavage fractures can form during fast unloading from high compressive stresses well below shock regime conditions. Thus, quartz cleavage fracturing might also be expected in tectonic fault or shear zone rocks deformed at sufficiently high and transient stresses, for example, at hypocentral depths of major earthquakes, where high stresses during coseismic deformation only transiently prevail with subsequent rapid stress relaxation (e.g., Ellis and Stöckhert, 2004b; Nüchter and Ellis, 2010).

Cataclasis during shearing is well-known as a prerequisite for melting and pseudotachylyte generation during seismic rupturing (e.g., Curewitz and Karson, 1999; Di Toro et al., 2005b; Fabbri et al., 2000; Maddock, 1992; Magloughlin, 1992, 1989; Ray, 1999; Spray, 1995, 1992; Swanson, 1992; Wenk, 1978). Dynamically propagating shear rupture models (e.g., Petley-Ragan et al., 2019; Swanson, 1992) illustrate that the initiation of brittle rupture with symmetric fracturing at the tip (process zones) is followed by fragmentation and asymmetric damage near and directly behind the fault front (damage zone). The asymmetric stress/strain field is characterized by transient compressional and tensional domains on the opposite sides of the fracture plane (e.g., Di Toro et al., 2005a; Freund, 1990; Kame et al., 2003; Poliakov et al., 2002; Rice et al., 2005; Swanson, 1992). The tensional domain is located where the shear motion is oriented in the opposite direction to fracture propagation (Di Toro et al., 2005a; Samudrala et al., 2002). As tensile rock strength is considerably lower than compressive strength, tensile fracturing takes place preferentially along this tensional side of the fault (e.g., Andrews, 2005; Dalguer et al., 2003; Griffith et al., 2009; Xia and Yao, 2015; Xu and Ben-Zion, 2017; Zhang and Zhao, 2014). Within the tensional domain, dynamic pseudotachylytic and cataclastic materials can intrude inside the developed tensile fractures (e.g., Di Toro and Pennacchioni, 2005; Di Toro et al., 2005a; Grocott, 1981; Sibson, 1975; Swanson, 1992). Although tensile fracturing is well-known to occur related to the formation of endogenic pseudotachylytes (Di Toro et al., 2005a; Griffith et al., 2012; Ngo et al., 2012; Petley-Ragan et al., 2019; Rosakis, 2002; Rowe et al., 2012), cleavage fracturing has not yet been associated to seismic faulting. This might be related to later modification during the prolonged thermal history before exhumation, particularly from hypocentral depths of major earthquakes at the base of the seismogenic zone of the continental crust close to the 300 °C isotherm (e.g., Marone and Scholz, 1988). Especially quartz deformed at transient high stresses during coseismic loading at hypocentral depths is prone to later modification, where static recrystallization can occur after deformation at quasi-isostatic stress conditions controlled by stress relaxations (e.g., Trepmann and Stöckhert, 2003; Trepmann et al., 2017, 2007; Hentschel et al., 2022). Moreover, an increase in temperature after brittle deformation of quartz can result in recrystallization along former fractures (e.g., van Daalen et al., 1999). A transient increase in the availability of pore fluids can, furthermore, lead to brittle deformation in shear zone rocks otherwise undergoing creep and thus lead to healing and sealing of fractures (e.g., Derez et al., 2015; Goncalves et al., 2016; Kjøll et al., 2015; Menegon et al., 2008).

In this study, strings of fine-grained quartz that occur in sets along planes parallel to *r*- and *z*-rhombohedra in coarse quartz host grains within vein-quartz clasts from pseudotachylyte breccias of the Silvretta basal thrust and gneisses shocked to relatively low shock conditions (<20 GPa) of the Vredefort impact structure are compared and contrasted. The aim is to identify the controlling conditions for the formation of these microfabrics, which are valuable indicators of the deformation and stress history.

## 7.2 Sample material

For this study gneisses of two fundamentally different tectonic settings, the Silvretta basal thrust at the southwestern border of the Engadine Window (Figs. 1.2; 3.1 and 3.2) and the Vredefort impact structure (Fig. 7.1) are investigated. Pseudotachylyte-bearing breccias of the Silvretta crystalline in the central European Alps studied here were sampled at Hexenkopf, Ochsental, and Jamtal in Austria, as well as Val Tuoi in Switzerland (LB14: 47°01'11" N / 10°28'28" E; LB15: 47°01'00" N / 10°28'00" E; LB26: 46°53'27" N /10°11'26" E; Appendix A1 and A2). The investigated samples from the Vredefort impact structure, central Kaapvaal Craton, South Africa, derived from the Archean amphibolite- to granulite-facies migmatitic gneisses of the 40-50 km diameter dome (e.g., Hart et al., 1990; Lana et al., 2004, 2003; Stepto, 1990) and were shocked to less than 20 GPa (Dellefant et al., 2022) (Fig. 7.1). Sample V2 2.5 (26°58'15.4" S / 27°23'19.3" E, see Carporzen et al., 2012; Dellefant et al., 2022) was drilled at depths of 13 cm. Studies from the same locality as sample VT445 (26°58' S / 27°26' E) are reported by Schreyer and Medenbach (1981) and Fricke et al. (1990) (Appendix A1).

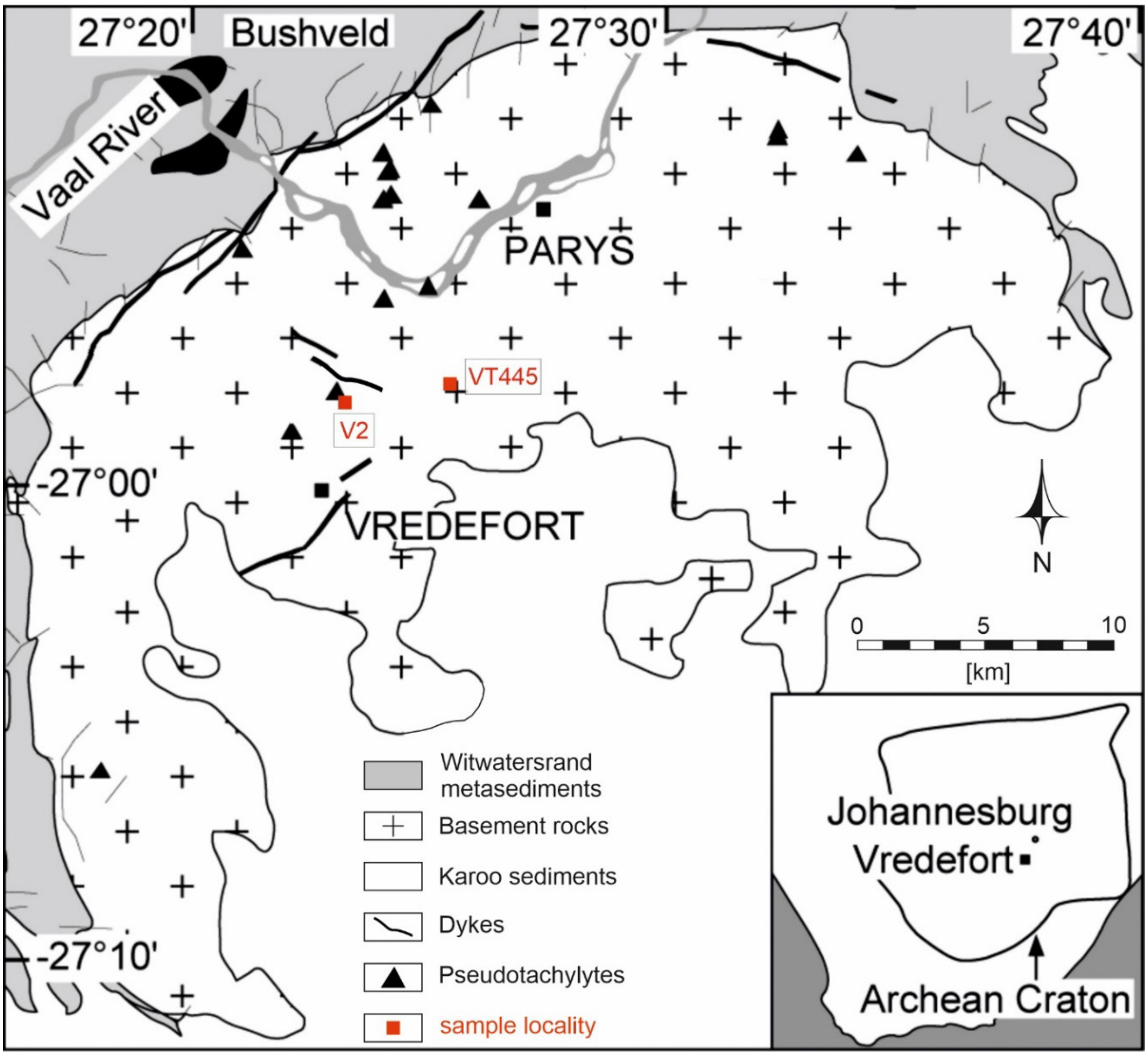

**Figure 7.1:** Schematic geological map of the Vredefort impact structure, South Africa with the drill core sample V2 2.5 (Carporzen et al. 2012; Dellefant et al., 2022) and sample VT445 (Fricke et al., 1990; Medenbach and Schreyer, 1981).

## 7.3 Geological setting of the Vredefort impact structure

The Vredefort impact structure located in the Witwatersrand Basin, central Kaapvaal Craton, South Africa (Fig.7.1), was formed by a meteorite impact ca. 2.02 Ga ago (Gibson et al., 1997; Kamo et al., 1996). Numerical simulations of the Vredefort impact with impactor diameters of 25 km and 20 km as well as 15 km/s and 25 km/s, respectively (Allen et al., 2022), resulted in a crater diameter of ca. 250 km and matched the overall shock pressure profile, which is based on shock effects, such as planar deformation features (PDFs) in quartz (Grieve et al., 1990; Leroux et al., 1994; Reimold, 1990). However, due to the extensive erosion and resulting uncertainties, smaller crater diameters of 120 km to 200 km were also suggested (Ivanov, 2005; Turtle et al., 2003; Turtle and Pierazzo, 1998). Based on geobarometric analyses (Gibson et al., 1998), numerical models (Gibson and Reimold, 2005; Ivanov, 2005), geophysical considerations (Henkel and Reimold, 1998), and regional stratigraphic studies (McCarthy et al., 1990), the amount of erosion is estimated to be 5-11 km since impact. Analyses of fluid inclusions along shock-induced PDFs indicate trapping depths of 7-15 km (Fricke et al., 1990). Thus, the target rocks exposed today in the Vredefort Dome were at a depth of about 23 km at the time of the impact, based on structural uplift of about ca. 11 km and erosion of ca. 12 km (Gibson, 2019; Gibson et al., 1998; Gibson and Reimold, 2005; Ivanov, 2005). Therefore, relatively high pre-shock temperatures must be considered, which can affect the development of PDFs, as well as the formation of diaplectic glass at already lower shock pressures with higher pre-shock temperatures (e.g., Langenhorst and Deutsch, 1994). Consistent with high pre-shock temperatures, post-shock temperatures in the Archean basement target rocks (Fig. 7.1) were on the order of 650 to 725 °C indicated by Dauphiné twins associated with planar features in quartz (Dellefant et al., 2022) and reaction fabrics (orthopyroxene-plagioclase coronas and cordierite-orthopyroxene symplectites) in metapelites of the Archean basement, which were interpreted to have formed after the impact (Perchuk et al., 2002). The shock effects were considerably modified during the prolonged thermal history of the deep part of the Vredefort impact structure, which obscures the estimations of the pressure conditions that acted during impact (e.g., Fricke et al., 1990; Gibson and Reimold, 2005; Grieve et al., 1990; Schreyer and Medenbach, 1981). Recrystallization of quartz is predominant in the center of the dome. In contrast, at increasing distance from the center, the number of recrystallized grains decreases with an increase of new grains, aligned along strings within coarse quartz grains, which are discussed to represent annealed planar features (Fricke et al., 1990; Grieve et al., 1990; Hart et al., 1991; Leroux et al., 1994; Lilly, 1981; Reimold, 1990; Schreyer and Medenbach, 1981). Shock effects in feldspar suggest locally very heterogeneous shock conditions in the central part of the dome with pressures ranging from 30 GPa to 35 GPa and locally more than 45 GPa, whereas, at 20 km distance from the center, microstructural evidence indicates shock pressures of ~10 GPa (Fricke et al., 1990; Gibson and Reimold, 2005; Grieve et al., 1990; Leroux et al., 1994; Lilly, 1981; Reimold, 1990; Schreyer and Medenbach, 1981).

## 7.4 Results

### *7.4.1 Silvretta fault rocks*

#### *7.4.1.1 Pseudotachylyte breccia veins*

Silvretta host rocks of the investigated pseudotachylyte-bearing breccias comprise amphibole- and biotite-rich gneisses, as well as vein quartz, which likewise occur as clasts of a few cm in diameter within the pseudotachylytic veins (Fig. 7.2). The vein-quartz comprises typically >95 % quartz, minor amounts of opaque phases, and locally calcite. The gneisses are mainly composed of amphibole (60-70 %), plagioclase (10-30 %), K-feldspar (10-20 %), and mica (10-20 %; biotite and white mica), accompanied by accessory sphene, zircon, stilpnomelane, rutile, epidote, and carbonates (e.g., Brückner et al., 2023; Brückner and Trepmann, 2021; Koch and Masch, 1992). The composition of pseudotachylytes and different host gneisses depend strongly on the local host lithologies.

Pseudotachylyte breccias form a few cm-wide layers consisting of rounded cm-scale gneiss and vein-quartz clasts within a fine-grained pseudotachylytic matrix (Fig. 7.2). They generally show sharp contacts with the surrounding host rocks and can be subparallel or slightly oblique to the foliation of the host gneisses and concordant quartz veins (Fig. 7.2a, b). However, they also occur discordant at higher angles to the foliation (Fig. 7.2c-f). A layer of pseudotachylyte breccia discordant to the foliation of different gneisses at the top and at the bottom of the breccia layer indicates that the contacts represent faults that significantly offset the host gneisses (Fig. 7.2c, d). From these faults, few-mm scaled curved injection veins intrude at a high angle into the clasts of the pseudotachylyte breccia layer (Fig. 7.2c-f; white arrows). However, no injection veins penetrate the fault's opposite side into the surrounding host gneisses. A characteristic and systematic curvature of the injection veins is observed at the upper and lower fault, respectively (Fig. 7.2d). Assuming that no significant later rotation of the clasts occurred after formation of the injection veins, their systematic curvatures suggest a sense of shear and the fault propagation direction, as the injection veins intrude similar to tensional wing cracks into the tensional domains opposite to the shear direction (Di Toro et al., 2009, 2005a; Samudrala et al., 2002). Following this concept, the curvature of the injection veins indicates a dextral and sinistral sense of shear at the upper and lower fault, respectively, and a propagating direction for both the top fault and bottom fault, from left to right in Figure 7.2c-f (red arrows). In the following, microstructures in the cm-scale of rounded vein-quartz clasts within the pseudotachylyte-bearing breccias are presented, which can be commonly found in localities with a frequent occurrence of pseudotachylytes and rare mylonites (Figs. 1.2 and 7.2; Appendix A2).

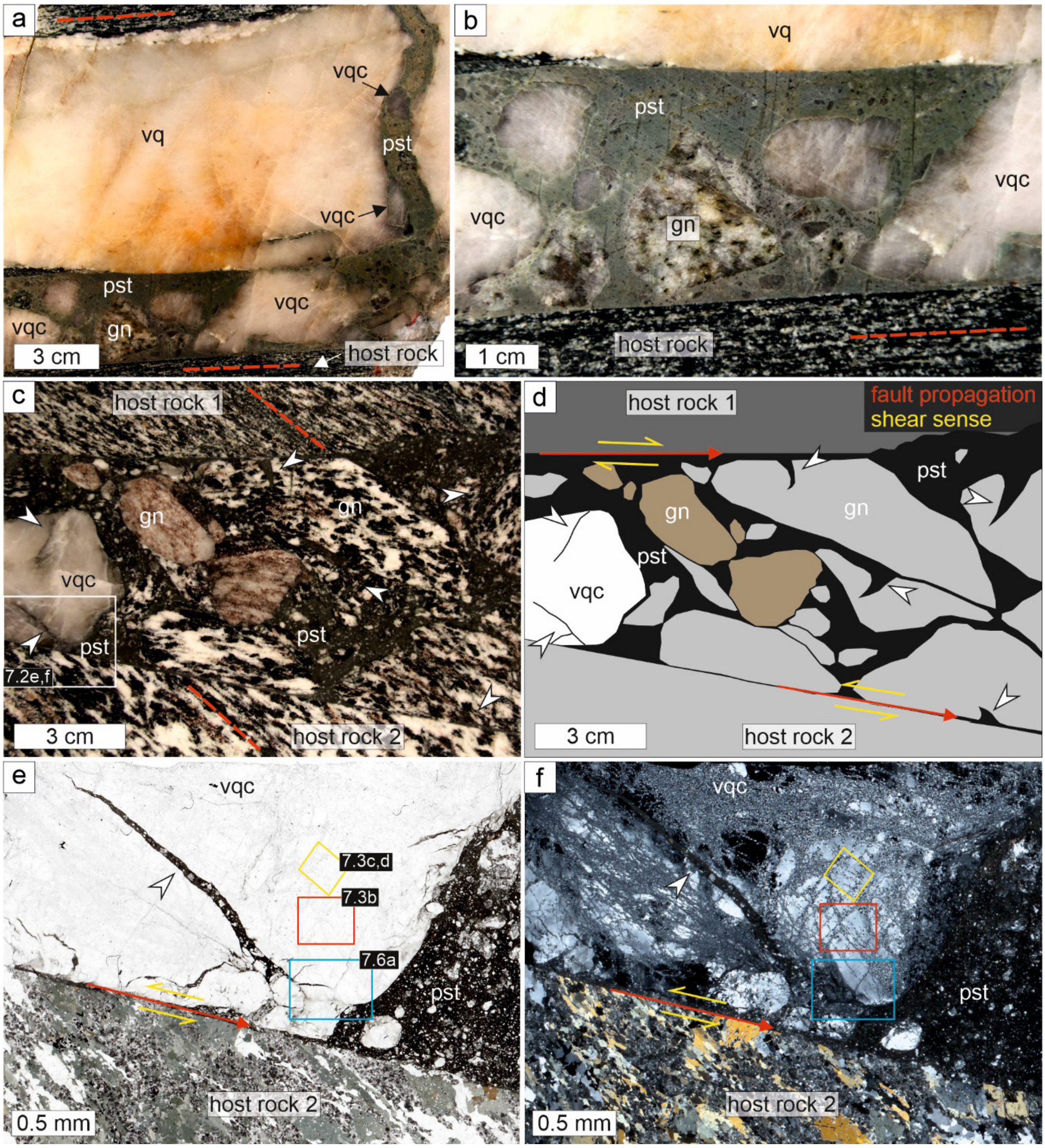

**Figure 7.2:** Silvretta pseudotachylyte breccias. **(a, b)** Sample LB26 with a pseudotachylyte (pst) breccia layer concordant to the foliation of the amphibole-rich host rock and a quartz vein (vq). The breccia contains clasts of pure vein quartz (vqc) and gneisses (gn) of a different lithology compared to the adjacent host gneiss. The straight injection vein, which penetrates from the parent pseudotachylyte at a high angle into the quartz vein in (a), also contains large vein-quartz clasts (black arrows). **(c, d)** Field micrograph and conceptual sketch, respectively, of a pseudotachylyte breccia layer discordant to the foliation (red dashed lines) of two different amphibole-rich gneisses (host rock 1 and 2) at the top and the bottom of the layer, sample LB15. The breccia contains cm-scale rounded clasts of pure vein quartz (vqc) and gneisses (gn). Small-scaled wedge-shaped pseudotachylyte injection veins (white arrows) intrude into the clasts and indicate a sinistral and dextral sense of shearing at the lower and upper fault of the pseudotachylyte breccia, respectively (yellow arrows in (d)). The fault propagates from left to right, as indicated by the red arrow in (d), see text for discussion. **(e, f)** LB15c thin section micrograph; (f) is taken with crossed polarizers.

### *7.4.1.2 Strings of fine-grained quartz along cleavage planes of the host*

The vein-quartz clasts in the Silvretta pseudotachylyte-bearing breccias (Fig. 7.2) commonly show small grains localized along strings, which follow two sets of the positive $r\{10\bar{1}1\}$ (Fig. 7.3a-d) or the negative $z\{01\bar{1}1\}$ (Fig. 7.3e-g) rhombohedral planes, as indicated by EBSD in comparison with U-stage measurements (Figs. 7.3 and 7.4). These strings that show no shear offset of the host quartz crystal are interpreted to follow former cleavage fractures. No comparable strings occur in quartz from the hosting quartz vein or gneisses.

The strings can be a few tens of µm in width defined by the diameter of one single grain aligned along it, i.e., just one grain-wide (Fig. 7.3d, white arrows), or display widths of up to 200 µm containing several grains (Fig. 7.3d, black arrows). The spacing of the strings is highly variable, ranging from about 100 to 300 µm (average: 226 ± 100 µm). The new grains show diameters of about 10 ± 6 µm (Figs. 7.3 and 7.4a, b) and are mostly isometric but can be slightly elongated parallel to the cleavage planes with an aspect ratio of 1.7 ± 0.5 (Fig. 7.4e). They have largely dispersed orientations with a weak maximum related to the host crystal (Fig. 7.4c, d) and an almost random crystallographic orientation as evident from the misorientation angle distributions (Fig. 7.4f). They show low internal misorientations with angles below a few degrees (Fig. 7.4b). The host quartz typically contains Dauphiné twin boundaries (Fig. 7.4a), few subgrain boundaries (Figs. 7.3b-d and 7.4b), and an internal relative misorientation mostly below 10° (Fig. 7.4b). In quartz clasts, especially in samples from the Jamtal and Val Tuoi (Fig. 1.2), Dauphiné twins are common. The Dauphiné twin operation represents the transformation of the positive to the negative forms (i.e., rotation of 180° around the *c*-axis). The dominating domain is taken to be the host and the subordinate domain is interpreted to be the Dauphiné twin. Associated with the Dauphiné twins, strings parallel to the positive $r\{10\bar{1}1\}$ or negative $z\{01\bar{1}1\}$ rhombohedra occur (Fig. 7.3e-g).

Within Hexenkopf samples (sample LB14, Fig. 1.2 and Appendix A2), rarely coarse calcite needles appear along the strings of recrystallized grains (Fig. 7.5). The long axis of calcite needles is 50-200 µm and the width is 20-40 µm. Calcite can be twinned (Fig. 7.5a, b) and the needles are either subparallel or nearly perpendicular to the strings of new quartz grains (Fig. 7.5c, d). Single fractures that do not correspond to crystallographic planes can be sealed with calcite and palisade-shaped quartz grains, i.e., the long axis of grains is at a high angle to the calcite grains (Fig. 7.5b). Generally, the vein-quartz clasts show a high number of pores (black spots in EBSD images, Figs. 7.3f; 7.4a, b and 7.5c-e).

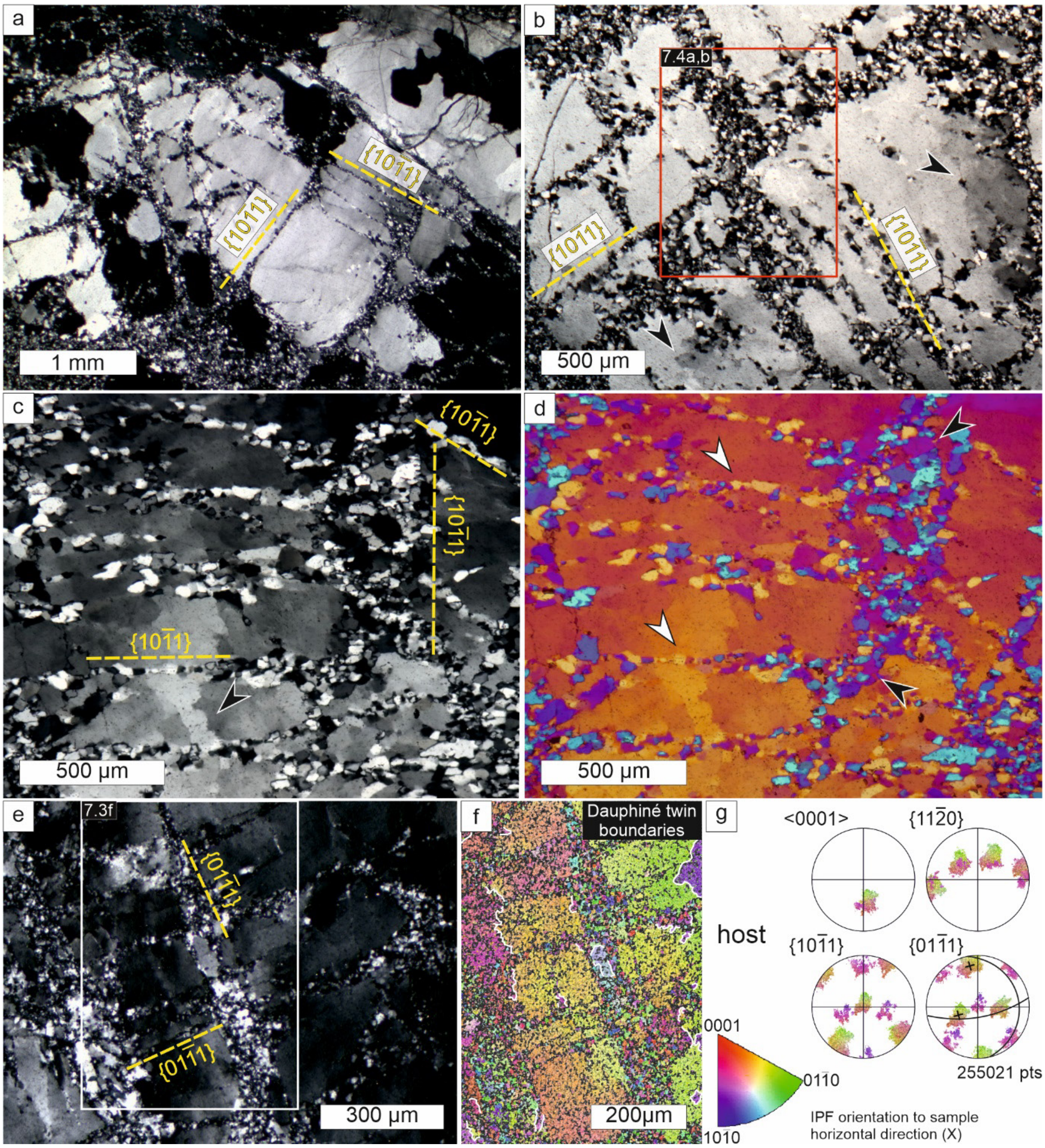

**Figure 7.3:** Strings of fine-grained quartz in sets parallel to *r*- and *z*-rhombohedral planes within Silvretta pseudotachylyte breccias. **(a-e)** Polarized light micrographs of quartz strings taken with crossed polarizers. **(a)** Overview of fine-grained quartz along $\{10\bar{1}1\}$ planes, sample LB26c. **(b-d)** Fine-grained quartz along $\{10\bar{1}1\}$ cleavage planes, as well as subgrain boundaries (black arrow in (c)) and undulatory extinction, sample LB15c (compensator plate inserted in (d), white and black arrows point to one grain-wide and several grain-wide strings, respectively; positions are indicated by red and yellow rectangles in Fig. 7.2e, f). **(e)** Quartz strings parallel to $z\{01\bar{1}1\}$ cleavage planes, sample LB26c. **(f).** EBSD map (position marked by the white rectangle in (e)) with inverse pole figure (IPF) color coding for the horizontal direction (x). Dauphiné twin boundaries are indicated by white lines. Quartz is characterized by a high porosity (black spots). **(g)** Equal-area projection of poles to c-, a-, *r*- and *z*-planes of the host quartz orientation corresponding to the map in (f). Compared U-stage measurements are indicated in black.

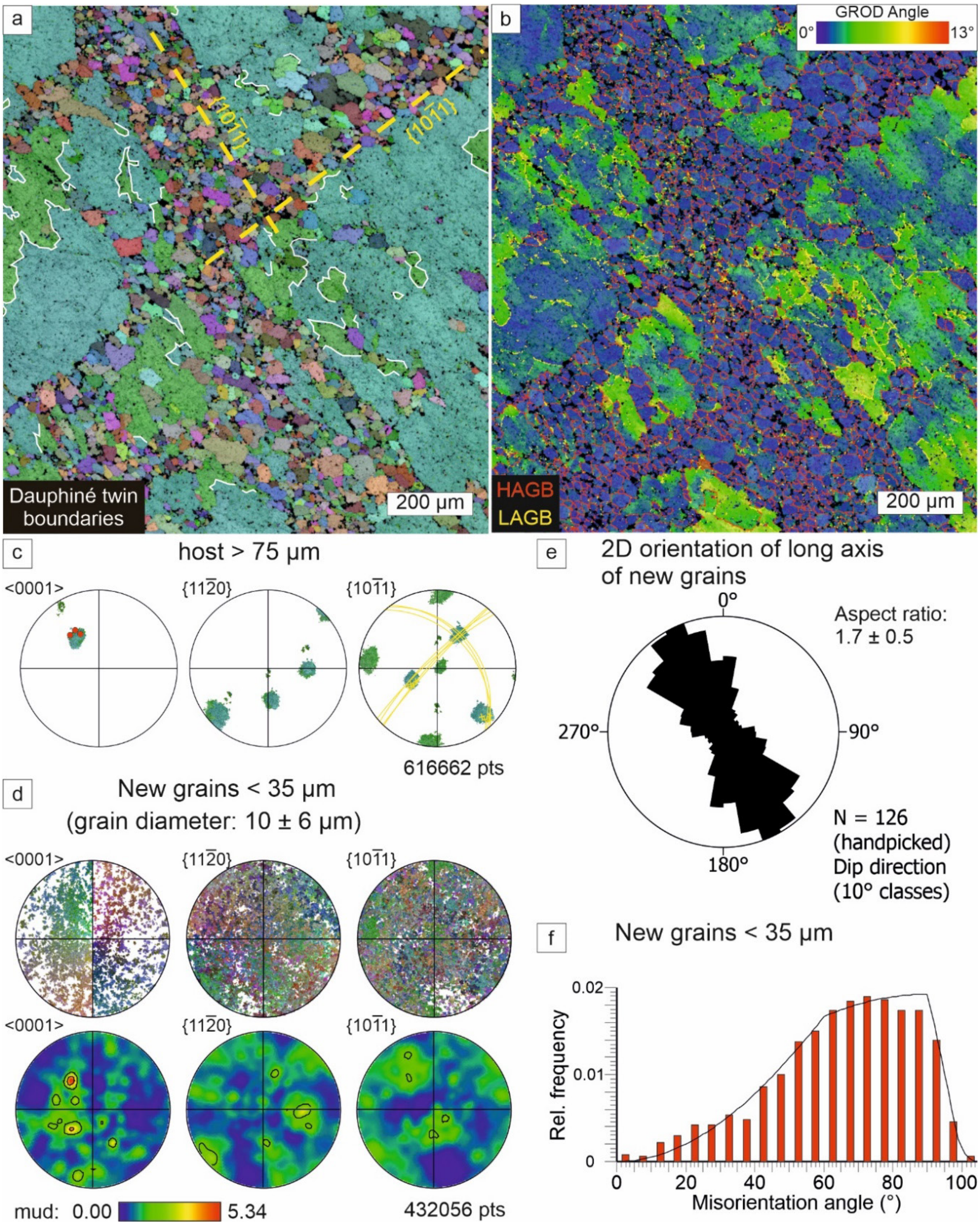

**Figure 7.4:** EBSD data of fine-grained quartz along $\{10\bar{1}1\}$ cleavage planes of the host quartz (red rectangle in Fig. 7.3b), Silvretta pseudotachylyte, sample LB15c. **(a)** EBSD map displaying the crystallographic orientations (all Euler angles color coding) and Dauphiné twin boundaries (white lines). **(b)** Grain Reference Orientation Distribution (GROD) map displaying the deviation angle from mean grain orientation plotted for each pixel. High (HAGB, >10°) and low angle (LAGB, 3-10°) grain boundaries are marked by red and yellow lines, respectively. **(c)** Pole figures (colors correspond to map in (a)) of the host quartz orientation with great circles of cleavage planes (yellow) and quartz c-axes (red) measured by U-stage. **(d)** Pole figures and density plots of new grains along $\{10\bar{1}1\}$ cleavage planes. Colors correspond to the map in (a)**.** **(e)** Rose diagram (2D orientation of long axis) visualizing the shape preferred orientation (SPO) of new quartz grains along cleavage planes. **(f)** Misorientation angle distribution histogram of new quartz grains along $\{10\bar{1}1\}$ cleavage planes. Theoretic random distribution is shown by black solid line.

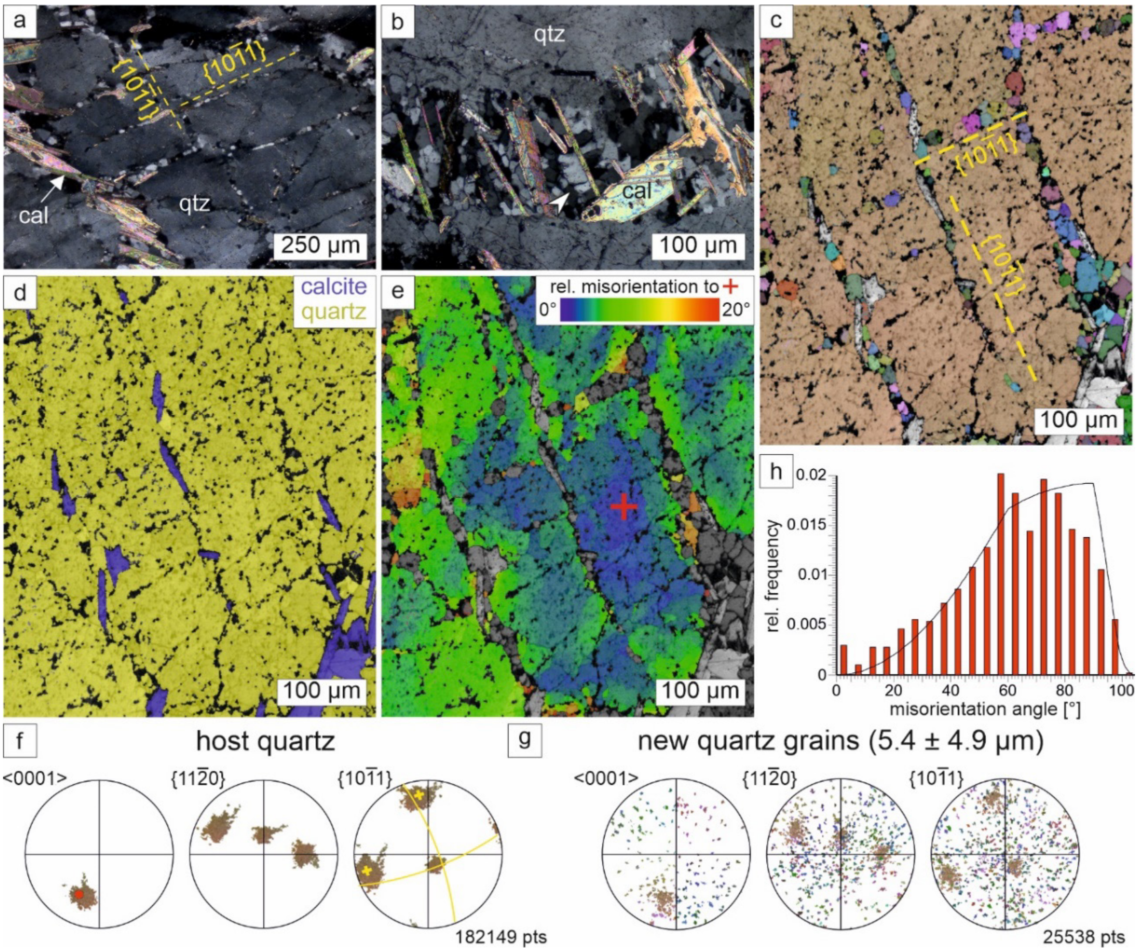

**Figure 7.5:** Microfabrics and EBSD data of quartz with $\{10\bar{1}1\}$ cleavage planes decorated by quartz and calcite, Silvretta pseudotachylyte, sample LB14a. **(a, b)** Polarized light micrograph (crossed polarizers) showing twinned calcite (cal) needles subparallel or perpendicular to quartz (qtz) cleavage planes (yellow dashed lines) or sealed cracks, respectively. Quartz in contact with coarse calcite needles can be palisade-shaped (white arrow). **(c, e)** EBSD maps displaying crystallographic orientations (all Euler angles color coding) in (c), phase distribution in (d), and relative misorientation angle to reference orientation (red cross) in (e) of calcite and quartz. **(f)** Equal-area projections of orientation of the host quartz with U-stage measurements of cleavage planes (yellow great circles) and quartz c-axes (red). Colors correspond to all Euler angle map in (c). **(g)** Equal-area projections of orientation of new quartz grains. Colors correspond to all Euler angle map in (c). **(h)** Misorientation angle distribution histogram of new quartz grains along $\{10\bar{1}1\}$ cleavage planes. Theoretic random distribution is shown by black solid line.

### *7.4.1.3 Quartz-rich cataclastic zones*

Fine-grained (<10 µm in diameter) quartz-rich zones of a few hundred µm in length and tens of µm in width can be found at the boundary of quartz clasts to the pseudotachylytic matrix (Figs. 7.2e, f and 7.6). In contrast to the strings of new grains, they occur as single zones and not in sets following crystallographic planes. The geometry of these fine-grained zones is similar to pseudotachylyte injection veins in the direct vicinity (Fig. 7.6a-c). The zones display a sinistral sense of shearing (Fig. 7.6b-d) corresponding to the shear fracture propagation direction (compared to Fig. 7.2d-f). BSE images and EDS data reveal homogenously distributed secondary phases enriched in Al, Ca, K, Fe, Mg, and Na of a few µm in diameter (Fig. 7.6e, f). The porosity is markedly lower in the cataclastic zones compared to the pure quartz clast (Fig. 7.6e, f).

The small isometric quartz grains with diameters of 2.8 ± 0.7 µm within the quartz-rich layer show a large spread of crystallographic orientations with a very weak host control of c-axes close to the periphery of the pole figure (Fig. 7.7a, b; yellow area). The EBSD band contrast is poor in the fine-grained quartz-rich layer, which can be explained by the small grain diameters and the finely dispersed secondary phases (Figs. 7.6e, f and 7.7a, c). With decreasing distance to the core of the microcrystalline quartz-rich layers, the grain diameters increase to about 7 ± 4 µm (Fig. 7.7a, c, d). These slightly coarser grains also show a large spread of crystallographic orientations and statistically distributed misorientation angles (Fig. 7.7b-d).

## *7.4.2 Quartz microfabrics in shocked Vredefort gneisses*

The investigated Vredefort gneisses contain feldspar (60-75 %), quartz (20-40 %), biotite (<5 %), and about 1-5 % opaque minerals (mainly ilmenite and magnetite), as well as chlorite (Fig. 7.8a). Accessory minerals are apatite, zircon, and calcite. Feldspar, quartz, and biotite grain diameters typically range from hundreds of µm to mm. Within sample VT445, shear zones occur with widths of up to hundreds of µm, where adjacent quartz is recrystallized (Fig. 7.8a). A foliation is not apparent.

Strings of new grains in the host quartz occur in sets mostly parallel to the positive $r\{10\bar{1}1\}$ or negative $z\{01\bar{1}1\}$ rhombohedral planes and, more rarely, also along (0001) planes (Fig. 7.8b-e). These strings of new grains are interpreted to occur along former cleavage fractures, as suggested for the Silvretta fault rocks (compare Fig. 7.2). The small grains show diameters of ca. 15 µm (Figs. 7.8b-e and 7.9). These new grains have an average aspect ratio of 1.7 ± 0.7 and are elongated with the long axis parallel to the cleavage planes (Fig. 7.9a-c, f). The strings of small grains exhibit a spacing ranging from a few tens of µm to a few hundred µm (on average 171 ± 111 µm). Commonly, their width can be defined by just one grain along them (Figs. 7.8b, c; 7.9 and 7.10). However, they also may be wider, containing several quartz grains (Figs. 7.8e; 7.9 and 7.10). The small grains show a large scatter in their crystallographic orientation, locally, with a weak maximum controlled by the crystallographic orientation of the host quartz (Fig. 7.9d, e). In general, the small quartz grains show a low internal misorientation with angles generally below a few degrees (Fig. 7.9c) and an almost random misorientation angle distribution (Fig. 7.9g). Dauphiné twins are common such that it is difficult to distinguish the host from twin domains and the boundaries often lie parallel to the cleavage planes (Fig. 7.9b). Accordingly, the strings may be either parallel to the *r*- or the *z*-rhombohedral planes (Fig. 7.9b, d). Usually, the strings of new grains are restricted to one host crystal given their crystallographic control parallel to $\{10\bar{1}1\}$ and (0001) planes. However, the strings of new grains can cross grain boundaries, where $\{10\bar{1}1\}$ planes can be parallel in adjacent grains or where (0001) in one grain is parallel to a $\{10\bar{1}1\}$ plane in the other (Figs. 7.8d and 7.10a, b).

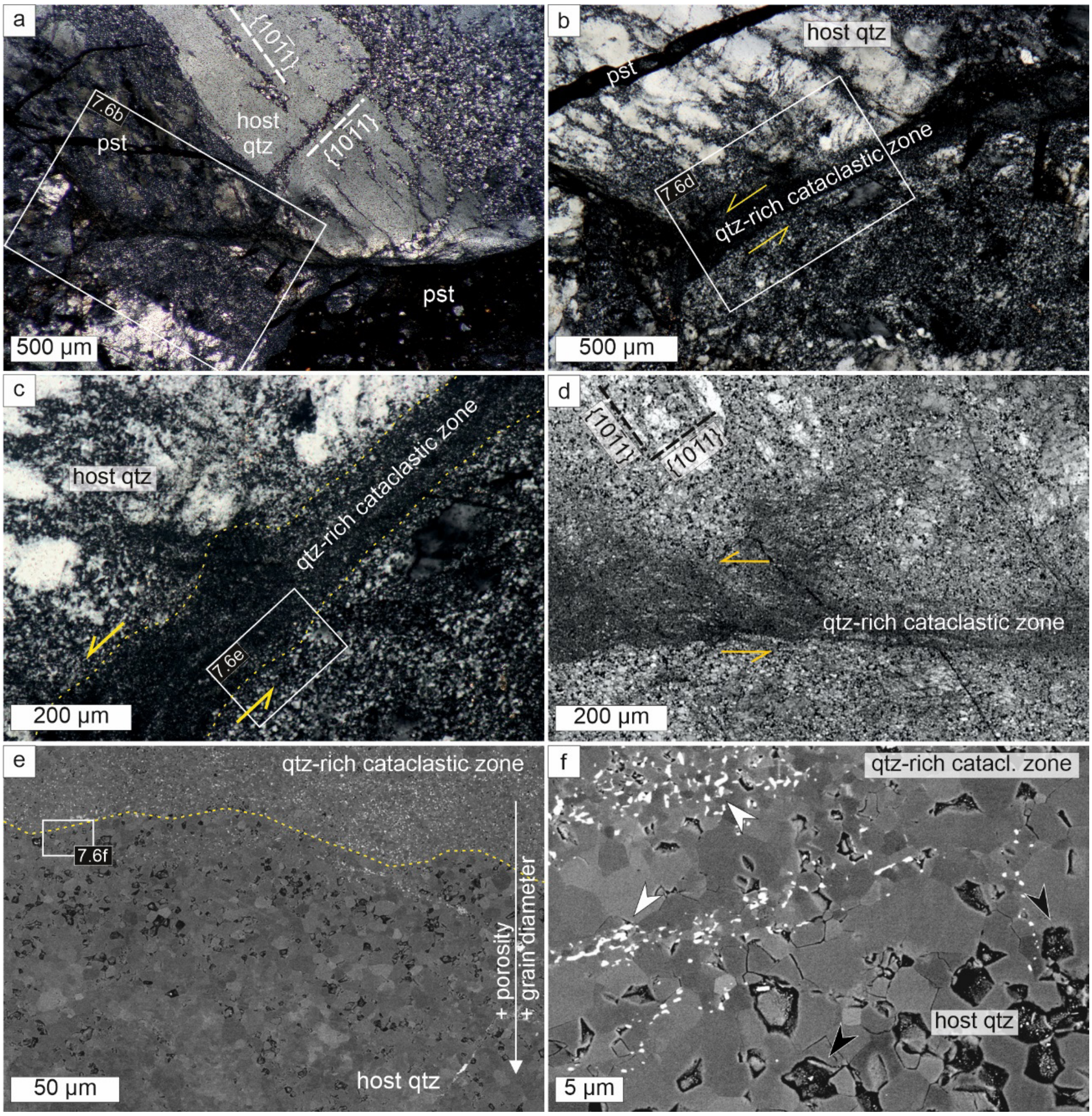

**Figure 7.6:** Microfabrics of quartz-rich (qtz) cataclastic zones within Silvretta pseudotachylyte breccia, sample LB15c. **(a-c)** Polarized light micrographs (position of (a) is shown by blue rectangles in Fig. 7.2e, f. White rectangles in Fig. 7.6a–c refer to the position of the image in b, d, and e, respectively, and (c) corresponds to a close-up of (b)). Vein-quartz clast (host qtz) containing pseudotachylyte (pst) injection veins and cataclastic zone (indicated by yellow dashed line) with shear offset (yellow arrows). **(d)** EBSD image (band contrast) of the quartz-rich cataclastic zone showing sinistral shear offset (yellow arrows). **(e, f)** BSE images of the border (yellow dashed line) between the cataclastic zone and clast of pure vein-quartz. Porosity and grain diameters increase with increasing distance from the cataclastic zone. The quartz-rich cataclastic zone is enriched with secondary phases (white arrows in (f)).

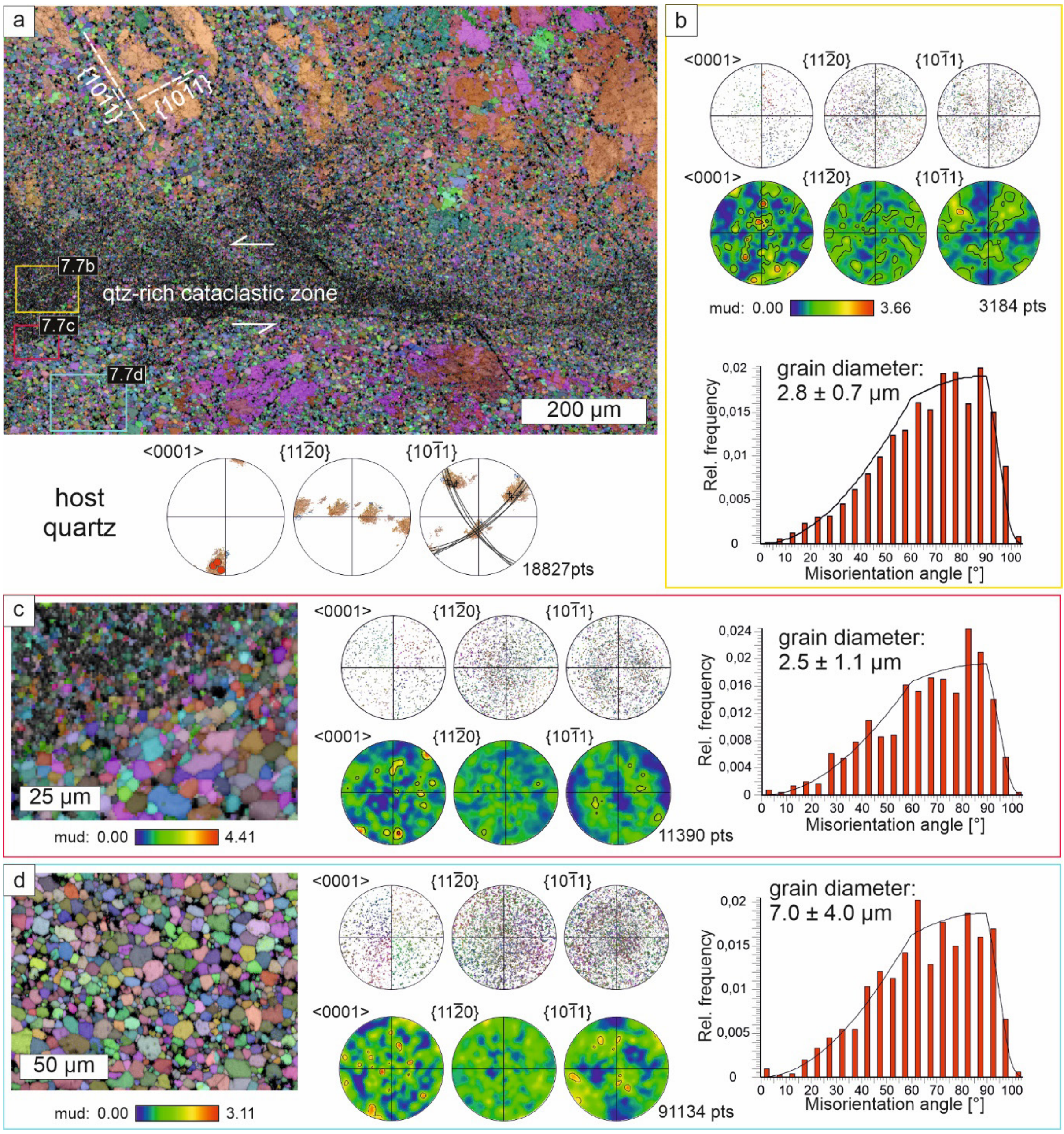

**Figure 7.7:** EBSD data of quartz-rich (qtz) cataclastic zone with shear offset in vein quartz clast (host quartz), Silvretta pseudotachylyte, sample LB15c, position is shown by white rectangle in Fig. 7.6b. **(a)** EBSD map displaying different crystallographic orientations (all Euler angles) and equal-area projection of the orientation of the host quartz with U-stage measurements of cleavage planes shown by great circles (black) and c-axes (red). White arrows indicate the sinistral shear sense. **(b-d)** Euler angle EBSD maps (position indicated by yellow, red, and blue rectangles in (a), pole figures (colors correspond to map in (a)), density plots, and misorientation angle distribution (theoretic random distribution is shown by black solid line) for new quartz grains of the cataclastic zone and within the adjacent host quartz, respectively.

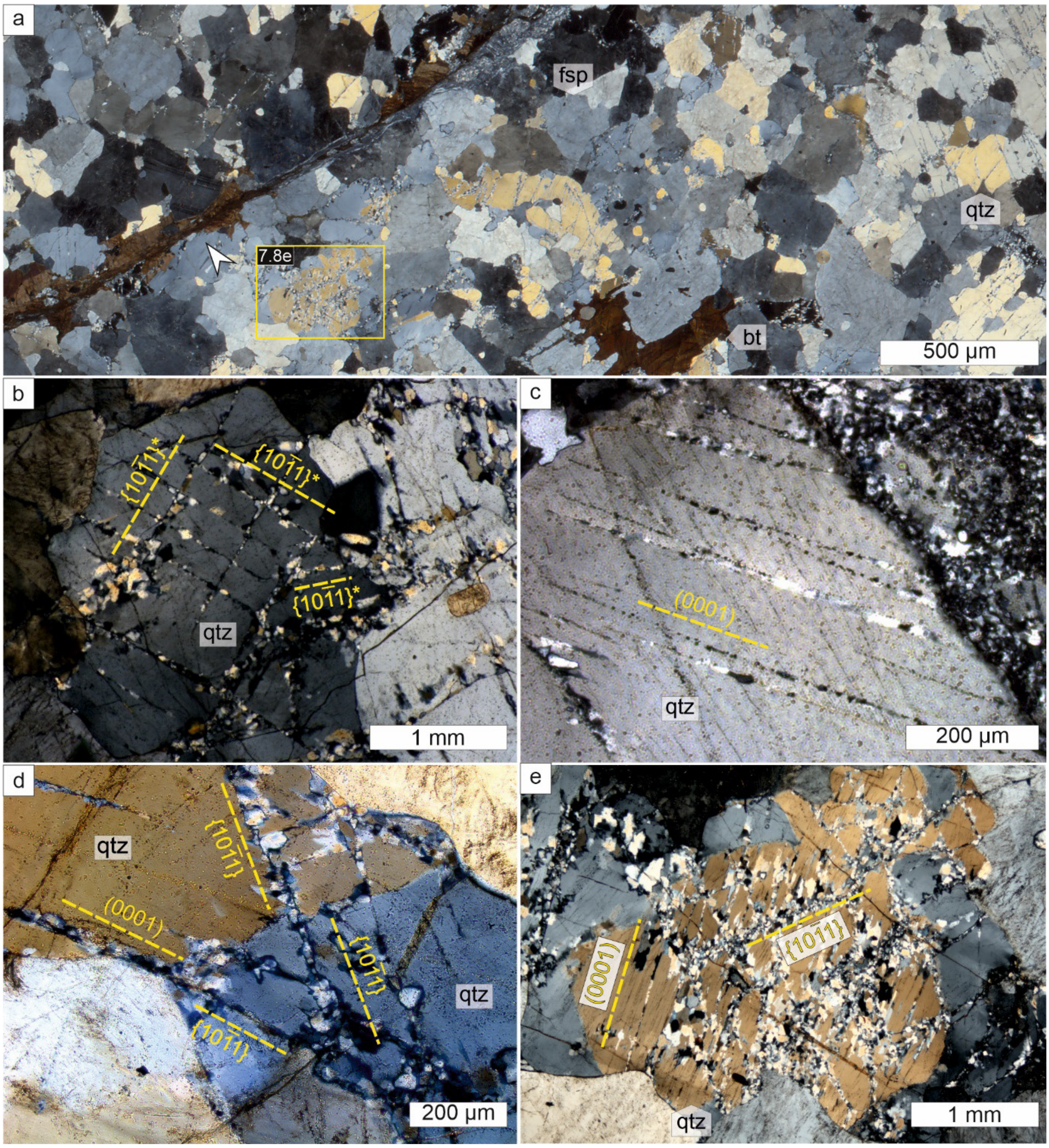

**Figure 7.8:** Quartz microfabrics of Vredefort impact target gneisses (polarized light micrographs with crossed polarizers). **(a)** Gneiss containing quartz (qtz), feldspar (fsp), and biotite (bt). Note the shear zone (white arrow) with a local enrichment of biotite, sample VT445. **(b)** Quartz grain displaying new grains along cleavage planes (yellow dashed lines). (*) Note that no distinction between the positive $\{10\bar{1}1\}$ and the negative form $\{01\bar{1}1\}$ is made given the presence of Dauphiné twins indicated by EBSD measurements (see Fig. 7.9), sample VT445. **(c)** Quartz host with new grains along cleavage planes parallel (0001), sample V2 2.5. **(d)** Fine-grained quartz strings along cleavage planes crossing grain boundaries. Cleavage plane orientations are parallel $\{10\bar{1}1\}$ and/or (0001) of the respective host crystal, sample VT445. **(e)** Strings of new grains along (0001) and $\{10\bar{1}1\}$, sample VT445.

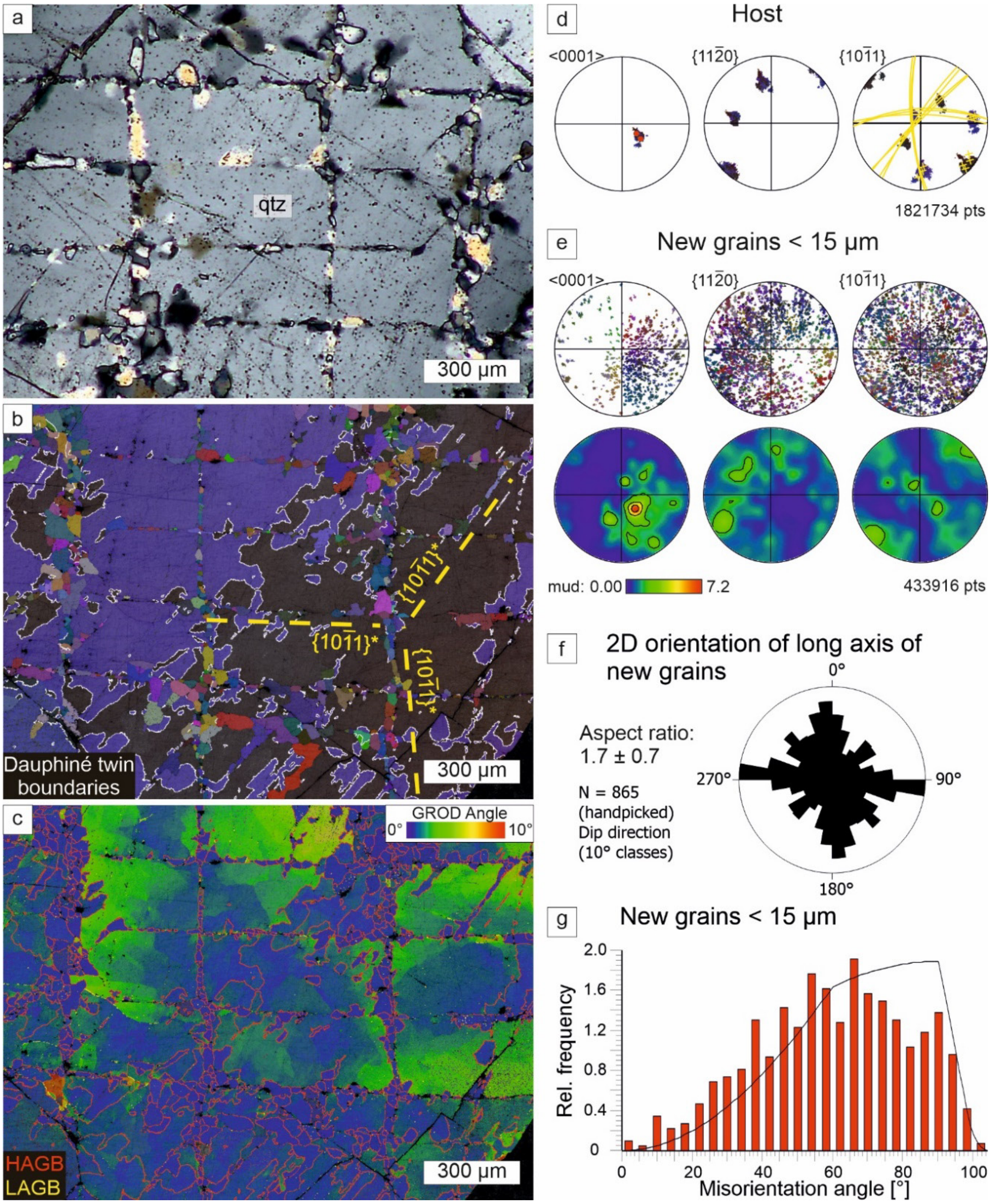

**Figure 7.9:** EBSD data of fine-grained strings of new grains along the cleavage planes of the host quartz within Vredefort impact target gneiss, sample VT445. **(a)** Optical micrograph with crossed polarizers shows new quartz (qtz) grains along cleavage planes within quartz. **(b)** EBSD map displaying crystallographic orientations (all Euler angles) and new grains along cleavage planes. Dauphiné twins are indicated by the white lines. (*) Note that no distinction between the positive $\{10\bar{1}1\}$ and the negative form $\{01\bar{1}1\}$ is made, given the high amount of Dauphiné twins indicated by EBSD measurements. **(c)** Grain Reference Orientation Distribution map (GROD) displaying the angular deviation from the average grain orientation with high angle (HAGB, >10°) and low angle (LAGB, 3-10°) grain boundaries. **(d)** Pole figures of the orientation of the host quartz compared with U-stage measurements of the c-axis (red) and cleavage planes (yellow great circles). Colors correspond to map in (b). **(e)** Pole figures of new quartz grains (<15 µm). Colors correspond to map in (b). **(f)** Rose diagram (2D orientation of long axis) visualizing the shape preferred orientation (SPO) of new quartz grains along cleavage planes. **(g)** Misorientation angle distribution histogram of new quartz grains along $\{10\bar{1}1\}$ cleavage planes (theoretic statistical distribution is indicated by the black line).

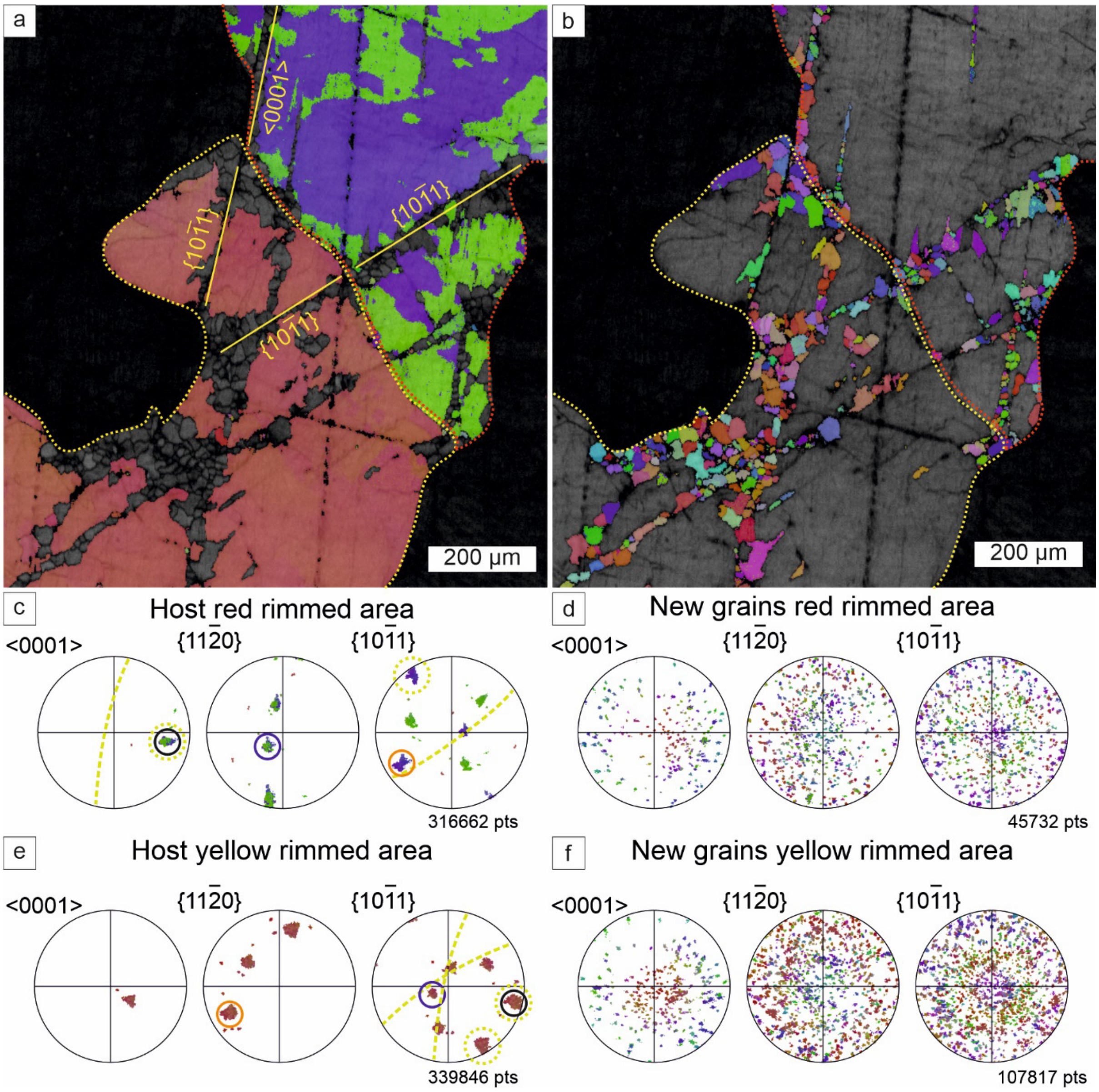

**Figure 7.10:** EBSD data of quartz grains and new grains along cleavage planes, Vredefort gneiss, sample VT445. **(a)** Orientation map (all Euler angle) of host grains (red- and yellow-rimmed) with planar fractures controlled by the host crystallographic orientation, respectively, as depicted in (c) and (e). **(b)** Orientation map (all Euler angle) of recrystallized grains within the top and bottom grains. **(c-f)** Pole figures (colors correspond to map in (a) and (b), respectively) of the orientation of the host quartz and new grains within the (c, d) red- and (e, f) yellow-rimmed area, respectively. **(c, e)** Host quartz grains orientations with cleavage planes (yellow dashed great circles and yellow dashed circles around pole points) are depicted in (a). Note the orientation relationship of specific orientations of the top (red-rimmed) and the bottom (yellow-rimmed) host indicated by the black, blue, and orange circles. **(d, f)** New grains aligned along cleavage planes display dispersed orientations.

## 7.5 Discussion

Strings of small, strain-free isometric quartz grains in sets parallel to $\{10\bar{1}1\}$ and $\{01\bar{1}1\}$ rhombohedral planes, as observed within the Silvretta fault rocks (Figs. 7.2-7.5) and Vredefort gneisses (Figs. 7.8-7.10) are remarkably similar despite the different geologic settings. Both involve cleavage fracturing and the growth of new grains. The observed grain microstructure with isometric grain shape, low internal misorientations, and a weak CPO controlled by the orientation of the host quartz grain (Figs. 7.4; 7.5; 7.7; 7.9 and 7.10) indicates that the grains are not deformed and grew *after* deformation at quasi-isostatic stress conditions, i.e., nominally zero differential stresses. First, the fracturing process, then the growth of new grains, and finally, the implications for the specific geological setting are discussed.

### *7.5.1 Cleavage fracturing*

The controlling criteria discussed for cleavage fracturing include bond density, elastic modulus, surface free energy, and fracture toughness of the crystallographic planes in dependence on grain size and crystallographic orientation (e.g., Armstrong, 2015; Schultz et al., 1994). Fairbairn (1939) showed that for quartz, the number of Si-O-bonds per face unit for the *r*- and *z*-rhombohedra have a minimum, corresponding with a minimum of coherence, followed by $\{10\bar{1}0\}$ and (0001) planes. However, from tectonically deformed rocks, cleavage along (0001) is rarely observed and even more along $\{10\bar{1}0\}$. Schultz et al. (1994) suggested that the fracture toughness of the crystallographic planes is the most appropriate criterion for cleavage fracturing. The fracture toughness of the negative and positive rhombohedra of quartz are 0.85 and 1.0 MPa m$^{1/2}$ (Atkinson, 1984), respectively, which would indicate that the negative rhombohedron is the more likely cleavage plane, compared to the positive rhombohedron. Yet, the observations from Flörke et al. (1981) yield that cleavage of quartz is more commonly occurring along the positive rhombohedra. The authors described that the minimum free surface energy (i.e., a minimum of loose Si-O-bonds after cleavage) is the most important criterion for quartz cleavage. They argued that the cleavage strength of the *r*-rhombohedra at low temperatures is the least as for any other form. Yet, as the surface energy differences for the *r*- and *z*-planes decrease above 300 °C, the cleavage strength gets similar at greenschist facies conditions (Flörke et al., 1981). A combination of differential stress and sufficiently high confining pressure with the resolved shear stress exceeding the critical cleavage stress is suggested to be necessary to generate cleavage in quartz (Flörke et al., 1981). Furthermore, these authors interpreted tectonically induced thermal shock with a temperature rise of about 100 °C to have caused quartz cleavage. Papa et al. (2018) discussed the importance of chemical frictional heating during pseudotachylyte formation to produce thermal stresses on the order of GPa over a few tens of milliseconds. Thermal stresses are higher for anisotropic materials and positively correlate with grain size, which both influence the thermal resistance of the material (Ishihara et al., 2002; Wang et al., 2015).

Kimberley et al. (2010) demonstrated in “interrupted” quasi-isostatic and dynamic compression experiments (strain rates: $10^{-3}$ to $10^{3}$ $s^{-1}$) that cleavage fractures formed along the *r*- and *z*-rhombohedral planes as tensile fractures upon unloading, after compression to a stress level of about half of the failure strength, using a high-speed camera for visualization of failure. These authors argued that friction between quartz and the surrounding steel plates in the experimental setup during unloading played a significant role in the cleavage fracturing of quartz. In the Silvretta fault rocks, the frequently observed *r*- and *z*-cleavage (Figs. 7.3-7.5) is restricted to the clasts within pseudotachylyte breccias representing the tensional domain during rupture propagation (e.g., Di Toro et al., 2005a; Freund, 1990; Kame et al., 2003; Poliakov et al., 2002; Rice et al., 2005; Swanson, 1992) and systematically missing in the host rocks of the opposite domain (Fig. 7.2). The tensional domain during seismic fracture propagation is characterized by transient tensile stresses (Di Toro et al., 2009, 2005; Samudrala et al., 2002) and subsequent fast unloading. Furthermore, this domain is preferentially injected by pseudotachylytic melts, generating a thermal pulse. The amphibole-rich clasts and host rocks in the pseudotachylyte-bearing breccias (Fig. 7.2) were documented to contain $(\bar{1}01)[101]$ mechanical twins that indicate differential stress of at least 400 MPa during deformation (Brückner and Trepmann, 2021). These specific conditions in the tensional domains, with transient high stresses probably in addition to thermal stresses are suggested to result from the injection of pseudotachylytic melts, caused cleavage fracturing along the *r*- and *z*-planes of minimum free surface energy in the coarse vein quartz clasts.

In the Vredefort gneisses, the observed quartz cleavage parallel to the *r*- and *z*-rhombohedral but also along the basal plane (0001) is interpreted to be generated by tensile fracturing during fast unloading from the dynamic high compressive shock stresses. That cleavage occurs additionally along basal planes besides the more common *r*- and *z*-cleavage planes in the Vredefort gneisses is explained by the differences in stress and time scales: During impact cratering, the shock duration is dependent on the diameter of the projectiles on the order of milliseconds to 1 s for large structures (e.g., Langenhorst et al., 2003; Melosh, 1989). Differential stresses during meteorite impact are on the order of a few GPa (e.g., Rae et al., 2021, 2019) even for relatively low shock pressure conditions as for the samples discussed here (<20 GPa, Dellefant et al., 2022). In contrast, the time scales for coseismic stress redistribution during seismic rupture are on the order of a few seconds determined by the duration of the slip event along a fault (e.g., Wald and Heaton, 1994) and coseismic stresses for the Silvretta fault rocks are >400 MPa (Brückner and Trepmann, 2021). The higher magnitudes and shorter duration (on the order of milliseconds to 1 s) of transient peak stresses are interpreted to be responsible for higher resolved stresses along the respective planes favoring cleavage also along planes with higher cleavage strengths (i.e., with higher fracture toughness, higher surface energies, and/or higher bond densities). Overall, the findings are consistent with the experiments by Kimberley et al. (2010), which showed that cleavage fracturing occurs during stress unloading.

### *7.5.2. Growth of new grains*

Menegon et al. (2011) reported localized dynamic recrystallization along *r*-twins in quartz porphyroclasts, which were deformed under greenschist facies conditions. Yet, in the samples from both localities described here, Dauphiné twinning is common, but recrystallized grains do not follow Dauphiné twin boundaries (Figs. 7.4a and 7.9b). Furthermore, the new grains observed here along the strings do not show evidence of deformation, i.e., no dynamic recrystallization. Precipitation of quartz from the fluid along open fractures at greenschist facies conditions is commonly reported (e.g., Derez et al., 2015; Goncalves et al., 2016; Kjøll et al., 2015; Menegon et al., 2008). However, in the Silvretta fault rocks studied here, evidence of precipitation from the pore fluid along the former quartz cleavage fractures is indicated only rarely by the occurrence of calcite from one locality at the Hexenkopf, which is associated with single tensile fractures sealed with calcite and palisade-shaped quartz (Fig. 7.5 and Appendix A1; 2). This precipitation of calcite and quartz is interpreted to have postdated the cleavage fracturing and pseudotachylyte-formation event and occurred during post-seismic hydrothermal activity. In contrast, mostly, the cleavage planes from both the Silvretta fault rocks and the Vredefort gneisses, are decorated by isometric pure quartz grains, where no evidence of major dilation is evident (Figs. 7.3; 7.4 and 7.8-7.10). Therefore, precipitation from the fluid along open cleavage fractures (e.g., Derez et al., 2015; Goncalves et al., 2016; Kjøll et al., 2015; Menegon et al., 2008) appears not to be the dominant process for the formation of new grains along the cleavage planes. The crystallographic orientations of new grains are dispersed with maxima similar to the hosts, suggesting they grew in situ to replace deformed material by recrystallization from the damage zone around the cleavage fractures. The replacement of a deformed crystal volume with a high amount of stored strain energy involves recovery and subgrain rotation with the formation of high-angle grain boundaries and grain boundary migration, as described for Silvretta fault rocks (Trepmann et al., 2017) in comparison to deformation-annealing ("*kick-and-cook*") experiments by Trepmann et al., (2007). In these experiments, the initial high-stress crystal plasticity of quartz resulted in highly damaged zones with cellular structures characterized by a high amount of dislocations surrounding dislocation-poor crystalline volumes. New grains with crystallographic orientation largely deviating from that of the host grew during subsequent annealing at quasi-isostatic stress conditions after deformation, i.e., by static recrystallization. Yet, here, the former fractures are crystallographically controlled, in contrast to the "kick-and-cook" experiments by Trepmann et al., (2007). However, cleavage fracturing likewise involves dislocation pile-up at the fracture tip during fracture propagation (e.g., Armstrong, 2015). Thus, the damage zones surrounding the cleavage fractures can be expected to be local sites of increased dislocation density, which act as sites for recrystallization after deformation at temperatures still sufficiently high for recovery, subgrain rotation, and grain boundary migration of quartz (≥250 – 300 °C). The commonly observed slightly elongated new grains with the long axis parallel to the cleavage planes (Figs. 7.4a, b, e; 7.8 and 7.9a-c, f) are consistent with their growth along the damage zone of the cleavage cracks. The restricted occurrence of strain-free recrystallized grains along cleavage planes demonstrates that recrystallization ceased due to a limited driving force for recrystallization, i.e., no further deformation with the generation of dislocations that would have allowed dynamic recrystallization. This indicates quasi-isostatic conditions during the formation of the new grains and rapid stress relaxation after transient peak stresses that caused the cleavage fracturing at temperature conditions sufficient for recrystallization of quartz (≥250-300 °C). Generally, the described samples from both localities do not show evidence of deformation after static recrystallization along the cleavage planes.

The observation of static recrystallization of quartz, as well as cleavage along both *r*- and *z*-rhombohedral planes (given the decreasing difference in surface energy for the *r*- and *z*-planes at 300 °C, Flörke et al. 1981), is consistent with ambient greenschist facies conditions at which the pseudotachylytes of the Silvretta fault rocks formed (e.g., Brückner et al. 2023; Koch and Masch, 1992; Trepmann et al., 2017).

In the Vredefort gneisses, static recrystallization took place during cooling from post-shock temperatures of 650-725 °C, indicated by Dauphiné twins associated with planar features in quartz (Dellefant et al., 2022) and reaction fabrics in metapelites of the Archean basement, which were interpreted to have formed after the impact (Perchuk et al., 2002).

### *7.5.3 Relation between shearing and cleavage fracturing*

Localized microcrystalline quartz-rich zones occur in spatial relation to Silvretta pseudotachylytes at the boundary to quartz clasts that contain strings of recrystallized grains following cleavage planes (Figs. 7.6 and 7.7). These are markedly different from the strings that occur in sets, as they are single zones with injection vein-like geometry, they contain finely distributed secondary phases and display a shear offset with a shear sense that correlates with the main fracture propagation direction (Figs. 7.2; 7.6 and 7.7). The grains in the cataclastic zone show a random crystallographic orientation and a grain size gradient with increasing diameters from the center of the zones (Figs. 7.6 and 7.7). Although a relatively sharp contact between these cataclastic zones and the hosting quartz clasts with strings of recrystallized grains was observed, no clear crosscutting relationships between them could be detected (Fig. 7.6), indicating different formation yet simultaneous processes.

During seismic fracture propagation, comminution and cataclasis involving grain rolling and grain size reduction predate subsequent frictional sliding and melting (e.g., Curewitz and Karson, 1999; Di Toro et al., 2005b; Fabbri et al., 2000; Maddock, 1992; Magloughlin, 1992, 1989; Ray, 1999; Sibson, 1977; Spray, 1995, 1992; Swanson, 1992; Wenk, 1978). Due to the high melting temperature of quartz at 1720 °C (Deer et al., 2013), quartz commonly remains as clasts within pseudotachylytes (Figs. 7.2a-d and 7.3a-c). However, high-velocity friction experiments of Lee et al. (2017) demonstrate that quartz is capable of melting already at lower temperatures of 1350-1500 °C, at sliding velocities of 1.3 $ms^{-1}$, which is a typical seismic slip rate of faults (1-3 $ms^{-1}$) recorded by pseudotachylytes in association with cataclasis (Di Toro et al., 2009; Sibson, 1986; Spray, 1992; and references within). Bestmann et al. (2012, 2011) reported localized fine-grained quartz micro shear zones associated with pseudotachylytic veins that were generated by recovery and dynamic recrystallization due to transient high temperatures along and around the slip plane with the production of superheated (T >1200 °C) frictional melts.

The microcrystalline quartz-rich zones observed here (Figs. 7.2; 7.6 and 7.7) are interpreted to have formed by comminution and cataclasis during shearing. Secondary material and quartz are potentially derived from adjacent host rock material from pseudotachylytic melts. Whether localized melting of quartz was involved in forming the quartz-rich cataclastic shear zones cannot be excluded, but no microstructural evidence besides restricted phase mixing has been observed. The comminution and cataclasis are interpreted to have occurred almost simultaneously with cleavage fracturing, which is consistent with the interpretation that cleavage fracturing occurs in the tensile domain during fault tip propagation, causing cataclasis and eventually pseudotachylytic melts.

Shear zones also occur in the Vredefort gneisses (Fig. 7.8a). Furthermore, individual shear fractures were described along $\{10\overline{1}1\}$, and in particular along (0001), with shear offsets up to several tens of µm, but these are not decorated with recrystallized quartz grains (see Dellefant et al. 2022: Fig. 2c, e). Locally, shear fractures with associated feather features occur (see Dellefant et al., 2022: Fig. 2c, d, h). Similar to pseudotachylyte-bearing fault rocks from shear zones (Di Toro et al., 2005a), feather features mostly occur on one side of the fracture, which represents the tensional domain during fracture propagation characterized by transient tensile stresses (Ebert et al., 2020; Poelchau and Kenkmann, 2011).

Overall, the deformation conditions in deep parts of large meteorite impact structures, as for Vredefort, though characterized by shorter time-scales, can be comparable to those that are realized coseismically at or below hypocentral depth during major earthquakes in the continental crust, where stresses can reach transiently the order of GPa (e.g., Brückner and Trepmann, 2021; Campbell and Menegon, 2022; Trepmann and Stöckhert, 2001). As the recognition of transient and episodic deformation in tectonic settings at these depths is commonly obscured by modification during a prolonged thermal history after deformation, a comparison to irrefutable transient deformation during impact cratering is valuable and allows evaluating material behavior at non-steady-state conditions.

## 7.6 Conclusions

Strings of recrystallized quartz grains along cleavage planes in host quartz crystals have been compared and contrasted from two fundamentally different geological settings, the Silvretta basal thrust and the Vredefort impact structure. They are interpreted to result from fast stress unloading after transient peak stresses, probably associated with thermal shock caused by frictional heating. In the Silvretta fault rocks, the new grains along cleavage planes exclusively occur in the tensional domain, arising from the asymmetry of the propagating fault tip and associated with the injection of pseudotachylytic melts. In contrast, microcrystalline quartz-rich zones with a minor shear component, enriched with secondary comminuted material, along planes of high shear strain (i.e., pseudotachylytes) develop due to comminution and cataclasis during shearing almost simultaneously with cleavage fracturing. The higher rates of stress (un)loading during meteorite impacting compared to seismic faulting favor cleavage along planes with higher cleavage strengths, i.e., in addition to the most favorable *r*- and *z*-rhombohedra, the basal planes in the shocked Vredefort gneisses. In the Silvretta basal thrust and the Vredefort impact structure, new grains of pure quartz form by subgrain rotation and strain-induced grain boundary migration along the damage zone surrounding the cleavage fractures at quasi-isostatic stress conditions after deformation. The record of these new grains along cleavage planes is diagnostic for fast stress unloading at pressure and temperature conditions high enough to allow for static quartz recrystallization after fracturing, i.e., temperature conditions of ≥250-300 °C. The study demonstrates that the deformation conditions that transiently prevail coseismically at hypocentral depth during major earthquakes can be comparable to those realized in deep parts of large meteorite impact structures at relatively low shock pressures.

# 8 Transient deformation and long-term tectonic activity in the Eastern Alps recorded by mylonitic pegmatites

This chapter is based on the manuscript: Hentschel et al. (2022). Transient deformation and long-term tectonic activity in the Eastern Alps recorded by mylonitic pegmatites. *Journal of Structural Geology*, 155, 104507. https://doi.org/10.1016/j.jsg.2021.104507

## 8.1 Introduction

Although being of vital importance in Earth Sciences, the relation between long-term lithospheric deformation and episodic deformation related to the seismic cycle remains poorly understood. This is partly because of the complex deformation behavior of rocks along seismic active faults, where the changing stress and strain-rate conditions during the seismic cycle facilitate deformation by both, brittle and dislocation glide-controlled mechanisms even at low ambient pressure and temperature conditions (e.g., Ohl et al., 2021; Pozzi et al., 2021). Also, the interaction between the seismogenic and the aseismic zone during the seismic cycle, which is crucial for an understanding of the large-scale transport of crustal blocks during orogeny, is largely unknown. Coseismic slip within the seismogenic zone can induce transient high stresses below hypocentral depth (e.g., Nur and Mavko, 1974; Savage and Prescott, 1978), triggering episodic deformation (Ellis and Stöckhert, 2004a, 2004b; Nüchter and Ellis, 2010). In turn, accelerated creep below hypocentral depths can reload the seismogenic zone during interseismic periods, as described by the "deep slip model" sensu (Scholz, 2002). The base of the seismogenic zone in the continental crust (Marone and Scholz, 1988) coincides with the temperature-depth onset of crystal-plastic deformation of quartz at temperatures around 300 °C, i.e., at greenschist facies conditions (e.g., Voll, 1976; Hirth and Tullis, 1994; Dunlap et al., 1997; Stöckhert et al., 1999; van Daalen et al., 1999; Hirth et al., 2001; Stipp et al., 2002). It is well known that quartz-rich microstructures formed at these depths can record such episodic ductile deformation during the seismic cycle (e.g., Famin et al., 2004; Küster and Stöckhert, 1999; Nüchter and Stöckhert, 2008, 2007; Trepmann and Stöckhert, 2003). Peak stresses can transiently be several hundred MPa as indicated by jadeite and amphibole twin paleopiezometry (Brückner and Trepmann, 2021; Trepmann and Stöckhert, 2001). The role of stress-loading rates and the characteristic time scales for coseismic deformation (minutes) and postseismic creep (hundreds of years) have been constrained by the comparison of natural quartz microstructures and "*kick-and-cook*" quartz deformation experiments (Trepmann and Seybold, 2019; Trepmann et al., 2017). The deformation behavior of rocks in this pressure-temperature range of greenschist facies conditions is consequently extremely relevant for an understanding of the relationship between deformation during seismic cycles and long-term shear zone activity.

Yet, most of the studies on natural microstructures at hypocentral depth document just one episode of deformation at initially high and then relaxing stresses (Nüchter et al., 2013). Other cycles are either masked due to overprinting or are of lower intensity compared to the dominating well-recorded one. For thrust fault settings with the formation of pseudotachylytes, the model of Nüchter et al. (2013) explains an unique imprint of one single high-stress deformation event at one specific location by coseismic thrust fault propagation. The central idea of the model of Nüchter et al. (2013) is that, depending on the distance to the propagating fault tip, a characteristic sequence of deformation structures develops. With decreasing distances to the fault tip, ductile (e.g., kink bands) to brittle structures (quartz veins) and finally pseudotachylytes, as the last imprint, develop. Strain after passage of the fault front is localized in the next rock increment. Once a crystalline nappe is decoupled, its transport over large horizontal distances requires low shear stresses (Davis et al., 1983). During transport further strain is localized in weak lithologies and areas of high pore fluid pressure (Bachmann et al., 2009; Cook and Aitken, 1976; Davis and Engelder, 1985; King Hubbert and Rubey, 1959; Koch and Masch, 1992; Laubscher, 1983; Rodgers et al., 1962).

For strike-slip tectonic settings, the Austroalpine basement to the north of the Defereggen-Antholz-Vals (DAV) shear zone in the Eastern Alps (Figs. 3.1 and 3.3) represents an ideal field area to investigate episodic deformation at the base of the seismogenic zone. Because these rocks were resident at the critical PT range within greenschist facies conditions from the middle Cretaceous to the Oligocene for about 70 Ma in a tectonically active setting (e.g., Mancktelow et al., 2001; Steenken et al., 2002; Stöckhert, 1984). In such a setting, recurrent seismic events are expected, which potentially have imprinted the rock's microfabric. Vein quartz microstructures from this area document transient high-stress deformation at greenschist facies conditions at relatively slow stress relaxation compared to quartz microfabrics from pseudotachylytes related to the Silvretta basal thrust fault (Trepmann et al., 2017).

In this study, microfabrics from pegmatites of the Austroalpine basement north of the DAV near the village of Weitental (Figs. 3.1 and 3.3) are investigated to evaluate the long-term deformation and stress history through the prolonged time at greenschist facies conditions and to discuss, whether several stages of transient high-stress deformation are recorded. The focus is on this specific site at Weitental because (1) there, the Permian pegmatites show a marked mylonitic foliation and second shear band foliation (Fig. 8.1; Mancktelow et al., 2001), (2) the pegmatites contain fluorapatite-allanite-epidote coronae around monazite similar to those that were dated to 60 Ma by Hentschel et al. (2020) and therefore serve as important reference microstructure to evaluate the relative sequence of deformation and (3) in addition, cataclasites containing components of mylonitic pegmatites occur.

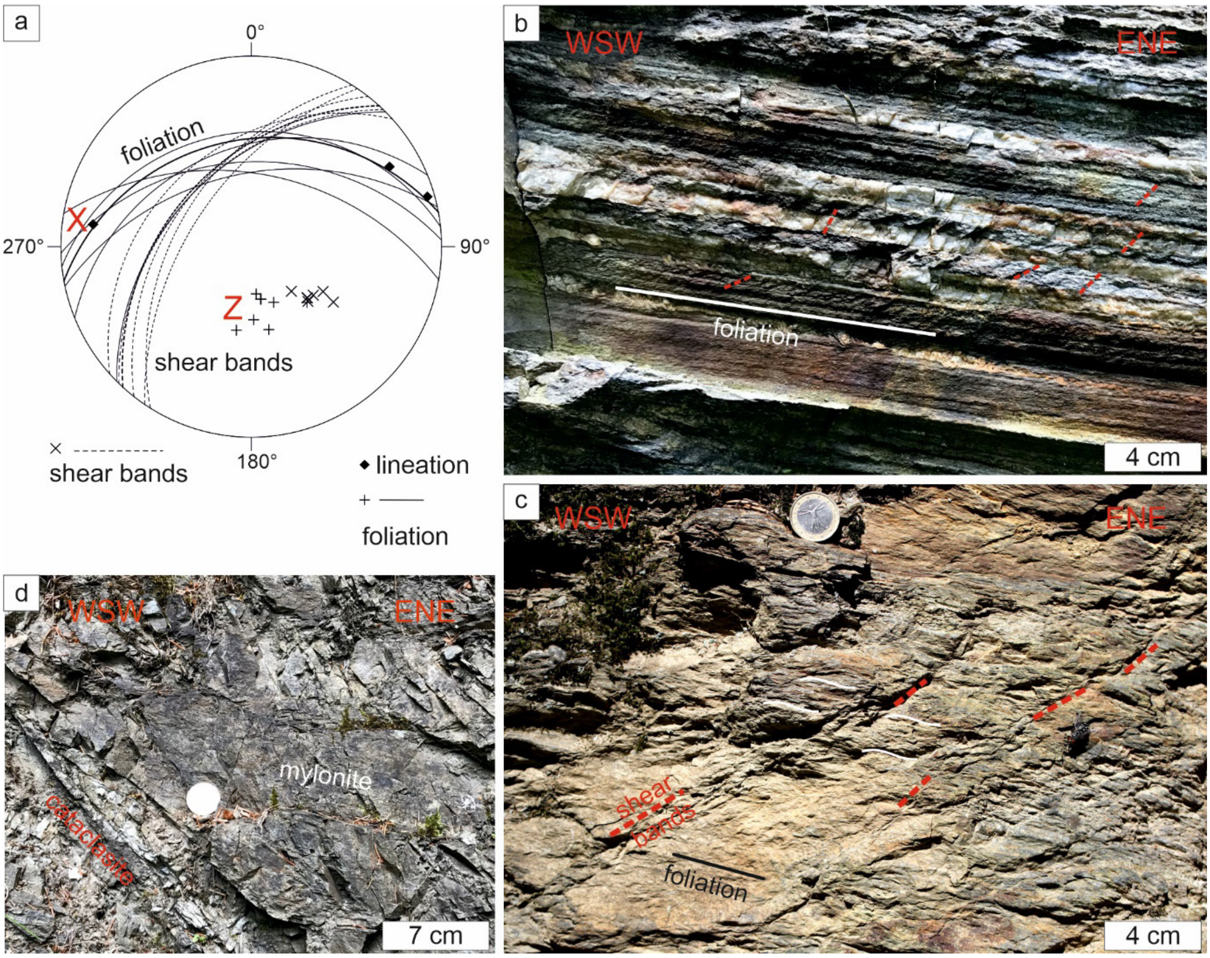

**Figure 8.1:** DAV rocks within the study area. **(a)** Stereographic projection (lower hemisphere) of the main mylonitic foliation, shear bands and lineation. **(b, c)** Field photographs of pegmatitic gneisses with main foliation (solid line) and shear bands (dashed lines) dipping to the NW. **(d)** Field photograph of a cataclasite and its relation to the mylonitic pegmatites.

## 8.2 Results

### *8.2.1 Sample description*

Pegmatites were sampled at Weitental north of the DAV shear zone (46°51’12” N / 11°42’48.6” E) (Fig. 3.3; Appendix A1). The focus was on two specific samples, a mylonitic pegmatite with a well-developed shear band foliation (FH36) and a cataclasite with components of mylonitic pegmatites (FH123). At Weitental, the main mylonitic foliation of the pegmatites dip with 30-50° to the N or NW and the lineation plunges gently E-NE or WNW (Fig. 8.1). The shear band foliation dips to the NW (Fig. 8.1). The intersection of the shear band foliation and the first foliation is about normal to the sample’s lineation within the foliation plane (Fig. 8.1a). Cataclasites with mylonitic components from the same location occur along faults that dip at 30-45° to the ENE (Fig. 8.1d).

The mineral assemblage of the mylonitic pegmatites from Weitental is quartz (ca. 85 %), albitic plagioclase (ca. 5 %), K-feldspar (ca. 5 %), and white mica (ca. 5 %), accompanied by accessory tourmaline, garnet, fluorapatite, monazite, allanite, and pyrite (proportions are estimated from thin section observations). In the cataclasites, additionally zeolites can be present. Monazite is surrounded by allanite-epidote-fluorapatite coronae, as described by (Hentschel et al., 2020). The shear bands generally indicate a sinistral sense of shear and cross-cut the mylonitic foliation (S) at an average angle of 40°, ranging within 25-50° (Figs. 8.1a and 8.2). The shear bands are short, anastomosing, and wavy and are in synthetic orientation. They are classified as C'-type shear bands (Berthé et al., 1979; Gapais and White, 1982; Passchier and Trouw, 2005; Platt and Vissers, 1980).

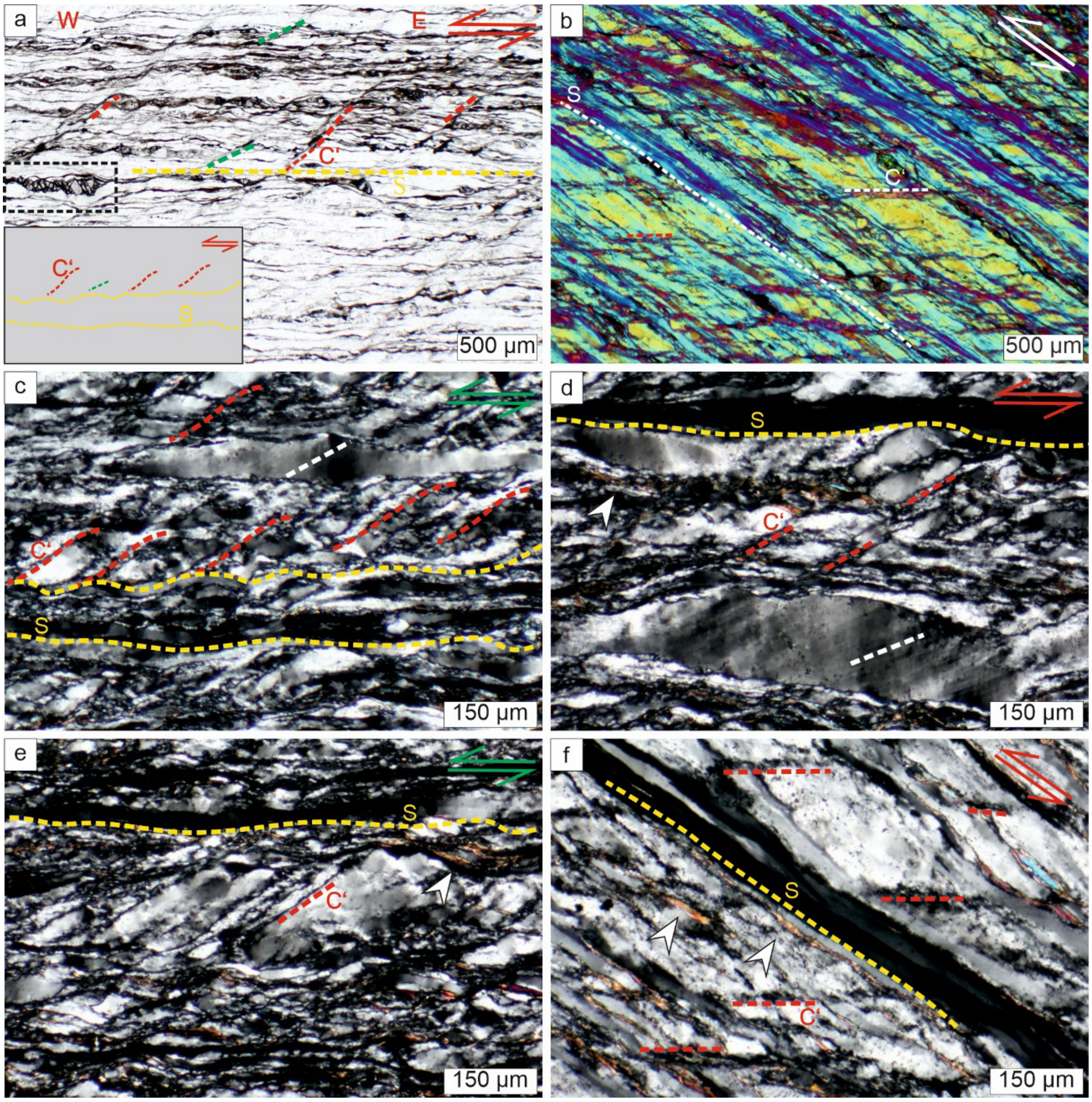

**Figure 8.2:** Polarized light micrographs of a mylonitic pegmatite from Weitental, sample FH36. **(a)** Shear band foliation. Shear planes are typically at an angle of about 40° (red dashed lines) in both mica-rich (upper part) and quartz-rich (lower part), but as low as 25° (green dashed lines) to the main foliation (S, yellow dashed line). Black box in (a) is indicating a cataclastically deformed garnet, compare Fig. 8.5. **(b)** Shear band foliation is horizontal, the first foliation at about 40° (micrograph is taken with crossed polarizers and compensator plate). **(c-f)** Shear bands in quartz-rich domain at 40° (red dashed lines) to the main foliation (crossed polarizers). Flakes of white mica are indicated by white arrows. A few 10s of µm thick elongate quartz grains in the foliation plane (S) are oriented with [c]-axis perpendicular to the thin section (isotropic cut, no birefringence). 100-200 µm thick elongate grains in the foliation plane either contain deformation lamellae (white dashed lines) in (c, d) or are cut by shear bands in (c-e).

The main foliation is defined by elongate quartz grains of tens to hundreds of µm thickness (Fig. 8.2a-c) sometimes separated by thin mica layers (Fig. 8.2d-f). Plagioclase is a subordinate phase, occurring as roundish or slightly elongate grains of a few tens of µm in diameter isolated within the foliation. Some sericite occurs in the cores of plagioclase grains. The shear band foliation is evenly spaced by a few hundred µm and is well-developed not only in mica-rich layers but especially within quartz-rich layers (Fig. 8.2a, b). The shear bands consist of finer-grained zones within quartz grains of specific orientations (Fig. 8.2b-f). The shear offset along the shear bands is typically low, of the order of a few tens of microns (Fig. 8.2a-c).

The quartz grains that define the main mylonitic foliation can be categorized into two groups:

(a) Bent elongate quartz grains with long axes of several hundreds of µm and a width of a few tens of µm. They show mostly very low interference colors indicating an isotropic cut with the [c]-axis perpendicular to the thin section plane (Fig. 8.2c-f), i.e., [c] closely subparallel to the Y-axis of the sample (Fig. 8.3a, b, f). These high aspect ratio grains (in average about 10 to 12 measured in XZ cuts) are either not affected by the C’-type shear bands (Fig. 8.2c-f) or are slightly bent (Fig. 8.3a, b).

(b) Elongate grains of 100-200 µm thickness that either contain sub-basal deformation lamellae (white dashed lines in Figs. 8.2c, d and 8.3a) or are truncated by shear bands (Figs. 8.2c-e and 8.3a, b). These grains systematically have a different crystallographic orientation with the [c]-axis being oriented at a slight angle (<10°) counterclockwise with respect to the normal of the main foliation, Z (Figs. 8.2c, d and 8.3b, g). The sub-basal deformation lamellae are oriented at low angles to the C’-type shear bands (Figs. 8.2d and 8.3a).

Quartz grains that are truncated by the shear bands show [c]-axes preferentially at an orientation ca. 10° clockwise with respect to the normal of the foliation, Z (Fig. 8.3b, h). There, the shear bands (Fig. 8.4a, b) contain isometric grains with diameters of only few µm that show pores along straight or smoothly curved grain boundaries (Fig. 8.4c, d). The small grains show preferred orientations of the [c]-axis at high angle to the shear band foliation (Fig. 8.3b, c). Smaller grains outside the shear bands occur surrounding the elongate grains and show a preferred orientation of the [c]-axis perpendicular to the mylonitic foliation plane (S), i.e., parallel Z (Fig. 8.3b, d).

Garnet grains are fractured forming bookshelf structures with evenly spaced antithetic subparallel fractures forming aggregates of sheared fragments aligned within the mylonitic foliation (Figs. 8.2a and 8.5). The bookshelf structure itself can be affected by synthetic shear planes (Fig. 8.5a). The sense of shear of the bookshelf structure is sinistral, consistent with that indicated by the shear band foliation. The garnet fragments are rotated around the Y-axis and do not show an internal misorientation (Fig. 8.5c, d). Garnet composition is almandine rich ($Alm_{60-70}Gro_{20-30}Sp_{3-6}Py_{5-7}$). Also, tourmaline can show a similar bookshelf structure (Fig. 8.6a). Single fractures in allanite (Fig. 8.6b) and zircon (Fig. 8.6c) are mostly at a higher angle to the foliation. Between these fragments, biotite, epidote and/or quartz precipitated (Fig. 8.6b, c).

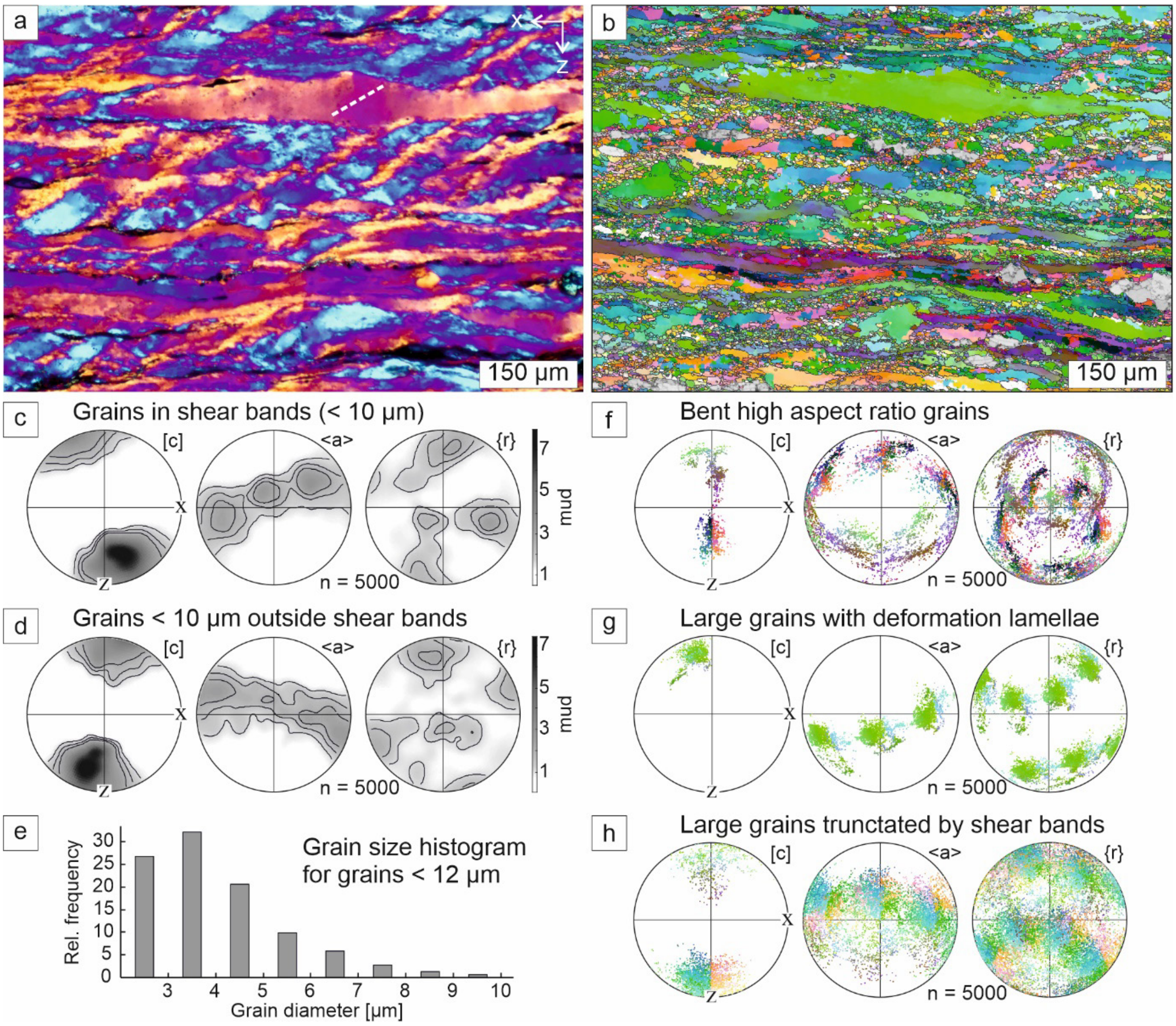

**Figure 8.3:** EBSD-data of quartz shear band foliation, sample FH36. **(a)** Polarized light micrograph with crossed polarizers and compensator plate inserted, compare Fig. 8.1a. **(b)** EBSD-map with Euler angle color coding. **(c, d)** Density plots (lower hemisphere, equal angle projections) showing crystallographic orientation of grains with diameter <10 µm within and outside of shear bands. **(e)** Grain size histogram for grains with diameters smaller than 12 µm. **(f-h)** Pole figures color coded after the EBSD-map in (b). **(f)** Bent elongate quartz grains have preferred orientations with the [c]-axis oriented at high angles to the X-axis and with a maximum at ~30-70° to the Z-axis. **(g)** Quartz grains that are only weakly affected by the shear bands have a preferred orientation with a [c]-axis about 10° counter-clockwise rotated to the Z-axis. **(h)** Quartz grains that are truncated by the shear bands show [c]-axes preferentially at 10° clockwise rotated to Z.

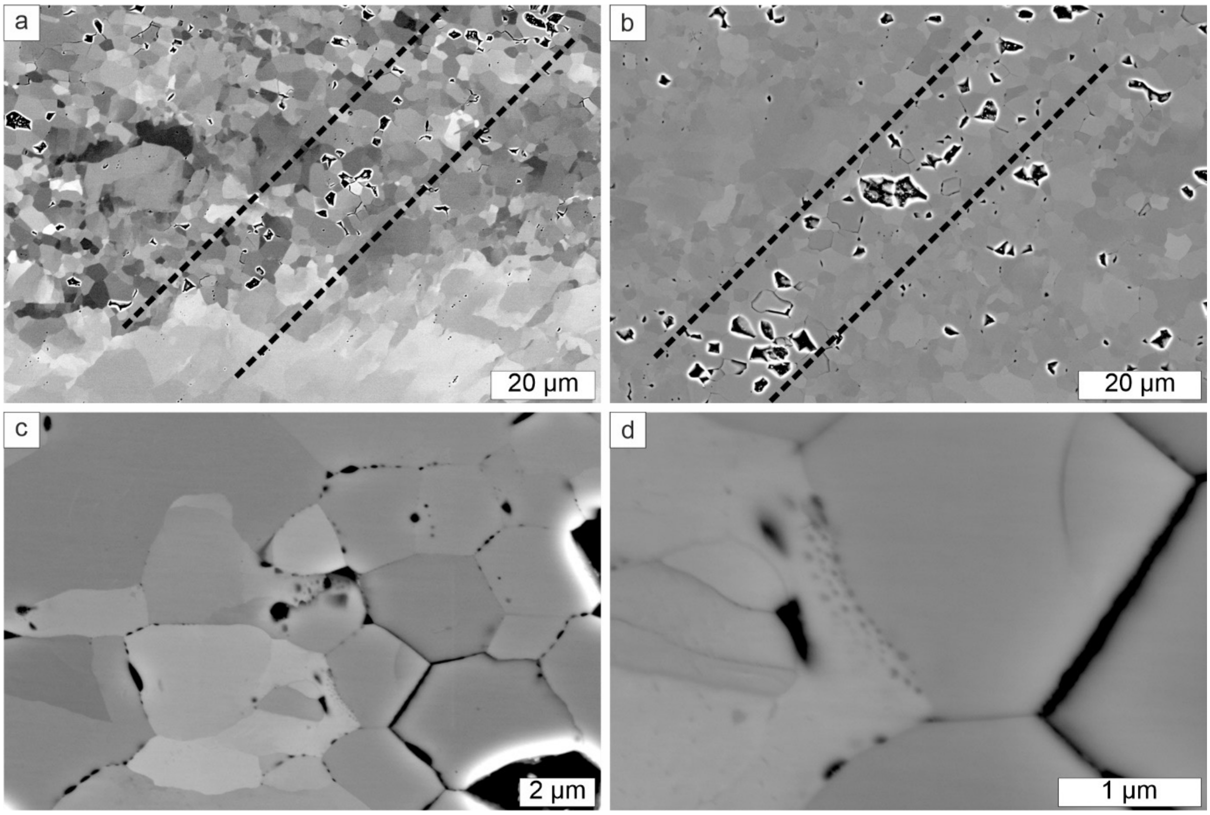

**Figure 8.4:** BSE images, sample FH36. **(a, b)** Orientation contrast of grains with high aspect ratio (bottom) and partly recrystallized grains affected by shear bands and grains within the shear bands. The shear band boundaries are indicated by dashed black lines. Note that the larger pores probably result from polishing. **(c, d)** BSE images of isometric quartz grains within the shear bands with grain boundary porosity.

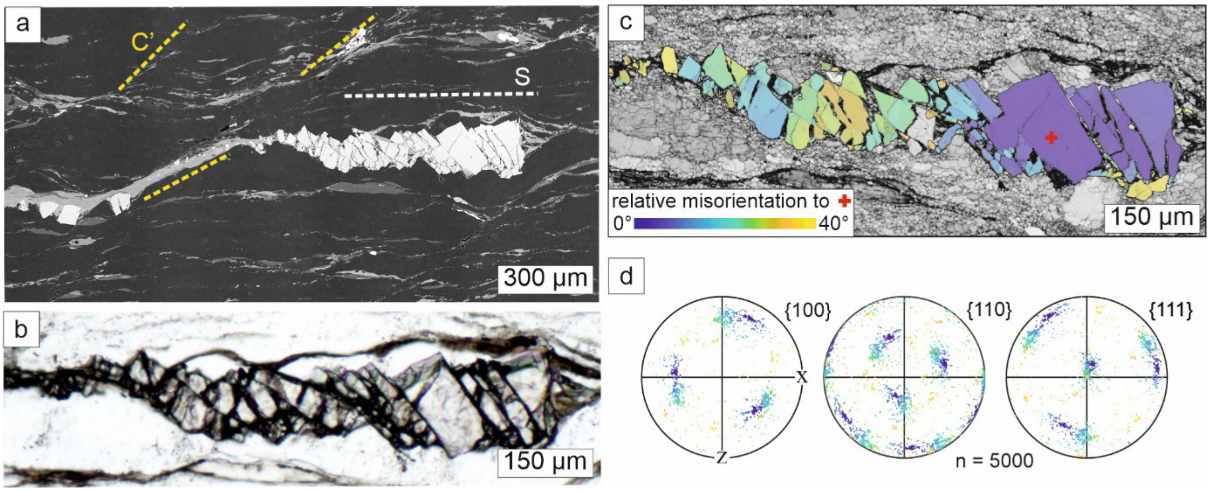

**Figure 8.5:** Cataclastically deformed garnet (see Fig. 8.2a), sample FH36. **(a)** BSE image of garnet with bookshelf structure. **(b)** Polarized light micrograph of the cataclastic garnet shown in (a). **(c)** EBSD map, color coded by relative misorientation. **(d)** Pole figures showing crystallographic orientation of fragment, color coded corresponding to the map in (b).

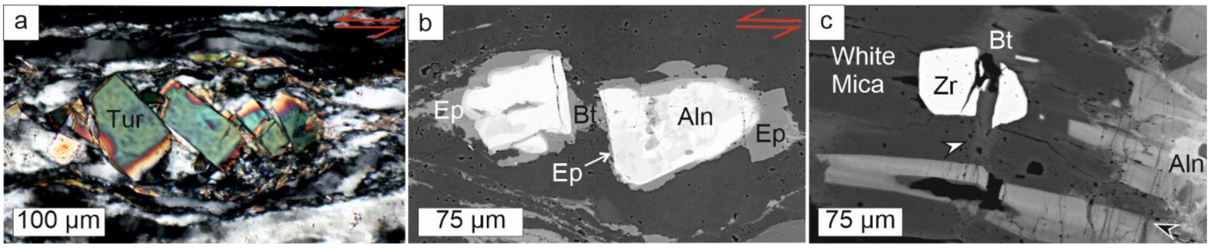

**Figure 8.6:** Fractured accessory minerals, sample FH36. **(a)** Polarized light micrograph of tourmaline (Tur) bookshelf structure, crossed polarizers. **(b)** BSE image showing a fractured allanite (Aln) sealed with biotite (Bt) and epidote (Ep). **(c)** BSE image of fractured zircon (Zr) sealed with biotite (white arrow). Note also fractured allanite sealed with biotite (black arrow).

### *8.2.2 Deformed corona microstructures around monazite*

In the mylonitic pegmatites, monazite grains are surrounded by fluorapatite, allanite and epidote forming elongate corona microstructures (Fig. 8.7). The monazites were investigated by EMP (± 10 measurements per grain, depending on the size of the monazites). The corona microstructures show the same characteristics as those investigated in detail by Hentschel et al. (2020). For four monazites, ages from 70 to 286 Ma are inferred by EMP dating (Fig. 8.7f). The ages represent the Permian magmatic crystallization age (250-287 Ma), as well as mixed ages due to Alpine metamorphic reactions. These reactions are associated with the incomplete replacement by secondary monazite being enriched in U, Pb, Y and Ca (Fig. 8.7e), during formation of the corona microstructure (Hentschel et al., 2020).

The corona microstructures are elongate and aligned along the foliation. The mylonitic foliation is deflected around the corona microstructures, which are in turn affected by the shear bands (Fig. 8.8a). While bent elongate quartz grains have [c]-axes subparallel or slightly rotated clockwise to Z (Fig. 8.8b, c), quartz within the shear bands show [c]-axes at a high angle to the shear band boundaries (Fig. 8.8d, e). The monazite in the core is a single crystal with an internal misorientation below 10° (Fig. 8.9a, b). The surrounding fluorapatite and allanite grains are polycrystalline with random texture, except for a slight clustering of the fluorapatite c-axes (Fig. 9c, d).

### *8.2.3 Cataclasite with mylonitic components*

The cataclasite consists of components of mylonitic pegmatites of up to several cm in diameter within a fine-clastic matrix (Fig. 8.10). The mineral assemblage and microfabric of the components are very similar to that described for the mylonitic pegmatite (compare Figs. 8.2f and 8.10d). The mylonitic foliation is likewise represented by elongate quartz grains of a few tens of micrometer wide and with a length on the order of several hundred microns to a millimeter (Fig. 8.10d, e). Also, the most elongate grains are commonly nearly isotropic in the X-Z thin sections, thus indicating a crystallographic orientation close to the Y-axis of the mylonitic component. Yet, a comparably well-developed second shear band foliation has not been observed in the cataclasites. Instead, the elongate quartz grains can be cut-off by irregular, branching cataclastic zones (Fig. 8.10e). The fine-clastic matrix consists mostly of mica, feldspar, quartz, and Fe-hydroxides, as well as heulandite, as identified by EDS and Raman spectroscopy. Heulandite is present in strain shadows of mylonitic components, indicating precipitation from a pore fluid during deformation (Fig. 8.10f).

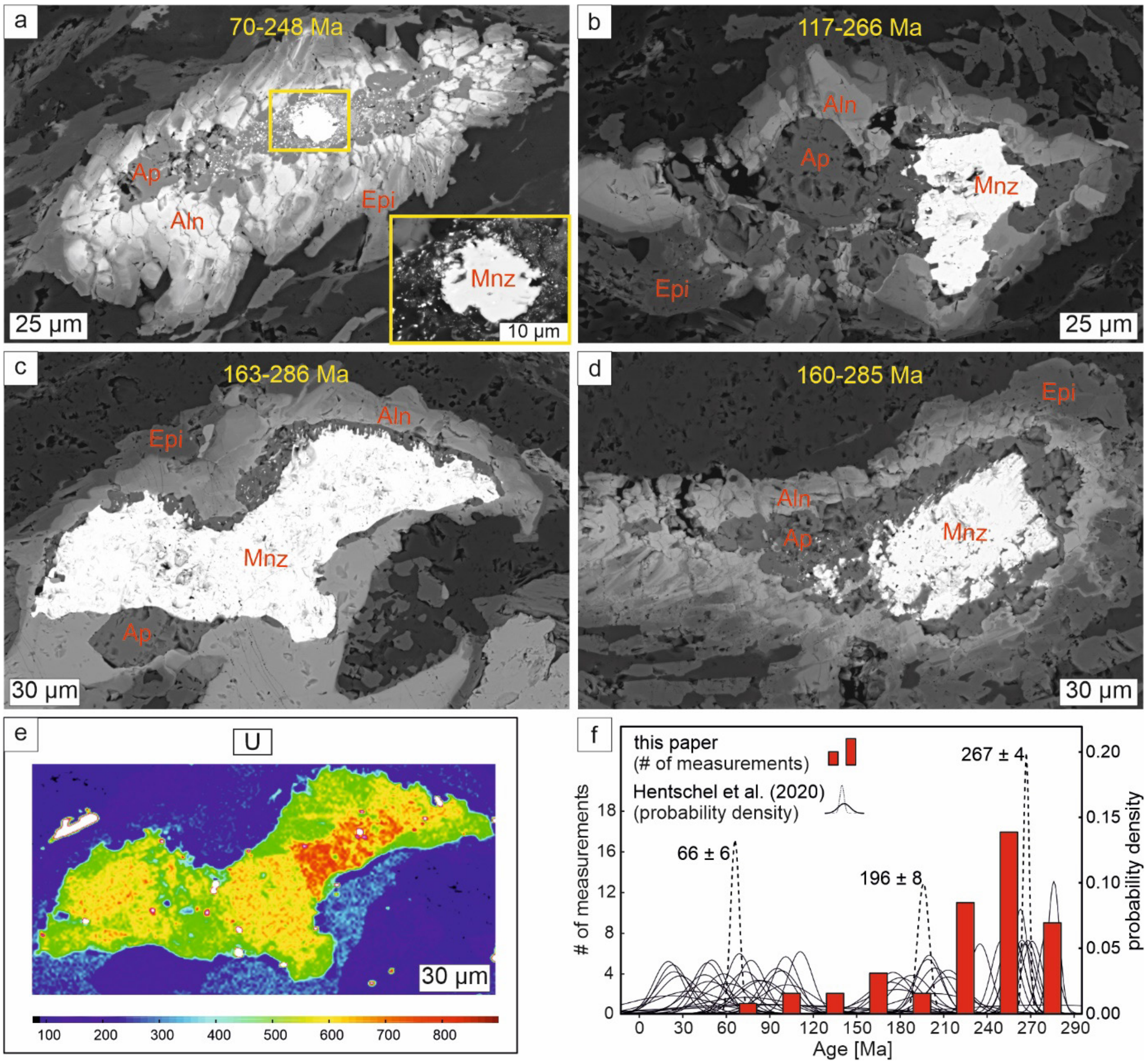

**Figure 8.7:** BSE images of corona microstructures around monazite used for EMP-dating, sample FH36 (yellow numbers represent range of measured EMP ages). **(a)** Large remnant monazite (Mnz) with small rim of fluorapatite (Ap), allanite (Aln), and epidote (Epi). **(b)** Asymmetric shape of corona microstructure aligned in the foliation. **(c)** Largely replaced monazite in elongate corona microstructure aligned along the foliation deflected in a shear band. **(d)** Heterogeneous corona microstructure. **(e)** Uranium distribution map for the monazite in (c). **(f)** Histogram showing EMP-ages of monazite, partly preserving their Permian magmatic age, as well as mixed ages due to the replacement reactions of monazite during the Alpine tectonometamorphism. The distribution data show the ages of monazite from other pegmatites from the studied area (Hentschel et al., 2020).

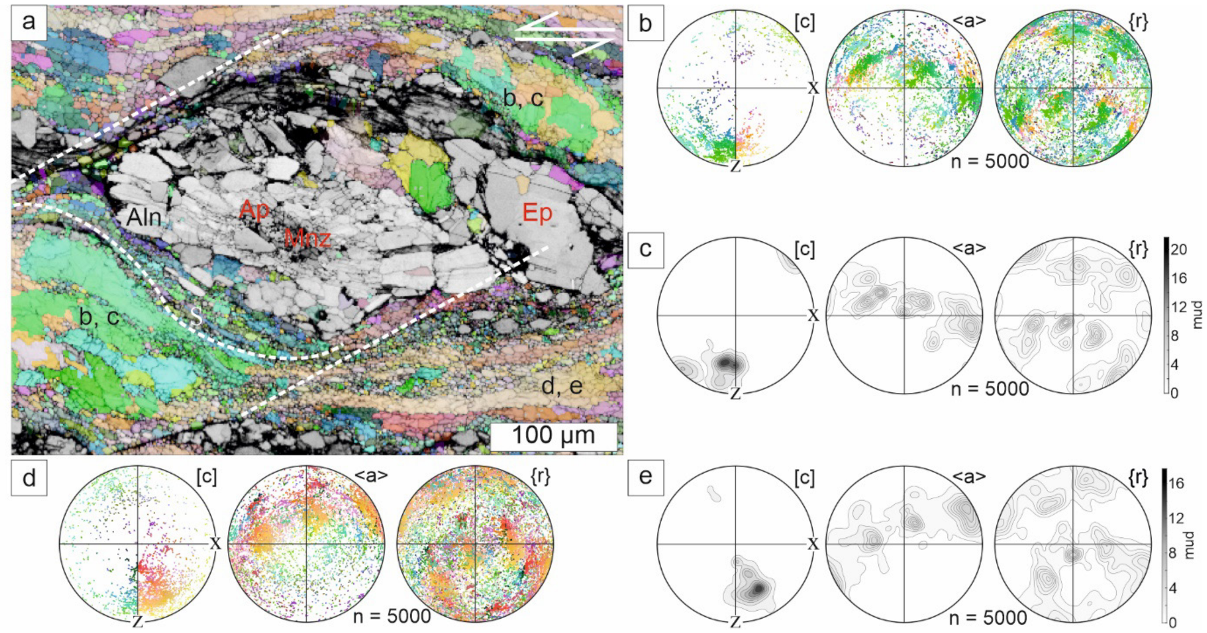

**Figure 8.8:** EBSD data, corona, sample FH36. **(a)** EBSD-map of corona microstructure color coded by Euler angles around monazite (Mnz), surrounded by fluorapatite (Ap), allanite (Aln), and epidote (Ep). **(b, c)** Corresponding pole figure and density plot of quartz grain orientations at the lower left and upper right quadrants around the corona microstructure. **(d, e)** Corresponding pole figure and density plot of quartz grain orientations at the upper left and lower right quadrants around the corona microstructure.

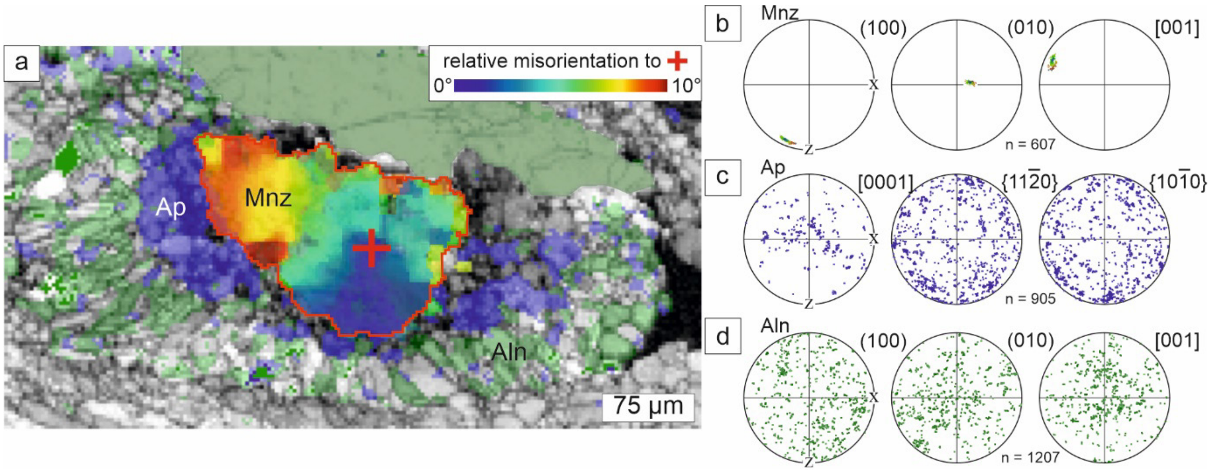

**Figure 8.9:** EBSD data, corona, sample FH36. **(a)** EBSD-map of corona microstructure color coded by relative misorientation for monazite (Mnz; 10°), fluorapatite (Ap) is in blue and allanite (Aln) in green colors. **(b-d)** Corresponding pole figures of monazite, fluorapatite, and allanite orientations, respectively.

## 8.3 Discussion

### *8.3.1 Quartz deformation and shear band formation*

The influence of crystallographic orientation on the flow strength of quartz during dislocation creep has been investigated by deformation experiments of Muto et al. (2011) and in naturally deformed quartz in veins of the Rieserferner pluton just to the east of the study area by Ceccato et al. (2017). That the relative rates of dislocation glide, recrystallization, as well as microfracturing depend on the crystallographic orientation of quartz is well reflected also by the systematically varying textural and microstructural properties of the quartz grains distinguished here in four different microstructures:

1) Bent high aspect ratio grains with the [c]-axis oriented preferentially subparallel to the Y-axis of the sample (Figs. 8.2c; d and 8.3a, b, f) indicate rhombohedral and prism-<a> dislocation glide (e.g., Ceccato et al., 2017; Kilian and Heilbronner, 2017; Law, 1990; Linker et al., 1984; Morales et al., 2011; Muto et al., 2011; Passchier, 1985; Schmid and Casey, 1986; Toy et al., 2008). They show no deformation lamellae and no subgrains; they are not truncated by shear bands and do not show sutured grain boundaries. These bent high aspect ratio grains indicate dislocation glide-controlled deformation. They are interpreted to have been in a favorable crystallographic orientation to activate dislocation glide with respect to the stress-strain field during deformation. Similar elongate quartz grains in mylonites that occur associated with pseudotachylytes in the Saint-Barthélemy massif, French Pyrenees, have been attributed to high differential stress conditions (Passchier, 1985, 1982).

2) Grains with the [c]-axis oriented preferentially at about 10° counterclockwise (synthetically) to Z, normal to the foliation, commonly show sub-basal deformation lamellae (Figs. 8.2d and 8.3a). They are surrounded by subgrains and new grains of similar shape and similar crystallographic orientation (Fig. 8.3a-c, g), indicating dislocation glide and subgrain rotation recrystallization, i.e., dislocation creep (e.g., Drury and Urai, 1990; Hirth and Tullis, 1992; Poirier, 1985; Stipp and Kunze, 2008; Trepmann and Stöckhert, 2009). Deformation lamellae are known to occur together with microfractures, short wavelength undulatory extinction (SWUE), and dislocation tangles. They are characteristic of dislocation glide with limited dislocation climb at high-stress crystal plasticity (e.g., Derez et al., 2015; Drury, 1993; McLaren and Hobbs, 1972; Palazzin et al., 2018; Trepmann and Stöckhert, 2013, 2003). Here, the grains with deformation lamellae are interpreted to be in an orientation not as effective for dislocation glide compared to those described in 1), causing dislocation pile up, consistent with the observation that they have a lower aspect ratio and a systematically different crystallographic orientation (Fig. 8.3). Strain concentration at the boundary of these grains further caused some recrystallization by subgrain rotation recrystallization.

3) Grains with the [c]-axis oriented preferentially at about 10° clockwise (antithetically) to *Z* are truncated by C'-type shear bands (Figs. 8.2e; 8.3a-c, h and 8.4a, b). The grains also contain subgrains and recrystallized grains of similar size and crystallographic orientations, indicating a combination of dislocation glide, subgrain rotation recrystallization, and brittle

deformation. These grains are interpreted to have been in an unfavorable crystallographic orientation to activate dislocation glide with respect to the stress-strain field during deformation, consistent with the findings of Ceccato et al. (2017) and Papeschi and Musumeci, (2019). They deformed by a combination of fracturing and dislocation glide with recrystallization at sites of high dislocation densities.

The quartz microstructures 1) to 3) are interpreted to represent a sequence of decreasing strain by dislocation glide and increasing strain by microfracturing depending on crystallographic orientation. Recrystallization is concentrated at sites of increased accumulated dislocation densities, e.g., grain boundaries, in agreement with the findings of Ceccato et al. (2017).

4) C'-type shear bands are usually interpreted to develop as a second foliation in a primarily foliated mylonite with strong anisotropy at a late stage of shear zone development (Bukovská et al., 2016; Finch et al., 2020; Gillam et al., 2014; Passchier and Trouw, 2005; Platt and Vissers, 1980). Here, the most frequently observed orientation is with in average 40° to the foliation slightly steeper than the most commonly observed angles of 15-30° for C'-type shear bands in mica-rich rocks (Passchier and Trouw, 2005). Bukovská et al. (2016) also observed shear bands at relatively high angles to the foliation, which initiated by fracturing at high differential stresses of 250 MPa. Finch et al. (2020) showed in numerical models that depending on the viscosity contrast >5-15 % weak phases are required to form C'-type shear bands. There is only a low amount of micas (ca. 5 %), which, however, appears here to be not the weak phase controlling the formation of the shear bands. In contrast, the C'-type shear bands are observed to be restricted to the relative high strength quartz layers. Similar to the findings of Bukovská et al. (2016), the shear bands are interpreted to were initiated by microcracking of the quartz grains in unfavorable orientation for dislocation glide. Once fractured, these planes act as weak planes. Notably, the orientation is close to that of extensional T-fractures in brittle fault zones (Passchier and Trouw, 2005; Petit, 1987). Thus, the C'-type shear bands represent planes of low normal stress as opposed to high resolved shear stress, consistent with the relative low amount of shear offset and in accordance with the numerical experiments by Finch et al. (2020). Together with the occurrence of small isometric quartz grains with high grain-boundary porosity within the shear bands (Fig. 8.4), it is suggested that they correspond to vein-like, tensile structures. The quartz in unfavorable orientation for dislocation glide fractured along planes of low normal stress and new quartz precipitated from a pore fluid, similar to the model proposed by Kjøll et al. (2015). Consistently, mesoscopic-scale C'-type shear bands are observed associated to quartz veins (e.g., Trepmann and Seybold, 2019). The shear experiments on polycrystalline quartz by Palazzin et al. (2018) report on very similar C'-type shear bands at 35° to the foliation. They found that the water content of initially fluid-inclusion-rich porphyroclasts decreases during recrystallization and dilatant shear bands act as sinks for $H_2O$ during deformation allowing for precipitation of quartz. The isometric shape and the grain boundary porosity observed for the shear band grains are well consistent with this interpretation and similar to the findings reported on naturally deformed quartz (Kjøll et al., 2015). Furthermore, during recrystallization, water can be drained out along the

migrating grain boundaries (e.g., Jessell et al., 2003; Schenk and Urai, 2005; Trepmann et al., 2010; Urai et al., 1986), with the shear bands acting as sites of quartz precipitation. Quartz in pegmatites is usually containing a high amount of submicroscopic fluid inclusions and can therefore be considered volatile-rich. In this way, recrystallization of the porphyroclasts served as a local (and transient) source for fluids.

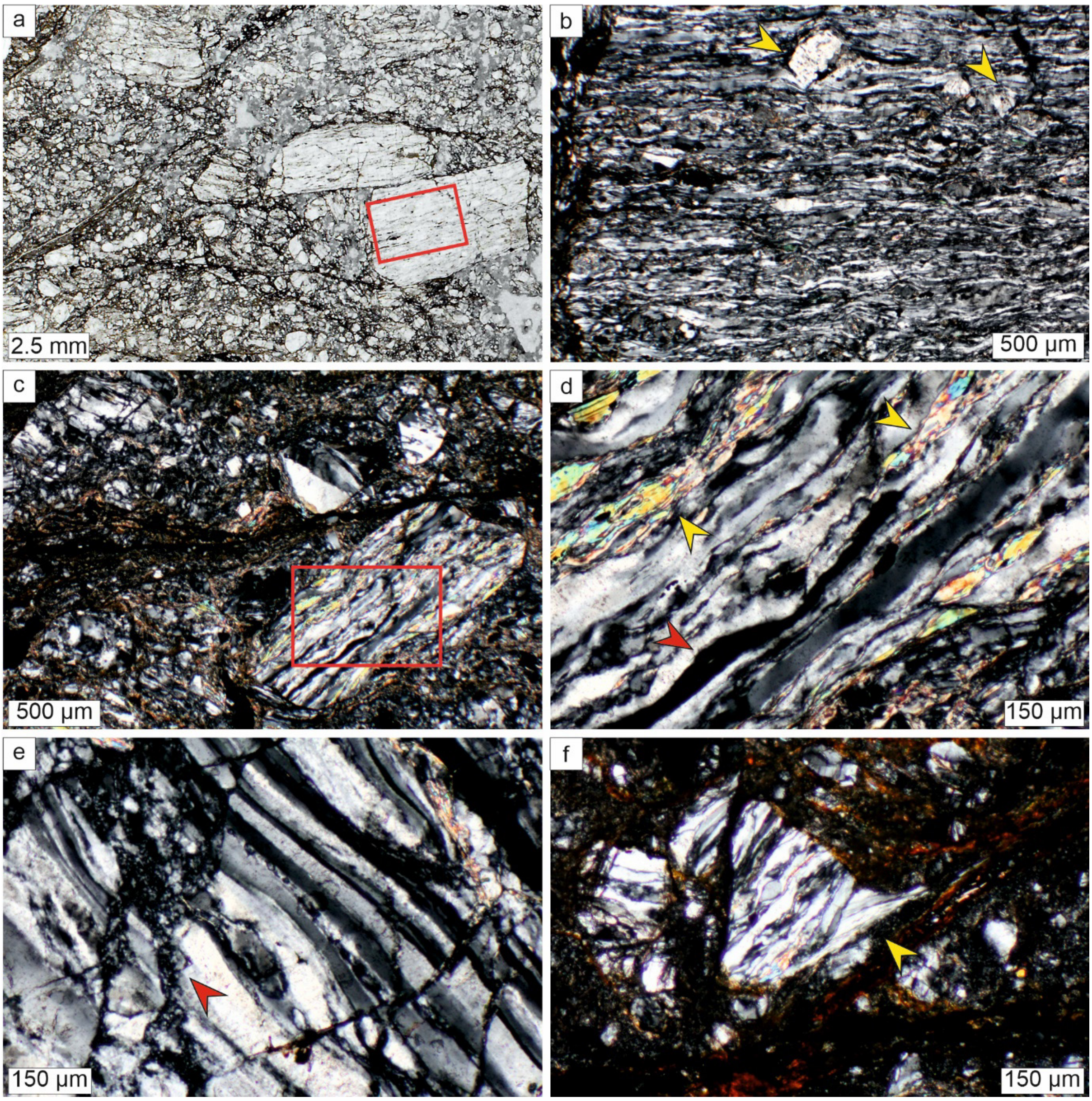

**Figure 8.10:** Polarized light micrographs of cataclasites ((b-f) with crossed polarizers), Weitental, sample FH123. **(a)** Sheared components of mylonitic pegmatite in foliated matrix. **(b)** Close-up of the mylonitic fragment from the area indicated in (a) with yellow arrows indicating feldspar porphyroclasts. **(c, d)** Mylonitic component with elongate quartz grain with [c]-axis at high angle to the thin section (red arrow) and micas along the main foliation (yellow arrows). **(e)** Mylonite component with elongate quartz grains cut off by cataclastic zones (red arrow). **(f)** Heulandite (yellow arrow) in a strain shadow around mylonitic pegmatite-component.

The crystallographic orientation of the grains within shear bands with [c]-axes at a high angle to the shear band boundaries (Fig. 8.3c) might be explained by a combination of epitactic precipitation from the pore fluid and subsequent rigid body rotation during progressive shearing consistent with the sinistral sense of shear in the shear bands, similar to the model proposed by Kjøll et al. (2015). Growth of grains with the [c]-axis perpendicular to the substratum is also known for quartz vein growth (e.g., Bons et al., 2012 and references therin). Furthermore, experimentally deformed quartz with peripheral [c]-axis maxima has been suggested by Kilian and Heilbronner (2017) to rather result from nucleation and growth than to dislocation creep with basal-<a> dislocation glide. Consistently, the strain-free isometric quartz grains in the shear band with high grain boundary porosity and peripheral [c]-axis maximum are interpreted to be due to nucleation and growth with major influence of precipitation from the pore fluid in dilatational sites as opposed to dislocation creep at sites of high shear stress. The straight or smoothly curved grain boundaries of the strain-free new grains in the shear bands furthermore suggest that the interfacial free energy controlled the grain boundary microstructure, representing already an annealed stage at low stresses (Küster and Stöckhert, 1999; Trepmann and Stöckhert, 2003; Trepmann et al., 2010).

### *8.3.2 Quasi-instantaneous distributed fracturing*

The fracturing of quartz in unfavorable orientations can be interpreted as the initial process during formation of the shear band foliation. The even spacing and homogenous angle of the shear bands (Fig. 8.2a-c) are suggesting that the fracturing is a unique, single event as opposed to have occurred continuously during creep. If fracturing would have occurred at different sites continuously during creep, a larger spread in angles and spacings is expected, as discussed for mid-point fracturing of rigid particles in a viscous matrix (e.g., Ji and Zhao, 1994; Zhao and Ji, 1997). The same holds true for the bookshelf structures of, both, garnet (Fig. 8.5) and tourmaline (Fig. 8.6a). If fracturing of both minerals would have been due to progressive mid-point fracturing in a continuously creeping matrix, a systematically different spacing of cracks would be expected, which is not observed. Consistently, Le et al. (2005) found a theoretical solution for distributed instantaneous fracturing of brittle inclusions in a ductile matrix, which requires high stress-loading rates. Cataclastic deformation of garnet in an otherwise viscously flowing matrix has been related to transient high stresses, commonly associated with coseismic deformation (e.g., Austrheim et al., 2017; Hawemann et al., 2019; Song et al., 2020; Trepmann and Stöckhert, 2002).

The cataclastic deformation of garnet and tourmaline is suggested to have been coeval with distributed fracturing of quartz in unfavorable orientation for dislocation glide at transient high stresses (Fig. 8.11). Subsequently at decreasing stresses, quartz underwent further dislocation creep and new grains precipitated along the shear bands, whereas the rigid garnet and tourmaline fragments rotated with a sinistral sense forming the antithetic bookshelf structures. The distributed microcracking occurred at a discrete stage of transiently high stresses and strain-rates.

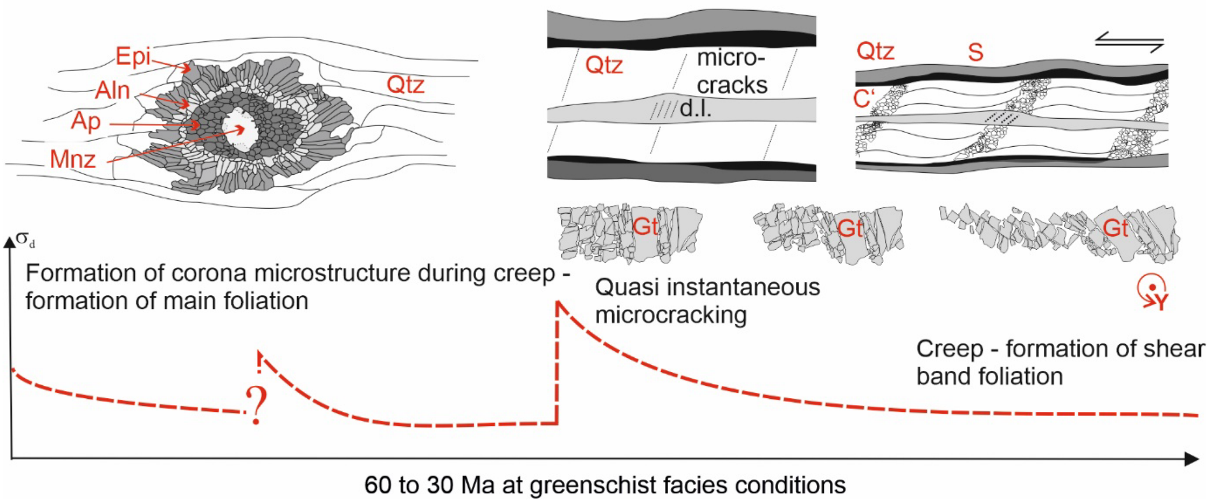

**Figure 8.11:** Synoptic sketch of deformation history inferred from the mylonitic pegmatite at systematically changing stress and more or less constant greenschist facies conditions. Question marks refers to the uncertainty that earlier variations in stress are likely but not equivocally recorded. Epidote (Epi), allanite (Aln), fluorapatite (Ap), monazite (Mnz), garnet (Gt), and (d.l.) refers to deformation lamellae in quartz (Qtz). See text for discussion.

### *8.3.3 Relation between the deformation microstructures in mylonites and cataclasites*

Before and after the discrete stage of distributed microcracking representing the initiation of the shear band foliation, creep occurred at lower stresses and greenschist facies conditions. The epidote-allanite-fluorapatite coronae (Figs. 8.7-8.9) represent valuable reference microstructures and can be used to further elucidate the deformation history. Hentschel et al. (2020) revealed an age of 60 ± 6 Ma for the formation of very similar corona microstructures in pegmatites from the same area by U-Th-Pb in situ dating of allanite by laser ablation inductively coupled mass spectrometry, which is consistent with the youngest of the monazite EMP ages (Fig. 8.7). As the corona microstructures are aligned within the foliation, some deformation is coeval and likely also predated corona formation (Hentschel et al. 2020). However, given that the mylonitic foliation is deflected by the corona microstructure and the shear bands are affecting the outer epidote-allanite zone of the corona (Figs. 8.8 and 8.9), both, mylonitic main foliation, as well as the shear band foliation are interpreted to postdate the corona formation at 60 Ma. It therefore took place after the Eoalpine tectonometamorphic event in the Cretaceous, but at prevailing greenschist facies conditions, as indicated by biotite and epidote precipitation in fractures of the corona minerals (Fig. 8.6b, c). The Austroalpine basement to the south of the western Tauern Window was at temperatures between 300 °C and 350 °C from the Eoalpine tectonometamorphic event in the Cretaceous until uplift and cooling to below greenschist facies conditions in the Oligocene (Stöckhert, 1984), consistent with other geochronological data from this area (Klotz et al., 2019; Steenken et al., 2002). Thus, the recorded deformation took place in the time between 60 Ma and 30 Ma at more or less constant greenschist facies conditions. Only heulandite present in strain shadows (Fig. 8.10e) and veins of the cataclasites indicates precipitation from the pore fluid during deformation at already slightly lower temperature conditions (e.g., Weisenberger and Bucher, 2010). This deformation therefore may have occurred already during uplift to below 300 °C at 30 Ma, the main activity of the DAV shear zone (e.g., Klotz et al., 2019; Mancktelow et al., 2001; Müller et al., 2000; Stöckhert, 1984). The components show very similar microfabrics compared to the mylonitic pegmatites with strongly elongate quartz grains (Fig. 8.10d-f). Yet, no equally well-developed shear band foliation has been observed in any component. Therefore, it cannot be excluded that the formation of the cataclasites might be coeval with the formation of the shear bands. However, in the cataclasites, unlike the shear bands, very little creep strain postdated brittle fracturing.

### *8.3.4 Changing deformation mechanisms at greenschist facies conditions*

Changing deformation mechanisms at unvarying PT-conditions require a change of other factors, which can be fluid availability, microstructure (crystallographic orientation, grain size, phase distribution, etc.) and/or stress and strain-rate. These factors are not independent of each other and change during deformation and metamorphic reactions within the rock system. Furthermore, stresses at the base of the seismogenic zone can change "externally" during seismic activity in the overlying seismogenic crust (e.g., Ellis and Stöckhert, 2004a, 2004b; Nüchter and Ellis, 2010; Scholz, 2002). These "internal" and "external" stress/strain variations do not exclude each other. On the contrary, an increase in stress and strain-rate below hypocentral depth due to seismic slip in the overlying seismogenic zone can be expected to amplify the plastic anisotropy: the higher the stresses and strain-rates the more important are local heterogeneities. Continuous dislocation creep of quartz at greenschist facies would result in homogeneous microstructures (e.g., Trepmann and Stöckhert, 2003). The importance of local stress-strain heterogeneities during creep are evident by the strong control of crystallographic orientation on deformation behavior of quartz in the mylonitic pegmatites described here. The heterogeneity of the microstructure with evidence of quasi-instantaneous microcracking of quartz with unfavorable orientation for dislocation glide, coeval with cataclastic deformation of garnet and tourmaline requires fast stress built up and reflects the short-lived character of deformation (Küster and Stöckhert, 1999; Nüchter and Stöckhert, 2007; Trepmann and Stöckhert, 2003, 2002, 2001).

A fast stress-built up to high stresses required for the quasi-instantaneous distributed microcracking is not compatible with high pore fluid pressures, which would result in low effective stresses (e.g., Küster and Stöckhert, 1999; Nüchter and Stöckhert, 2008). Consistently, the mylonitic pegmatites described here and comparable rocks from the area, show relatively little evidence of fluid-induced alteration, e.g., replacement of garnet by chlorite and of feldspar by sericite (Hentschel et al., 2020, 2019). Transient availability of fluids, however, is documented by the corona microstructures that result from incomplete breakdown reactions of monazite (Gaidies et al., 2017; Hentschel et al., 2020). Locally and transiently increased availability of fluids is also represented by the shear band foliation. The fluid stored in (sub-)microscopic inclusion in the original quartz from the pegmatites was expelled along the migrating grain boundaries during recrystallization, where the shear bands acted as sinks, consistent with the findings from Palazzin et al. (2018) and Kjøll et al. (2015).

As the relevant depths are not directly accessible for stress measurements, absolute constraints on stress mostly rely on a comparison of experimentally calibrated and natural microstructures as well as experimentally derived flow laws (e.g., Poirier, 1985), assuming that the steady state microstructures are not significantly modified during the later geological history. Although microstructural development at non-steady state conditions and varying stress is rather the rule than the exception, paleopiezometers are still widely used (e.g., Hawemann et al., 2019; Papa et al., 2020), which might reflect the stress conditions at a certain but not constrained stage of the geological history. Especially, quartz microfabrics are known to be largely modified during deformation at the systematically changing stresses during the seismic cycle well-below hypocentral depths (Trepmann and Stöckhert, 2003). Even experiments performed at similar PT-conditions, though different initial microstructures and water contents, largely yield different stress conditions during deformation (Palazzin et al., 2018). Given the quartz-rich lithology of the mylonitic pegmatites, they unfortunately do not provide meaningful quantitative constraints on the stress. However, the microfabric can be used to qualitatively analyze the sequence of changing deformation conditions. They record that microstructure and stress changed episodically between Eoalpine tectonometamorphism and Oligocene uplift (Fig. 8.11).

### *8.3.5 Transient deformation and long-term tectonic activity*

The model proposed by Nüchter et al. (2013) explained the unique imprint of deformation at peak stress after a preceding stage of creep at lower stresses by deformation at systematically decreasing distance to the tip of a propagating seismic active thrust fault at crustal depth corresponding to the base of the seismogenic zone (i.e., at constant greenschist facies conditions). Their model, was developed for the Preveli crystalline nappe on Crete, Greece, where pseudotachylytes represent the final imprint before the nappe got detached from its substratum.

The DAV, however, represents a strike-slip fault with a vertical component, where the northern block moved upwards in the Oligocene (e.g., Kleinschrodt, 1987; Klotz et al., 2019; Mancktelow et al., 2001). There, several discrete stages of transiently high stresses during the tectonically active time at greenschist facies conditions between the Eoalpine tectonometamorphic event in the Cretaceous and final uplift in the Oligocene are expected.

The mylonitic pegmatites from Weitental north of the DAV record one dominant event of transiently high stresses with distributed microcracking of quartz, garnet and tourmaline at greenschist facies conditions between stages of creep, as indicated by the bookshelf structures and the shear band foliation offsetting the mylonitic foliation. The intersection of the two foliations is about normal to the sample's lineation (Fig. 8.1a), indicating that both foliations formed in a not markedly changed, similar tectonic setting. It is considered very likely that the first stage of mylonitic foliation represents a stage of accelerated creep, but cannot be unambiguously proven because of major modification during the subsequent deformation. Consistently, Passchier, (1985, 1982), observed elongate quartz crystals, which are similar to those that characterize the first mylonitic foliation in the investigated samples, to occur episodically and coeval with pseudotachylytes at the same metamorphic conditions, which requires changing stress and strain-rate conditions. Therefore, formation of the corona microstructure dated to 60 Ma also in other pegmatitic mylonites from the same area (Hentschel et al., 2020) is considered to reflect an earlier transient stage at the same pressure-temperature conditions. The mylonitic foliation is also very well-developed within the components of the cataclasites, except without the presence of a clear shear band foliation (Fig. 8.10b, d, e). The cataclasites, however, might either be coeval or a subsequent final stage of transient deformation at slightly lower pressure-temperature conditions, as discussed above.

During the long-term tectonic activity from the Eoalpine tectonometamorphic event to the uplift in the Oligocene, discrete stages of transient deformation at high stresses after and before creep at lower stresses and greenschist facies conditions have occurred (Fig. 8.11). This episodic deformation most probably occurred distributed in space and time within the northern block and was probably related to activity of a precursor of the DAV, respectively, an evolving DAV. This interpretation is consistent with the observations of a high amount of smaller scaled shear zones within the rocks of the northern block (Hentschel et al., 2019; Mancktelow et al., 2001), as well as the recent geochronological data with evidence of Miocene activity of a successor DAV by Klotz et al. (2019).

## 8.4 Conclusions

The mylonitic pegmatites from Weitental just to the north of the DAV record discrete stages of transient deformation after and before creep at decreasing stresses at more or less constant greenschist facies PT-conditions between the Eoalpine tectonometamorphic event and uplift in the Oligocene. The main foliation is coeval or postdates formation of corona microstructures around monazite (around 60 Ma) and predates the formation of the shear band foliation. The shear bands reflect the different mechanical behavior of quartz dependent on crystallographic orientation: (1) rhombohedral and prism-<a> dislocation glide in the most suitable orientation, (2) dislocation glide, formation of deformation lamellae and localized recrystallization in less well oriented grains and (3) distributed microcracking in unfavorable orientations for dislocation glide. Distributed microcracking of quartz is interpreted to be coeval with cataclastic deformation of garnet and tourmaline. It occurred quasi-instantaneously, as indicated by the homogeneous spacing of the fractures and the low spread in angles to the foliation for the respective microstructures. Quasi-instantaneous microcracking of quartz, garnet and tourmaline requires transient high stresses and low pore-fluid pressure. During subsequent creep at decreasing stresses, the rigid garnet and tourmaline fragments rotated in the creeping quartz matrix with quartz precipitating from the pore fluid along the shear band boundaries. The recrystallization of the fluid-inclusion-rich original quartz grains acted as local source for fluids and the shear band boundaries as sinks. A coeval or subsequent high-stress event at slightly lower temperatures is recorded by cataclasites with mylonitic components and heulandite in strain shadows.

The mylonitic pegmatites from the Austroalpine basement are documenting the importance of discrete events of transient high-stress deformation during long-term tectonic activity in the Eastern Alps from the Eoalpine tectonometamorphic event in the Cretaceous to the uplift below greenschist facies conditions in the Oligocene. Stress and strain-rate variations are the controlling factors, as opposed to changes in temperature.

# 9 Conclusions

In this thesis the investigated data were used to unravel characteristic microstructural evidence for the deformation processes at hypocentral depth, i.e., at greenschist facies conditions., not directly accessible for in situ measurements. The microstructural record of the fault rocks allowed to obtain information on (i) the peak stresses during pseudotachylyte formation (>400 MPa), (ii) the rheology and relative strength of different lithologies dependent on the propagating fault tip (high-stress crystal plasticity at low distances, creep at large distances), (iii) the transient deformation after unloading from peak stresses in relation to shocked rocks, and (iv) the relation between transient deformation and long-term shear zone activity.

## 9.1 Stresses during Pseudotachylyte formation

The microstructural record of the Silvretta fault rocks offered the unique possibility to constrain the stress conditions which control seismic faulting at hypocentral depth. A propagating seismic thrust fault is assumed, controlling the varying deformation behavior of crustal rocks, to explain the recorded differences in the deformation microfabrics, at the same pressure-temperatures conditions at more or less constant depths, which requires transient high stress-loading rates and rapidly decreasing stresses. At low distance to the propagating thrust fault mechanical twinning of clinoamphiboles and kink bands are associated with cataclasis and pseudotachylyte formation, together with high-stress crystal plasticity of quartz. High stresses exceeding 400 MPa during pseudotachylyte formation are indicated by mechanical $(\bar{1}01)[101]$ twins. At these conditions, quartz deforms by dislocation glide preferentially within coarse grains. In contrast, at large distance to the propagating active fault, quartz-rich lithologies display a decreasing or missing strain gradient towards the amphibole-rich lithologies and evidence of long-term dislocation creep. Homogenous recrystallized quartz, with systematic variation in distribution and grain sizes depending on the distance to the fault, indicate deformation at lower differential stresses of ~10 MPa to ~100 MPa. This reveals that at greenschist facies conditions the amphibole-rich gneisses were accumulating a higher amount of strain relative to quartz-rich lithologies, representing the lower strength phase during coseismic high-stress/high strain-rate deformation, but the higher strength phase during long-term creep. Since subsequent deformation at lower stresses does not obscure the deformation record of twinned amphiboles, they offer an ideal opportunity to detect transient peak stresses during coseismic deformation at the base of the seismogenic zone. The characteristic microstructural record of the various lithologies reveals different deformation mechanisms represented by an "inverse" strength relationship. This is explained to be controlled by the dependence on the distance to a propagating seismic fault tip during nappe decoupling, rather than by internal feedback mechanisms due to the mechanical contrast of the different lithologies.

## 9.2 Time-dependent rock Rheology during the Seismic Cycle at Hypocentral Depth

Investigations of the overprinting relationship of various Silvretta fault rocks highlight the importance of time-dependent rheology during the seismic cycle at hypocentral depth, as they show within the same rock volume two independent stages of high-stress coseismic rupturing, reflected by pristine pseudotachylytes crosscutting deformed pseudotachylytes, that are separated by an intermittent stage of creep at lower stresses. As all stages occurred at greenschist facies-related conditions, the changes in deformation mechanisms and the related varying stresses and strain-rates are interpreted to be controlled by the distance to the coseismically thrust fault, as opposed to being mainly controlled by variations in pressure and temperature. The stage of creep, represented by ultramylonites (i.e., deformed pseudotachylytes) and mylonites, reveals preceding deformation at a large distance to the active rupture tip, i.e., lower stress/strain-rate conditions, whereas frequently pristine pseudotachylytes represent the final microstructural imprint of the seismic fault, where strain is localized in the next rock increment after the passage of the rupture front.

During creep, the fine-grained polyphase pseudotachylytes accumulate a higher amount of strain in relation to the coarse host gneisses. In contrast, during coseismic deformation, microfabrics indicative of high-stress crystal plasticity (i.e., dislocation glide and microfracturing) develop within mylonitic quartz veins, whereas the first pseudotachylyte generation is unaffected. Thus, pseudotachylytes have a lower viscosity during creep at a larger distance to the fault tip (i.e., representing the weaker phase), whereas the coarse-grained quartz accumulates a higher amount of strain, i.e., they are the lithology of lower viscosity during coseismic high-stress crystal plasticity. The different rheological behavior causes that during coseismic rupturing, deformation affects dominantly rocks that have not been ruptured in the same event before, whereas strain is localized in the fault rocks during creep.

## 9.3 Record of fast Stress Unloading from transient Peak Stresses

Silvretta fault rocks, as well as shocked gneisses from the Vredefort impact structure, contain remarkably similar microstructures indicating fast unloading from transiently peak stresses, as evident by quartz cleavage fracturing and strings of small strain-free recrystallized quartz grains in sets along $r\{10\overline{1}1\}$ and $z\{01\overline{1}1\}$ rhombohedral planes. In the Silvretta fault rocks, these quartz microstructures occur exclusively within tensional domains, characterized by transiently high stresses, as a result of shear fracture propagation during thrusting. The restricted occurrence of strain-free grains along cleavage planes indicates, that static recrystallization ceased due to a limited driving force (i.e., no further deformation). Thus, they formed in situ, along the damage zone surrounding the cleavage fractures at quasi-isostatic conditions, and reflect rapid stress relaxation after transient peak stresses, which caused the cleavage fracturing. Vredefort gneisses display in addition cleavage fractures along planes with higher cleavage strength, i.e., the basal plane, caused by the higher stresses. The conspicuous microstructures for both fundamentally different tectonic settings are diagnostic for fast stress unloading from peak stress conditions, consistent with stress unloading related to pseudotachylyte formation at ambient greenschist facies conditions, as well as unloading from relatively low shock stresses at depths.

The deformation conditions that prevail for a shorter duration (milli-sec.) during impact cratering can be comparable to those realized coseismically at hypocentral depth during major earthquakes with stress (un)loading on the order of hundreds of MPa (sec.-min.). Therefore, to recognize structures induced by transient coseismic deformation and in general, to evaluate the rheological behavior at non-steady-state stress conditions, a comparison to shocked rocks, which irrefutably underwent transient deformation, is valuable.

## 9.4 Transient Deformation and Long-Term Shear Zone activity

Several transient high-stress stages are expected to be recorded by quartz microstructure of the Defereggen-Antholz-Vals (DAV) strike-slip shear zone, as the rocks were resident at constant greenschist facies conditions during the long-term tectonic activity of the area. Coronae around monazite constrains the timing of the development of the main mylonitic and shear band foliation of pegmatites. Quartz shear bands reflect the strong crystallographic control on the mechanical behavior of quartz and the importance of local stress-strain heterogeneities during transient deformation. Differences within the quartz microstructures are interpreted to represent a sequence of decreasing strain by dislocation glide and increasing strain by microfracturing depending on the crystallographic orientation, revealing transient high differential stresses. Quartz dislocation glide occurs in low Schmid factor orientations (i.e., favorable orientations for dislocation glide), whereas microfracturing of quartz grains arise in unsuitable orientations for dislocation glide (i.e., high Schmid factors) with respect to the stress-strain field during deformation. Distributed microfracturing occurs coeval with cataclastic deformation of all mineral phases, indicating quasi-instantaneous loading to high stresses and represents one dominant transient deformation event. This implies that quartz is not the weak phase during coseismic high-stress conditions, as opposed to subsequent creep at decreasing stresses (consistent with the findings from the Silvretta fault rocks). A coeval or subsequent high-stress event during uplift is recorded by mylonitic components within cataclasites. The heterogeneity of the preserved microstructures, which requires rapid stress loading rates, demonstrates clearly the short-lived character of deformation at the base of the seismogenic zone with discrete stages of high-stress deformation during the long-term tectonic shear zone activity. Thus, a change in stress/strain-rate conditions is the controlling factor for the evolution of the various microstructures rather than a change in temperature, indicating a variation in deformation processes during spatially and temporally distributed episodic deformation under similar metamorphic conditions.

## 9.5 Highlights

The geological record of the Silvretta fault rocks exhibits microstructural features, which are uniquely seismic, beyond the presence of pseudotachylytes, as they indicate high differential stresses exceeding 400 MPa during seismic faulting. High stresses are evident from mechanical twinned amphiboles and quartz deformed due to high-stress crystal plasticity, as well as by quartz recrystallites which grew in situ at quasi-isostatic conditions restricted to the damage zone of the high-stress imprint. This is also true for strike-slip tectonic settings represented by mylonitic DAV pegmatites, although these do not contain appropriate paleopiezometers. There, microstructural evidence of high-stress transients is indicated by quasi-instantaneous microfracturing and high-stress crystal plasticity of quartz, in dependence on the crystallographic orientation. At the same pressure-temperature conditions quartz microfabrics also indicate creep-related deformation within both localities. The preservation of the various microstructures requires transient high-stress conditions characterized by high-stress loading rates and followed by fast relaxation rates. Furthermore, fast unloading from peak stresses at hypocentral depth is also indicated by cleavage fracturing of quartz at deformation conditions, that can be comparable to those realized during meteorite impacting.

The systematic variations in deformation mechanisms at the same greenschist facies conditions are controlled by the distance to the tip of the propagating active fault, rather than being generated by the mechanical contrast of the lithologies or local heterogeneities, respectively. During rupturing, specific stress and strain-rate conditions are the controlling factors regarding the rheological behavior, as opposed to a change in pressure-temperature conditions. The investigated rock record expresses clearly, that the different deformation conditions during coseismic deformation and creep, as well as their implications on the strength of the various fault rocks during the different stages of the seismic cycle, are important for the assignment of coseismic rupturing events to the long-term activity of shear zones. During high-stress plasticity Silvretta pseudotachylytes are the higher strength phase relative to the host gneisses, reflecting the last stage of rupturing and therefore the final nappe decoupling, respectively. Crosscutting different generations of pseudotachylytes, demonstrate two stages of coseismic transient high-stress deformation separated by a stage of creep, indicating discrete tectonic events, as opposed to an interaction of simultaneous ruptures. For further assignment to the Alpine stages, new specific radiometric dating of the different pseudotachylytes is required.

The thesis demonstrates the importance of distinguishing the different strengths of crustal rocks at specific stress/strain-rate conditions, depending on the distance to the propagating fault tip. This is required to model and understand crustal strength during long-term tectonic activity and orogeny. Exhumed fault rocks deformed at hypocentral depth can serve as the most direct evidence of the stress and strain history during the seismic cycle.

# Bibliography

Allen, N.H., Nakajima, M., Wünnemann, K., Helhoski, S., Trail, D., 2022. A Revision of the Formation Conditions of the Vredefort Crater. Journal of Geophysical Research: Planets 127. https://doi.org/10.1029/2022JE007186

Allen, J.L., 2005. A multi-kilometer pseudotachylyte system as an exhumed record of earthquake rupture geometry at hypocentral depths (Colorado, USA). Tectonophysics 402, 37–54. https://doi.org/10.1016/j.tecto.2004.10.017

Altenberger, U., Prosser, G., Grande, A., Günter, C., Langone, A., 2013. A seismogenic zone in the deep crust indicated by pseudotachylytes and ultramylonites in granulite-facies rocks of Calabria (Southern Italy). Contributions to Mineralogy and Petrology 166, 975–994. https://doi.org/10.1007/s00410-013-0904-3

Altenberger, U., Prosser, G., Ruggiero, M., Günter, C., 2011. Microstructure and petrology of a Calabrian garnet-bearing pseudotachylyte - A link to lower-crustal seismicity. Geol Soc Spec Publ 359, 153–168. https://doi.org/10.1144/SP359.9

Andersen, T.B., Austrheim, H., 2006. Fossil earthquakes recorded by pseudotachylytes in mantle peridotite from the Alpine subduction complex of Corsica. Earth Planet Sci Lett 242, 58–72. https://doi.org/10.1016/j.epsl.2005.11.058

Anderson, J.L., 1945. Deformation Planes And Crystallographic Directions In Quartz. Geol Soc Am Bull 56, 409–430. https://doi.org/10.1130/0016-7606(1945)56[409:DPACDI]2.0.CO;2

Andrews, D.J., 2005. Rupture dynamics with energy loss outside the slip zone. J Geophys Res Solid Earth 110, 1–14. https://doi.org/10.1029/2004JB003191

Armstrong, R.W., 2015. Material grain size and crack size influences on cleavage fracturing. Philosophical Transactions of the Royal Society A: Mathematical, Physical and Engineering Sciences 373, 20140124. https://doi.org/10.1098/rsta.2014.0124

Atkinson, B.K., 1984. Subcritical crack growth in geological materials. J Geophys Res Solid Earth 89, 4077–4114. https://doi.org/10.1029/JB089iB06p04077

Austrheim, H., Boundy, T.M., 1994. Pseudotachylytes Generated During Seismic Faulting and Eclogitization of the Deep Crust. Science (1979) 265, 82–83. https://doi.org/10.1126/science.265.5168.82

Austrheim, H., Dunkel, K.G., Plümper, O., Ildefonse, B., Liu, Y., Jamtveit, B., 2017. Fragmentation of wall rock garnets during deep crustal earthquakes. Sci Adv 3. https://doi.org/10.1126/sciadv.1602067

Bachmann, F., Hielscher, R., Schaeben, H., 2010. Texture Analysis with MTEX – Free and Open Source Software Toolbox. Solid State Phenomena 160, 63–68. https://doi.org/10.4028/www.scientific.net/SSP.160.63

Bachmann, R., Oncken, O., Glodny, J., Seifert, W., Georgieva, V., Sudo, M., 2009. Exposed plate interface in the European Alps reveals fabric styles and gradients related to an ancient seismogenic coupling zone. J Geophys Res Solid Earth 114, 1–23. https://doi.org/10.1029/2008JB005927

Bak, J., Korstgård, J., Sørensen, K., 1975. A major shear zone within the Nagssugtoqidian of West Greenland. Tectonophysics 27, 191–209. https://doi.org/10.1016/0040-1951(75)90016-5

Baratoux, L., Schulmann, K., Ulrich, S., Lexa, O., 2005. Contrasting microstructures and deformation mechanisms in metagabbro mylonites contemporaneously deformed under different temperatures (c. 650 °C and c. 750 °C). Geol Soc Spec Publ 243, 97–125. https://doi.org/10.1144/GSL.SP.2005.243.01.09

Barker, S.L.L., 2005. Pseudotachylyte-generating faults in Central Otago, New Zealand. Tectonophysics 397, 211–223. https://doi.org/10.1016/j.tecto.2004.12.005

Ben-Zion, Y., Andrews, D.J., 1998. Properties and implications of dynamic rupture along a material interface. Bulletin of the Seismological Society of America 88, 1085–1094. https://doi.org/10.1785/BSSA0880041085

Ben-Zion, Y., Shi, Z., 2005. Dynamic rupture on a material interface with spontaneous generation of plastic strain in the bulk. Earth Planet Sci Lett 236, 486–496. https://doi.org/10.1016/j.epsl.2005.03.025

Berger, A., Stünitz, H., 1996. Deformation mechanisms and reaction of hornblende: Examples from the Bergell tonalite (Central Alps). Tectonophysics 257, 149–174. https://doi.org/10.1016/0040-1951(95)00125-5

Berthé, D., Choukroune, P., Jegouzo, P., 1979. Orthogneiss, mylonite and non coaxial deformation of granites: the example of the South Armorican Shear Zone. J Struct Geol 1, 31–42. https://doi.org/10.1016/0191-8141(79)90019-1

Bestmann, M., Pennacchioni, G., Frank, G., Göken, M., de Wall, H., 2011. Pseudotachylyte in muscovite-bearing quartzite: Coseismic friction-induced melting and plastic deformation of quartz. J Struct Geol 33, 169–186. https://doi.org/10.1016/j.jsg.2010.10.009

Bestmann, M., Pennacchioni, G., Nielsen, S., Göken, M., de Wall, H., 2012. Deformation and ultrafine dynamic recrystallization of quartz in pseudotachylyte-bearing brittle faults: A matter of a few seconds. J Struct Geol 38, 21–38. https://doi.org/10.1016/j.jsg.2011.10.001

Biermann, C., 1981. (100) Deformation twins in naturally deformed amphiboles. Nature 292, 821–823. https://doi.org/https://doi.org/10.1038/292821a0

Biermann, C., Van Roermund, H.L.M., 1983. Defect structures in naturally deformed clinoamphiboles - a TEM study. Tectonophysics 95, 267–278. https://doi.org/10.1016/0040-1951(83)90072-0

Birtel, S., Stöckhert, B., 2008. Quartz veins record earthquake-related brittle failure and short term ductile flow in the deep crust. Tectonophysics 457, 53–63. https://doi.org/10.1016/j.tecto.2008.05.018

Bloss, F.D., Gibbs, G. V., 1963. Cleavage in quartz. American Mineralogist: Journal of Earth and Planetary Materials 48, 821–838.

Bons, P.D., Elburg, M.A., Gomez-Rivas, E., 2012. A review of the formation of tectonic veins and their microstructures. J Struct Geol 43, 33–62. https://doi.org/10.1016/j.jsg.2012.07.005

Borg, I.Y., 1972. Some Shock Effects in Granodiorite to 270 Kilobars at the Piledriver Site. Geophysical Monograph Series 16, 293–311. https://doi.org/doi.org/10.1029/GM016p0293

Borsi, S., Del Moro, A., Sassi, F.P., Zanferrari, A., Zirpoli, G., 1978. New geopetrologic and radiometric data on the Alpine history of the Austridic continental margin south of the Tauern window (Eastern Alps). Mem. Sci. Geol. 32, 1–19.

Braathen, A., Osmundsen, P.T., Gabrielsen, R.H., 2004. Dynamic development of fault rocks in a crustal-scale detachment: An example from western Norway. Tectonics 23, n/a-n/a. https://doi.org/10.1029/2003TC001558

Brace, W.F., Byerlee, J.D., 1970. California Earthquakes: Why Only Shallow Focus? Science (1979) 168, 1573–1575. https://doi.org/10.1126/science.168.3939.1573

Brace, W.F., Kohlstedt, D.L., 1980. Limits on lithospheric stress imposed by laboratory experiments. J Geophys Res Solid Earth 85, 6248–6252. https://doi.org/10.1029/JB085iB11p06248

Braeck, S., Podladchikov, Y.Y., 2007. Spontaneous thermal runaway as an ultimate failure mechanism of materials. Phys Rev Lett 98, 1–4. https://doi.org/10.1103/PhysRevLett.98.095504

Brietzke, G.B., Cochard, A., Igel, H., 2009. Importance of bimaterial interfaces for earthquake dynamics and strong ground motion. Geophys J Int 178, 921–938. https://doi.org/10.1111/j.1365-246X.2009.04209.x

Brodie, K.H., Rutter, E.H., 1985. On the relationship between deformation and metamorphism, with special reference to the behavior of basic rocks., in: Thompson, A.B., Rubie, D.C. (Eds.), Metamorphic Reactions: Kinetics, Textures, and Deformation. Springer, New York, NY, pp. 138–179. https://doi.org/10.1007/978-1-4612-5066-1_6

Brückner, L.M., Dellefant, F., Trepmann, C.A., 2024. Quartz cleavage fracturing and subsequent recrystallization along the damage zone recording fast stress unloading. Journal of Structural Geology, 178, 105008. https://doi.org/10.1016/j.jsg.2023.105008

Brückner, L.M., Trepmann, C.A., 2021. Stresses during pseudotachylyte formation - Evidence from deformed amphibole and quartz in fault rocks from the Silvretta basal thrust (Austria). Tectonophysics 817, 229046. https://doi.org/10.1016/j.tecto.2021.229046

Brückner, L.M., Trepmann, C.A., Kaliwoda, M., 2023. Rheology Dependent on the Distance to the Propagating Thrust Tip—(Ultra-)Mylonites and Pseudotachylytes of the Silvretta Basal Thrust. Tectonics 42. https://doi.org/10.1029/2023TC008010

Brune, J.N., Brown, S., Johnson, P.A., 1993. Rupture mechanism and interface separation in foam rubber models of earthquakes: a possible solution to the heat flow paradox and the paradox of large overthrusts.

Buck, P., 1970. Verformung von Hornblende-Einkristallen bei Drucken bis 21kb. Contributions to Mineralogy and Petrology 28, 62–71. https://doi.org/10.1007/BF00389228

Bukovská, Z., Jeřábek, P., Morales, L.F.G., 2016. Major softening at brittle-ductile transition due to interplay between chemical and deformation processes: An insight from evolution of shear bands in the South Armorican Shear Zone. Journal of Geophysical Research-Solid Earth 121, 2798–2812. https://doi.org/10.1002/2015JB012319.Received

Bürgmann, R., Dresen, G., 2008. Rheology of the Lower Crust and Upper Mantle: Evidence from Rock Mechanics, Geodesy, and Field Observations. Annu Rev Earth Planet Sci 36, 531–567. https://doi.org/10.1146/annurev.earth.36.031207.124326

Burkhard, M., 1993. Calcite twins, their geometry, appearance and significance as stress-strain markers and indicators of tectonic regime: a review. J Struct Geol 15, 351–368. https://doi.org/10.1016/0191-8141(93)90132-T

Burov, E.B., Watts, A.B., 2006. The long-term strength of continental lithosphere: "Jelly sandwich" or "crème brûlée"? GSA Today. https://doi.org/10.1130/1052-5173(2006)016<4:TLTSOC>2.0.CO;2

Caggianelli, A., de Lorenzo, S., Prosser, G., 2005. Modelling the heat pulses generated on a fault plane during coseismic slip: Inferences from the pseudotachylites of the Copanello cliffs (Calabria, Italy). Tectonophysics 405, 99–119. https://doi.org/10.1016/j.tecto.2005.05.017

Camacho, A., Vernon, R.H., Fitz Gerald, J.D., 1995. Large volumes of anhydrous pseudotachylyte in the Woodroffe Thrust, eastern Musgrave Ranges, Australia. J Struct Geol 17, 371–383. https://doi.org/10.1016/0191-8141(94)00069-C

Campbell, L.R., Menegon, L., 2022. High Stress Deformation and Short-Term Thermal Pulse Preserved in Pyroxene Microstructures From Exhumed Lower Crustal Seismogenic Faults (Lofoten, Norway). J Geophys Res Solid Earth 127. https://doi.org/10.1029/2021JB023616

Campbell, L.R., Menegon, L., 2019. Transient High Strain Rate During Localized Viscous Creep in the Dry Lower Continental Crust (Lofoten, Norway). J Geophys Res Solid Earth 124, 10240–10260. https://doi.org/10.1029/2019JB018052

Campbell, L.R., Menegon, L., Fagereng, Pennacchioni, G., 2020. Earthquake nucleation in the lower crust by local stress amplification. Nat Commun 11, 1–9. https://doi.org/10.1038/s41467-020-15150-x

Cao, S., Liu, J., Leiss, B., 2010. Orientation-related deformation mechanisms of naturally deformed amphibole in amphibolite mylonites from the Diancang Shan, SW Yunnan, China. J Struct Geol 32, 606–622. https://doi.org/10.1016/j.jsg.2010.03.012

Carporzen, L., Weiss, B.P., Gilder, S.A., Pommier, A., Hart, R.J., 2012. Lightning remagnetization of the Vredefort impact crater: No evidence for impact-generated magnetic fields. J Geophys Res Planets 117. https://doi.org/10.1029/2011JE003919

Carter, N.L., Christie, J.M., Griggs, D.T., 1964. Experimental Deformation and Recrystallization of Quartz. J Geol 72, 687–733. https://doi.org/10.1086/627029

Ceccato, A., Pennacchioni, G., Menegon, L., Bestmann, M., 2017. Crystallographic control and texture inheritance during mylonitization of coarse grained quartz veins. Lithos 290–291, 210–227. https://doi.org/10.1016/j.lithos.2017.08.005

Chao, E.C.T., 1967. Shock Effects in Certain Rock-Forming Minerals. Science (1979) 156, 192–202. https://doi.org/10.1126/science.156.3772.192

Christie, J.M., Griggs, D.T., Carter, N.L., 1964. Experimental Evidence of Basal Slip in Quartz. J Geol 72, 734–756.

Clarke, G.L., Norman, A.R., 1993. Generation of pseudotachylite under granulite facies conditions, and its preservation during cooling. Journal of Metamorphic Geology 11, 319–335. https://doi.org/10.1111/j.1525-1314.1993.tb00151.x

Cook, D.G., Aitken, J.D., 1976. Two cross-sections across selected Franklin Mountain structures and their implications for hydrocarbon exploration: Geological Survey of Canada. Paper 76–1B, 315–322.

Corel Coporation, 2022. Corel DRAW (Version 23.1.0.389) [software].

Cowan, D.S., 1999. Do faults preserve a record of seismic slip? A field geologist's opinion. J Struct Geol 21, 995–1001. https://doi.org/10.1016/S0191-8141(99)00046-2

Cowie, P.A., Scholz, C.H., 1992a. Growth of faults by accumulation of seismic slip. J Geophys Res 97, 11085. https://doi.org/10.1029/92JB00586

Cowie, P.A, Scholz, C.H., 1992b. Physical explanation for the displacement-length relationship of faults using a post-yield fracture mechanics model. J Struct Geol 14, 1133–1148. https://doi.org/10.1016/0191-8141(92)90065-5

Cowie, P.A, Scholz, C.H., 1992c. Displacement-length scaling relationship for faults: data synthesis and discussion. J Struct Geol 14, 1149–1156. https://doi.org/10.1016/0191-8141(92)90066-6

Cumbest, R.J., 1988. Crystal-Plastic Deformation and Chemical Evolution of Clinoamphibole - Dissertation. Virginia Polytechnic Institute and State University.

Cumbest, R.J., Drury, M.R., van Roermund, H.L.M., Simpson, C., 1989. Dynamic recrystallization and chemical evolution of clinoamphibole from Senja, Norway. Contributions to Mineralogy and Petrology 101, 339–349. https://doi.org/10.1007/BF00375318

Curewitz, D., Karson, J.A., 1999. Ultracataclasis, sintering, and frictional melting in pseudotachylytes from East Greenland. J Struct Geol 21, 1693–1713. https://doi.org/10.1016/S0191-8141(99)00119-4

Dalguer, L.A., Irikura, K., Riera, J.D., 2003. Simulation of tensile crack generation by three-dimensional dynamic shear rupture propagation during an earthquake. J Geophys Res Solid Earth 108. https://doi.org/10.1029/2001jb001738

Daly, R.A., 1947. The Vredefort Ring-Structure of South Africa. J Geol 55, 125–145. https://doi.org/10.1086/625423

Davis, D., Suppe, J., Dahlen, F.A., 1983. Mechanics of fold-and- thrust belts and accretionary wedges. J Geophys Res 88, 1153–1172. https://doi.org/10.1029/JB088iB02p01153

Davis, D.M., Engelder, T., 1985. The role of salt in fold-and-thrust belts. Tectonophysics 119, 67–88. https://doi.org/10.1016/0040-1951(85)90033-2

Davis, D.M., Suppe, J., Dahlen, F.A., 1983. Mechanics of fold-and-thrust belts and accretionary wedges. Journal Geophysical Research 88, 1153–1172. https://doi.org/10.1029/JB088iB02p01153

Dawers, N.H., Anders, M.H., Scholz, C.H., 1993. Growth of normal faults: Displacement-length scaling. Geology 21, 1107. https://doi.org/10.1130/0091-7613(1993)021<1107:GONFDL>2.3.CO;2

Deer, W.A., Howie, R.A., Zussmann, J., 2013. An Introduction to the Rock Forming Minerals, 3rd ed. Longman Scientific and Technical.

Dellefant, F., Trepmann, C.A., Gilder, S.A., Sleptsova, I.V., Kaliwoda, M., Weiss, B.P., 2022. Ilmenite and magnetite microfabrics in shocked gneisses from the Vredefort impact structure, South Africa. Contributions to Mineralogy and Petrology 177. https://doi.org/10.1007/s00410-022-01950-5

Derez, T., Pennock, G., Drury, M., Sintubin, M., 2015. Low-temperature intracrystalline deformation microstructures in quartz. J Struct Geol. https://doi.org/10.1016/j.jsg.2014.07.015

Di Toro, G., Nielsen, S., Pennacchioni, G., 2005a. Earthquake rupture dynamics frozen in exhumed ancient faults. Nature 436, 1009–1012. https://doi.org/10.1038/nature03910

Di Toro, G., Pennacchioni, G., 2005. Fault plane processes and mesoscopic structure of a strong-type seismogenic fault in tonalites (Adamello batholith, Southern Alps). Tectonophysics 402, 55–80. https://doi.org/10.1016/j.tecto.2004.12.036

Di Toro, G., Pennacchioni, G., 2004. Superheated friction-induced melts in zoned pseudotachylytes within the Adamello tonalites (Italian Southern Alps). Journal of Structural Geology 26, 1783–1801. https://doi.org/10.1016/j.jsg.2004.03.001

Di Toro, G., Pennacchioni, G., Nielsen, S., 2009. Chapter 5 Pseudotachylytes and Earthquake Source Mechanics, in: International Geophysics. Academic Press, pp. 87–133. https://doi.org/10.1016/S0074-6142(08)00005-3

Di Toro, G., Pennacchioni, G., Teza, G., 2005b. Can pseudotachylytes be used to infer earthquake source parameters? An example of limitations in the study of exhumed faults. Tectonophysics 402, 3–20. https://doi.org/10.1016/j.tecto.2004.10.014

Díaz Aspiroz, M., Lloyd, G.E., Fernández, C., 2007. Development of lattice preferred orientation in clinoamphiboles deformed under low-pressure metamorphic conditions. A SEM/EBSD study of metabasites from the Aracena metamorphic belt (SW Spain). Journal of Structural Geology 29, 629–645. https://doi.org/10.1016/j.jsg.2006.10.010

Dixon, J.E., Dixon, T.H., 1989. Vesicles, amygdales and similar structures in fault-generated pseudotachylites - Comment. Lithos 23, 225–229.

Dollinger, G., Blacic, J.D., 1975. Deformation mechanisms in experimentally and naturally deformed amphiboles. Earth Planet Sci Lett 26, 409–416. https://doi.org/10.1016/0012-821X(75)90016-3

Drury, M.R., 1993. Deformation lamellae in Metals and Minerals, in: Boland, J.N., Fitz Gerald, J.D. (Eds.), Defects and Processes in the Solid State: Geoscience Applications. Elsevier, Amsterdam, pp. 195–212.

Drury, M.R., Urai, J.L., 1990. Deformation-related recrystallization processes. Tectonophysics 172, 235–253.

Dunlap, W.J., Hirth, G., Teyssier, C., 1997. Thermomechanical evolution of a ductile duplex. Tectonics 16, 983–1000. https://doi.org/10.1029/97TC00614

Ebert, M., Poelchau, M.H., Kenkmann, T., Schuster, B., 2020. Tracing shock-wave propagation in the Chicxulub crater: Implications for the formation of peak rings. Geology 48, 814–818. https://doi.org/10.1130/G47129.1

Eggleton, R.A., 1972. The crystal structure of stilpnomelane. Part II. The full cell. Mineral Mag 38, 693–711. https://doi.org/10.1180/minmag.1972.038.298.06

Eggleton, R.A., Chappell, B.W., 1978. The crystal structure of stilpnomelane. Part III: Chemistry and physical properties. Mineral Mag 42, 361–368. https://doi.org/10.1180/minmag.1978.042.323.06

Ellis, S., Beavan, J., Eberhart-Phillips, D., Stöckhert, B., 2006. Simplified models of the Alpine Fault seismic cycle: stress transfer in the mid-crust. Geophys J Int 166, 386–402. https://doi.org/10.1111/j.1365-246X.2006.02917.x

Ellis, S., Stöckhert, B., 2004a. Elevated stresses and creep rates beneath the brittle-ductile transition caused by seismic faulting in the upper crust. J Geophys Res Solid Earth 109. https://doi.org/10.1029/2003JB002744

Ellis, S., Stöckhert, B., 2004b. Imposed strain localization in the lower crust on seismic timescales. Earth, Planets and Space 56, 1103–1109. https://doi.org/10.1186/BF03353329

Evans, B., Kohlstedt, D.L., 1995. Rheology of Rocks, in: Ahrens, T.J. (Ed.), Rock Physics and Phase Relations - A Handbook of Physical Constants. American Geophysical Union Reference Shelf, Washington, pp. 148–165. https://doi.org/10.1029/RF003p0148

Fabbri, O., Lin, A., Tokushige, H., 2000. Coeval formation of cataclasite and pseudotachylyte in a Miocene forearc granodiorite, southern Kyushu, Japan. J Struct Geol 22, 1015–1025. https://doi.org/10.1016/S0191-8141(00)00021-3

Fairbairn, H.W., 1939. Correlation of quartz deformation with its crystal structure. American Mineralogist: Journal of Earth and Planetary Materials 24, 351–368.

Famin, V., Philippot, P., Jolivet, L., Agard, P., 2004. Evolution of hydrothermal regime along a crustal shear zone, Tinos Island, Greece. Tectonics 23. https://doi.org/10.1029/2003TC001509

Finch, M.A., Bons, P.D., Steinbach, F., Griera, A., Llorens, M.G., Gomez-Rivas, E., Ran, H., de Riese, T., 2020. The ephemeral development of C′ shear bands: A numerical modelling approach. J Struct Geol 139. https://doi.org/10.1016/j.jsg.2020.104091

Flörke, O.W., Mielke, H.G., Weichert, J., Kulke, H., 1981. Quartz with rhombohedral cleavage from Madagascar. American Mineralogist 66, 596–600.

Fredrich, J.T., Evans, B., Wong, T.-F., 1990. Effect of grain size on brittle and semibrittle strength: Implications for micromechanical modelling of failure in compression. J Geophys Res 95, 10907. https://doi.org/10.1029/JB095iB07p10907

Freed, A.M., 2005. Earthquake triggering by static, dynamic, and postseismic stress transfer. Annu Rev Earth Planet Sci 33, 335–367. https://doi.org/10.1146/annurev.earth.33.092203.122505

French, B.M., Cordua, W.S., Plescia, J.B., 2004. The Rock Elm meteorite impact structure, Wisconsin: Geology and shock-metamorphic effects in quartz. Bulletin of the Geological Society of America 116, 200–218. https://doi.org/10.1130/B25207.1

French, B.M., Koeberl, C., 2010. The convincing identification of terrestrial meteorite impact structures: What works, what doesn't, and why. Earth Sci Rev 98, 123–170. https://doi.org/10.1016/j.earscirev.2009.10.009

Freund, L.B., 1990. Dynamic Fracture Mechanics. Cambridge University Press, New York.

Fricke, A., Medenbach, O., Schreyer, W., 1990. Fluid inclusions, planar elements and pseudotachylites in the basement rocks of the Vredefort structure, South Africa. Tectonophysics 171, 169–183. https://doi.org/10.1016/0040-1951(90)90097-R

Frisch, W., Neubauer, F., 1989. Pre-Alpine terranes and tectonic zoning in the Eastern Alps, in: Dallmeyer, R.D. (Ed.), Terranes in the Circum-Atlantic Paleozoic Orogens. The Geological Society of America, pp. 91–99.

Froitzheim, N., Schmid, S.M., Conti, P., 1994. Repeated change from crustal shortening to orogen-parallel extension in the Austroalpine units of Graubünden. Eclogae Geologicae Helvetiae 87, 559–612.

Froitzheim, N., Schmid, S.M., Frey, M., 1996. Mesozoic paleogeography and the timing of eclogite-facies metamorphism in the Alps: a working hypothesis. Eclogae Geologicae Helvetiae 89, 81–110.

Frondel, C., 1962. The System of Mineralogy, 7th ed. Wiley, New York.

Gaidies, F., Milke, R., Heinrich, W., Abart, R., 2017. Metamorphic mineral reactions: Porphyroblast, corona and symplectite growth. Mineral reaction kinetics: Microstructures, textures, chemical and isotopic signatures. https://doi.org/10.1180/EMU-notes.16.14

Gapais, D., White, S.H., 1982. Ductile Shear Bands in a Naturally Deformed Quartzite. Textures Microstruct V 5, 1–17. https://doi.org/10.1155/tsm.5.1

Gibson, R.L., 2019. The Mesoarchaean Basement Complex of the Vredefort Dome—A Mid-Crustal Section Through the Central Kaapvaal Craton Exposed by Impact. pp. 109–132. https://doi.org/10.1007/978-3-319-78652-0_5

Gibson, R.L., Armstrong, R.A., Reimold, W.U., 1997. The age and thermal evolution of the Vredefort impact structure: A single-grain U-Pb zircon study, Geochimica et Cosrnochimica Acta.

Gibson, R.L., Reimold, W.U., 2005. Shock pressure distribution in the Vredefort impact structure, South Africa, in: Large Meteorite Impacts III. Geological Society of America. https://doi.org/10.1130/0-8137-2384-1.329

Gibson, R.L., Reimold, W.U., Stevens, G., 1998. Thermal-metamorphic signature of an impact event in the Vredefort dome, South Africa. Geology 26, 787. https://doi.org/10.1130/0091-7613(1998)026<0787:TMSOAI>2.3.CO;2

Gillam, B.G., Little, T.A., Smith, E., Toy, V.G., 2014. Reprint of Extensional shear band development on the outer margin of the Alpine mylonite zone, Tatare Stream, Southern Alps, New Zealand. J Struct Geol 64, 115–134. https://doi.org/10.1016/j.jsg.2013.10.007

Gleason, G.C., Tullis, J., 1995. A flow law for dislocation creep of quartz aggregates determined with the molten salt cell. Tectonophysics 247, 1–23. https://doi.org/10.1016/0040-1951(95)00011-B

Goncalves, P., Poilvet, J.C., Oliot, E., Trap, P., Marquer, D., 2016. How does shear zone nucleate? An example from the Suretta nappe (Swiss Eastern Alps). J Struct Geol 86, 166–180. https://doi.org/10.1016/j.jsg.2016.02.015

Grand'Homme, A., Janots, E., Seydoux-Guillaume, A.M., Guillaume, D., Magnin, V., Hövelmann, J., Höschen, C., Boiron, M.C., 2018. Mass transport and fractionation during monazite alteration by anisotropic replacement. Chem Geol 484, 51–68. https://doi.org/10.1016/j.chemgeo.2017.10.008

Grieve, R.A.F., Coderre, J.M., Robertson, P.B., Alexopoulos, J., 1990. Microscopic planar deformation features in quartz of the Vredefort structure: Anomalous but still suggestive of an impact origin. Tectonophysics 171, 185–200. https://doi.org/https://doi.org/10.1016/0040-1951(90)90098-S

Griffith, W.A., Mitchell, T.M., Renner, J., Di Toro, G., 2012. Coseismic damage and softening of fault rocks at seismogenic depths. Earth Planet Sci Lett 353–354, 219–230. https://doi.org/10.1016/j.epsl.2012.08.013

Griffith, W.A., Rosakis, A., Pollard, D.D., Ko, C.W., 2009. Dynamic rupture experiments elucidate tensile crack development during propagating earthquake ruptures. Geology 37, 795–798. https://doi.org/10.1130/G30064A.1

Grocott, J., 1981. Fracture geometry of pseudotachylyte generation zones: a study of shear fractures formed during seismic events. J Struct Geol 3, 169–178. https://doi.org/10.1016/0191-8141(81)90012-2

Guermani, A., Pennacchioni, G., 1998. Brittle precursors of plastic deformation in a granite: An example from the Mont Blanc massif (Helvetic, western Alps). J Struct Geol 20, 135–148. https://doi.org/10.1016/S0191-8141(97)00080-1

Guggenheim, S., Eggleton, R.A., 1994. A comparison of the structures and geometric stabilities of stilpnomelane and parsettensite: A distance least-squares (DLS) study. American Mineralogist 79, 438–442.

Hacker, B.R., Christie, J.M., 1990. Brittle/Ductile and Plastic/Cataclastic Transitions in Experimentally Deformed and Metamorphosed Amphibolite, in: Duba, A.G., Durham, W.B., Handin, J.W., Wang, H.F. (Eds.), The Brittle-Ductile Transition in Rocks. Geophysical Monograph Series, pp. 127–147. https://doi.org/https://doi.org/10.1029/GM056p0127

Hall, E.O., 1951. The deformation and ageing of mild steel: III Discussion of results. Proceedings of the Physical Society. Section B 64, 747–753. https://doi.org/10.1088/0370-1301/64/9/303

Hammer, W., 1914. Das Gebiet der Bündnerschiefer im tirolischen Oberinntal. Jahrbuch d. k. k. geol. Reichsanstalt 64, 443–566.

Handy, M.R., 1989. Deformation regimes and the rheological evolution of fault zones in the lithosphere: the effects of pressure, temperature, grainsize and time. Tectonophysics 163, 119–152. https://doi.org/10.1016/0040-1951(89)90122-4

Handy, M.R., Braun, J., Brown, M., Kukowski, N., Paterson, M.S., Schmid, S.M., Stöckhert, B., Stüwe, K., Thompson, A.B., Wosnitza, E., 2001. Rheology and geodynamic modelling: The next step forward. International Journal of Earth Sciences 90, 149–156. https://doi.org/10.1007/s005310000161

Handy, M.R., Hirth, G., Hovius, N., 2007. Continental fault structure and rheology from the frictional-to-viscous transition downward, in: Tectonic Faults -Agents of Change on a Dynamic Planet. MIT Press, Cambridge, pp. 139–181.

Hanmer, S., 1988. Great Slave Lake Shear Zone, Canadian Shield: reconstructed vertical profile of a crustal-scale fault zone. Tectonophysics 149, 245–264. https://doi.org/10.1016/0040-1951(88)90176-X

Hanmer, S., Williams, M., Kopf, C., 1995. Modest movements, spectacular fabrics in an intracontinental deep-crustal strike-slip fault: Striding-Athabasca mylonite zone, NW Canadian Shield. J Struct Geol 17, 493–507. https://doi.org/10.1016/0191-8141(94)00070-G

Hart, R.J., Andreoli, M.A.G., Reimold, W.U., Tredoux, M., 1991. Aspects of the dynamic and thermal metamorphic history of the Vredefort cryptoexplosion structure: implications for its origin. Tectonophysics 192, 313–331. https://doi.org/10.1016/0040-1951(91)90106-3

Hart, R.J., Andreoli, M.A.G., Smith, C.B., Otter, M.L., Durrheim, R., 1990. Ultramafic rocks in the center of the Vredefort structure (South Africa): Possible exposure of the upper mantle? Chem Geol 83, 233–248. https://doi.org/10.1016/0009-2541(90)90282-C

Hawemann, F., Mancktelow, N., Wex, S., Pennacchioni, G., Camacho, A., 2019. Fracturing and crystal plastic behaviour of garnet under seismic stress in the dry lower continental crust (Musgrave Ranges, Central Australia). Solid Earth 10, 1635–1649. https://doi.org/10.5194/se-10-1635-2019

Hawemann, F., Mancktelow, N.S., Wex, S., Camacho, A., Pennacchioni, G., 2018. Pseudotachylyte as field evidence for lower-crustal earthquakes during the intracontinental Petermann Orogeny (Musgrave Block, Central Australia). Solid Earth 9, 629–648. https://doi.org/10.5194/se-9-629-2018

Hayward, K.S., Cox, S.F., Fitz Gerald, J.D., Slagmolen, B.J.J., Shaddock, D.A., Forsyth, P.W.F., Salmon, M.L., Hawkins, R.P., 2016. Mechanical amorphization, flash heating, and frictional melting: Dramatic changes to fault surfaces during the first millisecond of earthquake slip. Geology 44 (12), 1043 – 1046, https://doi:10.1130/G38242.1

Heesakkers, V., Murphy, S., Reches, Z., 2011. Earthquake Rupture at Focal Depth, Part I: Structure and Rupture of the Pretorius Fault, TauTona Mine, South Africa. Pure Appl Geophys 168, 2395–2425. https://doi.org/10.1007/s00024-011-0354-7

Henkel, H., Reimold, W.U., 1998. Integrated geophysical modelling of a giant, complex impact structure: anatomy of the Vredefort Structure, South Africa. Tectonophysics 287, 1–20. https://doi.org/10.1016/S0040-1951(98)80058-9

Hentschel, F., Janots, E., Magnin, V., Brückner, L.M., Trepmann, C.A., 2022. Transient deformation and long-term tectonic activity in the Eastern Alps recorded by mylonitic pegmatites. J Struct Geol 155, 104507. https://doi.org/10.1016/j.jsg.2021.104507

Hentschel, F., Janots, E., Trepmann, C.A., Magnin, V., Lanari, P., 2020. Corona formation around monazite and xenotime during greenschist-facies metamorphism and deformation. European Journal of Mineralogy 32, 521–544. https://doi.org/10.5194/ejm-32-521-2020

Hentschel, F., Trepmann, C.A., Janots, E., 2019. Deformation of feldspar at greenschist facies conditions – the record of mylonitic pegmatites from the Pfunderer Mountains, Eastern Alps. Solid Earth 10, 95–116. https://doi.org/10.5194/se-10-95-2019

Heuberger, H., Masch, L., Preuss, E., Schrocker, A., 1984. Quaternary Landslides and Rock Fusion in Central Nepal and in the Tyrolean Alps. Mt Res Dev 4, 345. https://doi.org/10.2307/3673238

Hirth, G., Teyssier, C., Dunlap, W.J., 2001. An evaluation of quartzite flow laws based on comparisons between experimentally and naturally deformed rocks. International Journal of Earth Sciences 90, 77–87. https://doi.org/10.1007/s005310000152

Hirth, G., Tullis, J., 1994. The brittle-plastic transition in experimentally deformed quartz aggregates. J Geophys Res Solid Earth 99, 11731–11747. https://doi.org/10.1029/93JB02873

Hirth, G., Tullis, J., 1992. Dislocation creep regimes in quartz aggregates. J Struct Geol 14, 145–159. https://doi.org/10.1016/0191-8141(92)90053-Y

Hirth, J.P., 1972. The influence of grain boundaries on mechanical properties. Metallurgical Transactions 3, 3047–3067. https://doi.org/10.1007/BF02661312

Hobbs, B.E., 1968. Recrystallization of single crystals of quartz. Tectonophysics 6, 353–401.

Hobbs, B.E., Ord, A., 1988. Plastic instabilities: implications for the origin of intermediate and deep focus earthquakes. J Geophys Res 93, 10521–10540.

Hobbs, B.E., Ord, A., Teyssier, C., 1986. Earthquakes in the ductile regime? Pure and Applied Geophysics PAGEOPH 124, 309–336. https://doi.org/10.1007/BF00875730

Hofmann, K.H., Kleinschrodt, R., Lippert, R., Mager, D., Stöckhert, B., 1983. Geologische Karte des Altkristallins südlich des Tauernfensters zwischen Pfunderer Tal und Tauferer Tal (Südtirol). Schlern 57, 572–590.

Hoinkes, G., Koller, F., Rantitsch, G., Dachs, E., Höck, V., Neubauer, F., Schuster, R., 1999. Alpine metamorphism of the Eastern Alps. Schweizerische Mineralogische und Petrographische Mitteilungen 79, 155–181.

Hoinkes, G., Kostner, A., Thöni, M., 1991. Petrologic constraints for eoalpine eclogite facies metamorphism in the austroalpine Ötztal basement. Mineral Petrol 43, 237–254. https://doi.org/10.1007/BF01164529

Horiba Scientific, 2022. LabSpec 6 Spectroscopy Suite [Software]. Retrieved from https://www.horiba.com/aut/scientific/products/detail/action/show/Product/labspec-6-spectroscopy-suite-software-1843/

Huc, M., Hassani, R., Chéry, J., 1998. Large earthquake nucleation associated with stress exchange between middle and upper crust. Geophys Res Lett 25, 551–554. https://doi.org/10.1029/98GL00091

Hurford, A.J., Flisch, M., Jäger, E., 1989. Unravelling the thermo-tectonic evolution of the Alps: A contribution from fission track analysis and mica dating. Geol Soc Spec Publ 45, 369–398. https://doi.org/10.1144/GSL.SP.1989.045.01.21

Imon, R., Okudaira, T., Kanagawa, K., 2004. Development of shape- and lattice-preferred orientations of amphibole grains during initial cataclastic deformation and subsequent deformation by dissolution-precipitation creep in amphibolites from the Ryoke metamorphic belt, SW Japan. J Struct Geol 26, 793–805. https://doi.org/10.1016/j.jsg.2003.09.004

Ishihara, S., Goshima, T., Iwawaki, S., Shimizu, M., Kamiya, S., 2002. Evaluation of Thermal Stresses Induced in Anisotropic Material during Thermal Shock. Journal of Thermal Stresses 25, 647–661. https://doi.org/10.1080/01495730290074351

Ivanov, B.A., 2005. Numerical Modeling of the Largest Terrestrial Meteorite Craters. Solar System Research 39, 381–409. https://doi.org/10.1007/s11208-005-0051-0

Jessell, M.W., Kostenko, O., Jamtveit, B., 2003. The preservation potential of microstructures during static grain growth. Journal of Metamorphic Geology 21, 481–491. https://doi.org/10.1046/j.1525-1314.2003.00455.x

Ji, S., Zhao, P., 1994. Strength of two-phase rocks: a model based on fiber-loading theory. J Struct Geol 16, 253–262.

John, T., Medvedev, S., Rüpke, L.H., Andersen, T.B., Podladchikov, Y.Y., Austrheim, H., 2009. Generation of intermediate-depth earthquakes by self-localizing thermal runaway. Nat Geosci 2, 137–140. https://doi.org/10.1038/ngeo419

Kame, N., Rice, J.R., Dmowska, R., 2003. Effects of prestress state and rupture velocity on dynamic fault branching. J Geophys Res Solid Earth 108. https://doi.org/10.1029/2002JB002189

Kamo, S.L., Reimold, W.U., Krogh, T.E., Colliston, W.P., 1996. A 2.023 Ga age for the Vredefort impact event and a first report of shock metamorphosed zircons in pseudotachylitic breccias and Granophyre. Earth Planet Sci Lett 144, 369–387. https://doi.org/https://doi.org/10.1016/S0012-821X(96)00180-X

Kaus, B.J.P., Podladchikov, Y.Y., 2006. Initiation of localized shear zones in vizcoelastoplastic rocks. J Geophys Res Solid Earth 111, 1–18. https://doi.org/10.1029/2005JB003652

Kenkmann, T., 2000. Processes controlling the shrinkage of porphyroclasts in gabbroic shear zones. J Struct Geol 22, 471–487. https://doi.org/10.1016/S0191-8141(99)00177-7

Kenner, S.J., 2004. Rheological controls on fault loading rates in northern California following the 1906 San Francisco earthquake. Geophys Res Lett 31, L01606. https://doi.org/10.1029/2003GL018903

Kilian, R., Heilbronner, R., 2017. Analysis of crystallographic preferred orientations of experimentally deformed Black Hills Quartzite. Solid Earth 8, 1095–1117. https://doi.org/10.5194/se-8-1095-2017

Kim, J.W., Ree, J.H., Han, R., Shimamoto, T., 2010. Experimental evidence for the simultaneous formation of pseudotachylyte and mylonite in the brittle regime. Geology 38, 1143–1146. https://doi.org/10.1130/G31593.1

Kimberley, J., Ramesh, K.T., Barnouin, O.S., 2010. Visualization of the failure of quartz under quasi-static and dynamic compression. J Geophys Res Solid Earth 115. https://doi.org/10.1029/2009JB007006

King Hubbert, M., Rubey, W.W., 1959. Role of fluid pressure in mechanics of overthrust faulting: I. Mechanics of fluid-filled porous solids and its application to overthrust faulting. Bulletin of the Geological Society of America 70, 115–166. https://doi.org/10.1130/0016-7606(1959)70[115:ROFPIM]2.0.CO;2

Kirby, S.H., 1980. Tectonic stresses in the lithosphere: Constraints provided by the experimental deformation of rocks. J Geophys Res Solid Earth 85, 6353–6363. https://doi.org/10.1029/JB085iB11p06353

Kirby, S.H., Christie, J.M., 1977. Mechanical twinning in diopside Ca(Mg,Fe)Si2O6: Structural mechanism and associated crystal defects. Phys Chem Miner 1, 137–163. https://doi.org/10.1007/BF00307315

Kirkpatrick, J.D., Shipton, Z.K., 2009. Geologic evidence for multiple slip weakening mechanisms during seismic slip in crystalline rock. J Geophys Res Solid Earth 114. https://doi.org/10.1029/2008JB006037

Kjøll, H. J., Viola, G., Menegon, L., Sørensen, B.E., 2015. Brittle-viscous deformation of vein quartz under fluid-rich lower greenschist facies conditions. Solid Earth 6, 681–699. https://doi.org/10.5194/se-6-681-2015

Kleinschrodt, R., 1987. Quarzkorngefügeanalyse im Altkristallin südlich des westlichen Tauernfensters (Südtirol_Italien). Erlanger geologische Abhandlungen 114, 1–82.

Klotz, T., Pomella, H., Reiser, M., Fügenschuh, B., Zattin, M., 2019. Differential uplift on the boundary between the Eastern and the Southern European Alps: Thermochronologic constraints from the Brenner Base Tunnel. Terra Nova 31, 281–294. https://doi.org/10.1111/ter.12398

Koch, N., 1990. Licht- und elektronenmikroskopische Untersuchungen zur Deformationsgeschichte von Myloniten und Pseudotachyliten der Basis der Silvretta-Decke (Graubünden, Tirol) und Vergleich mit Myloniten der ZEV (Zone von Erbendorf-Vohenstraub, Oberpfalz) - Dissertati (Ph.D. Thesis). Ludwig-Maximilians-University, Munich.

Koch, N., Masch, L., 1992. Formation of Alpine mylonites and pseudotachylytes at the base of the Silvretta nappe, Eastern Alps. Tectonophysics 204, 289–306. https://doi.org/10.1016/0040-1951(92)90313-U

Kohlstedt, D.L., Evans, B., Mackwell, S.J., 1995. Strength of the lithosphere: constraints imposed by laboratory experiments. J Geophys Res 100. https://doi.org/10.1029/95jb01460

Kranz, R.L., 1983. Microcracks in rocks: A review. Tectonophysics 100, 449–480. https://doi.org/10.1016/0040-1951(83)90198-1

Kruse, R., Stünitz, H., 1999. Deformation mechanisms and phase distribution in mafic high-temperature mylonites from the Jotun Nappe, southern Norway. Tectonophysics 303, 223–249. https://doi.org/10.1016/S0040-1951(98)00255-8

Kuebler, K.E., 2013. A combined electron microprobe (EMP) and Raman spectroscopic study of the alteration products in Martian meteorite MIL 03346. J Geophys Res Planets 118, 347–368. https://doi.org/10.1029/2012JE004244

Küster, M., Stöckhert, B., 1999. High differential stress and sublithostatic pore fluid pressure in the ductile regime - microstructural evidence for short-term post-seismic creep in the Sesia Zone, Western Alps. Tectonophysics 303, 263–277. https://doi.org/10.1016/S0040-1951(98)00256-X

Lana, C., Gibson, R.L., Kisters, A.F.M., Reimold, W.U., 2003. Archean crustal structure of the Kaapvaal craton, South Africa – evidence from the Vredefort dome. Earth Planet Sci Lett 206, 133–144. https://doi.org/10.1016/S0012-821X(02)01086-5

Lana, C., Reimold, W.U., Gibson, R.L., Koeberl, C., Siegesmund, S., 2004. Nature of the archean midcrust in the core of the Vredefort dome, Central Kaapvaal Craton, South Africa. Geochim Cosmochim Acta 68, 623–642. https://doi.org/10.1016/S0016-7037(00)00447-2

Langenhorst, F., Boustie, M., Deutsch, A., Hornemann, U., Matignon, Ch., Migault, A., Romain, J.P., 2003. Experimental Techniques for the Simulation of Shock Metamorphism: A Case Study on Calcite, in: High-Pressure Shock Compression of Solids V. Springer New York, New York, pp. 1–27. https://doi.org/10.1007/978-1-4613-0011-3_1

Langenhorst, F., Deutsch, A., 1994. Shock experiments on pre-heated α- and β-quartz: I. Optical and density data. Earth and Planetary Science Letters 125, 407–420. https://doi.org/10.1016/0012-821X(94)90229-1

Laubscher, H. P., 1983. Detachment, shear, and compression in the central Alps, in: Robert D. Hatcher Jr., Harold Williams, Isidore Zietz (Eds.), Contributions to the Tectonics and Geophysics of Mountain Chains. Geological Society of America, pp. 191–211. https://doi.org/10.1130/MEM158-p191

Law, R.D., 1990. Crystallographic fabrics: A selective review of their applications to research in structural geology. Geol Soc Spec Publ 54, 335–352. https://doi.org/10.1144/GSL.SP.1990.054.01.30

Le, K.C., Korobeinik, M., Hackl, K., 2005. Estimation of crack density due to fragmentation of brittle ellipsoidal inhomogeneities embedded in a ductile matrix. Archive of Applied Mechanics 74, 439–448. https://doi.org/10.1007/s00419-004-0367-0

Lee, S.K., Han, R., Kim, E.J., Jeong, G.Y., Khim, H., Hirose, T., 2017. Quasi-equilibrium melting of quartzite upon extreme friction. Nat Geosci 10, 436–441. https://doi.org/10.1038/ngeo2951

Legros, F., Cantagrel, J.M., Devouard, B., 2000. Pseudotachylyte (frictionite) at the base of the Arequipa volcanic landslide deposit (Peru): Implications for emplacement mechanisms. Journal of Geology 108, 601–611. https://doi.org/10.1086/314421

Leroux, H., Reimold, W.U., Doukhan, J.-C., 1994. A TEM investigation of shock metamorphism in quartz from the Vredefort dome, South Africa. Tectonophysics 230, 223–239. https://doi.org/https://doi.org/10.1016/0040-1951(94)90137-6

Lilly, P.A., 1981. Shock metamorphism in the Vredefort collar: evidence for internal shock sources. J Geophys Res 86, 10689–10700. https://doi.org/10.1029/JB086iB11p10689

Lin, A., 2008a. Seismic slip in the lower crust Inferred from granulite-related pseudotachylyte in the Woodroffe thrust, Central Australia. Pure Appl Geophys 165, 215–233. https://doi.org/10.1007/s00024-008-0301-4

Lin, A., 2008b. Fossil Earthquakes: The Formation and Preservation of Pseudotachylytes, Lecture Notes in Earth Sciences. Springer Berlin Heidelberg, Berlin, Heidelberg. https://doi.org/10.1007/978-3-540-74236-4

Lin, A., Maruyama, T., Aaron, S., Michibayashi, K., Camacho, A., Kano, K., 2005. Propagation of seismic slip from brittle to ductile crust: Evidence from pseudotachylyte of the Woodroffe thrust, central Australia. Tectonophysics 402, 21–35. https://doi.org/10.1016/j.tecto.2004.10.016

Lin, A., Shimamoto, T., 1998. Selective melting processes as inferred from experimentally generated pseudotachylytes. J Asian Earth Sci 16, 533–545. https://doi.org/10.1016/S0743-9547(98)00040-3

Lin, A., Sun, Z., Yang, Z., 2003. Multiple generations of pseudotachylyte in the brittle to ductile regimes, Qinling-Dabie Shan ultrahigh-pressure metamorphic complex, central China. Island Arc 12, 423–435. https://doi.org/10.1046/j.1440-1738.2003.00407.x

Linker, M.F., Kirby, S.H., Ord, A., Christie, J.M., 1984. Effects of Compression Direction on the Plasticity and Rheology of Hydrolytically Weakened Synthetic Quartz Crystals At Atmospheric Pressure. J Geophys Res 89, 4241–4255. https://doi.org/10.1029/jb089ib06p04241

Luan, F.C., Paterson, M.S., 1992. Preparation and deformation of synthetic aggregates of quartz. J Geophys Res 97, 77–87. https://doi.org/https://doi.org/10.1029/91JB01748

Maddock, R.H., 1992. Effects of lithology, cataclasis and melting on the composition of fault-generated pseudotachylytes in Lewisian gneiss, Scotland. Tectonophysics 204, 261–278. https://doi.org/10.1016/0040-1951(92)90311-S

Maddock, R.H., 1986. Partial melting of lithic porphyroclasts in fault-generated pseudotachylites. Neues Jahrbuch für Mineralogie. Abhandlungen 155, 1–14.

Maddock, R.H., 1983. Melt origin of fault-generated pseudotachylytes demonstrated by textures. Geology 11, 105–108. https://doi.org/10.1130/0091-7613(1983)11<105:MOOFPD>2.0.CO;2

Maggetti, M., Flisch, M., 1993. Evolution of the Silvretta nappe, in: Raumer, J.F., Neubaue, F. (Eds.), Pre-Mesozoic Geology in the Alps. Springer Berlin Heidelberg, Berlin, Heidelberg, pp. 469–484.

Magloughlin, J.F., 1992. Microstructural and chemical changes associated with cataclasis and frictional melting at shallow crustal levels: the cataclasite-pseudotachylyte connection. Tectonophysics 204, 243–260. https://doi.org/10.1016/0040-1951(92)90310-3

Magloughlin, J.F., 1989. The nature and significance of pseudotachylite from the Nason terrane, North Cascade Mountains, Washington. J Struct Geol 11, 907–917. https://doi.org/10.1016/0191-8141(89)90107-7

Magloughlin, J.F., Spray, J.G., 1992. Frictional melting processes and products in geological materials: introduction and discussion. Tectonophysics 204, 197–204. https://doi.org/10.1016/0040-1951(92)90307-R

Mancktelow, N.S., Stöckli, D., Grollimund, B., Müller, W., Fügenschuh, B., Viola, G., Seward, D., Villa, I.M., 2001. The DAV and Periadriatic fault systems in the Eastern Alps south of the Tauern window. International Journal of Earth Sciences 90, 593–622. https://doi.org/10.1007/s005310000190

Mandl, G.W., 2000. The Alpine sector of the Tethyan shelf-Examples of Triassic to Jurassic sedimentation and deformation from the Northern Calcareous Alps. Mitteilungen der österreichischen geologischen Gesellschaft 92, 61–77.

Marone, C., Scholz, C.H., 1988. The depth of seismic faulting and the upper transition from stable to unstable slip regimes. Geophys Res Lett 15, 621–624. https://doi.org/10.1029/GL015i006p00621

Martin, R.J., Durham, W.B., 1975. Mechanisms of crack growth in quartz. J Geophys Res 80, 4837–4844. https://doi.org/10.1029/jb080i035p04837

Masch, L., 1974. Untersuchung der Aufschmelzung und Deformation der Pseudotachylite der Silvretta (Österreich, Schweiz). Neues Jahrbuch für Mineralgie - Monatshefte 11, 485–509.

Masch, L., 1970. Die Pseudotachylite der Silvretta, eine Untersuchung ihrer Aufschmelzung und Deformation - Dissertation (Dissertation). Ludwig-Maximilians-University, Munich.

Matysiak, A.K., Trepmann, C.A., 2012. Crystal–plastic deformation and recrystallization of peridotite controlled by the seismic cycle. Tectonophysics 530–531, 111–127. https://doi.org/10.1016/j.tecto.2011.11.029

McCarthy, T.S., Stanistreet, I.G., Robb, L.J., 1990. Geological studies related to the origin of the Witwatersrand Basin and its mineralization-an introduction and a strategy for research and exploration. South African Journal of Geology 93, 1–4.

McKenzie, D., Brune, J.N., 1972. Melting on Fault Planes During Large Earthquakes. Geophysical Journal of the Royal Astronomical Society 29, 65–78. https://doi.org/10.1111/j.1365-246X.1972.tb06152.x

McLaren, A.C., Hobbs, B.E., 1972. Transmission Electron Microscope Investigation of Some Naturally Deformed Quartzites. Geophysical Monograph Series 16, 55–66. https://doi.org/10.1029/gm016p0055

Melosh, H.J., 1989. Impact Cratering: a geological process. Oxford University Press, New York.

Menegon, L., Nasipuri, P., Stünitz, H., Behrens, H., Ravna, E., 2011. Dry and strong quartz during deformation of the lower crust in the presence of melt. J Geophys Res Solid Earth 116. https://doi.org/10.1029/2011JB008371

Menegon, L., Pennacchioni, G., Heilbronner, R., Pittarello, L., 2008. Evolution of quartz microstructure and c-axis crystallographic preferred orientation within ductilely deformed granitoids (Arolla unit, Western Alps). J Struct Geol 30, 1332–1347. https://doi.org/10.1016/j.jsg.2008.07.007

Menegon, L., Pennacchioni, G., Malaspina, N., Harris, K., Wood, E., 2017. Earthquakes as Precursors of Ductile Shear Zones in the Dry and Strong Lower Crust. Geochemistry, Geophysics, Geosystems 18, 4356–4374. https://doi.org/10.1002/2017GC007189

Mercolli, I., Oberhänsli, R., 1988. Variscan tectonic evolution in the Central Alps: a working hypothesis. Schweizerische mineralogische und petrographische Mitteilungen 68, 491–500.

Mitchell, T.M., Ben-Zion, Y., Shimamoto, T., 2011. Pulverized fault rocks and damage asymmetry along the Arima-Takatsuki Tectonic Line, Japan. Earth Planet Sci Lett 308, 284–297. https://doi.org/10.1016/j.epsl.2011.04.023

Mitchell, T.M., Toy, V., Di Toro, G., Renner, J., Sibson, R.H., 2016. Fault welding by pseudotachylyte formation. Geology 44, 1059–1062. https://doi.org/10.1130/G38373.1

Moecher, D.P., Steltenpohl, M.G., 2009. Direct calculation of rupture depth for an exhumed paleoseismogenic fault from mylonitic pseudotachylyte. Geology 37, 999–1002. https://doi.org/10.1130/G30166A.1

Montel, J.-M., Michèle Veschambre, S.F., Nicollet, C., Provost, A., 1996. Electron-microprobe dating of monazite: The story. Chem Geol 131, 37–53. https://doi.org/https://doi.org/10.1016/j.chemgeo.2017.11.001

Morales, L.F.G., Mainprice, D., Lloyd, G.E., Law, R.D., 2011. Crystal fabric development and slip systems in a quartz mylonite: An approach via transmission electron microscopy and viscoplastic self-consistent modelling. Geol Soc Spec Publ 360, 151–174. https://doi.org/10.1144/SP360.9

Morauf, W., 1982. Rb-Sr- und K-Ar-Evidenz für eine intensive alpidische Beeinflussung der Paragesteine in Kor- und Saualpe, SE-Ostalpen, Österreich. TMPM Tschermaks Mineralogische und Petrographische Mitteilungen 29, 255–281. https://doi.org/10.1007/BF01091796

Morauf, W., 1980. Die permische Differentiation und die alpidische Metamorphose des Granitgneises von Wolfsberg, Koralpe, SE-Ostalpen, mit Rb-Sr- und K-Ar-Isotopenbestimmungen. TMPM Tschermaks Mineralogische und Petrographische Mitteilungen 27, 169–185. https://doi.org/10.1007/BF01082367

Morrison-Smith, D.J., 1976. Transmission electron microscopy of experimentally deformed hornblende. American Mineralogist 61, 272–280.

Müller, B., Klötzli, U., Flisch, M., 1995. U-Pb and Pb-Pb zircon dating of the older orthogneiss suite in the Silvretta nappe, eastern Alps: Cadomian magmatism in the upper Austro-Alpine realm. Geologische Rundschau 84, 457–465. https://doi.org/10.1007/BF00284513

Müller, W., Mancktelow, N.S., Meier, M., 2000. Rb–Sr microchrons of synkinematic mica in mylonites: an example from the DAV fault of the Eastern Alps. Earth Planet Sci Lett 180, 385–397. https://doi.org/10.1016/S0012-821X(00)00167-9

Müller, W., Prosser, G., Mancktelow, N.S., Villa, I.M., Kelley, S.P., Viola, G., Oberli, F., 2001. Geochronological constraints on the evolution of the Periadriatic Fault System (Alps). International Journal of Earth Sciences 90, 623–653. https://doi.org/10.1007/s005310000187

Muto, J., Hirth, G., Heilbronner, R., Tullis, J., 2011. Plastic anisotropy and fabric evolution in sheared and recrystallized quartz single crystals. J Geophys Res Solid Earth 116, 1–18. https://doi.org/10.1029/2010JB007891

Neubauer, F., Genser, J., Handler, R., 2000. The Eastern Alps: Result of a two-stage collision process. Mitteilungen der Österreichischen Geologischen Gesellschaft 92, 117–134.

Ngo, D., Huang, Y., Rosakis, A., Griffith, W.A., Pollard, D., 2012. Off-fault tensile cracks: A link between geological fault observations, lab experiments, and dynamic rupture models. J Geophys Res Solid Earth 117. https://doi.org/10.1029/2011JB008577

Nicolas, A., Poirier, J.P., 1976. Crystalline Plasticity and Solid State Flow in Metamorphic Rocks. Wiley-Interscience, New York.

Nüchter, J.-A., Ellis, S., 2011. Mid-crustal controls on episodic stress-field rotation around major reverse, normal and strike-slip faults. Geological Society, London, Special Publications 359, 187–201. https://doi.org/10.1144/SP359.11

Nüchter, J.-A., Ellis, S., 2010. Complex states of stress during the normal faulting seismic cycle: Role of midcrustal postseismic creep. J Geophys Res 115, 1–15. https://doi.org/10.1029/2010JB007557

Nüchter, J.-A., Stöckhert, B., 2008. Coupled stress and pore fluid pressure changes in the middle crust: Vein record of coseismic loading and postseismic stress relaxation. Tectonics 27, 1–23. https://doi.org/10.1029/2007TC002180

Nüchter, J.-A., Stöckhert, B., 2007. Vein quartz microfabrics indicating progressive evolution of fractures into cavities during postseismic creep in the middle crust. J Struct Geol 29, 1445–1462. https://doi.org/10.1016/j.jsg.2007.07.011

Nüchter, J.-A., Wassmann, S., Stöckhert, B., 2013. Cyclic ductile and brittle deformation related to coseismic thrust fault propagation: Structural record at the base of a basement nappe (Preveli, Crete). Tectonics 32, 1272–1293. https://doi.org/10.1002/tect.20079

Nur, A., Mavko, G., 1974. Postseismic Viscoelastic Rebound. Science (1979) 183, 204–206. https://doi.org/10.1126/science.183.4121.204

Nyman, M.W., Law, R.D., Smelik, E.A., 1992. Cataclastic deformation mechanism for the development of core-mantle structures in amphibole. Geology 20, 455–458. https://doi.org/10.1130/0091-7613(1992)020<0455:CDMFTD>2.3.CO;2

O'Hara, K., 2001. A pseudotachylyte geothermometer. Journal of Structural Geology 23, 1345–1357. https://doi.org/10.1016/S0191-8141(01)00008-6

O'Hara, K., 1992. Major- and trace-element constraints on the petrogenesis of a fault-related pseudotachylyte, western Blue Ridge province, North Carolina. Tectonophysics 204, 279–288. https://doi.org/10.1016/0040-1951(92)90312-T

Ohl, M., Nzogang, B., Mussi, A., Wallis, D., Drury, M., Plümper, O., 2021. Crystal-Plastic Deformation in Seismically Active Carbonate Fault Rocks. J Geophys Res Solid Earth 126, 1–20. https://doi.org/10.1029/2020JB020626

Oxford Instruments, 2020. AZtec (Version 4.2) [Software].

Palazzin, G., Raimbourg, H., Stünitz, H., Heilbronner, R., Neufeld, K., Précigout, J., 2018. Evolution in H2O contents during deformation of polycrystalline quartz: An experimental study. J Struct Geol 114, 95–110. https://doi.org/10.1016/j.jsg.2018.05.021

Papa, S., Pennacchioni, G., Angel, R.J., Faccenda, M., 2018. The fate of garnet during (deep-seated) coseismic frictional heating: The role of thermal shock. Geology 46, 471–474. https://doi.org/10.1130/G40077.1

Papa, S., Pennacchioni, G., Menegon, L., Thielmann, M., 2020. High-stress creep preceding coseismic rupturing in amphibolite-facies ultramylonites. Earth Planet Sci Lett 541, 116260. https://doi.org/10.1016/j.epsl.2020.116260

Papeschi, S., Musumeci, G., 2019. Fluid-Assisted Strain Localization in Quartz at the Brittle/Ductile Transition. Geochemistry, Geophysics, Geosystems 20, 3044–3064. https://doi.org/10.1029/2019GC008270

Park, Y., Jung, S., Jung, H., 2020. Lattice preferred orientation and deformation microstructures of glaucophane and epidote in experimentally deformed epidote blueschist at high pressure. Minerals 10, 1–21. https://doi.org/10.3390/min10090803

Passchier, C.W., 1985. Water-deficient mylonite zones - An example from the Pyrenees. Lithos 18, 115–127. https://doi.org/10.1016/0024-4937(85)90014-3

Passchier, C.W., 1982a. Mylonitic deformation in the Saint-Barthélemy massif, French Pyrenees, with emphasis on the genetic relationship between ultramylonite and pseudotachylyte. GUA Papers of Geology Series.

Passchier, C.W, 1982b. Pseudotachylyte and the development of ultramylonite bands in the Saint-Barthélemy Massif, French Pyrenees. J Struct Geol 4, 69–79.

Passchier, C.W., Trouw, R.A.J., 2005. Microtectonics. 2nd ed. Springer Berlin Heidelberg, Berlin, Heidelberg. https://doi.org/10.1007/978-3-662-08734-3

Passelègue, F.X., Tielke, J., Mecklenburgh, J., Violay, M., Deldicque, D., Di Toro, G., 2021. Experimental Plastic Reactivation of Pseudotachylyte-Filled Shear Zones. Geophys Res Lett 48. https://doi.org/10.1029/2020GL091538

Pec, M., Stünitz, H., Heilbronner, R., Drury, M., de Capitani, C., 2012. Origin of pseudotachylites in slow creep experiments. Earth Planet Sci Lett 355–356, 299–310. https://doi.org/10.1016/j.epsl.2012.09.004

Pennacchioni, G., Cesare, B., 1997. Ductile-brittle transition in pre-Alpine amphibolite facies mylonites during evolution from water-present to water-deficient conditions (Mont Mary nappe, Italian Western Alps). Journal of Metamorphic Geology 15, 777–791. https://doi.org/10.1111/j.1525-1314.1997.00055.x

Perchuk, L.L., Tokarev, D.A., Van Reenen, D.D., Varlamov, D.A., Gerya, T. V., Sazonova, L. V., Fel'dman, V.I., Smit, C.A., Brink, M.C., Bischoff, A.A., 2002. Dynamic and Thermal History of the Vredefort Explosion Structure in the Kaapvaal Craton, South Africa. Petrology 10, 395–432.

Petch, N.J., 1953. The cleavage strength of polycrystals. Journal of the Iron Steel Institute London 174, 25–28.

Petit, J.P., 1987. Criteria for the sense of movement on fault surfaces in brittle rocks. J Struct Geol 9, 597–608. https://doi.org/10.1016/0191-8141(87)90145-3

Petley-Ragan, A., Ben-Zion, Y., Austrheim, H., Ildefonse, B., Renard, F., Jamtveit, B., 2019. Dynamic earthquake rupture in the lower crust. Sci Adv 5, 913–944. https://doi.org/10.1126/sciadv.aaw0913

Pfiffner, O.A., 2009. Geologie der Alpen. UTB.

Philpotts, A.R., 1964. Origin of pseudotachylites. American Journal of Science 262, 1008–1035. https://doi.org/10.2475/ajs.262.8.1008

Pittarello, L., Levi, N., Wegner, W., Stehlik, H., 2022. The pseudotachylytes at the base of the Silvretta Nappe: A newly discovered recent generation and the tectonomometamophic evolution of the Nappe. Tectonophysics 822. https://doi.org/10.1016/j.tecto.2021.229185

Pittarello, L., Pennacchioni, G., Di Toro, G., 2012. Amphibolite-facies pseudotachylytes in Premosello metagabbro and felsic mylonites (Ivrea Zone, Italy). Tectonophysics 580, 43–57. https://doi.org/10.1016/j.tecto.2012.08.001

Platt, J.P., Vissers, R.L.M., 1980. Extensional structures in anisotropic rocks. J Struct Geol 2, 397–410. https://doi.org/10.1016/0191-8141(80)90002-4

Poelchau, M.H., Kenkmann, T., 2011. Feather features: A low-shock-pressure indicator in quartz. J Geophys Res 116, B02201. https://doi.org/10.1029/2010JB007803

Poirier, J.-P., 1985. Creep of crystals: High-temperature deformation processes in metals, ceramics and minerals. Cambridge University Press, Cambridge. https://doi.org/https://doi.org/10.1017/CBO9780511564451

Poliakov, A.N.B., Dmowska, R., Rice, J.R., 2002. Dynamic shear rupture interactions with fault bends and off-axis secondary faulting. J Geophys Res Solid Earth 107, ESE 6-1-ESE 6-18. https://doi.org/10.1029/2001JB000572

Pollard, D.D., Segall, P., 1987. Theoretical Displacements and Stresses Near Fractures in Rock: With Applications To Faults, Joints, Veins, Dikes, and Solution Surfaces, Fracture Mechanics of Rock. Academic Press Limited. https://doi.org/10.1016/b978-0-12-066266-1.50013-2

Pozzi, G., De Paola, N., Nielsen, S.B., Holdsworth, R.E., Tesei, T., Thieme, M., Demouchy, S., 2021. Coseismic fault lubrication by viscous deformation. Nat Geosci 14, 437–442. https://doi.org/10.1038/s41561-021-00747-8

Price, N.A., Johnson, S.E., Gerbi, C.C., West, D.P., 2012. Identifying deformed pseudotachylyte and its influence on the strength and evolution of a crustal shear zone at the base of the seismogenic zone. Tectonophysics 518–521, 63–83. https://doi.org/10.1016/j.tecto.2011.11.011

Rae, A.S.P., Collins, G.S., Poelchau, M., Riller, U., Davison, T.M., Grieve, R.A.F., Osinski, G.R., Morgan, J. V., IODP-ICDP Expedition 364 Scientists, 2019. Stress-Strain Evolution During Peak-Ring Formation: A Case Study of the Chicxulub Impact Structure. J Geophys Res Planets 124, 396–417. https://doi.org/10.1029/2018JE005821

Rae, A.S.P., Poelchau, M.H., Kenkmann, T., 2021. Stress and strain during shock metamorphism. Icarus 370, 114687. https://doi.org/10.1016/j.icarus.2021.114687

Raleigh, C.B., 1968. Mechanisms of plastic deformation of olivine. J Geophys Res 73, 5391–5406. https://doi.org/10.1029/jb073i016p05391

Ray, S.K., 1999. Transformation of cataclastically deformed rocks to pseudotachylyte by pervasion of frictional melt: inferences from clast-size analysis. Tectonophysics 301, 283–304. https://doi.org/10.1016/S0040-1951(98)00229-7

Regenauer-Lieb, K., Yuen, D., 2004. Positive feedback of interacting ductile faults from coupling of equation of state, rheology and thermal-mechanics. Physics of the Earth and Planetary Interiors 142, 113–135. https://doi.org/10.1016/j.pepi.2004.01.003

Reimold, W.U., 1990. The controversial microdeformations in quartz from the Vredefort structure, South Africa - a discussion. S Afr J Geol 93, 645–663.

Rempe, M., Mitchell, T., Renner, J., Nippress, S., Ben-Zion, Y., Rockwell, T., 2013. Damage and seismic velocity structure of pulverized rocks near the San Andreas Fault. J Geophys Res Solid Earth 118, 2813–2831. https://doi.org/10.1002/jgrb.50184

Rice, J.R., Sammis, C.G., Parsons, R., 2005. Off-fault secondary failure induced by a dynamic slip pulse. Bulletin of the Seismological Society of America 95, 109–134. https://doi.org/10.1785/0120030166

Rockwell, T., Sisk, M., Girty, G., Dor, O., Wechsler, N., Ben-Zion, Y., 2009. Chemical and physical characteristics of pulverized Tejon lookout granite adjacent to the San Andreas and Garlock faults: Implications for earthquake physics. Pure Appl Geophys 166, 1725–1746. https://doi.org/10.1007/s00024-009-0514-1

Rodgers, C. L., de Cserna, Z., Ojeda Rivera, J., Taverna Amezcua, E., van Vloten, R., 1962. Tectonic framework of an area within the Sierra Madre Oriental and adjacent Mesa Central, north central Mexico. Short papers in geology and hydrology: US Geol. Survey Prof. Paper 450, 21–24.

Röller, K., Trepmann, C.A., 2003. Stereo32 (Version 1.0.3) [Software].

Rooney, T.P., Riecker, R.E., Ross, M., 1975. Hornblende deformation features. Geology 3, 364–366. https://doi.org/https://doi.org/10.1130/0091-7613(1975)3<364:HDF>2.0.CO;2

Rooney, T.P., Riecker, R.E., Ross, M., 1970. Deformation twins in Hornblende. Science (1979) 169, 173–175. https://doi.org/10.1126/science.169.3941.173

Rosakis, A.J., 2002. Intersonic shear cracks and fault ruptures. Adv Phys 51, 1189–1257. https://doi.org/10.1080/00018730210122328

Rowe, C.D., Griffith, W.A., 2015. Do faults preserve a record of seismic slip: A second opinion. J Struct Geol. https://doi.org/10.1016/j.jsg.2015.06.006

Rowe, C.D., Kirkpatrick, J.D., Brodsky, E.E., 2012. Fault rock injections record paleo-earthquakes. Earth Planet Sci Lett 335–336, 154–166. https://doi.org/10.1016/j.epsl.2012.04.015

Rowe, C.D., Ross, C., Swanson, M.T., Pollock, S., Backeberg, N.R., Barshi, N.A., Bate, C.E., Carruthers, S., Coulson, S., Dascher-Cousineau, K., Harrichhausen, N., Peña Castro, A.F., Nisbet, H., Rakoczy, P., Scibek, J., Smith, H., Tarling, M.S., Timofeev, A., Young, E., 2018. Geometric Complexity of Earthquake Rupture Surfaces Preserved in Pseudotachylyte Networks. J Geophys Res Solid Earth 123, 7998–8015. https://doi.org/10.1029/2018JB016192

Sammis, C.G., Ben-Zion, Y., 2008. Mechanics of grain-size reduction in fault zones. J Geophys Res 113, B02306. https://doi.org/10.1029/2006JB004892

Samudrala, O., Huang, Y., Rosakis, A.J., 2002. Subsonic and intersonic shear rupture of weak planes with a velocity weakening cohesive zone. J Geophys Res 107, 2170. https://doi.org/10.1029/2001JB000460

Savage, J.C., Prescott, W.H., 1978. Asthenosphere readjustment and the earthquake cycle. J Geophys Res Solid Earth 83, 3369–3376. https://doi.org/10.1029/JB083iB07p03369

Schaltegger, U., Nägler, T.N., Corfu, F., Maggetti, M., Galetti, G., Stosch, H.G., 1997. A Cambrian island arc in the Silvretta nappe: constraints from geochemistry and geochronology. Schweizerische mineralogische und petrographische Mitteilungen 77, 337–350.

Schenk, O., Urai, J.L., 2005. The migration of fluid-filled grain boundaries in recrystallizing synthetic bischofite: First results of in-situ high-pressure, high-temperature deformation experiments in transmitted light. Journal of Metamorphic Geology 23, 695–709. https://doi.org/10.1111/j.1525-1314.2005.00604.x

Schlische, R.W., Young, S.S., Ackermann, R. V., Gupta, A., 1996. Geometry and scaling relations of a population of very small rift-related normal faults. Geology 24, 683. https://doi.org/10.1130/0091-7613(1996)024<0683:GASROA>2.3.CO;2

Schmid, S.M., Casey, M., 1986. Complete Fabric Analysis of Some Commonly Observed Quartz C-Axis Patterns, in: Hobbs, B.E., Heard, H.C. (Eds.), Mineral and Rock Deformation: Laboratory Studies. Geophysical Monograph Series 36, pp. 263–286.

Schmid, S.M., Fügenschuh, B., Kissling, E., Schuster, R., 2004. Tectonic map and overall architecture of the Alpine orogen. Eclogae Geologicae Helvetiae 97, 93–117. https://doi.org/10.1007/s00015-004-1113-x

Schmid, S.M., Scharf, A., Handy, M.R., Rosenberg, C.L., 2013. The Tauern Window (Eastern Alps, Austria): A new tectonic map, with cross-sections and a tectonometamorphic synthesis. Swiss J Geosci 106, 1–32. https://doi.org/10.1007/s00015-013-0123-y

Schmutz, H.-U., 1995. Geologische Untersuchungen im SW-Teil des Unterengadiner Fensters: Teil II, Die makroskopische Geometrie der Pseudotachylite in der Silvretta-Decke am NW-Rand des Unterengadiner Fensters. Baumgartner Druck AG, Burgdorf 166.

Scholz, C.H., 2002. The Mechanics of Earthquakes and Faulting, 2nd ed. Cambridge University Press, New York.

Scholz, C.H., 1998. Earthquakes and friction laws. Nature 391, 37–42.

Scholz, C.H., 1988. The brittle-plastic transition and the depth of seismic faulting. Geologische Rundschau 77, 319–328. https://doi.org/10.1007/BF01848693

Schreyer, W., Medenbach, O., 1981. CO2-Rich Fluid Inclusions Along Planar Elements of Quartz in Basement Rocks of the Vredefort Dome, South Africa. Contributions to Mineralogy and Petrology 77, 93–100.

Schultz, R.A., Jensen, M.C., Bradt, R.C., 1994. Single crystal cleavage of brittle materials. Int J Fract 65, 291–312. https://doi.org/10.1007/BF00012370

Schulz, B., 1994. Microstructural evolution of metapelites from the Austroalpine basement north of Staller Sattel during pre-Alpine and Alpine deformation and metamorphism (Eastern Tyrol, Austria). Jahrbuch Der Geologischen Bundesanstalt 137, 197–212.

Schulz, B., 1989. Jungalpidische Gefügeentwicklung entlang der Defereggen-Antholz-Vals-Linie (Osttirol, Österreich). Jahrbuch der Geologischen Bundesanstalt Wien 132, 775–789.

Schweinehage, R., 1993. Metamorphite der Silvrettadecke / Ostalpen: Thermobarometrische und geochemische Untersuchungen zur präalpidischen Entwicklung. PhD thesis 40. https://doi.org/http://dx.doi.org/10.18419/opus-691

Shand, S.J., 1916. The Pseudotachylyte of Parijs (Orange Free State), and its Relation to 'Trap-Shotten Gneiss' and 'Flinty Crush-Rock.' Quarterly Journal of the Geological Society 72, 198–221. https://doi.org/10.1144/GSL.JGS.1916.072.01-04.12

Shaw, C.A., Allen, J.L., 2007. Field rheology and structural evolution of the Homestake shear zone, Colorado. Rocky Mountain Geology 42, 31–56. https://doi.org/10.2113/gsrocky.42.1.31

Shelley, D., 1994. Spider texture and amphibole preferred orientations. J Struct Geol 16, 709–717. https://doi.org/10.1016/0191-8141(94)90120-1

Sherlock, S.C., Hetzel, R., 2001. A laser-probe 40Ar/39Ar study of pseudotachylite from the Tambach Fault Zone, Kenya: direct isotopic dating of brittle faults. J Struct Geol 23, 33–44. https://doi.org/10.1016/S0191-8141(00)00082-1

Shi, Z., Ben-Zion, Y., 2006. Dynamic rupture on a bimaterial interface governed by slip-weakening friction. Geophys J Int 165, 469–484. https://doi.org/10.1111/j.1365-246X.2006.02853.x

Sibson, R.H., 1986. Earthquakes and rock deformation in crustal fault rocks. Annual Reviews of Earth Planetary Sciences 14, 149–175.

Sibson, R.H., 1983. Continental fault structure and the shallow earthquake source. J Geol Soc London 140, 741–767. https://doi.org/10.1144/gsjgs.140.5.0741

Sibson, R.H., 1980. Transient discontinuities in ductile shear zones. J Struct Geol 2, 165–171. https://doi.org/10.1016/0191-8141(80)90047-4

Sibson, R.H., 1977. Fault rocks and fault mechanisms. J Geol Soc London 133, 191–213. https://doi.org/10.1144/gsjgs.133.3.0191

Sibson, R.H., 1975. Generation of Pseudotachylyte by Ancient Seismic Faulting. Geophysical Journal of the Royal Astronomical Society 43, 775–794. https://doi.org/10.1111/j.1365-246X.1975.tb06195.x

Sibson, R.H., 1974. Frictional constraints on thrust, wrench and normal faults. Nature 249, 542–544. https://doi.org/10.1038/249542a0

Sibson, R.H., Toy, V.G., 2006. The habitat of fault-generated pseudotachylyte: Presence vs. absence of friction-melt, in: Geophysical Monograph Series. Blackwell Publishing Ltd, pp. 153–166. https://doi.org/10.1029/170GM16

Skrotzki, W., 1992. Defect structure and deformation mechanisms in naturally deformed hornblende. Physica Status Solidi (a) 131, 605–624. https://doi.org/10.1002/pssa.2211310232

Sobott, R.J.G., 1979. Hornblende Twinning on (-101) in an Amphibolite from Barra, Outer Hebrides, Scotland. Mineral Mag 43, 177–178. https://doi.org/10.1180/minmag.1979.043.325.21

Song, B.R., Johnson, S.E., Song, W.J., Gerbi, C.C., Yates, M.G., 2020. Coseismic damage runs deep in continental strike-slip faults. Earth Planet Sci Lett 539, 116226. https://doi.org/10.1016/j.epsl.2020.116226

Spiess, R., Cesare, B., Mazzoli, C., Sassi, R., Sassi, F.P., 2010. The crystalline basement of the Adria microplate in the eastern Alps: A review of the palaeostructural evolution from the Neoproterozoic to the Cenozoic, in: Rend. Fis. Acc. Lincei. pp. 31–50. https://doi.org/10.1007/s12210-010-0100-6

Spray, J.G., 2010. Frictional melting processes in planetary materials: From hypervelocity impact to earthquakes. Annu Rev Earth Planet Sci 38, 221–254. https://doi.org/10.1146/annurev.earth.031208.100045

Spray, J.G., 1998. Localized shock-and friction-induced melting in response to hypervelocity impact. Geological Society of London 140, 195–204. https://doi.org/https://doi.org/10.1144/GSL.SP.1998.140.01.14

Spray, J.G., 1995. Pseudotachylyte controversy: Fact or friction? Geology 23, 1119. https://doi.org/10.1130/0091-7613(1995)023<1119:PCFOF>2.3.CO;2

Spray, J.G., 1992. A physical basis for the frictional melting of some rock-forming minerals. Tectonophysics 204, 205–221. https://doi.org/https://doi.org/10.1016/0040-1951(92)90308-S

Spray, J.G., 1987. Artificial generation of pseudotachylyte using friction welding apparatus: simulation of melting on a fault plane, Journal of Structural Geology.

Steenken, A., Siegesmund, S., Heinrichs, T., Fügenschuh, B., 2002. Cooling and exhumation of the Rieserferner Pluton (Eastern Alps, Italy/Austria). International Journal of Earth Sciences 91, 799–817. https://doi.org/10.1007/s00531-002-0260-4

Stein, R.S., King, G.C.P., Rundle, J.B., 1988. The Growth of Geological Structures by Repeated Earthquakes 2. Field Examples of Continental Dip-Slip Faults. J Geophys Res 93, 13,319-13,331. https://doi.org/10.1029/jb093ib11p13307

Stepto, D., 1990. The geology and gravity field in the central core of the Vredefort structure. Tectonophysics 171, 75–103. https://doi.org/10.1016/0040-1951(90)90091-L

Stipp, M., Kunze, K., 2008. Dynamic recrystallization near the brittle-plastic transition in naturally and experimentally deformed quartz aggregates. Tectonophysics 448, 77–97. https://doi.org/10.1016/j.tecto.2007.11.041

Stipp, M., Stünitz, H., Heilbronner, R., Schmid, S.M., 2002. Dynamic recrystallization of quartz: Correlation between natural and experimental conditions. Geol Soc Spec Publ 200, 171–190. https://doi.org/10.1144/GSL.SP.2001.200.01.11

Stipp, M., Tullis, J., 2003. The recrystallized grain size piezometer for quartz. Geophys Res Lett 30, 1–5. https://doi.org/10.1029/2003GL018444

Stöckhert, B., 1987. Das Uttenheimer Pegmatit-Feld (Ostalpines Altkristallin, Südtirol) Genese und alpine Überprägung. Erlanger Geol. Abh. 114, 83–106.

Stöckhert, B., 1984. K-Ar determinations on muscovites and phengites from deformed pegmatites, and the minimum age of the Old Alpine deformation in the Austridic basement to the south of the western Tauern window (Ahrn valley, Southern Tyrol, Eastern Alps). Neues Jahrbuch für Mineralogie Abhandlungen 150, 103–120.

Stöckhert, B., 1982. Deformation und retrograde Metamorphose im Altkristallin S' des westlichen Tauernfensters (Südtirol). Friedrich-Alexander-Universität Erlangen-Nürnberg.

Stöckhert, B., Brix, M.R., Kleinschrodt, R., Hurford, A.J., Wirth, R., 1999a. Thermochronometry and microstructures of quartz - a comparison with experimental flow laws and predictions on the temperature of the brittle - plastic transition. J Struct Geol 21, 351–369. https://doi.org/10.1016/S0191-8141(98)00114-X

Stöffler, D., Langenhorst, F., 1994. Shock metamorphism of quartz in nature and experiment: I. Basic observation and theory*. Meteoritics 29, 155–181. https://doi.org/10.1111/j.1945-5100.1994.tb00670.x

Stünitz, H., Thust, A., Heilbronner, R., Behrens, H., Kilian, R., Tarantola, A., Fitz Gerald, J.D., 2017. Water redistribution in experimentally deformed natural milky quartz single crystals-Implications for $H_2O$-weakening processes. J Geophys Res Solid Earth 122, 866–894. https://doi.org/10.1002/2016JB013533

Swanson, M.T., 2006. Late Paleozoic strike-slip faults and related vein arrays of Cape Elizabeth, Maine. J Struct Geol 28, 456–473. https://doi.org/10.1016/j.jsg.2005.12.009

Swanson, M.T., 1992. Fault structure, wear mechanisms and rupture processes in pseudotachylyte generation. Tectonophysics 204, 223–242. https://doi.org/10.1016/0040-1951(92)90309-T

Takagi, H., Goto, K., Shigematsu, N., 2000. Ultramylonite bands derived from cataclasite and pseudotachylyte in granites, northeast Japan. J Struct Geol 22, 1325–1339. https://doi.org/10.1016/S0191-8141(00)00034-1

Thatcher, W., 1983. Nonlinear strain buildup and the earthquake cycle on the San Andreas Fault. J Geophys Res Solid Earth 88, 5893–5902. https://doi.org/10.1029/JB088iB07p05893

Thielmann, M., Rozel, A., Kaus, B.J.P., Ricard, Y., 2015. Intermediate-depth earthquake generation and shear zone formation caused by grain size reduction and shear heating. Geology 43, 791–794. https://doi.org/10.1130/G36864.1

Thompson, A.W., Knott, J.F., 1993. Micromechanisms of brittle fracture. Metallurgical Transactions A 24, 523–534. https://doi.org/10.1007/BF02656622

Thöni, M., 2006. Dating eclogite-facies metamorphism in the Eastern Alps - Approaches, results, interpretations: A review, in: Mineralogy and Petrology. Springer Wien, pp. 123–148. https://doi.org/10.1007/s00710-006-0153-5

Thöni, M., 1988. Rb-Sr isotopic resetting in mylonites and pseudotachylites: Implications for the detachment and thrusting of the Austroalpine basement nappes in the Eastern Alps. Jahrbuch der Geologischen Bundesanstalt 131, 169–201.

Thöni, M., 1981. Degree and Evolution of the Alpine Metamorphism in the Austroalpine Unit W of the Hohe Tauern in the light of K-Ar and Rb-Sr Age Determinations on Micas. Jahrbuch der Geologischen Bundesanstalt 124, 111–174.

Toy, V.G., Prior, D.J., Norris, R.J., 2008. Quartz fabrics in the Alpine Fault mylonites: Influence of pre-existing preferred orientations on fabric development during progressive uplift. J Struct Geol 30, 602–621. https://doi.org/10.1016/j.jsg.2008.01.001

Trepmann, C.A., 2008. Shock effects in quartz: Compression versus shear deformation — An example from the Rochechouart impact structure, France. Earth Planet Sci Lett 267, 322–332. https://doi.org/10.1016/j.epsl.2007.11.035

Trepmann, C.A., Hsu, C., Hentschel, F., Döhler, K., Schneider, C., Wichmann, V., 2017. Recrystallization of quartz after low-temperature plasticity – The record of stress relaxation below the seismogenic zone. J Struct Geol 95, 77–92. https://doi.org/10.1016/j.jsg.2016.12.004

Trepmann, C.A., Lenze, A., Stöckhert, B., 2010. Static recrystallization of vein quartz pebbles in a high-pressure – low-temperature metamorphic conglomerate. Journal of Petrology 32, 202–215. https://doi.org/10.1016/j.jsg.2009.11.005

Trepmann, C.A., Renner, J., Druiventak, A., 2013. Experimental deformation and recrystallization of olivine- processes and timescales of damage healing during postseismic relaxation at mantle depths. Solid Earth 4, 423–450. https://doi.org/10.5194/se-4-423-2013

Trepmann, C.A., Seybold, L., 2019. Deformation at low and high stress-loading rates. Geoscience Frontiers 10, 43–54. https://doi.org/10.1016/j.gsf.2018.05.002

Trepmann, C.A., Stöckhert, B., 2013. Short-wavelength undulatory extinction in quartz recording coseismic deformation in the middle crust - an experimental study. Solid Earth 4, 263–276. https://doi.org/10.5194/se-4-263-2013

Trepmann, C.A., Stöckhert, B., 2009. Microfabric of folded quartz veins in metagreywackes: Dislocation creep and subgrain rotation at high stress. Journal of Metamorphic Geology 27, 555–570. https://doi.org/10.1111/j.1525-1314.2009.00842.x

Trepmann, C.A., Stöckhert, B., 2003. Quartz microstructures developed during non-steady state plastic flow at rapidly decaying stress and strain rate. J Struct Geol 25, 2035–2051. https://doi.org/10.1016/S0191-8141(03)00073-7

Trepmann, C.A., Stöckhert, B., 2002. Cataclastic deformation of garnet: A record of synseismic loading and postseismic creep. J Struct Geol 24, 1845–1856. https://doi.org/10.1016/S0191-8141(02)00004-4

Trepmann, C.A., Stöckhert, B., 2001. Mechanical twinning of jadeite - An indication of synseismic loading beneath the brittle-plastic transition. International Journal of Earth Sciences 90, 4–13. https://doi.org/10.1007/s005310000165

Trepmann, C.A., Stöckhert, B., Dorner, D., Moghadam, R.H., Küster, M., Röller, K., 2007. Simulating coseismic deformation of quartz in the middle crust and fabric evolution during postseismic stress relaxation - An experimental study. Tectonophysics 442, 83–104. https://doi.org/10.1016/j.tecto.2007.05.005

Tullis, J., 1990. Experimental studies of deformation mechanisms and microstructures in quartzo-feldspathic rocks, in: Deformation Processes in Minerals, Ceramics and Rocks. Springer Netherlands, Dordrecht, pp. 190–227. https://doi.org/10.1007/978-94-011-6827-4_9

Tullis, J., Christie, J., Griggs, D.T., 1973. Microstructures and Preferred Orientations of Experimentally Deformed Quartzites. Geol Soc Am Bull 84, 297. https://doi.org/10.1130/0016-7606(1973)84<297:MAPOOE>2.0.CO;2

Tullis, T.E., 1980. The use of mechanical twinning in minerals as a measure of shear stress magnitudes. J Geophys Res Solid Earth 85, 6263–6268. https://doi.org/10.1029/jb085ib11p06263

Turtle, E.P., Pierazzo, E., 1998. Constraints on the size of the Vredefort impact crater from numerical modeling. Meteoritics & Planetary Science 33, 483–490. https://doi.org/10.1111/j.1945-5100.1998.tb01652.x

Turtle, E.P., Pierazzo, E., O'Brien, D.P., 2003. Numerical modeling of impact heating and cooling of the Vredefort impact structure. Meteoritics & Planetary Science 38, 293–303. https://doi.org/10.1111/j.1945-5100.2003.tb00265.x

Urai, J.L., Means, W.D., Lister, G.S., 1986. Dynamic Recrystallization of Minerals, in: Hobbs, B.E., Heard, H.C. (Eds.), Mineral and Rock Deformation: Laboratory Studies. Geophysical Monograph Series, pp. 161–199. https://doi.org/https://doi.org/10.1029/GM036p0161 van Daalen, M., Heilbronner, R., Kunze, K., 1999. Orientation analysis of localized shear deformation in quartz fibres at the brittle–ductile transition. Tectonophysics 303, 83–107. https://doi.org/10.1016/S0040-1951(98)00264-9

Voll, G., 1976. Recrystallization of Quartz, Biotite and Feldspars from Erstfeld to the Leventina Nappe, Swiss Alps, and its Geological Significance. Schweizerische mineralogische und petrographische Mitteilungen 56, 641–647.

Wald, D.J., Heaton, T.H., 1994. Spatial and temporal distribution of slip for the 1992 Landers, California, earthquake. Bulletin of the Seismological Society of America 84, 668–691. https://doi.org/10.1785/BSSA0840030668

Walsh, J.J., Watterson, J., 1988. Analysis of the relationship between displacements and dimensions of faults. J Struct Geol 10, 239–247. https://doi.org/10.1016/0191-8141(88)90057-0

Wang, B., Li, J.E., Yang, C., 2015. Thermal shock fracture mechanics analysis of a semi-infinite medium based on the dual-phase-lag heat conduction model. Proceedings of the Royal Society A: Mathematical, Physical and Engineering Sciences 471, 20140595. https://doi.org/10.1098/rspa.2014.0595

Watterson, J., 1979. Strain and strain rate gradients at the ductile levels of fault displacements. US Geol. Surv. Open File Rep 79–1239.

Wechsler, N., Allen, E.E., Rockwell, T.K., Girty, G., Chester, J.S., Ben-Zion, Y., 2011. Characterization of pulverized granitoids in a shallow core along the San Andreas Fault, Littlerock, CA. Geophys J Int 186, 401–417. https://doi.org/10.1111/j.1365-246X.2011.05059.x

Weisenberger, T., Bucher, K., 2010. Zeolites in fissures of granites and gneisses of the Central Alps. Journal of Metamorphic Geology 28, 825–847. https://doi.org/10.1111/j.1525-1314.2010.00895.x

Wenk, E., 1934. Beiträge zur Petrographie und Geologie des Silvrettakristallins. Schweizerische Mineralogische und Petrographische Mitteilungen 14, 196–278.

Wenk, H.R., 1978. Are pseudotachylites products of fracture or fusion? Geology 6, 507–511. https://doi.org/10.1130/0091-7613(1978)6<507:APPOFO>2.0.CO;2

Wenk, H.-R., Johnson, L.R., Ratschbacher, L., 2000. Pseudotachylites in the Eastern Peninsular Ranges of California, Tectonophysics.

White, J.C., 2012. Paradoxical pseudotachylyte - Fault melt outside the seismogenic zone. J Struct Geol 38, 11–20. https://doi.org/10.1016/j.jsg.2011.11.016

White, J.C., 2004. Instability and localization of deformation in lower crust granulites, Minas fault zone, Nova Scotia, Canada. Geological Society, London, Special Publications 224, 25–37. https://doi.org/10.1144/GSL.SP.2004.224.01.03

White, J.C., 1996. Transient discontinuities revisited: Pseudotachylyte, plastic instability and the influence of low pore fluid pressure on deformation processes in the mid-crust. J Struct Geol 18, 1471–1477. https://doi.org/10.1016/S0191-8141(96)00059-4

White, S.H., 1973. Syntectonic Recrystallization and Texture Development in Quartz. Nature 244, 276–278. https://doi.org/10.1038/244276a0

White, S.H., Burrows, S.E., Carreras, J., Shaw, N.D., Humphreys, F.J., 1980. On mylonites in ductile shear zones. J Struct Geol 2, 175–187. https://doi.org/10.1016/0191-8141(80)90048-6

Whitmeyer, S.J., Simpson, C., 2003. High strain-rate deformation fabrics characterize a kilometers-thick Paleozoic fault zone in the Eastern Sierras Pampeanas, central Argentina. J Struct Geol 25, 909–922. https://doi.org/10.1016/S0191-8141(02)00118-9

Wilks, K.R., Carter, N.L., 1990. Rheology of some continental lower crustal rocks. Tectonophysics 182, 57–77. https://doi.org/10.1016/0040-1951(90)90342-6

Williams, R.T., Fagereng, Å., 2022. The Role of Quartz Cementation in the Seismic Cycle: A Critical Review. Reviews of Geophysics 60. https://doi.org/10.1029/2021RG000768

Wilson., B., Dewers, T., Reches, Z.E., Brune, J., 2005. Particle size and energetics of gouge from earthquake rupture zones. Nature 434, 749–752.

Xia, K., Yao, W., 2015. Dynamic rock tests using split Hopkinson (Kolsky) bar system – A review. Journal of Rock Mechanics and Geotechnical Engineering 7, 27–59. https://doi.org/10.1016/j.jrmge.2014.07.008

Xu, S., Ben-Zion, Y., 2017. Theoretical constraints on dynamic pulverization of fault zone rocks. Geophys J Int 209, ggx033. https://doi.org/10.1093/gji/ggx033

Yeats, R.S., 1997. The geology of earthquakes. Oxford University Press, New York.

Zhang, Q.B., Zhao, J., 2014. A Review of Dynamic Experimental Techniques and Mechanical Behaviour of Rock Materials. Rock Mech Rock Eng 47, 1411–1478. https://doi.org/10.1007/s00603-013-0463-y

Zhao, P., Ji, S., 1997. Refinements of shear-lag model and its applications. Tectonophysics 279, 37–53. https://doi.org/10.1016/S0040-1951(97)00129-7

# Appendix

## A1 Sample list

**A1:** List of all samples with localities and short sample description, including special microstructures. Pst: Pseudotachylyte; Pst-Pst: Pseudotachylyte deformed/crosscutted by another pseudotachylyte; Br: Brecciated pseudotachylyte; Um: Ultramylonite (deformed pseudotachylyte); Stilp: Stilpnomelane; Cf: Quartz cleavage fractures; Qtz-rich catacl. zones: Quartz-rich cataclastic zones.

| Sample | Locality | Coordinates | Description | Pst structure | Thin sections |
|---|---|---|---|---|---|
| LB 11 | Serfaus, Tirol, Austria | 42°09‘15“ N / 13°30‘24“ E | Gneiss with two schistosities | | 4<br>(a-d) |
| LB 12 | Serfaus, Tirol, Austria | 47°00‘58“ N / 10°27‘59“ E | Pst with quartz<br>Cf<br>Qtz-rich catacl. zones | Pst-Pst<br>Br | 3<br>(a-c) |
| LB 13 | Serfaus, Tirol, Austria | 47°00‘58“ N / 10°27‘59“ E | Pst with quartz | | 3<br>(a-c) |
| LB 14 | Serfaus, Tirol, Austria | 47° 1‘11“ N / 10°28‘28“ E | Deformed pegmatite<br>Cf | | 1<br>(a) |
| LB 15 | Ochsental, Voralberg, Austria | 47°01‘00“ N / 10°28‘00“ E | Dioritic deformed gneiss (pearl gneiss?) with Pst partially intact with minor shear zones. Quartz veins together with Pst.<br>Cf<br>Qtz-rich catacl. zones | | 4<br>(a-d) |
| LB 16 | Ochsental, Voralberg, Austria | 47°01‘00“ N / 10°28‘00“ E | Dioritic deformed gneiss with Pst and breccias, no intact structure | | 2<br>(a-b) |
| LB 17 | Ochsental, Voralberg, Austria | 47°01‘00“ N / 10°28‘00“ E | Strongly foliated gneiss with Pst<br>Very narrow-spaced foliation, partial breccias. Partial mylonitic | | 4<br>(a-d) |
| LB 18 | Ochsental, Voralberg, Austria | 47°01‘00“ N / 10°28‘00“ E | Gneiss with Pst and concordant breccia layer. Quartz-feldspar-rich layer directly adjacent to breccia.<br>Partial mylonitic<br>First brittle deformation-> Pst and then ductile shear zone in quartz with offset | | 3<br>(a-c) |
| LB 19 | Ochsental, Voralberg, Austria | 47°01‘00“ N / 10°28‘00“ E | Dioritic gneiss with Pst and breccia layer | | 5<br>(a-e) |
| LB 20 | Ochsental, Voralberg, Austria | 47°01‘00“ N / 10°28‘00“ E | Dioritic gneiss with Pst and large breccia layer | Pst-Pst<br>Br | 5<br>(a-e) |
| LB 21 | Ochsental, Voralberg, Austria | 47°01‘00“ N / 10°28‘00“ E | Dioritic deformed gneiss with Pst and quartz layers, partially sheared | | 7<br>(a-g) |
| LB 22 | Ochsental, Voralberg, Austria | 47°01‘00“ N / 10°28‘00“ E | Dioritic deformed gneiss with Pst and quartz | | 5<br>(a-e) |
| LB 23 | Ochsental, Voralberg, Austria | 47°01‘00“ N / 10°28‘00“ E | Strongly deformed gneiss, ductile deformation, with quartz and Pst? | | 4<br>(a-d) |

| | | | | | |
|---|---|---|---|---|---|
| LB 24 | Ochsental, Voralberg, Austria | 47°01‘00“ N / 10°28‘00“ E | Quartzite with Pst and coarser quartz layers | Br | 7 (a-g) |
| LB 25 | Ochsental, Voralberg, Austria | 47°01‘00“ N / 10°28‘00“ E | Light-colored gneiss with strongly deformed layers and discordant Pst-vein | | 2 (a-b) |
| LB 26 | Jamtal, Tirol, Austria | 46°53‘27“ N / 10°11‘26“ E | Amphibolite with concordant quartz-vein and Pst-breccia<br>Cf<br>Qtz-rich catacl. zones | | 3 (a-c) |
| LB 27 | Jamtal, Tirol, Austria | 46°53‘23“ N / 10°11‘16“ E | Quartz-feldspar-rich pegmatite with Pst and garnet<br>Cf<br>Qtz-rich catacl. zones | Um | 3 (a-c) |
| LB 28 | Jamtal, Tirol, Austria | 46°53‘23“ N / 10°11‘16“ E | amphibole-gneisses with ultramylonitic layer and large gneiss clasts<br>Stilp | Um | 8 (a-h) |
| LB 29 | Jamtal, Tirol, Austria | 46°52‘51“ N / 10° 10‘17“ | quartz-amphibole-gneiss (pegmatitic) with Pst | | 2 (a-b) |
| LB 30 | Jamtal, Tirol, Austria | 46°52‘31“ N / 10°10‘17“ E | amphibole-quartz-gneisses with Pst | | 2 (a-b) |
| LB 31 | Jamtal, Tirol, Austria | 46°52‘31“ N / 10°10‘17“ E | amphibole- gneiss with concordant quartz veins and Pst | | 4 (a-d) |
| LB 32 | Jamtal, Tirol, Austria | 46°52‘29“ N / 10°10‘15“ E | Layered amphibolite and quartz-gneiss with Pst | Pst-Pst | 2 (a-b) |
| LB 33 | Jamtal, Tirol, Austria | 46°52‘29“ N / 10°10‘15“ E | Layered amphibolite and quartz-gneiss with Pst | | 4 (a-d) |
| LB 34 | Jamtal, Tirol, Austria | 46°52‘16“ N / 10°10‘00“ E | Amphibolite (fine-grained) with Pst | Pst-Pst<br>Br | 6 (a-f) |
| LB 35 | Jamtal, Tirol, Austria | 46°52‘16“ N / 10°10‘00“ E | Amphibolite (fine-grained) with Pst | Pst-Pst | 2 (a-b) |
| LB 36 | Jamtal, Tirol, Austria | 46°52‘16“ N / 10°10‘00“ E | Amphibolite (fine-grained) and subparallel quartz veins. Partially Pst and micro shear zones<br>Cf<br>Qtz-rich catacl. zones | Pst-Pst | 4 (a-d) |
| LB 37 | Jamtal, Tirol, Austria | 46°52‘57“ N / 10°12‘57“ E | Amphibolite with garnets and Pst | | 4 (a-d) |
| LB 38 | Jamtal, Tirol, Austria | 46°52‘57“ N / 10°12‘57“ E | Garnet-rich amphibolite with Pst | Pst-Pst | 3 (a-c) |
| LB 39 | Jamtal, Tirol, Austria | 46°52‘57“ N / 10°12‘57“ E | Garnet-rich amphibolite with Pst | | 2 (a-b) |
| LB 40 | Jamtal, Tirol, Austria | 46°52‘57“ N / 10°12‘57“ E | Pegmatite with quartz vein (boudins) and crosscutting Pst | Pst-Pst<br>Br | 4 (a-d) |
| LB 41 | Jamtal, Tirol, Austria | 46°52‘57“ N / 10°12‘57“ E | Epidote-rich gneiss with concordant quartz layers and Pst | | 3 (a-c) |
| LB 42 | Jamtal, Tirol, Austria | 46°52‘57“ N / 10°12‘57“ E | Amphibolite with quartz layers and Pst<br>Stilp | Pst-Pst<br>Um | 3 (a-c) |
| LB 43 | Jamtal, Tirol, Austria | 46°52‘57“ N / 10°12‘57“ E | Epidote-rich gneiss with quartz layer and thin Pst<br>Qtz-rich catacl. zones | Pst-Pst<br>Um | 3 (a-c) |
| LB 44 | Jamtal, Tirol, Austria | 46°52‘45“ N / 10°10‘52“ E | Amphibolite with quartz-vein and Pst (flow structures)<br>Cf<br>Qtz-rich catacl. zones | | 3 (a-c) |
| LB 45 | Jamtal, Tirol, Austria | 46°52‘45“ N / 10°10‘52“ E | Amphibole-rich gneiss with quartz layer and thin Pst | | 2 (a-b) |

| | | | | | |
|---|---|---|---|---|---|
| LB 46 | Jamtal, Tirol, Austria | 46°52‘45“ N / 10°10‘52“ E | amphibole-epidote-gneiss with concordant quartz-feldspar-layers | | 1<br>(a) |
| LB 47 | Jamtal, Tirol, Austria | 46°52‘45“ N / 10°10‘52“ E | Augengneis with quartz-layers | | 2<br>(a-b) |
| LB 48 | Jamtal, Tirol, Austria | 46°52‘42“ N / 10°10‘59“ E | Quartz-layer with concordant Pst-breccia layer containing different host gneiss clasts<br>Cf<br>Qtz-rich catacl. zones | | 2<br>(a-b) |
| LB 49 | Jamtal, Tirol, Austria | 46°52‘42“ N / 10°10‘59“ E | Quartz-feldspar-rich gneiss with concordant quartz veins and Pst<br>Stilp | | 2<br>(a-b) |
| LB 50 | Jamtal, Tirol, Austria | 46°52‘38“ N / 10°11‘17“ E | Amphibolite with concordant quartz-biotite-rich gneiss and quartz layers with Pst<br>Offset along discordant Pst<br>Stilp | | 1<br>(a) |
| LB 51 | Jamtal, Tirol, Austria | 46°52‘38“ N / 10°11‘17“ E | amphibolite with Pst network | Br | 5<br>(a-e) |
| LB52 | Val Tuoi, Graubünden, Switzerland | 46°49‘34“ N / 10°08‘40“ E | Gneiss with quartz-layer | | - |
| LB 53 | Val Tuoi, Graubünden, Switzerland | 46°49‘28“ N / 10°09‘01“ E | Mylonitic gneiss with ultramylonites (directly from the thrust fault)<br>Cf<br>Qtz-rich catacl. zones | Um | 3<br>(a-c) |
| LB 54 | Val Tuoi, Graubünden, Switzerland | 46°49‘28“ N / 10°09‘01“ E | Mylonitic gneiss with concordant ultramylonites (directly from the thrust fault) | Um | 1<br>(a) |
| LB 55 | Val Tuoi, Graubünden, Switzerland | 46°49‘35“ N / 10°09‘13“ E | Mylonitic gneiss with concordant ultramylonites (directly from the thrust fault) | Um | 2<br>(a-b) |
| LB 56 | Val Tuoi, Graubünden, Switzerland | 46°49‘35“ N / 10°09‘13“ E | Mylonitic gneiss with ultramylonites (directly from the thrust fault) | Um | 2<br>(a-b) |
| LB 57 | Val Tuoi, Graubünden, Switzerland | 46°48'54" N / 10°10'15" E | amphibole- gneiss | Um | 2<br>(a-b) |
| LB 58 | Val Tuoi, Graubünden, Switzerland | 46°48'54" N / 10°10'15" E | amphibole-feldspar-gneiss with Pst and quartz veins | Pst-Pst | 2<br>(a-b) |
| LB 59 | Val Tuoi, Graubünden, Switzerland | 46°48'54" N / 10°10'15" E | mylonite | Um | 1<br>(a) |
| LB 60 | Val Tuoi, Graubünden, Switzerland | 46°48'54" N / 10°10'15" E | Amphibolite with concordant quartz veins | Um | 2<br>(a-b) |
| LB 61 | Val Tuoi, Graubünden, Switzerland | 46°50'04" N / 10°08'59" E | Biotite-rich gneiss (Augengneis) with concordant quartz layer (strain-gradient) | | 2<br>(a-b) |
| LB 62 | Val Tuoi, Graubünden, Switzerland | 46°50'04" N / 10°08'59" E | Mylonite with tiny quartz lenses and Pst | | - |
| LB 63 | Val Tuoi, Graubünden, Switzerland | 46°50'04" N / 10°08'59" E | quartz-feldspar-pegmatite with garnet and tourmaline in contact with amphibole-rich gneiss | | 2<br>(a-b) |

| | | | | | |
|---|---|---|---|---|---|
| LB 64 | Val Tuoi, Graubünden, Switzerland | 46°50'04" N / 10°08'59" E | Feldspar-rich gneiss with quartz clasts and Pst(-breccia)<br>Stilp | | 4<br>(a-d) |
| LB 65 | Val Tuoi, Graubünden, Switzerland | 46°48'03" N / 10°09'06" E | Mylonitic gneiss with ultramylonites<br>Stilp | | 2<br>(a-b) |
| LB 65-1 | Val Tuoi, Graubünden, Switzerland | 46°48'03" N / 10°09'06" E | Mylonitic gneiss with ultramylonites<br>Cf<br>Qtz-rich catacl. zones | Um | 3<br>(a-c) |
| LB 66 | Val Tuoi, Graubünden, Switzerland | 46°48'03" N / 10°09'06" E | Mylonitic gneiss with concordant ultramylonites | | - |
| LB 67 | Val Tuoi, Graubünden, Switzerland | 46°48'03" N / 10°09'06" E | Feldspar-rich gneiss with foliated Pst<br>Cf<br>Qtz-rich catacl. zones | Um | 2<br>(a-b) |
| LB 68 | Val Tuoi, Graubünden, Switzerland | 46°48'00" N / 10°10'53" E | Reddish gneiss (?) without Pst | | - |
| LB 69 | Val Tuoi, Graubünden, Switzerland | 46°48'00" N / 10°10'53" E | Biotite-Feldspar-rich gneiss with Pst and incorporated quartz layers<br>Cf<br>Qtz-rich catacl. zones | | 5<br>(a-e) |
| LB 70 | Val Tuoi, Graubünden, Switzerland | 46°46'42" N / 10°07'56" E | Reddish quartzite | | - |
| LB 71 | Val Tuoi, Graubünden, Switzerland | 46°46'40" N / 10°07'25" E | Quartzite | | - |
| LB 72 | Val Tuoi, Graubünden, Switzerland | 46°46'40" N / 10°07'25" E | Feldspar-rich amphibolite with feldspar-quartz-layer | | 1<br>(a) |
| LB 73 | Val Tuoi, Graubünden, Switzerland | 46°46'40" N / 10°07'25" E | Layered amphibole-quartz-feldspar gneiss | | 1<br>(a) |
| LB 74 | Val Tuoi, Graubünden, Switzerland | 46°46'40" N / 10°07'25" E | Mica shist | | - |
| LB 75 | Val Tuoi, Graubünden, Switzerland | 46°46'40" N / 10°07'25" E | Pegmatitic quartz-layers in contact with amphibolite and with Pst | | 2<br>(a-b) |
| LB 76 | Val Tuoi, Graubünden, Switzerland | 46°46'40" N / 10°07'25" E | Amphibolite with concordant quartz layers | | 1<br>(a) |
| LB 77 | Val Tuoi, Graubünden, Switzerland | 46°46'00" N / 10°09'19" E | Amphibolite with concordant quartz layers | | - |
| LB 78 | Jamtal, Tirol, Austria | 46°52‘50“ N /10°10‘18“ E | Biotite-rich gneiss (Augengneis) with concordant quartz and Pst-breccia layers | Pst-Pst<br>Br<br>Um | 4<br>(a-d) |
| LB 79 | Jamtal, Tirol, Austria | 46°52‘50“ N /10°10‘18“ E | Amphibolite with Pst-breccia and garnet<br>Stilp | Pst-Pst<br>Br<br>Um | 6<br>(a-f) |
| LB 80 | Jamtal, Tirol, Austria | 46°52‘50“ N /10°10‘18“ E | Feldspar-rich amphibolite with Pst-breccia containing clasts of quartz-feldspar-rich gneisses<br>Stilp | | 2<br>(a-b) |

| | | | | | |
|---|---|---|---|---|---|
| LB 81 | Jamtal, Tirol, Austria | 46°51'39" N / 10°12'47" E | Partially mylonitic gneiss with network of different Pst | Pst-Pst<br>Br | 3<br>(a-c) |
| LB 82 | Jamtal, Tirol, Austria | 46°51'39" N / 10°12'47" E | Partially mylonitic gneiss with network of different Pst<br>Stilp<br>Cf | | 3<br>(a-c) |
| LB 83 | Jamtal, Tirol, Austria | 46°51'39" N / 10°12'47" E | Quartzite with Pst | | - |
| LB 84 | Jamtal, Tirol, Austria | 46°51'39" N / 10°12'47" E | Pegmatitic quartz-rich gneiss with Pst | Br<br>Um | 2<br>(a-b) |
| LB 85 | Jamtal, Tirol, Austria | 46°51'39" N / 10°12'47" E | Quarzitic mylonites with Pst | | - |
| LB 86 | Serfaus, Tirol, Austria | 47°3‘21“ N / 10°33‘07“ E | Schist of Penninic units | | - |
| LB 87 | Serfaus, Tirol, Austria | 47°2‘21“ N / 10°31‘37“ E | Layers feldspar-rich amphibolite with concordant quartz veins | | 1<br>(a) |
| LB 88 | Serfaus, Tirol, Austria | 47°2‘27“ N / 10°31‘37“ E | Quartz-feldspar gneiss with Pst | | 1<br>(a) |
| LB 89 | Serfaus, Tirol, Austria | 47°2‘27“ N / 10°31‘37“ E | Amphibolite with foliated Pst<br>Qtz-rich catacl. zones | Um | 1<br>(a) |
| LB 90 | Serfaus, Tirol, Austria | 47°2‘27“ N / 10°31‘37“ E | Mylonitic gneiss with ultramylonites and quartz veins | | 2<br>(a-b) |
| LB 91 | Serfaus, Tirol, Austria | 47°2‘07“ N / 10°31‘19“ E | Gneiss with network of different and partially foliated Pst. | Pst-Pst | 2<br>(a-b) |
| LB 92 | Serfaus, Tirol, Austria | 47°2‘07“ N / 10°31‘19“ E | Gneiss with network of different and partially foliated Pst | Pst-Pst<br>Br | 2<br>(a-b) |
| LB 93 | Serfaus, Tirol, Austria | 47°2‘07“ N / 10°31‘19“ E | Gneiss with network of different and partially foliated Pst | Pst-Pst<br>Br | 2<br>(a-b) |
| LB 94 | Ochsental, Voralberg, Austria | 46°51‘37“ N / 10°06‘45“ E | Augengneis with Pst | | - |
| LB 95 | Ochsental, Voralberg, Austria | 46°51‘59“ N / 10°07‘28“ E | Feldspar-amphibole-rich gneiss (Augengneis) with Pst and shear bands | | 2<br>(a-b) |
| LB 96 | Ochsental, Voralberg, Austria | 46°51‘59“ N / 10°07‘28“ E | Augengneis with amphibole layer and Pst | | - |
| LB 97 | Ochsental, Voralberg, Austria | 46°51‘59“ N / 10°07‘26“ E | Amphibolite with Pst and garnet | | 1<br>(a) |
| LB 98 | Ochsental, Voralberg, Austria | 46°51‘59“ N / 10°08‘25“ E | Gneiss with garnet, quartz-vein and Pst-breccia | | - |
| LB 99 | Ochsental, Voralberg, Austria | 46°51‘59“ N / 10°08‘25“ E | Amphibolite with garnet and concordant quartz-gneiss layers which shows an offset along Pst | | 2<br>(a-b) |
| LB 100 | Ochsental, Voralberg, Austria | 46°51‘50“ N / 10°07‘18“ E | Layered amphibolite with concordant quartz-rich layers and Pst(-breccias). Lenses (boudins) of amphibolites and quartz with networks of Pst injection veins<br>Cf<br>Qtz-rich catacl. zones | | 7<br>(a-g) |
| LB 101 | Ochsental, Voralberg, Austria | 46°51‘50“ N / 10°07‘18“ E | Quartz-feldspar-rich gneiss with concordant layers of amphibolite and quartz showing an offset along Pst | | 3<br>(a-c) |

| | | | | | |
|---|---|---|---|---|---|
| LB 102 | Ochsental, Voralberg, Austria | 46°51‘50“ N / 10°07‘18“ E | Amphibole-feldspar-rich gneiss with concordant layers of amphibolites and Pst | | 2<br>(a-b) |
| | | | | | |
| CT 621 | | 46°55‘21“ N / 10°10‘30“ E | Cf<br>Qtz-rich catacl. zones | | |
| CT 623 | | 46°55‘21“ N / 10°10‘30“ E | Amphibole-rick gneiss with concordant quartz and Pst(-breccia) layers | | 4<br>(a-d) |
| CT 626 | | 46°53‘15“ N / 10°10‘55“ E | Feldspar-quartz-rich gneiss with Pst<br>Cf<br>Qtz-rich catacl. zones | | 2<br>(a-b) |
| CT 627 | | 46°53‘15“ N / 10°10‘55“ E | Cf<br>Qtz-rich catacl. zones | | 1 |
| CT 628 | | 46°53‘15“ N / 10°10‘55“ E | Feldspar-quartz-rich gneiss with Pst | | 2<br>(a-b) |
| CT 629 | | 46°53‘15“ N / 10°10‘55“ E | Amphibole-rick gneiss with quartz and Pst(-breccia) | | 3<br>(a-c) |
| CT 630 | | 46°53‘15“ N / 10°10‘55“ E | Amphibole-rick gneiss with concordant quartz and Pst(-breccia) | | 2<br>(a-b) |
| CT 634 | | 46°53‘15“ N / 10°10‘55“ E | Mylonitic gneiss with structures of Pst-like geometries (Ultramyl?), mica-rich | | 3<br>(a-c) |
| CT 637 | | 46°53‘15“ N / 10°10‘55“ E | Gneiss | | |
| CT755 | | 46°48‘ N / 10°08‘ E | Strongly foliated clay-rich gneiss with clasts of feldspar and quartz<br>Deformation bands(?) | | 1 |
| CT 770 | | 46°48‘ N / 10°08‘ E | Feldspar-rich augengneiss with concordant Pst-layers (partially deformed) | Um | 2<br>(a-b) |
| CT 771 | | 46°49‘ N / 10°12‘ E | Quartz-rich gneiss with concordant amphibole-rich layers | | 1 |
| CT 772 | | 46°49‘ N / 10°11‘ E | Amphibole-rich gneiss with Pst and concordant quartz-layer displaying strain gradient towards lithological contact | | 1 |
| CT 773 | | 46°48‘ N / 10°08‘ E | Amphibole-feldspar-rich gneiss with concordant Pst-layers (partially deformed) and discordant pristine Pst | Pst-Pst Br(?) | 2<br>(a-b) |
| CT 774 | | 46°49‘ N / 10°09‘ E | Gneiss with garnets | | 1 |
| CT 775 | | 46°48‘ N / 10°08‘ E | Strongly foliated mica-rich gneiss with concordant deformed Pst-layers | Um | 2<br>(a-b) |
| CT 776 | | 46°46‘ N / 10°04‘ E | Gneiss with mica | | 2<br>(a-b) |
| CT 777 | | 46°46‘ N / 10°04‘ E | Layered amphibole-quartz-gneiss | | 1 |
| | | | | | |
| FH 36 | | 46°51’12.0” N / 11°42’48.6” E | Mylonitic pegmatite with well-developed shear band foliation and strong lineation<br>(orientation: 016/36) | | 3<br>(a-c) |

| | | | | | |
|---|---|---|---|---|---|
| FH 123 | | 46°51’12.0” N / 11°42’48.6” E | Cataclasite with components of mylonitic pegmatite (orientation: 048/50) | | 2 (a-b) |
| | | | | | |
| V2 2.5 | Vredefort impact structure, South Africa | 26°58‘15.4“ S / 27°23‘19.3“ E | Shocked gneiss see Carporzen et al., 2012 and Dellefant et al., 2022 | | 1 |
| VT 445 | Vredefort impact structure, South Africa | 26°58‘ S / 27°26‘ E | Shocked gneiss | | 1 |

## A2 Sample localities and distribution of microstructures

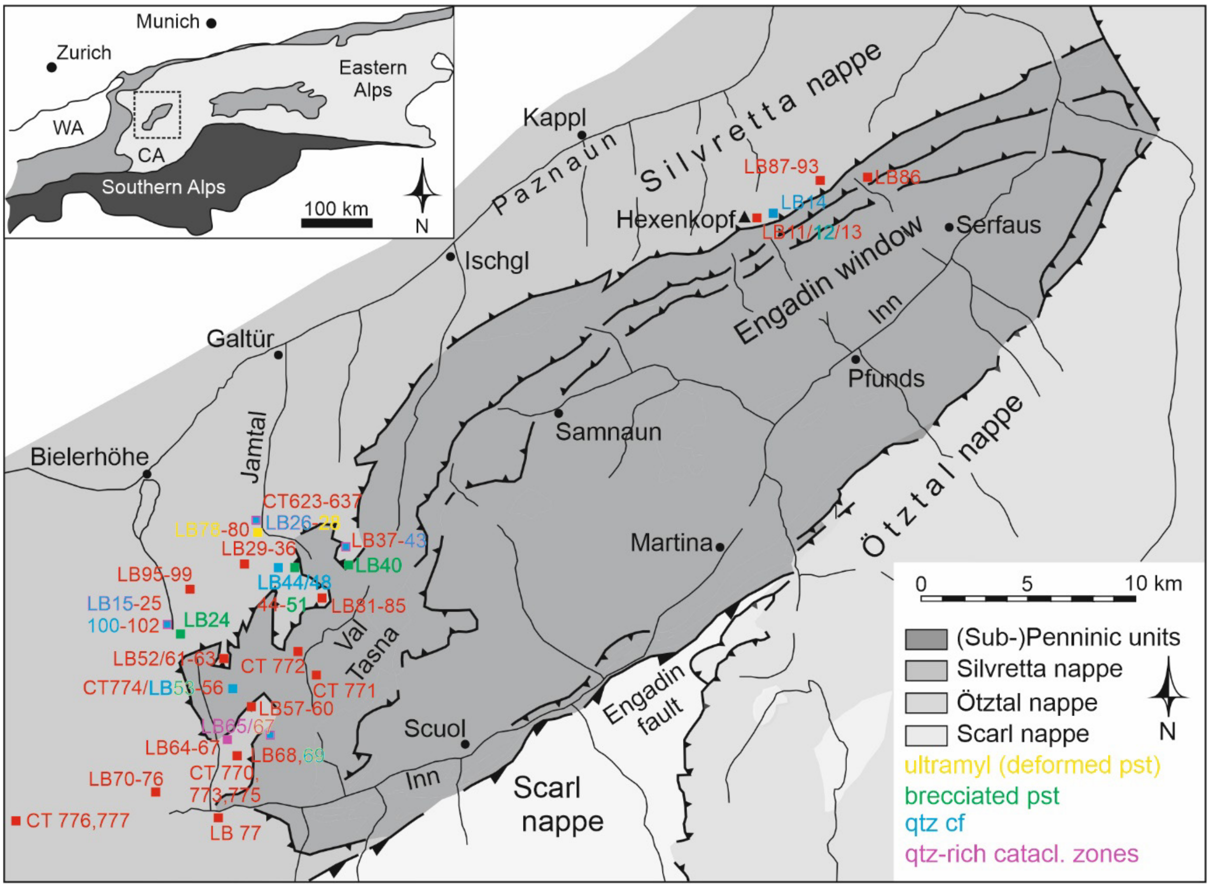

**A2:** Schematic geological map of the Silvretta nappe at the border of the Engadin Window with sample localities and special microstructures, including deformation of quartz (qtz) and pseudotachylytes (pst), ultramylonites (ultramyl), brecciated pseudotachylytes, quartz cleavage fractures (cf) and quartz-rich cataclastic (qtz-rich catacl.) zones. Close-up displays the position of the study area in the central Alps (CA). For exact sample localities see coordinates in A1 (modified after Koch and Masch (1992)).

# Acknowledgment

This work was enabled by a large number of people to whom I am greatly indebted.

First of all, and foremost, I want to thank my supervisor Claudia Trepmann, for her advice, guidance, and patience during discussions of (sometimes tough) issues concerning work, rocks, as well as life. With her casual and cheerful manner, she always brought back my motivation and was a great support over the course of the project. Especially during the last stage of writing the thesis, she promoted and inspired me. Possibly, the joint little spontaneous breaks with chocolate were also a good help. I am extremely lucky to have had her as a mentor and constant support over the past years.

My colleagues and Co-authors are greatly acknowledged for fruitful discussions, evaluation of results, and preparation of manuscripts. All coffee breaks were also highly appreciated.

I would like to thank all of those who assisted me during the field campaigns, in various laboratories and all the staff at LMU, who were always a friendly help, even for the little things. Rosa Susnjar and David Planner deserve great credit for always being immediately available providing fast support for administrative management and IT problems, respectively. I would particularly like to emphasize the team at the Dean's Office, especially Petra Roeske.

Many thanks to all my old friends from home and new Munich friends for providing many great moments of distraction from my work.

The German research foundation is acknowledged for funding the project (DFG Grants No. TR 534/8-1, as well as TR534-4-1, TR534-6-1, and TR 534/9-1).

Last but not least, I want to thank my whole family, for their love, encouragement, and belief in me from the beginning, in particular my grandparents, godfather and godmother. But mostly I am grateful to my parents, Frank and Regina Brückner, who have made all this possible for me and have always been role models, as well as my sister Sophie for her endurance of my moods. A special mention and thanks go to Malte Beiers, for his unconditional endorsement and the necessary support during the last years. Thank you for always being by my side.